An Experimental Study of Gas Lubricated Foil Journal Bearings Using an Instrumented Rotor with Wireless Telemetry

Thèse N° 9163

Présentée le 25 janvier 2019

à la Faculté des sciences et techniques de l'ingénieur
Laboratoire de conception mécanique appliquée
Programme doctoral en energie

pour l'obtention du grade de Docteur ès Sciences

par

KARIM MAGDI ZAKARIA ABDELRAHMAN SHALASH

Acceptée sur proposition du jury

Prof. K. A. J. Mulleners, présidente du jury
Prof. J. A. Schiffmann, directeur de thèse
Prof. M. Arghir, rapporteur
Prof. Ph. Bonello, rapporteur
Prof. P. Reis, rapporteur

2019

ÉCOLE POLYTECHNIQUE
FÉDÉRALE DE LAUSANNE

I shall be telling this with a sigh
Somewhere ages and ages hence:
Two roads diverged in a wood, and I—
I took the one less traveled by,
And that has made all the difference.

— Robert Frost

To my father…

Acknowledgements

During the course of this work many people influenced and encouraged me along the way, without them this work would have never seen the light.

First and foremost, I would like to thank Professor Jürg Schiffmann for giving me this opportunity, guiding me along the way, and most importantly, for believing in me at the darkest of moments. The most important lesson you taught me is that there is nothing "truly" great in the comfort zone. I will be always in debt to you. I would like to extend my gratitude to the jury members Professors Mihai Arghir, Philip Bonello, Pedro Reis, and Karen Mulleners for taking the time to read my thesis. Your constructive comments and suggestions certainly improved the quality of my work.

Julie, thank you for being there all the time and every time. Thank you for pushing me, provoking me, and most of all thank you for a friendship that I will always cherish. Christophe Darioli, you have been a great companion in my PhD journey, it was a great pleasure to work with you. Your technical support was irreplaceable, thank you. Kossi, you have been a great guide and mentor. Now I am a measurements master - thanks to you. I will certainly miss our conversations on the future of Africa.

Violette (Dr. Mounier), you were such a great accomplice and a true friend, you have been there for me whenever needed.....I would re-do my PhD with you anytime!!! Adeel and Ceyhun, I had too much fun working around you, I learned a lot from you, thank you for all the food. Eliott, you are one of the smartest people that I have ever worked with, I enjoyed every argument/debate that we had, you taught me a lot and kept me motivated maybe without noticing. Our mutual passion for Space (and Rick and Morty) will always be our thing. Cyril, sitting in front of me for nearly 3 years was a pleasure, an education, and most importantly fun! you saved me several times, and you certainly made me a better researcher. Now, I know that good science is done during a coffee break! Kevin, thank you for answering my thermodynamics questions on Whatsapp during weekends! Patrick (nearly Dr. Wagner), thank you for making this PhD journey very enjoyable, you are a great engineer and scientist to work with, and above all a true friend.

Eric, Suresh, Markus, Phillip, Lili, Chris, Ansgar, and Wanhui thank you for all the questions, comments, and challenges. You all made me a better researcher and engineer. Cécile Taverney

thank you for responding to all of my silly administrative questions. Marc Jeanneret, Marc Salle, Laurent Chevalley, Maxim Raton, Alfred Thomas, Pierre-André Despont, Joël Currit, Thai Tung Ly, David Naman, Nicholas, Thierry, Christophe, and Antonio your technical support is the cornerstone of this work.

I would like to acknowledge and thank several master students that allowed me to grow academically, technically, and above all personally.

Khalid Saqr, my mentor and friend, thank you for the support, the encouragement, and the guidance to see the bigger picture.

Dr. Christopher DellaCorte, your generosity is rare. I would like to thank you for all the long/detailed letters helping me understand the nature of foil bearings.

Grandfather, thank you for setting the bar too high - 63 years ago. Mom, thank you for the great sacrifice you made for me. I will always be in debt to you. Dad, thank you for being such a tremendous inspiration even after death did us part. I know you are proud.

Chaimaa...there are no words that describe my gratitude, thank you for "bearing" with me, you are all my reasons, I love you to Mars and back.

Joey...thank you for keeping me awake at night, you contributed to finishing this manuscript on time.

Hans Zimmer, Max Richter, Harry Gregson-Williams, Steve Jablonsky , and Jóhann Jóhannsson thank you for keeping me inspired for thousands of hours.

Finally, I would like to acknowledge the financial support of the Swiss National Science Foundation.

Neuchâtel, December 20th 2018
Karim Shalash

Abstract

In order to increase their efficiency and power-density, turbomachines are continuously pushed to run faster, and hotter rotors. These requirements create enormous engineering challenges that affect the design of turbomachines down to the component level. Among these challenges is the choice of an adequate bearing technology. Gas lubricated foil bearings showed competency to support several high-speed turbomachinery applications.

The foil bearing performance is governed by the properties of the gas film and the underlying compliant structure. A significant amount of research is dedicated to analyze the latter. However, the gas film was addressed only once in the experimental research efforts on foil bearings extending from the 1960s. This gap in the literature is due to the complexity of the foil bearing structure that hinders the placement of sensors through the bearing surface. As a consequence, the pressure profile inside the gas film of compliant foil journal bearings were never measured. The lack of such experimental data is hampering the conclusive validation of foil bearing models using pressure as the fundamental variable.

Subsynchronous vibrations are a key issue in the foil bearing technology, which can be the limiting factor on the rotational speed of a turbomachine. These vibrations limit the long life of the foil bearing, and can also destroy the rotor and the bearings. This problem is delaying the complete exploitation of the foil bearing potentials as an enabling technology for high-speed turbomachinery. The complete exploitation of the technology entails running heavier, faster, and hotter rotors, which requires pushing the boundaries of the foil bearing technology beyond the status-quo.

The goal of this thesis is to provide pressure profile measurements within the gas film of compliant foil journal bearings at different rotational speeds. The experimental data will be a step towards the validation of foil bearing models using gas film measurements. An instrumented rotor with embedded pressure probes and a wireless telemetry is used to execute that mission. The designed rotor is capable of measuring the pressure profile at two different axial planes inside the bearing.

The developed embedded pressure probes consisted of pressure transducers, and pneumatic channels to connect them to the measurement point on the surface of the rotor. Such layout required a special calibration procedure in order to account for the dynamics of the pneumatic channel that influences the pressure signal. A Siren Disk was designed and manufactured to produce periodic pressure signals with a controlled frequency and amplitude. Such signal was used to excite the pressure probes, and consequently identity their transfer functions, which are used to correct the pressure signals afterwards.

As a proof of concept, the instrumented rotor was tested on externally pressurized gas journal bearings up to a speed of 37.5 krpm. The test bearings were equipped with pressure taps to measure the spatially sampled pressure profiles from the bearing side. The two measurements were compared and were in good agreement at quasi-static conditions. The bearing side measurement was considered as a reference signal (input), and once compared to the rotor side measurement (output), an in-situ calibration and system identification is performed. The pressure measurements were used to validate an externally pressurized bearing model based on the compressible Reynolds equation at different rotational speeds and supply pressures.

The developed transfer function was subjected to several fitness tests before placing the instrumented rotor on foil bearings and measuring the pressure profiles at different rotational speeds. The developed transfer functions were used to correct the measured signal within the gas film of the foil bearing. Finally, the pressure profiles were compared to a foil bearing model based on the compressible Reynolds equation.

Key words: Gas Bearing, Foil Bearing, Pressure Measurement, Model Validation, Benchmark Data, Foil Bearing Manufacturing, System Identification.

Résumé

Afin d'accroître leur efficacité et leur densité de puissance, les turbomachines sont continuellement poussées à fonctionner plus rapidement avec des rotors plus chauds. Ces exigences créent d'énormes défis techniques qui affectent la conception des turbomachines jusqu'au niveau des composants. Parmi ces défis, il y a le choix d'une technologie de palier adéquate. Les paliers aérodynamiques ont démontré leur compatibilité avec plusieurs applications de turbomachines à grande vitesse.

La performance du palier aérodynamique à feuille dépend des propriétés du film de gaz et de sa structure flexible sous-jacente. Une quantité importante de recherches est consacrée à l'analyse de cette dernière. Cependant, le film de gaz n'a été étudié qu'une seule fois lors des travaux de recherche expérimentale sur les paliers à feuilles des années 1960. Cette lacune dans la littérature est due à la complexité de la structure du palier qui empêche le positionnement des capteurs à travers sa surface. En conséquence, le profil de pression à l'intérieur du film de gaz des paliers lisses en feuilles souples n'a jamais été mesuré. L'absence de telles données expérimentales bloque la validation définitive des modèles de palier utilisant la pression comme variable fondamentale.

Les vibrations sous-synchrones sont un élément clé de la technologie des paliers à feuilles, qui peut être le facteur limitant de la vitesse de rotation d'une turbomachine. Ces vibrations limitent la longévité du palier à feuilles et peuvent également détruire le rotor et les paliers. Ce problème entrave l'exploitation complète du potentiel d'utilisation des paliers à feuilles pour les turbomachines à grande vitesse. L'exploitation complète de la technologie implique de faire tourner des rotors plus lourds, plus rapides et plus chauds, ce qui nécessite de repousser les limites de la technologie au-delà de l'état de l'art.

Le but de cette thèse est de fournir des mesures de profil de pression dans le film de gaz de paliers à feuilles à différentes vitesses de rotation. Les données expérimentales constituent un pas en avant vers la validation des modèles de palier utilisant des mesures de film de gaz. Un rotor instrumenté avec des sondes de pression intégrées et une télémétrie sans fil sont utilisés pour accomplir cette mission. Le rotor conçu est capable de mesurer le profil de pression sur deux plans axiaux différents à l'intérieur du palier.

Les sondes de pression développées se composent de transducteurs de pression et de canaux pneumatiques pour les relier au point de mesure à la surface du rotor. Une telle disposition a nécessité une procédure d'étalonnage spéciale afin de tenir compte de la dynamique du canal pneumatique qui influence le signal de pression. Un disque de sirène a été conçu et fabriqué pour produire des signaux de pression périodiques avec une fréquence et une amplitude contrôlées. Ce signal était utilisé pour exciter les sondes de pression et, par conséquent, identifier leurs fonctions de transfert, qui servent ensuite à corriger les signaux de pression.

Comme preuve de concept, le rotor instrumenté a été testé sur des paliers à gaz sous pression externe jusqu'à une vitesse de 37,5 krpm. Les paliers d'essai ont été équipés de canaux de mesure pour mesurer les profils de pression échantillonnés dans l'espace depuis le côté du paliers. Les deux mesures ont été comparées et concordaient bien dans des conditions quasi-statiques. La mesure du côté du palier a été considérée comme un signal de référence (entrée) et, par rapport à la mesure côté rotor (sortie), un étalonnage in situ et une identification du système ont été effectués. Les mesures de pression ont été utilisées pour valider un modèle de paliers sous pression externe basé sur l'équation de Reynolds compressible à différentes vitesses de rotation et pressions d'alimentation.

La fonction de transfert développée a été soumise à plusieurs tests de vérification avant de placer le rotor instrumenté sur des paliers à feuilles et de mesurer les profils de pression à différentes vitesses de rotation. Les fonctions de transfert développées ont été utilisées pour corriger le signal mesuré. Enfin, les profils de pression ont été comparés à un modèle de palier basé sur l'équation de Reynolds compressible.

Mots clefs : Palier à gaz, palier à feuilles, mesure de pression, validation de modèle, données de référence, fabrication de paliers à feuilles, identification de système.

List of Publications

The work presented in this thesis is published as:

Journal Papers

- Shalash, K., and Schiffmann, J., 2017. ***On the manufacturing of compliant foil bearings.*** Journal of Manufacturing Processes, 25, pp.357-368.
- Shalash, K., Şahin, F.C. and Schiffmann, J., 2018. ***Non-linear transfer function identification of pressure probes using Siren Disks.*** Experimental Thermal and Fluid Science, 91, pp.459-469.
- Shalash, K., Guenat, E. and Schiffmann, J., 2018. ***Spatially Sampled Pressure Profile Measurements in Externally Pressurized Gas Journal Bearings.*** Tribology Transactions, pp.1-28.
- Shalash, K., and Schiffmann, J., 2019. ***An Instrumented High-Speed Rotor with Embedded Telemetry for the Continuous Spatial Pressure Profile Measurement in Gas Lubricated Bearings: A Proof of Concept.*** *[Submitted].*
- Shalash, K., and Schiffmann, J., 2019. ***Pressure Profile Measurements within the Gas Film of Journal Foil Bearings Using an Instrumented Rotor with Telemetry.*** *[Submitted].*

Conference Proceedings

- Shalash, K. and Schiffmann, J., 2017, June. ***Comparative Evaluation of Foil Bearings With Different Compliant Structures for Improved Manufacturability.*** In ASME Turbo Expo 2017: Turbomachinery Technical Conference and Exposition (pp. V07AT34A014-V07AT34A014). American Society of Mechanical Engineers.

Contents

Acknowledgements i

Abstract (English/Français) iii

List of Publications vii

List of figures xiii

List of tables xix

List of Acronyms xxi

Nomenclature xxiii

1 Introduction 1

1.1 Prelude 1
1.2 The Foil Bearing 1
1.3 Problem Statement 3
1.4 Goal and Objectives 5
1.5 Methodology and Thesis Outline 5
1.6 Specific Aspects of Novelty 6

2 Test-Rig Design 9

2.1 Design Specifications 9
2.2 Design Alternatives and Justification 10
  2.2.1 Single rotor driven by embedded motor 10
  2.2.2 Single rotor driven by embedded turbine 10
  2.2.3 Floating bearing 10
  2.2.4 Two coupled rotors configuration 10
  2.2.5 Design Choice and Justification 11
2.3 General Description 11
2.4 Rotor Assembly 12
  2.4.1 Test Rotor Design 12
  2.4.2 Coupling Design 13
  2.4.3 Modal Analysis of the Rotor Assembly 15

2.5 Alignment and Balancing 16
2.6 Measurements Capabilities 16
  2.6.1 Proximity Measurement 17
  2.6.2 Pressure Measurement 18
  2.6.3 Air Mass Flow Measurement 18
2.7 Limitations of the test rig – potential issues 19
2.8 Auxiliary Setups 19

3 Instrumented Rotor Design and Proof of Concept 23
3.1 Introduction 23
3.2 State of the Art 24
3.3 Instrumented Rotor Design 25
3.4 Design Limitations 28
3.5 Proof of Concept at Quasi-static Conditions 29
3.6 Effect of Centrifugal Force on Pressure Measurement 30
3.7 System Identification of Embedded Pressure Probes Using a Mockup and Siren Disk 31
  3.7.1 Siren Disk Description and Design 32
  3.7.2 Siren Disk Qualification 34
  3.7.3 Proof of Concept 37
  3.7.4 Non-linear Transfer Function Identification 39
  3.7.5 Signal Reconstruction 44
  3.7.6 Accuracy of Signal Reconstruction 45
3.8 In-situ System Identification of Embedded Pressure Probes on Externally Pressurized Bearings 47
3.9 Chapter Conclusions 52

4 Externally Pressurized Gas Journal Bearings Measurement Campaign 55
4.1 Introduction 55
4.2 Spatially Sampled Pressure Profile Measurements Using Instrumented bearings 57
  4.2.1 Numerical Modelling 57
  4.2.2 Test Bearing Description 59
  4.2.3 Dimensional Metrology of the Rotor and the Test Bearings 60
  4.2.4 Mass Flow Measurement and Discharge Coefficient Deduction 60
  4.2.5 Effect of Supply Pressure on Circumferential and Axial Pressure Profiles 63
  4.2.6 Effect of Rotational Speed on Circumferential and Axial Pressure Profiles 67
  4.2.7 Effect of Load on Displacement 69
  4.2.8 Effect of Static Load on Pressure Profiles and Mass Flow Rate 72
4.3 Continuous Pressure Profile Measurements Using the Instrumented Rotor . . . 74
  4.3.1 Quasi-static Pressure Field Measurement at Different Supply Pressures . 74
  4.3.2 Circumferential Pressure Profile Measurement at Different Rotational Speeds 79
4.4 Chapter Conclusions 80

5 Foil Bearing Manufacturing 83
5.1 Introduction . . . 83
5.2 Motivation and Nature of the Issue . . . 84
5.3 Goals and Objectives . . . 87
5.4 Manufacturing Process Assessment . . . 87
  5.4.1 Material selection . . . 87
  5.4.2 Foil shaping . . . 88
  5.4.3 Heat Treatment . . . 88
  5.4.4 Coating . . . 89
5.5 Non-Intrusive Geometry Measurement . . . 89
5.6 Optimization of the Manufacturing Process . . . 90
  5.6.1 Full Factorial and Modified Composite Designs . . . 91
5.7 Manufacturing Uncertainty Assessment . . . 94
5.8 Effect of Foil Bearing Manufacturing Errors on Local Clearance and Circularity 97
5.9 Finite Element Analysis of the Bump Foil Forming Process . . . 99
5.10 Improved die design . . . 103
5.11 Cantilever Type Compliant Structure . . . 106
5.12 Effect of Foil Bearing Manufacturing Errors on Rotordynamics . . . 108
5.13 Static Load-Displacement Measurements . . . 110
5.14 Chapter Conclusions . . . 114

6 Compliant Foil Journal Bearings Measurement Campaign 117
6.1 State of the Literature . . . 117
6.2 Description of Bearing Under Investigation . . . 118
  6.2.1 Load-Displacement . . . 120
  6.2.2 Bearing Preload Estimation . . . 121
6.3 Dynamic Response of Instrumented Rotor . . . 122
6.4 Static Eccentricity . . . 125
6.5 Rotor Orbits . . . 126
6.6 Liftoff Speed Identification . . . 127
6.7 Gas Film Pressure Measurement . . . 128
6.8 Model Description . . . 132
6.9 Model Validation Attempt . . . 132
6.10 Bearing Loading . . . 133
6.11 Chapter Conclusions . . . 136

7 Epilogue 137
7.1 Summary . . . 137
7.2 Deductions . . . 138
7.3 Impact and Relevance . . . 140
7.4 Future Work . . . 140

Bibliography 153

Curriculum Vitae **155**

List of Figures

1.1 A photograph of a partial sector in a journal foil bearing highlighting the sleeve, the bump foil, the top foil, and the rotor. 3

1.2 Technology Readiness Levels (TRL) as defined by the National Aeronautics and Space Administration. 4

2.1 Gas bearing test-rig indicating the position of the test bearings, the rotor center of gravity, and the electric driving spindle (dimensions are in mm). 11

2.2 Photograph of the test rig highlighting the driving spindle (left), the test rotor supported on externally pressurized bearings (right), and the quill shaft coupling (center). 12

2.3 R+W MKS miniature coupling with conical clamping rings connecting the electric motor (right) to the test rotor (left). 13

2.4 Undamped modal analysis of the full rotor assembly, motor supported on roller element bearings (10^8 N/m), and test rotor supported on externally pressurized air bearings (10^7 N/m). The first three modes highlights the fixation of the motor relative to the test rotor. 15

2.5 Undamped modal analysis of the test rotor supported on externally pressurized air bearings (10^7 N/m). The coupling is considered fixed from the motor end given the relatively high bearing stiffness supporting the motor. 16

2.6 Micrometric screw setup for the static calibration of proximity probes. The left side supports the tested proximity probe and a reference LVDT sensor, while the right side carries the target surface and a micrometric screw to adjust the gap. 17

2.7 (a) Optical Philtec probe used as a trigger on the test rotor. The trigger signal is generated due to the difference in reflectivity of a black mark on the rotor surface. (b) Sample of the analog trigger signal, highlighting a square like shape that is convenient for post-processing. 18

2.8 Top and side views of the load-displacement auxiliary setup 20

2.9 Top View of the foil bearing break-away torque test setup. 21

3.1 The instrumented rotor concept, highlighting the rotating telemetry system (blue), the pressure insert (red), and the pressure transducers (green). The measurements are executed at the free-end bearing (far from the coupling). . . 26

3.2 Photograph of the pressure insert before assembly inside the rotor. The o-rings are seal the exit of the pneumatic channel along with the rotor's inner bore. The transducers are sealed along with the pressure insert with red silicone (gasket maker). 26
3.3 The test externally pressurized bearing with pressure taps at the same plane as one of the rotating embedded probe. The instrumented rotor is moved axially in order to compare the other embedded probes with the bearing pressure taps. . 27
3.4 Photograph of the sealing test for the insert. Pressurizing the pneumatic channel in order to detect leaks. 28
3.5 Comparison of the gas film pressure profiles from the rotor and stator (bearing) sides at 8 bar supply pressure. The rotor side measurement exposes more details compared to the spatially sampled stator side measurements. The pressure peaks corresponds to the location of 18 air supply restrictors. 30
3.6 Pressure drop due to the centrifugal force subjected on the air column of the pneumatic channel up 37.5 krpm. 31
3.7 Photograph of the Siren disk calibration apparatus. 33
3.8 Holes of the siren disk and the relative positions of the probe and the reference transducer. 33
3.9 Schematic of the siren disk apparatus. 34
3.10 L-Shaped Pressure Probe Mockup Layout. 35
3.11 Pressure drop through the Siren Disk nozzle. 35
3.12 Frequency spectrum for (a) uninterrupted flow and (b) periodic flow at 3.5 kHz, measured by the reference transducer and Probe-3. 36
3.13 Pressure drop due to disk rotation. 36
3.14 Reference and test probe time domain signals for excitations of 10, 7, 3 and 1.2 kHz for Probe-3. 38
3.15 Reference data pressure levels for Probe-3. 38
3.16 Harmonics gains for Probe-3 - plotted with respect to absolute frequency values. 41
3.17 L-shaped probes offset gain and phase lag. 42
3.18 Harmonic gains for Probe-3 - Error bars cover 6 different pressure levels. 44
3.19 Measured and reconstructed signals for excitations of 1.2, 3, 7 and 9.5 kHz for Probe-3. 45
3.20 Goodness of fit values of reconstructed signals for L-Shaped probes (data set 6). 47
3.21 In-Situ transfer function of embedded Probe-1 using the instrumented EP bearing as a reference signal generator. 48
3.22 Pressure signal reconstruction of Probe-1 at 37.5 krpm and a supply pressure of 10 bar using 5 harmonics. 49
3.23 Testing the capability of the transfer function to reconstruct different sets of data at the same control and independent variables (gof > 70%). The transfer function is developed using a different data set than that reconstructed. 50

3.24 Testing the capability of the transfer function to reconstruct data at a different supply pressure and a constant rotational speed (gof > 85%). The transfer function is developed at 7 bar, and the reconstructed data is measured at 5 bar. 51

3.25 Testing the capability of the transfer function to reconstruct measurements using interpolated gain and phase values - (gof > 70%). A transfer function is developed by interpolating two transfer functions at 10 krpm and 20 krpm in order to reconstruct measurements at 15 krpm. 52

4.1 Pressure tap locations in bearing A for axial pressure profile measurement. . . . 59

4.2 Pressure tap locations in bearing B for circumferential pressure profile measurement. 59

4.3 (a) ⌀0.1mm bearing supply nozzle geometry (dimensions in mm), (b) nozzle and tap inspection and measurement using digital microscopy. 61

4.4 (a) Mass flow rate measurement for the two test bearings as a function of supply pressure ($\overline{W}$=0.04), and (b) corresponding deduced discharge coefficients. . . . 62

4.5 Measured and predicted circumferential and axial pressure profiles at different supply pressures ($\overline{W}$=0.04). 65

4.6 Numerical axial pressure profile with optimized nozzle diameters compared to measurement. 66

4.7 Effect of centrifugal growth on the fluid film pressure profile ($\overline{W}$=0.04). 68

4.8 (a) Measured normalized load capacity as a function of the eccentricity ratio at different supply pressures and at 0 rotational speed, and (b) corresponding deduced normalized stiffness. 70

4.9 Normalized measured load as a function of the eccentricity ratio compared to model data obtained (i) by imposing a constant measured Cd and (ii) by applying the Cd correlation from reference [1]. 71

4.10 Measured circumferential pressure profiles under different loads for a supply pressure of 0.7 MPa and zero rotational speed compared to model data obtained (i) by imposing a constant measured Cd and (ii) by applying the Cd correlation from reference [1]. 73

4.11 Effect of load on mass flow rate and effective throttling area at 0.7 MPa supply pressure. 74

4.12 Measured circumferential pressure profiles at different supply pressures comparing the rotor side to the bearing side measurements at $\overline{z} = -0.5$ ($\overline{W}$=0.04). . 76

4.13 Measured pressure field within the gas film of externally pressurized journal bearing B, at quasi-static conditions ($\overline{W}$=0.04), and at a supply pressure of 6 bar (gauge). 77

4.14 Measured pressure contours within the gas film of externally pressurized journal bearing B, at quasi-static conditions ($\overline{W}$=0.04), and at a supply pressure of 6 bar (gauge). 78

4.15 Dynamic response of the instrumented rotor in terms of (a) peak-peak amplitude, and (b) phase lag measured from the front and back bearing measured at a supply pressure of 10 bar (gauge). 79
4.16 Circumferential pressure profiles at different rotational speeds, $P_{supply} = 10 bar$ (gauge) , and at $\overline{z} = -0.5$. 80

5.1 Foil bearing construction elements 84
5.2 Geometrical design variables of a bump that influence its compliance 84
5.3 Qualitative effect of heat treatment temperature and duration on springback showing reduced residual error with increasing heat treatment temperature . . 85
5.4 Effect of bump radius (abscissa) and angle (ordinate) deviation on the normalized bump stiffness (contours) – bump foil stiffness map. The Iordanoff [2] model is used to calculate the stiffness. 86
5.5 Forming dies used to form the top (right) and the bump foils (left). The cut foils are placed into the dies, pressed and then submitted to the heat treatment process 89
5.6 Optical measurement of manufactured foils 90
5.7 ffect of heat treatment temperature on bump foil springback 94
5.8 Correlation between measured bump radius and angle springback errors suggesting a linear correlation 95
5.9 Effect of springback on the geometry of the bump 95
5.10 Scatter of measured bumps on the bump foil performance map suggesting significant increase in bump stiffness as a result of manufacturing deviations . 96
5.11 Augmented statistical distribution of measured normalized bump radii 96
5.12 Effect of springback error on bump height. 98
5.13 Sketch of amplified implications on the bearing geometry due to manufacturing deviations. 99
5.14 FE computational domain representing the two rigid dies and the undeformed foil before the die closing. 100
5.15 Von Mises stress on one bump during the closing of the die. 100
5.16 Effect of friction coefficient between the die and the formed foil on bump foil overall radius springback. 101
5.17 FE model validation with measured bump radius error (Top) and intersection angle θ (Bottom) for each bump. 102
5.18 Von Mises stress along the formed foil with local maxima indicating the transition between the bump and the land region and local minima occurring on the bumps themselves. 103
5.19 Original (a, and c)and modified (b, and d) die designs. 103
5.20 Die curvature and Von Mises stress along the formed foil comparing original and modified die designs. 104
5.21 Geometrical features of the modified bump foil eliminating the sharp theta angle.105

5.22 Kernel distribution of the normalized bump radius comparing the original die design to the modified die design and highlighting the improvement in robustness (precision) and accuracy. 105
5.23 Cantilever compliant foil bearing (all beams are in contact with the sleeve). . . 106
5.24 Dimensions of the cantilever beam foil. 106
5.25 Heat treatment of Cantilever beam foils. 107
5.26 Effect of bump foil manufacturing errors on the stability of foil bearings. Perfectly manufactured bearings should all lie over the black theoretical line. The results highlight the robustness of the cantilever beam design in terms of accuracy and precision. (Only feasible solutions are plotted) 110
5.27 Measured load-displacement and deduced stiffness-displacement for different foil bearings at three points inside the bearing. The results confirm the superiority of the cantilever beam foil bearing in terms of manufacturing robustness (precision). 113

6.1 Comparison between measured and predicted film thickness within the gas film of a journal foil bearing, highlighting a significant underestimation by the model. [Reproduced from reference [3], and used with permission of the National Aeronautics and Space Administration] 118
6.2 Photograph of the actual test foil bearing under investigation highlighting the location of the feedline, the direction of rotation, and the angular reference. . . 119
6.3 Circularity deviation measured in the middle of the foil bearing under investigation. ± 150 μm deviation in circularity is observed. A perfectly precise bearing should yield a horizontal straight line at 0 μm. 120
6.4 Load-displacement curve of the foil bearing under investigation (back bearing). No visible assembly clearance (displacement at no load) is observed. 121
6.5 Friction force versus static load used to quantify the bearing preload pressure. . 122
6.6 Waterfall plot of the instrumented rotor response measured from the front foil bearing [peaks are cropped for visibility, maximum amplitude is 150 μm at approximately 150 Hz]. 123
6.7 Waterfall plot of the instrumented rotor response measured from the back foil bearing where the pressure measurement are executed. 123
6.8 Dynamic response of the instrumented rotor in terms of (a) peak-peak amplitude, and (b) phase lag measured from the front and back bearings. 124
6.9 Static rotor position at different speeds measured from the horizontal and vertical proximity probe placed below the rotor. 125
6.10 Rotor orbits measured from the (a) front, and (b) back bearings at 30 krpm. . . 126
6.11 Rotor orbits measured from the (a) front, and (b) back bearings at 37.5 krpm. . 126
6.12 Friction torque as a function of rotational speed. 128

6.13 Pressure profile evolution with increasing number of harmonics used in signal reconstruction. Increasing the number of harmonics used in the signal reconstruction beyond 6 does not bring further improvement to the reconstructed signal. 129
6.14 GFJB pressure profiles measured at at different rotational speeds at (a) $\overline{z}=0$, and (b) $\overline{z}=-0.5$. Refer to figure 6.2 for reference coordinates. 130
6.15 Comparison of pressure profiles measured at $\overline{z}=0$, and -0.5 at different rotational speeds. 131
6.16 Comparison of measured and predicted pressure profiles for circular and non-circular GFJBs. 133
6.17 Photograph of the instrumented rotor supported on GFJBs and loaded using a simple foil under tension. 134
6.18 Loaded pressure profile measured at 35 krpm and 30 N in the middle of the GFJB and compared to the model predicted pressure profile. 135

List of Tables

3.1 Geomtry of the four L-shaped pressure probes 34

5.1 Full factorial experimental design 91
5.2 Statistical inference of full factorial design 92
5.3 Statistical inference of modified full factorial design 92
5.4 Composite experimental design 93
5.5 Statistical inference of composite design 93
5.6 Foil bearing model parameters 108
5.7 Test bearings under investigation 111

6.1 Foil bearing model parameters 132

List of Acronyms

CAF	Creep age forming
DoE	Design of Experiments
FFT	Fast Fourier transform
gof	Goodness of fit
hpf	Hole passing frequency (Hz)
Meas.	Measured
MTBF	Mean time between failure
Recon.	Reconstructed
Ref.	Reference

Nomenclature

Δh	Reduction in bearing clearance	m
A	Throttling area	m^2
A	Amplitude	-
$\bar{A}$	Mean	-
A_n, B_n, Q_n	Fourier series coefficients of nth harmonic	-
C	Bearing clearance	m, µm
$C_{Local_{act}}$	Actual local clearance	m
C_{Local_D}	Design local clearance	m
C_d	Discharge coefficient	-
D	Heat Treatment Duration	Hr
D	Rotor outer diameter	m
d	supply nozzle diameter	m
D	Bearing diameter	m
D	Probe diameter	mm
E	Young’s modulus	Pa
F	Loading force	N
f	Excitation frequency	Hz
f_{res}	1st resonant frequency	Hz
G_n	Gain in the nth harmonic	-
$h_{b_{act}}$	Actual bump height	m
h_{b_D}	Design bump height	m
h_b	Bump height	m
I	Second moment of area	m^4
K_s	Maximum stiffness	N/mm
l	supply nozzle length	m
L	Bearing length	m
L	Total probe length	mm
l_0	Bump half length	m
L_{beam}	Beam length	m

L_H	Horizontal length	mm
L_V	Vertical length	mm
M	Bearing center to bump side	m
$\dot{m}$	Mass flow rate	kg/s
$\dot{m}_{actual}$	Measured mass flow rate	kg/s
$\dot{m}_{isentropic}$	Isentropic mass flow rate	kg/s
M_{crit}	Critical mass	-
n	Harmonic order	-
n_h	Total number of harmonics	-
P	Forming Pressure	bar
$\overline{P}$	Normalized Pressure $\frac{P_{abs}}{P_{amb}}$	-
$\overline{p}_{exp}$	Measured pressure	Pa
$\overline{p}_{model}$	Estimated pressure	Pa
P_a, P_{amb}	Ambient pressure	Pa
P_{abs}	Absolute pressure	Pa
p_s	Supply Pressure	Pa, bar
Q	mass flow rate	kg/s
q	Unsteady signal	
q_0	Time averaged offset	
R	Bump radius	m
R	Shaft outer radius	m
r	Shaft inner radius	m
R_0	Bump foil overall radius	m
R_{act}	Actual bump radius	m
R_D	Design bump radius	m
R_{sleeve}	Bearing sleeve radius	m
S	Bump compliance	m/N
S_0	Bump pitch	m
t	Foil thickness	m
T	Heat Treatment Temperature	°C
t, T	Time (s)	
Λ	Bearing compressibility number	-
w	Beam width	m
$\overline{W}$	Load capacity	-
X	Model variable	-
x	Displacement	m
X_{act}	Actual bearing center to bump radius center	m
X_D	Design bearing center to bump radius center	m
Y	Model response	-
Z	Axial bearing position	m
α	Bump angle	°
α_{act}	Actual bump angle	°
α_{comp}	Bearing compliance coef.	-

α_D	Design bump angle	°
β	Model coefficient	-
γ	Loss factor	-
γ	Heat Capacity Ratio	-
γ_{eng}	Engagement chord	m
$\gamma_{eng_{disc}}$	Discretized engagement chord	m
δ	Bump deformation	m
δ_{def}	Actual bump deflection	m
ε	Model residual	-
ϵ	eccentricity ratio	-
θ	Bump intersection angle	°
θ	Circumferential angle	°
μ	Dynamic Viscosity	Pa.s
μ_f	Friction coefficient	-
ν	Poisson ratio	-
ρ_{Rot}	Rotor material density	kg/m^3
ρ_s	Supply Density	kg/ m^3
φ	Engagement angle	°
Φ_n	Phase angle of nth harmonic	°
Ω	Shaft rotational speed	1/s
ω	Frequency	Hz

1 Introduction

1.1 Prelude

Energy shaped societies throughout the history of humanity. It is also the main driver of economic growth and prosperity [4]. Efficient energy conversion machines will preserve resources, and hence play a pivotal role in today's society. Several concepts are proposed for efficient, sustainable, and future energy exploitation. Decentralized energy production [5], cogeneration [6], and waste heat recovery [7] are examples of these concepts, which are brought to life using several energy conversion technologies. Key components of energy conversion systems are turbomachines, which are capable of transferring energy from a rotor to a working moving fluid and a vice-versa.

In order to increase their efficiency and power-density, turbomachines are continuously pushed to run faster and hotter [8]. These requirements create engineering challenges that affect and limit the design of turbomachines down to the component level. Among these challenges are adequate bearings, which are an enabling technology for turbomachines.

The role of a journal bearing is to constrain the radial motion of the rotor, while allowing for its rotation. Bearings are also a source of stiffness and damping for the rotor, and should ensure adequate load capacity, as well as stable operation of the rotor. That being said, bearings can be the main obstacle for some high-speed turbomachinery designs due to the low threshold of instability (lack of adequate damping), the insufficient load capacity (lack of adequate stiffness), or the high level of losses.

1.2 The Foil Bearing

Fluid film bearings are a widely used technology to support rotating machinery. The technology relies on a fluid film between the rotor and the bearing to carry the load while permitting the rotation of the rotor. In ***dynamic*** fluid film bearings, the viscosity of the fluid, and the relative velocity between the rotor and the bearing allows the build-up of pressure inside the bearing clearance, which at a certain speed is sufficient to bear the load of the rotor. Such bearings operate by superimposing Poiseuille and Couette flows. In ***static*** (externally pressurized) fluid film bearings, the fluid is first pressurized in auxiliary systems and then injected into the bearing clearance, and hence yielding enough pressure to bear the load of the rotor even without a relative velocity between the rotor and the bearing (zero rotational speed). Fluid film bearings are ideal to support high-speed turbomachinery applications mainly due to their simplicity, and low specific losses. However, it should be highlighted that fluid film bearings suffer from stability thresholds, which are considered a bottleneck for some rotor designs.

Gas lubricated foil bearings showed competency in several high-speed turbomachinery applications. Foil bearings are categorized as self-acting (dynamic) gas lubricated fluid film bearings. They are constructed of three main components: (i) a top foil, which along with the rotor creates the aerodynamic wedge necessary for generating load capacity, (ii) a bump foil, which is serving as a compliant structure beneath the top foil, and (iii) a sleeve, where the bump and top foils are fixed. At the start of the machine, the rotor is in mechanical contact with the top foil, and at a given speed the rotor is rotating fast enough to yield enough pressure within the fluid film to lift-off the top foil. The strength of the foil bearing technology stems from their high load capacity, tolerance to misalignment and thermal gradients, soft failure attributes, and oil-free capabilities. The foil bearing technology is currently integrated in several applications where speed, high temperature, low maintenance requirements, and oil contamination are of paramount importance. These applications include air cycle machines [9], gas turbines [10], turbopumps [11], turbocompressors [12], and turbochargers [13].

Subsynchronous vibrations are the key issue of the foil bearing technology, which can be the limiting factor on the rotational speed of a turbomachine [14–16]. These vibrations may limit the long life of the foil bearing, and can also destroy the rotor and the bearings. This problem is hindering the complete exploitation of the foil bearing potentials as an enabling technology for high-speed turbomachinery.

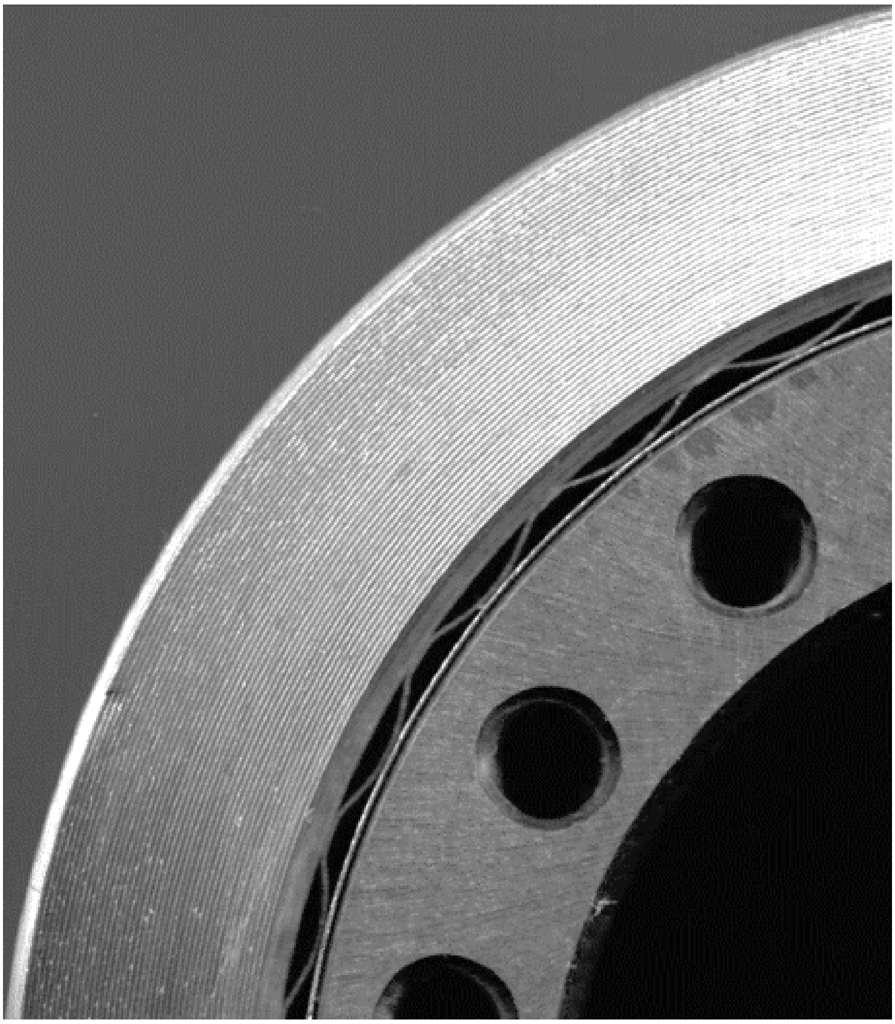

Figure 1.1 – A photograph of a partial sector in a journal foil bearing highlighting the sleeve, the bump foil, the top foil, and the rotor.

1.3 Problem Statement

In terms of first principles, a running foil bearing incorporates different physical phenomena. Fluid dynamics govern the gas film pressure, heat transfer and thermodynamics govern the thermal gradients within the bearing, and structural mechanics govern the compliance of the underlying structure (the bump foil). The interaction between the flow field, the thermal field, and the structure boils down to a complex fluid-structure-interaction problem that governs the gas film inside the bearing, and the deflection of the foils. Moreover, the solution to this problem governs the dynamic coefficients of the bearing (stiffness and damping), which in turn would dictate the rotor dynamics.

Given the complexity and the coupling of the different physical phenomena involved in the operation of a foil bearing, modelling such system is a tedious task. But most importantly, measuring basic quantities like the gas film pressure, temperature, and thickness, as well as the foil deflection is very difficult to execute [3]. The absence of these measurements hinders the conclusive validation of foil bearing models. Which is consequently obstructing the complete understanding and the identification of the root cause of foil bearing problems based on scientifically backed empirical evidence. That being said, and given the fact that foil bearing technologies are already integrated in several market products [9], it seems as if the foil bearing development path jumped several initial steps due to the complexity of the required measurements.

Considering the Technology Readiness Levels (TRL) scale developed by NASA in the 1980s, each newly developed technology shall pass through different phases of development with a precise exit criteria [17]. The scale starts with TRL-1, which is dedicated for basic principles observation and reporting; and ends with TRL-9 , which is the actual successful mission operation. The TRL scale is currently widely used by several technology development institutions including government and industry.

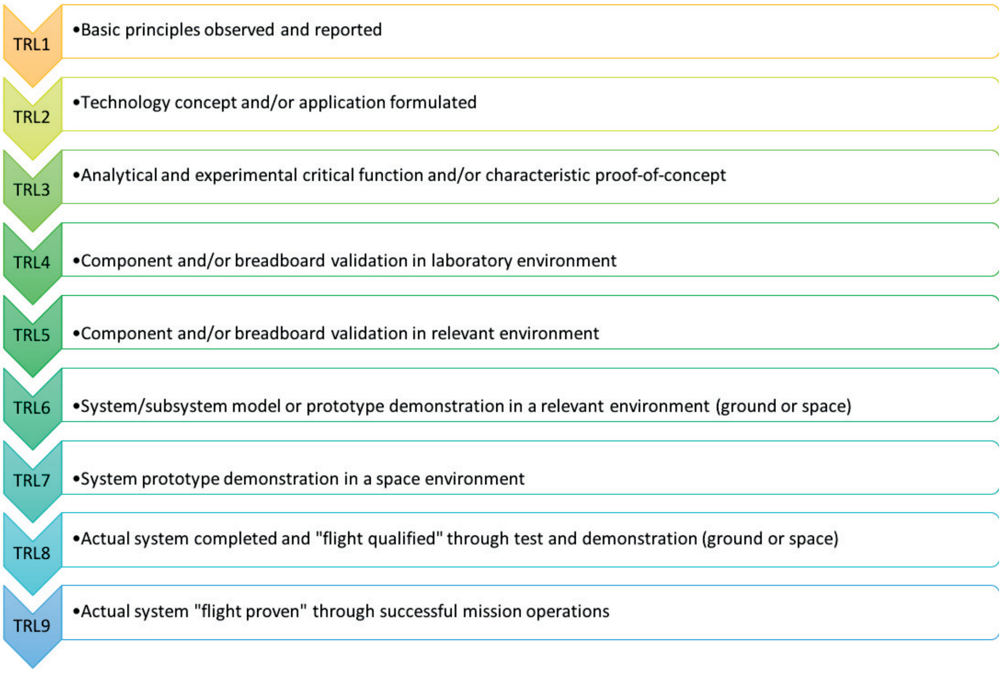

TRL1	•Basic principles observed and reported
TRL2	•Technology concept and/or application formulated
TRL3	•Analytical and experimental critical function and/or characteristic proof-of-concept
TRL4	•Component and/or breadboard validation in laboratory environment
TRL5	•Component and/or breadboard validation in relevant environment
TRL6	•System/subsystem model or prototype demonstration in a relevant environment (ground or space)
TRL7	•System prototype demonstration in a space environment
TRL8	•Actual system completed and "flight qualified" through test and demonstration (ground or space)
TRL9	•Actual system "flight proven" through successful mission operations

Figure 1.2 – Technology Readiness Levels (TRL) as defined by the National Aeronautics and Space Administration.

Foil bearings can be considered a TRL-9 technology. However, they are missing a thorough and a fully conclusive understanding of some physical phenomena manifested during their operation (e.g. subsynchronous vibration). Moreover, they also lack experimentally validated models, which is a consequence of the lack of experimental gas film measurements. At this point, it is worth mentioning that the majority of the experimental effort on foil bearings is either a proof of concept for a machine supported on foil bearings (i.e. ability to run heavy rotors, small rotors, fast, or hot applications), or studying high level performance metrics (i.e.

dynamic response, lift-off speed, startup torque, and structural stiffness and damping).

Only few experimental efforts were dedicated to investigate the fuid film properties of foil bearings on a fundamental level. The pioneering work of Ruscitto et al. [3] measured the gas film thickness in foil journal bearings up to 55 krpm and at different loads. The work of Radil and Zeszotek [18] was an attempt to measure the gas film temperature gradients in foil journal bearings at different speeds and loads.

A better fundamental understanding of the basic quantities governing the performance of foil bearings is required to push the boundaries and the limitations of the foil bearing technology. This requires further research at TRL-1, and 2. Such endeavor will eventually allow running heavier, faster, and hotter turbomachines.

1.4 Goal and Objectives

The goal of this thesis is to address the lack of experimental data hindering the conclusive validation of foil bearing models. Which in turn is expected to shed light on the problem of subsynchronous vibrations in foil bearings either directly through the measurements, or indirectly through the validated models. In order to attain this goal the following objectives are defined:

1. Designing and building of a test-rig capable of testing foil bearings beyond their liftoff speeds, and up to the instability thresholds of the rotors.
2. Designing and prototyping of an instrumented rotor capable of measuring the pressure within the gas film of foil bearings.
3. Manufacture serviceable journal foil bearings.
4. Measuring the pressure within the gas film of journal foil bearings.
5. Compare the measurements to a foil bearing model.

1.5 Methodology and Thesis Outline

As highlighted previously, the lack of experimental measurements is the main motivation behind this thesis work. Hence, the methodology adopted to address the research problem under investigation relies mainly on an experimental approach. This thesis is comprised of seven chapters, beyond the introduction and conclusion chapters, each chapter is addressing an independent stand-alone scientific or engineering challenge.

- **Chapter Two** introduces the test-rigs used throughout the experimental campaign. A description of the used instrumentation is also detailed. Furthermore, the chapter highlights the rationale behind the different design choices made, as well as the limitations of the designed test-rig.

- **Chapter Three** introduces the concept of the instrumented rotor measurement, and a detailed mechanical design for it. The development of the embedded pressure probes and their system identification procedure are also presented. A technique to recover distorted pressure signals (amplified, or attenuated) is discussed in this chapter. A proof of concept of the instrumented rotor pressure measurements are presented on externally pressurized bearings.
- **Chapter Four** is dedicated to the presentation and discussion of the pressure field measurements in within the gas film of externally pressurized journal bearings. The measurements are performed using the instrumented rotor, and also through the pressure taps spatially placed on the bearing circumference. The measurements are compared to a FDM Reynolds equation based bearing model. Comparison between the rotor and bearing side measurements are compared at different rotational speeds and supply pressures.
- **Chapter Five** is dedicated to discuss the manufacturing process of compliant foil bearings. A review of the available literature is presented, followed by a Design of Experiment optimization of the manufacturing process. Different compliant structures are compared in terms of ease of manufacturing and robustness. The effect of manufacturing errors on the bearing performance are also discussed.
- **Chapter Six** presents the experimental campaign studying foil bearings. The chapter presents and discusses the pressure measurements within the gas film of foil bearings. A comparison to a foil bearing model is presented, and discussed.
- **Chapter Seven** presents the conclusions of the thesis, and the recommendations for future work, as well as highlighting the remaining open questions.

1.6 Specific Aspects of Novelty

The presented thesis contains several aspects of novelty which are summarized in the following points:

- Prototyping an instrumented rotor capable of pressure measurement inside gas journal bearings up to 37.5 krpm (more than 30000 Gs at the rotor periphery) with a wirless telemetry system.
- Exploiting the pressure signal from the embedded pressure probes inside the instrumented rotor even beyond their resonance frequency.
- Measurement of continuous pressure fields within the gas film of externally pressurized gas journal bearings up to 37.5 krpm and at different supply pressures.

- Measurement of continuous pressure profiles within the gas film of compliant foil journal bearings up to 37.5 krpm and 30 N load.
- Comparing gas film measurements to the computations of a foil bearing model based on the compressible Reynolds equation.
- Optimizing the manufacturing process of foil bearings to improve the accuracy and robustness of manufacturing.
- Studying the effect of manufacturing errors on foil bearing performance.

2 Test-Rig Design

This chapter presents a detailed description of the gas bearing test-rig used in the experimental campaign. A justification of the selected design choices and comparisons with other alternatives are presented. A detailed design procedure of the test-rotor and the quill-shaft coupling are also described. Furthermore, the chapter describes the instrumentation and measurement capabilities of the test-rig, as well as two auxiliary setups used for stiffness and break-away torque measurements.

2.1 Design Specifications

The first step prior to embarking on the experimental campaign is to design and build a test-rig capable of simulating the desired test conditions, as well as controlling the independent and control variables, all while measuring the dependent variables. The objective of the test-rig is to characterize high-speed gas lubricated journal bearings. The main requirements of the test-rig are:

1. The capability of testing a $\varnothing 40$ mm gas journal bearing.
2. The versatility to test different types and sizes of journal bearings - within a certain range.
3. The capability of running at rotational speeds up to 60000 rpm.
4. Good rotor alignment and balancing.
5. The capability of running an instrumented rotor with embedded sensors.
6. Rotor orbit and rotational speed measurement capabilities, as well as generic pressure and mass flow rate measurement capacity.

2.2 Design Alternatives and Justification

There are different design concepts that would conform to the previosuly mentioned requirements. Four potential concepts are compared below:

2.2.1 Single rotor driven by embedded motor

A single test rotor with an embedded permanent magnet has the advantage of eliminating all the challenges of coupling two high speed rotors. However, the permanent magnet would not allowed the integration of sensors and a wireless telemetry system into the rotor. The work of von Osmanski et al. [19], and Sim and Park [20] are examples of the successful implementation of such design.

2.2.2 Single rotor driven by embedded turbine

A single rotor driven by an air turbine shares the same advantages of the first option, and would allow the instrumentation of the rotor. However, it would have required a large mass flow rate of compressed air to overcome the boundary lubrication torque of foil bearings during startup. Also, speed control and breaking would have been challenging due to the high inertia of the rotor. Moreover, the turbine would have acted as a heat sink, hence influencing the thermal management of the rotor. Furthermore, a thrust disk would have been required for axial load bearing. The NASA test-rig developed by Howard [21] is a successful implementation of the described design.

2.2.3 Floating bearing

Another option is the floating bearing configuration, which is a rotor rigidly supported on roller element bearings and driven by an embedded turbine (or motor). A test gas bearing is held with a wire overhung to this rotor in a floating configuration. In effect, this would allow much more control on test conditions for the floating journal bearing per se. However, it would yield different dynamics compared to the real-life applications, where the rotor is floating and not the bearing. The NASA test-rig by Ruscitto et al. [3] is a classic example of such layout.

2.2.4 Two coupled rotors configuration

The final option is driving a test rotor supported on gas bearings with an electric motor using a mechanical coupling - similar to Kim and San Andres [15]. Such design would fullfil all the main requirements, yet, it will impose the challenge of coupling two high speed rotors [22, 23].

2.2.5 Design Choice and Justification

The two coupled rotors configuration is selected as the design choice for the test-rig. The rationale behind the selection lies in its complete fulfillment of the required specifications. And also, due to its similarity to the common layout of an electric machine coupled to a turbomachine. Moreover, it is relatively simple to control using the electric motor.

2.3 General Description

The test-rig is comprised of a foundation, an electric motor, and a test section. The foundation is a large precision steel plate - Figure 2.1. A precision ruler guide is fixed on the foundation to ensure the alignment of the test section and the driving motor. The test section is comprised of a 40 mm test rotor and two test journal bearings. The test journal bearings are supported inside two slit clamp bearings holders, which are 160 mm apart. The test rotor is driven by an 18 kW electric motor via mechanical coupling. The electric motor is supported on rigid roller element bearings, which are capable of carrying radial and axial loads. Therefore, no axial bearing is needed in the test-section. The bearing holders are fixed relative to the ground, and the motor is freely adjustable to accommodate for different mechanical coupling designs. Figure 2.2 shows a photograph of the complete test-rig with an in-house designed quill-shaft coupling and the test rotor supported on externally pressurized gas journal bearings (EPGJB).

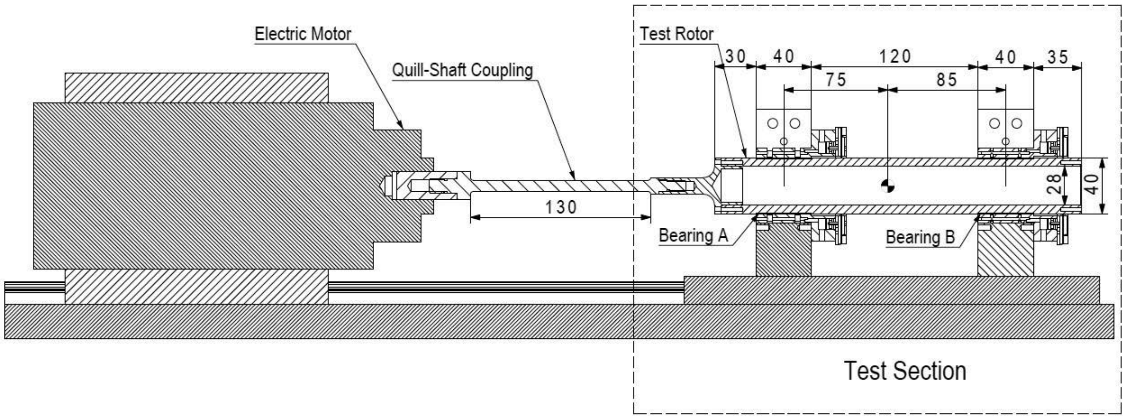

Figure 2.1 – Gas bearing test-rig indicating the position of the test bearings, the rotor center of gravity, and the electric driving spindle (dimensions are in mm).

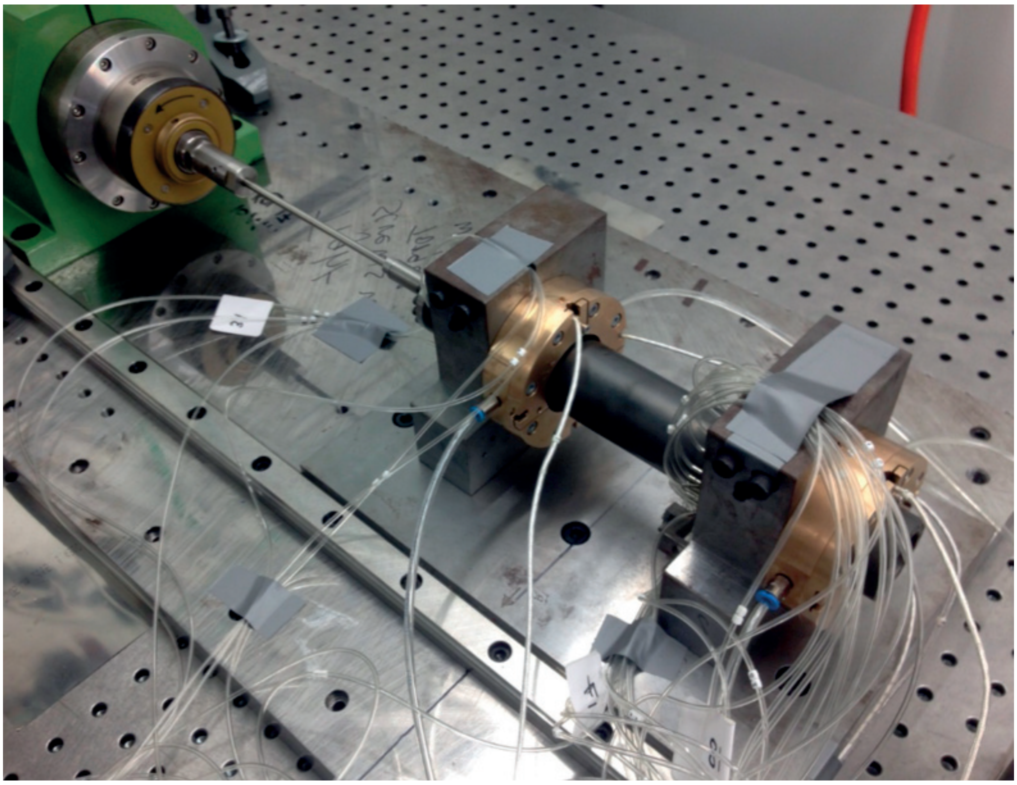

Figure 2.2 – Photograph of the test rig highlighting the driving spindle (left), the test rotor supported on externally pressurized bearings (right), and the quill shaft coupling (center).

2.4 Rotor Assembly

The full rotor assembly consists of three main parts: the rotor of the electric motor, a mechanical coupling, and the test rotor. The rotor of the bearings of the electric motor have a stiffness in the order of 10^8 N/m, such value is roughly one order of magnitude higher than externally pressurized bearings, and two orders of magnitude higher than foil bearings. The motor is connected to the coupling through a custom made HSK-C 25 tool holder. The test rotor has a connector attached to it with 16 circumferential screws, which acts as an interface between the test rotor and the coupling.

2.4.1 Test Rotor Design

The test rotor has a nominal diameter of 40 mm, a length of 265 mm, is made of 100Cr6 Steel, weighs 1.3 kg, and has a rotational and transverse inertia of $3.912\text{x}10^{-4}$ kgm^2 and $8\text{x}10^{-3}$ kgm^2 respectively. The outer surface of the rotor is coated with a Balinit DLC dry lubricant coating, which is stable up to 360°C. The rotor is coated with a dry lubricant in order to reduce the boundary lubrication friction during startup and shutdown.

A free-free modal analysis using the FEM package Ansys was performed to ensure that the first bending mode of the rotor is far beyond the available maximum speed of the test-rig (60000 rpm). The simulation results showed that the first bending mode is at approximately 2600 Hz (156000 rpm), hence the rotor is operating sub-critical.

2.4.2 Coupling Design

Coupling a rotor supported on gas lubricated bearings with another supported on roller element bearings is a challenging task. Preloads exerted from the assembly of the coupling and the rotors will impose a synchronous orbit or a static eccentricity on the rotor supported on gas bearings even at quasi-static conditions. For this reason a special attention was dedicated to the design and selection of the used coupling.

Commercial Couplings

Several commercial bellow couplings were tested, most of them were not fit to the task due to an initial bending in the coupling body that imposed a large preload and consequently a rotor orbit that scaled with the bearing clearance. The only successful commercial coupling was the R+W MKS miniature coupling with conical clamping rings – figure 2.3. Such design includes 4 fixing screws from each side to connect to the test rotor and the motor. These fixing screws allows the operator to adjust them individually to minimize the assembly preload. The coupling was tested up to 37500 rpm on both externally pressurized, and foil bearings.

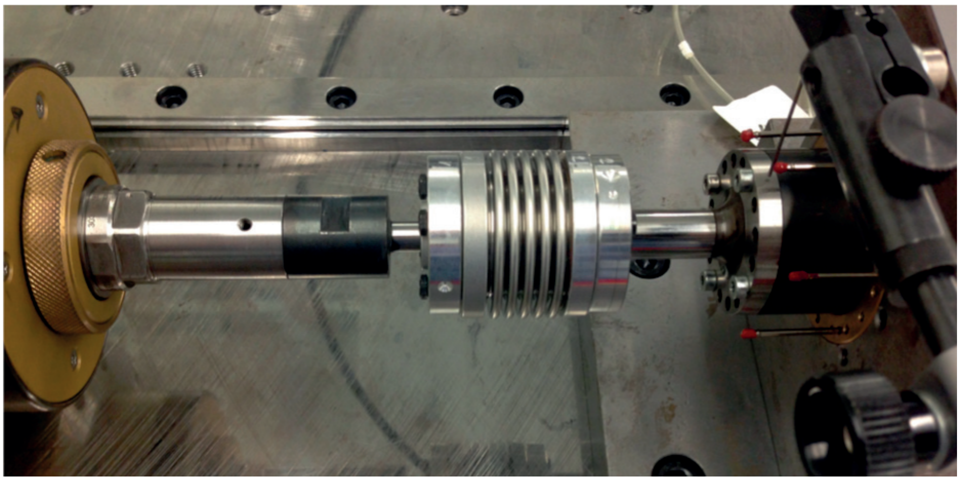

Figure 2.3 – R+W MKS miniature coupling with conical clamping rings connecting the electric motor (right) to the test rotor (left).

Custom Design Couplings

Another attempt was to tailor design a coupling for the test-rig operating conditions. An ideal coupling should be able to transmit the necessary torque, while dynamically isolating the coupled rotors. For this reason, a Stainless Steel quill-shaft coupling was designed and manufactured with a bending stiffness one order of magnitude lower than the stiffness of EP bearings, and the same order of magnitude as foil bearings.

The coupling radius r_c is defined as follows:

$$r_c = \left(\frac{2TF_s}{\tau_{max}\pi} \right)^{\frac{1}{3}} \tag{2.1}$$

where T is the torque, F_s is the factor of safety, and τ_{max} is the yield shear stress.

The coupling length is chosen to be the value to fulfill both bending and torsional stiffness constraints as follows:

$$l = \left(\frac{3EJ}{K_b} \right)^{\frac{1}{3}} \tag{2.2}$$

$$l = \frac{GJ}{K_\theta} \tag{2.3}$$

where E is the elastic modulus, J is the second moment of area, K_b is the bending stiffness, G is the shear modulus, and K_θ is the torsional stiffness.

A Finite Element Analysis (FEA) is performed to assess the combined effects of torque, and potential imbalance due to manufacturing (bow shaped). Local stress levels were ensured to be below the yield strength of the material.

Finally, a modal analysis for the complete rotor assembly is performed in order to identify the eigenfrequencies of the system. Since the rotor of the electric motor is rigidly mounted on roller element bearings, only the coupling and the test rotor are considered in the modal analysis. The coupling side connected to the motor is considered fixed, and the bearings were modeled as springs using measured stiffness values from the load-displacement tests on externally pressurized bearings - see chapter 5.

2.4.3 Modal Analysis of the Rotor Assembly

A second FEA was performed using the complete rotor assembly including the two rotors and the coupling, with the exact bearing locations, and with stiffness values that corresponds to the roller element bearings of the motor, and the gas bearings supporting the test rotor. Due to the high flexibility of the coupling, no rigid body modes were observed. The high stiffness roller element bearings in the electric motor shifts all the rotordynamics to the coupling and the test rotor. Modes are observed at 552 Hz, and 614 Hz, and a clear bending mode for the quill-shaft at 1359 Hz - Figure 2.4. The first two modes are conical modes from the point of view of the test rotor due to the high rigidity of the motor bearings.

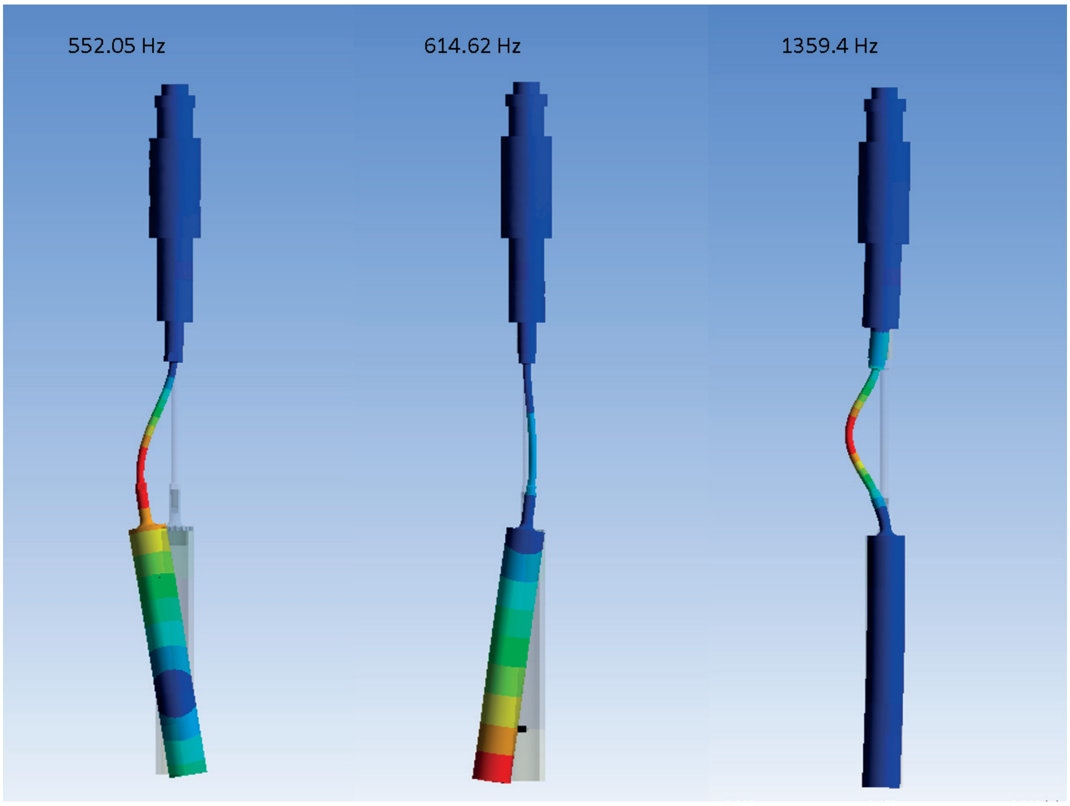

Figure 2.4 – Undamped modal analysis of the full rotor assembly, motor supported on roller element bearings (10^8 N/m), and test rotor supported on externally pressurized air bearings (10^7 N/m). The first three modes highlights the fixation of the motor relative to the test rotor.

The stiffness of the bearings supporting the motor are one order of magnitude higher than those supporting the test rotor. This allowed the complete disregard of the motor from the modal analysis, while keeping only a fixed HSK tool, the coupling, and the test rotor. The calculated lateral modes were nearly identical to the values resulting from the modal analysis of the complete assembly - Figure 2.5.

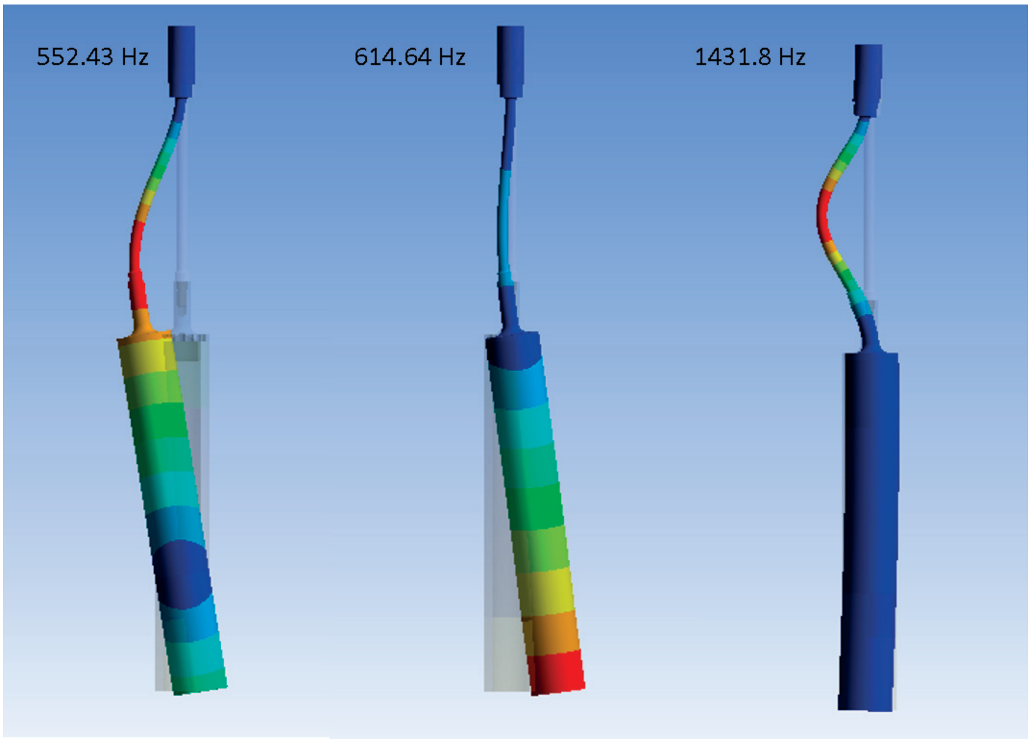

Figure 2.5 – Undamped modal analysis of the test rotor supported on externally pressurized air bearings (10^7 N/m). The coupling is considered fixed from the motor end given the relatively high bearing stiffness supporting the motor.

2.5 Alignment and Balancing

The alignment was executed using the reverse indicator technique, with an alignment tolerance below 10 μm along the length of the test-rig. Moreover, the bearing holders were manufactured in one "go", hence ensuring good alignment between bushings. The test rotor is pre-balanced to G1.0 and then in-situ balanced on the test-rig with the bearings in location and with the coupling attached. The in-situ balancing adopts the two plane influence coefficient method using the rotor displacement in order to ensure rotor excursions smaller than the bearing clearance.

2.6 Measurements Capabilities

The test-rig is equipped with different sensing capabilities for the purpose of measurement and monitoring. Proximity probes are used to monitor the rotor orbit and vibration. An optical probe is used as a tachometer to measure the rotor speed. A pressure scanner and a flowmeter are used to measure the pressure of the gas film within the bearing clearance, and the air mass flow rate that supplies externally pressurized bearings or cools foil bearings.

2.6.1 Proximity Measurement

The test-rig is equipped with 5 proximity probes, two pairs of Lion Precision capacitive probes for time resolved orbit and eccentricity measurements on each bearing (x-y configuration), and one Philtec optical probe acting as a trigger for speed and phase calculations.

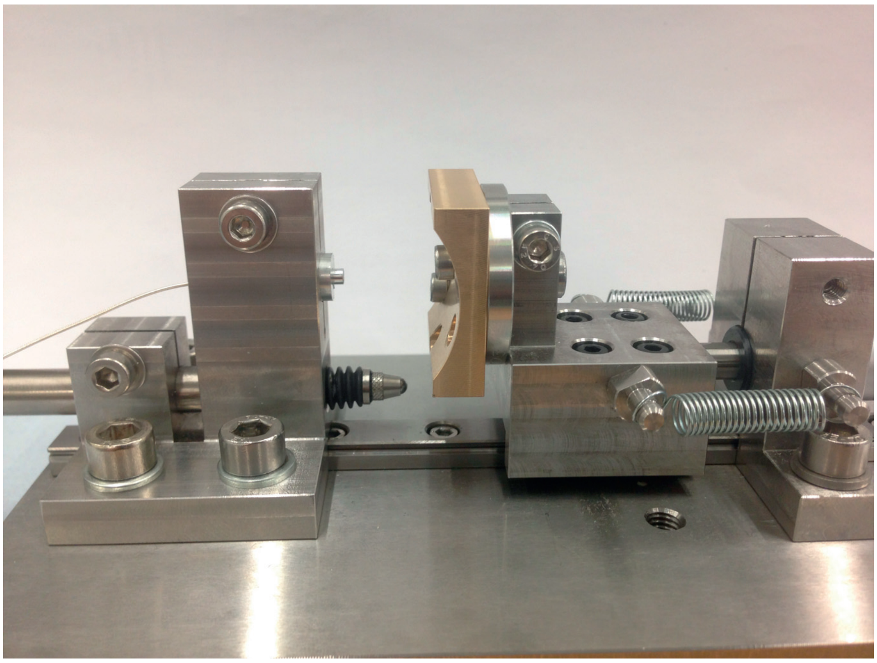

Figure 2.6 – Micrometric screw setup for the static calibration of proximity probes. The left side supports the tested proximity probe and a reference LVDT sensor, while the right side carries the target surface and a micrometric screw to adjust the gap.

Each of the pairs of the C6-D Lion Precision capacitive probes are fixed 90 degrees apart. The probes are not sensitive to the target material, and were re-calibrated using a micro-metric screw setup – as show in Figure 2.6 . The probe is fixed and a target is connected to a micrometric screw and moved relatively. The calibration procedure begins by contacting the target to the probe's sensing surface and defining a no-gap signal. Following that, the micro-metric screw is used to retreat the target gradually while noting the voltage change. The calibration curves were similar to the factory calibration sheet, with a calibrated range of 0.35 mm. The probes have a measurement uncertainty of ± 1.3% and a bandwidth of 14 kHz.

Although considered as a proximity probe, the D-20 Philtec probe is chosen as a trigger sensor due to its high sensitivity to reflective surfaces. A black mark is made on the shiny surface of the rotor knob – Figure 2.7a, yielding a square-like voltage signal that is adequate for data processing - Figure 2.7b.

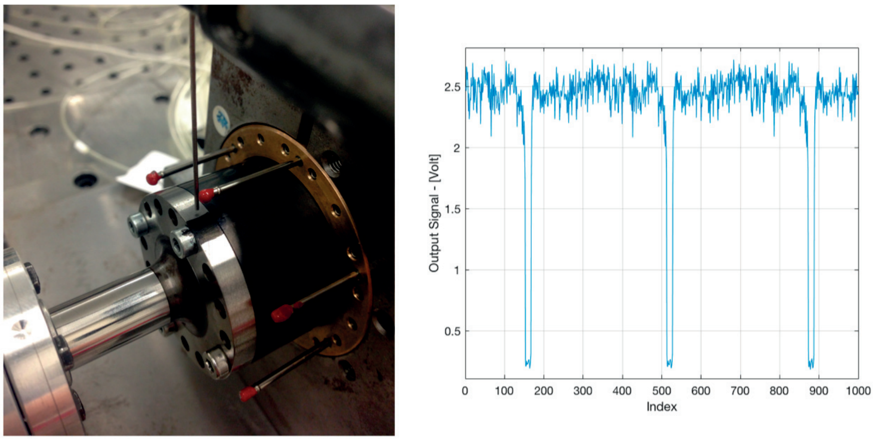

(a) Philtec probe as trigger sensor (b) Sample trigger output signal

Figure 2.7 – (a) Optical Philtec probe used as a trigger on the test rotor. The trigger signal is generated due to the difference in reflectivity of a black mark on the rotor surface. (b) Sample of the analog trigger signal, highlighting a square like shape that is convenient for post-processing.

2.6.2 Pressure Measurement

The test-rig is also equipped with pressure measurement capabilities that allow gas film and supply pressure measurements in bearings. Two Scanivalve pressure scanners are used (DSA 3217 and DSA 3218) with a measuring range of a 100 PSID and 250 PSID. Each scanner comprises 16 temperature compensated piezoresistive pressure transducers, with an accuracy of ±0.05% of the full scale. The scanners are only capable of measuring time averaged pressure with a sampling rate of 5 Hz, therefore, the scanners are only used to measure steady pressure signals.

2.6.3 Air Mass Flow Measurement

Measuring the supply mass flow rate is of paramount importance in the study of externally pressurized bearings, as it is the driving quantity in the characterization of such bearings. Mass flow rate measurement capabilities are also important in order to quantify the cooling supply to foil bearings. The mass flow rate is measured using two Proline Cubemass C-100 Coriolis flowmeters. The measurement accuracy lies between 0.67% (at 3 kg/hr), and 2.67% (at 0.75 kg/hr) depending on the flowrate. The pressure drop across the flowmeter ranges between 53 Pa (at 0.75 kg/hr) and 465 Pa (at 3 kg/hr) and is considered negligible compared to the bearing supply pressure.

2.7 Limitations of the test rig – potential issues

The main limitation of the test-rig is the inevitable effect of the coupling. Although it can be drastically mitigated, it can never be fully eliminated. The implications would be a minor synchronous orbit superimposed on the imbalance response, as well as a potential imposed static eccentricity.

Loading the two test bearings can only happen simultaneously, and the coupling – if connected – can carry part of the load. Hence, potential problems in the equal loading of the bearings may occur.

The measurement of the rotor's static eccentricity can be challenging due to slight misalignments and/or preloads, especially on compliant foil bearings where the vertical and horizontal zero clearance values are difficult to measure accurately.

The distance between the two test bearings is fixed to 160 mm, and the bearing holder diameter is fixed to 54 mm. Such design would limit the potential interchangeability of test bearings and rotors.

That being said, these limitations will not impede the execution of the planned experimental campaign. As they have been carefully taken into consideration during the planning and execution of the measurements.

2.8 Auxiliary Setups

Two auxiliary setups were developed for the measurement of load vs. displacement, and break-away torque. The first is an in-situ auxiliary setup that is attached to the test rotor while supported on the two test journal bearings - Figure 2.8. The setup is capable of the simultaneous measurement of load versus rotor displacement at zero speed, while gradually increasing the load. The loading is done via two torque arms connected via wires to the rotor shaft. The torque arms are connected to two containers which are slowly filled with water to ensure gradual loading. Two load cells are implemented within the loading loop to measure the force during pulling and pushing, the accuracy of the load cell is ±1%. Proximity probes are fixed on the bushing of each bearing in order to measure the resulting displacement due to the load. For externally pressurized bearings the Lion Precision capacitive probes are used, and for foil bearings the Philtec probes are adopted due to their extended range up to 1.27mm. The Philtec probes were calibrated similar to Lion Precision probes (±1.3% accuracy), however, the test rotor was used as an actual target during the calibration due to the sensitivity of the Philtec probes to reflectivity (color).

The second setup is developed to measure the breakaway torque in foil bearings - Figure 2.9, which allows the deduction of the foil bearing preload that is an important variable to characterize and compare different foil bearings, as well as facilitate reproducibility. In this

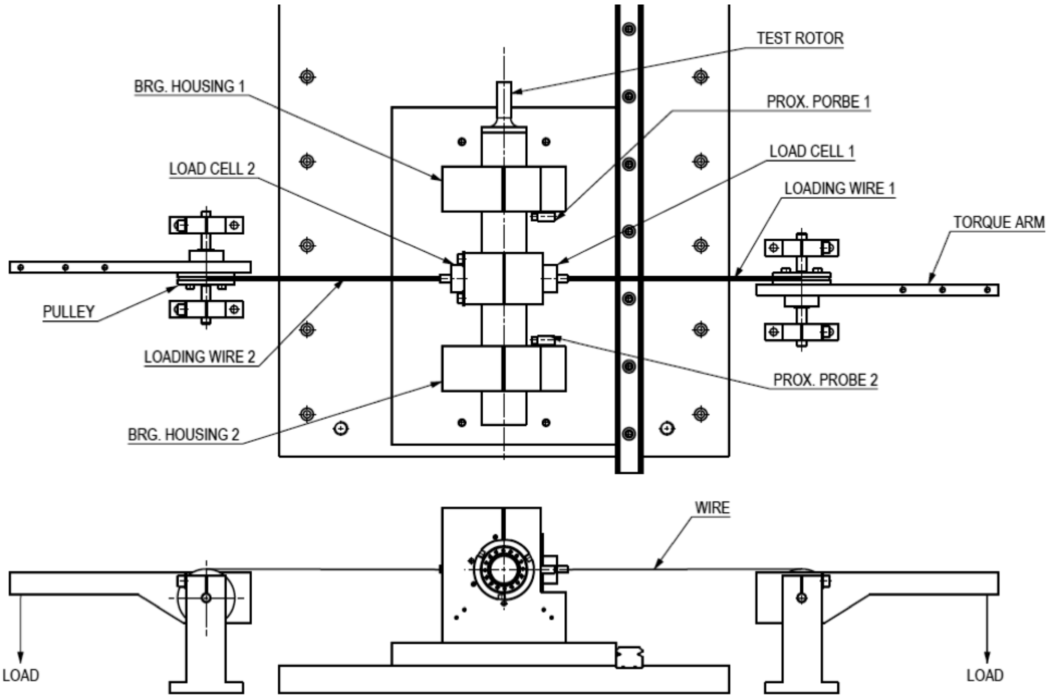
TEST ROTOR
BRG. HOUSING 1
PROX. PORBE 1
LOAD CELL 1
LOAD CELL 2
LOADING WIRE 1
TORQUE ARM
PULLEY
LOADING WIRE 2
PROX. PROBE 2
BRG. HOUSING 2
WIRE
LOAD
LOAD

Figure 2.8 – Top and side views of the load-displacement auxiliary setup

setup a mockup rotor is used with same diameter and surface coating as the actual test-rotor. The test foil bearing is held inside a bearing holder that is assembled to surround the mockup rotor. The bearing holder is connected to a torque arm in order to impose a normal load that is measured with a load cell. A second torque arm is connected to the mockup rotor in order to introduce a rotational torque, which is measured with a second load cell – knowing the length of the torque arm. A proximity probe – Philtec – is simultaneously measuring the position of the torque arm. At the moment of abrupt change in position the measured torque is considered the break-away torque. Further details on the processing of the data and the deduction are discussed in Chapter 6. The setup can also be used to measure load versus displacement by adding a second torque arm and attaching proximity probes to the bearing holder.

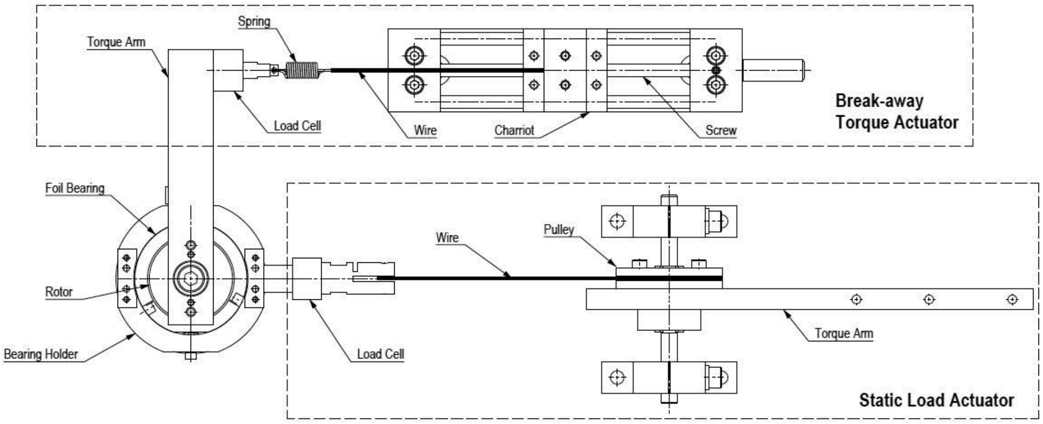
Spring
Torque Arm
Load Cell
Wire
Charriot
Screw
Break-away
Torque Actuator
Foil Bearing
Rotor
Bearing Holder
Wire
Pulley
Load Cell
Torque Arm
Static Load Actuator

Figure 2.9 – Top View of the foil bearing break-away torque test setup.

3 Instrumented Rotor Design and Proof of Concept

Knowledge of the pressure field and spatial position of the rotor inside the bearing are of paramount importance to the fundamental understanding of fluid film bearings. The objective of this chapter is to present an instrumented rotor designed for the onboard measurement of pressure in high speed gas lubricated bearings using embedded pressure probes and a wireless telemetry system. The chapter also includes the identification of the dynamic behavior of the pressure probes adopting two different techniques.

Part of the work presented in this chapter is published as:

- Shalash, K., Şahin, F.C., and Schiffmann, J., 2018. ***Non-linear transfer function identification of pressure probes using Siren Disks.*** Experimental Thermal and Fluid Science, 91, pp.459-469.

3.1 Introduction

Experimental measurements play a pivotal role in the development of rotating machinery. It is the tool by which physical phenomena are observed, and ultimately explained. It is also used to validate models using benchmark data. Such models – once validated - are a powerful tool to gain more insight into rotating machinery. Measurements are also used in prototyping to ensure the intended machine performance.

In bearing and seal applications, pressure, gap, and temperature are commonly measured variables. Conventionally, these variables are measured from the stator side. The pressure field defines the load capacity and the dynamic coefficients in fluid film bearings. The pressure is measured either by flush mounting pressure sensors on the point of measurement, or remotely connected to a measurement tap through a pneumatic channel. Stator side pressure measurements are easy to implement. However, they have the following limitations:

1. The measurements are at discrete measurement points, in order to measure profiles/-

gradients several closely placed taps have to be implemented.

2. The number of available pressure taps is constrained by the design and packaging limitations.
3. An excessive amount of taps can perturb the measured flow field.
4. Several sensors have to be used to acquire simultaneous pressure profile/gradient measurement.

On the other hand, rotor side measurement through an instrumented rotor will obtain the full circumferential pressure profile inside the bearing using a single measurement point on the shaft surface, and relying on its rotation to scan the full pressure profile/gradient. Such measurement system would overcome the limitations of the stator side measurements. Nonetheless, the implementation of an instrumented rotor is challenging, and care needs to be taken to design it due to the following issues:

1. The difficulty of the data and power transmission from the rotating sensors to the stationary data acquisition.
2. Limited measurement bandwidth due to the data communication cut-off frequency.
3. Rotor volume constraints that would limit the number of integrated sensors.
4. G-force levels exerted on the sensors and all auxiliary electronics.
5. Fixture of wires and cables inside the rotor and their direct effects on the balancing of the instrumented rotor.

The level of complexity is even higher for self-acting gas bearing supported rotors. That is due to the necessary high rotational speeds for load bearing. These constraints are limiting the possibilities of power and data transmission to: (i) rotating connectors, (ii) slip rings, and (iii) wireless telemetry systems. The first two technologies rely on mechanical contact for transmission. Which would significantly influence the dynamics of the bearing supported rotor. On the other hand, wireless telemetry would allow high rotational speeds, without constraining the motion of the rotor.

3.2 State of the Art

Surveying the literature yields a limited number of publications where instrumented shafts are used to measure within the fluid film of hydrodynamic journal bearings. Most of the previous work performed such measurements in oil lubricated bearings. The common observed limitation is the limited rotational speed of the instrumented rotor, and the use of a slip ring to connect the onboard sensors to the ground, which would influence the dynamics of rotors supported on fluid film bearings.

Ho and Chen [24] measured the pressure profile inside a six-pocket hydrostatic oil lubricated journal bearing from the rotor side. Pressure measurements were presented up to 1000 rpm using a metal diaphragm transducer. The signal was transmitted to the stator using a slip ring. A more detailed study was presented in a second paper by the same authors [25] where they used the same test rig to measure pressure profiles inside a six-pocket hydrostatic bearing, also up to 1000 rpm. Tonnesen and Hansen [26] designed an instrumented rotor capable of measuring gap, pressure, and temperature using three flush mounted sensors. A mercury slip ring was used for power and data transmission. The oil lubricated journal bearing under investigation had a diameter of 100 mm and was tested up to 8000 rpm. The measured pressure profiles were not in perfect quantitative agreement with simulation results. Roberts and Mason [27] used a mechanical slip ring and a rotor instrumented with two pressure transducers to measure the pressure inside a plain journal bearing with a circumferential oil inlet groove. Tests were performed up to 2186 rpm. The authors highlighted discrepancies in pressure profiles starting at the onset of the hydrodynamic transition region ($Re = 550 to 2000$) when compare to the laminar flow theory. Read and Flack [28] presented a similar campaign with a rotor instrumented by temperature, pressure, and gap sensors. They measured these variables inside the fluid film of an offset half bearing up to 2250 rpm. They compared these measurements to simultaneously measured pressure and temperature from the bearing side (stator). The two measurement approaches were in good agreement (5% error). Wang et al. [29] measured the pressure inside a rubber water lubricated bearing using a a rotor instrumented with 6 pressure sensors and a wireless telemetry up to 1000 rpm.

The only exception to the mainly low speed and oil lubricated bearings studied in the literature is the work of Ruscitto et al. [3] which was investigating gas foil bearings. Their pioneering work is the only reported instrumented rotor to measure within the gas film of a journal bearing. The authors measured -for the first and only time- the film thickness inside compliant gas foil bearing. The measurements were executed on a floating overhung bearing, and was transmitted via slip ring up to 60 krpm and 200 N load. The authors attempted to measure the pressure within the gas film, but were unsuccessful due to problems in their in-house made pressure sensor. As explained in the previous chapter, the floating bearing configuration results do not represent real service bearing conditions (different dynamics). Simulation results did not match the experimental measurements.

3.3 Instrumented Rotor Design

An instrumented rotor has been designed to measure the pressure profile within the gas film of journal bearings with minimum intrusion. The rotor has four embedded pressure probes at different axial position. A custom made wireless telemetry system powers the probes and transmits their signals back to the stator.

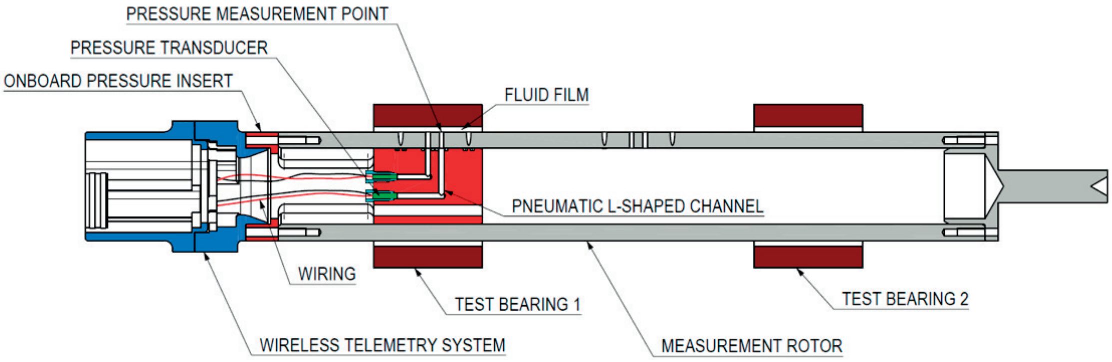
PRESSURE MEASUREMENT POINT
PRESSURE TRANSDUCER
ONBOARD PRESSURE INSERT
FLUID FILM
PNEUMATIC L-SHAPED CHANNEL
WIRING
TEST BEARING 1
TEST BEARING 2
WIRELESS TELEMETRY SYSTEM
MEASUREMENT ROTOR

Figure 3.1 – The instrumented rotor concept, highlighting the rotating telemetry system (blue), the pressure insert (red), and the pressure transducers (green). The measurements are executed at the free-end bearing (far from the coupling).

As no miniature pressure transducers were commercially found to sustain the large G-force level on the rotor periphery at top speed - around 80 000 Gs that is 8 times the maximum allowed for the transducers, it was imperative not to flush mount the transducers on the rotor outer surface. The adopted alternative was to place the transducer closer to the center of the rotor in order to reduce the level of the G-force, and remotely connect them to the rotor surface through a pneumatic channel.

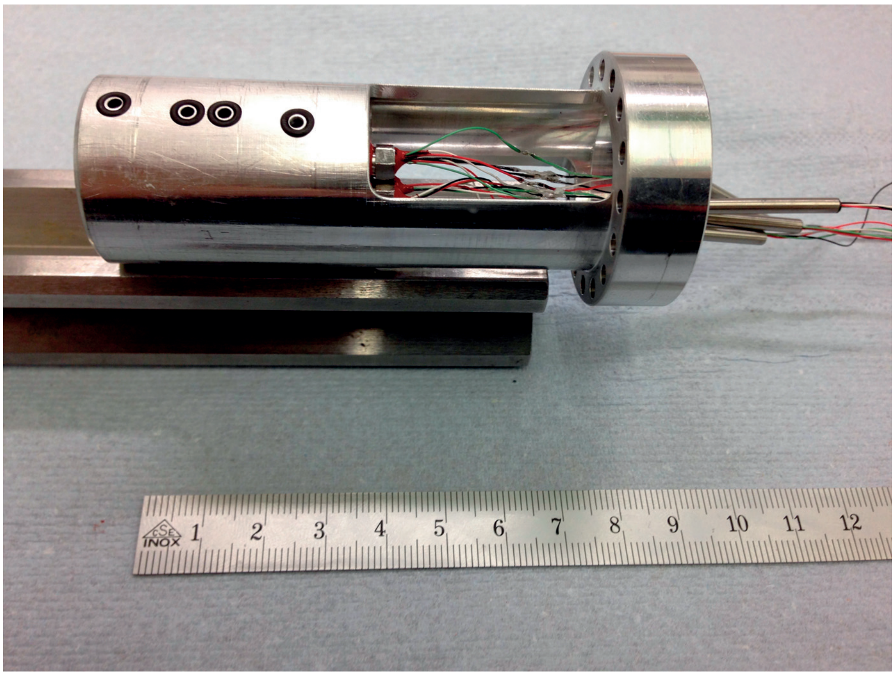
CSE INOX
1
2
3
4
5
6
7
8
9
10
11
12

Figure 3.2 – Photograph of the pressure insert before assembly inside the rotor. The o-rings are seal the exit of the pneumatic channel along with the rotor's inner bore. The transducers are sealed along with the pressure insert with red silicone (gasket maker).

The implementation of such design is done using a pressure insert that slides into the inner diameter of the rotor. The insert contains four XCQ Kulite pressure transducers and their connecting L-shaped pneumatic channels, as well as a special mounting for the telemetry system - figure 3.1. Such design allows the complete assembly of the pressure transducers, the transmitter of the telemetry system, and the fixture of the wires outside of the rotor, before assembling the insert inside the rotor - figure 3.2. The holes of the pneumatic channels in the insert are aligned with holes drilled through the rotor.

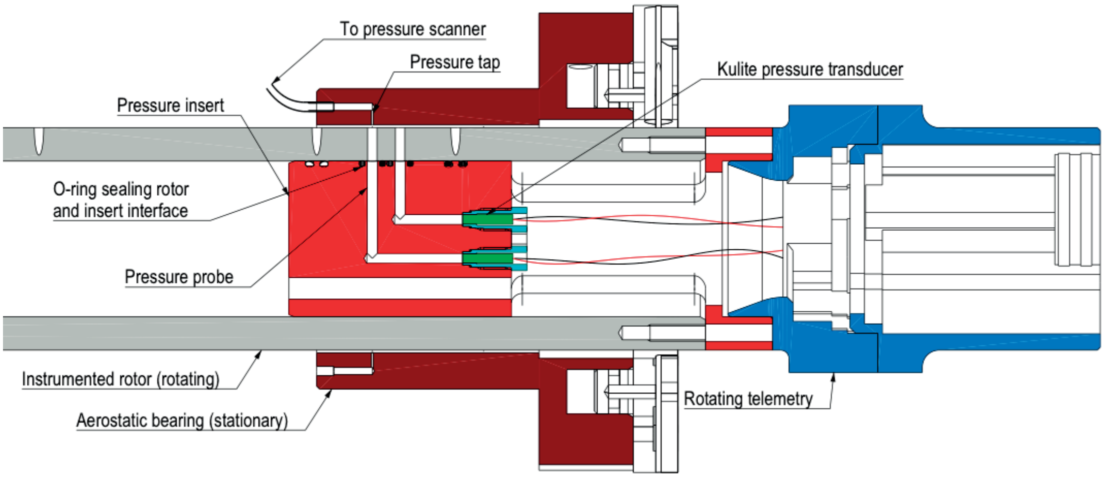
To pressure scanner
Pressure tap
Kulite pressure transducer
Pressure insert
O-ring sealing rotor
and insert interface
Pressure probe
Instrumented rotor (rotating)
Aerostatic bearing (stationary)
Rotating telemetry

Figure 3.3 – The test externally pressurized bearing with pressure taps at the same plane as one of the rotating embedded probe. The instrumented rotor is moved axially in order to compare the other embedded probes with the bearing pressure taps.

The sealing of the pneumatic channel is done using an o-ring on the outer surface of the insert, and surrounding the pneumatic channel, this ensures the sealing between the insert and the rotor - figure 3.3. The pressure transducers are sealed to the insert using a micro o-ring and gasket maker silicone. The sealing was later tested using a small setup that pressurizes the pneumatic channel - figure 3.4, while the insert is submerged in water, no sign of bubbles were observed, hence, good sealing was concluded.

The telemetry system used is a custom made system from Datatel Telemetry to fit the design requirements of the rotor. The telemetry system is constructed of two main supply chains, the first, is a wireless transmission and receiving via RF (radio frequency) for the sensor signals, the second, is a contactless induction power supply to power the sensors and the transmitter. The telemetry system is capable of accommodating 10 sensors, each having a 19 kHz bandwidth. Mechanically, the rotor part of the telemetry system was designed to fit as an overhung mass on the rotor, with safe operation up to 60 000 RPM.

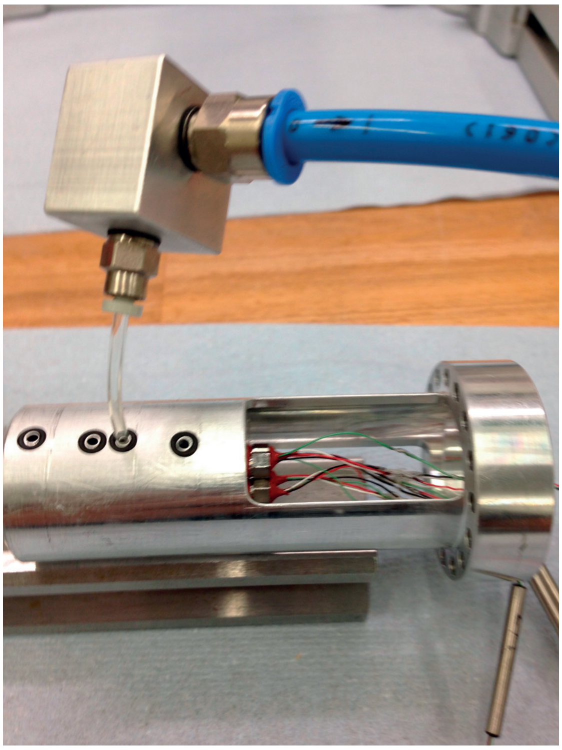

Figure 3.4 – Photograph of the sealing test for the insert. Pressurizing the pneumatic channel in order to detect leaks.

3.4 Design Limitations

Being a complex system design, with several conflicting design objectives, it is crucial to highlight and identify the limitations of the developed design:

1. As the sensor is connected to the measurement point through an L-shaped pneumatic channel, and the expected pressure signal is of a periodic nature, hence the knowledge of the dynamic response of the probe is of predominant importance. The integration of the pneumatic channel along with the pressure sensor creates a new pressure probe. Such probe exhibits a different dynamic response compared to that of the pressure transducer. The presence of the pneumatic channel will reduce the cutoff frequency of the probe compared to that of the pressure transducer. Hence, limiting the maximum frequency that can be measured accurately. In other words, such behavior is imposing a limitation on the maximum rotational speed where measurements are executed.

2. The rotation of the rotor imposes a centrifugal force on the pressure transducers, combined with the requirement of integrating four probes, and the limited volume, it was decided to place the pressure transducers on circle with a 7mm diameter around the center of the rotor. Such configuration will subject the transducers to their maximum allowable G-force at 54 000 RPM, an increase in speed would jeopardize the performance

of the transducers.

3. There is a trade-off between the probe's diameter and the cutoff frequency. Recalling basic principles, reducing the probe diameter would decrease its cutoff, yet it would average the measured pressure over a smaller area. For the developed system the probe's diameter is 1.7mm, hence details smaller than this scale would be averaged out.

4. In comparing the instrumented rotor, to a non-instrumented hollow rotor with the same dimensions, the former would be larger in mass. Such mass increase, would decrease the onset speed of instability, as well the bearing load when compared to the non-instrumented rotor. For the case of the externally pressurized journal bearings, the stability threshold dropped from 60 000 RPM to 40 000 RPM once the instrumented rotor was used at the same running conditions (air supply pressure of 7 bar).

5. One of the degrees of freedom of the test-rig is its capability for axial position adjustment - by moving the full rotor assembly axially. This would allow a complete pressure field measurement in the test bearing. However, by moving axially the center of of gravity of the rotor is shifting relative to the bearings, hence the bearing load is slightly changing between one axial position and another.

6. The maximum pressure measured is defined by the pressure transducers to be 7 bar absolute.

3.5 Proof of Concept at Quasi-static Conditions

The instrumented rotor was prototyped and assembled before being initially tested on EP bearings. The rationale behind using EP bearings as a test bed for the instrumented rotor is due to their pressurized gas film at zero rotational speed. The ⌀40mm journal bearing used is made out of DIN EN 1982 Bronze, and has two feeding rows of 18 restrictor nozzles (100μm diameter and 1.1mm long). The two rows are located at $\overline{z} = \pm 0.5$ where $\overline{z} = \frac{Z}{R}$. The bearing is also equipped with 25 ⌀0.3mm circumferential pressure taps that yields a spatially sampled circumferential pressure profile inside the bearing. The taps are connected via flexible tubes to the Scanivalve pressure scanners described in Chapter 2. The supply and measurements taps have two physically separated internal passages inside the bearing structure. The tested bearings have a nominal radial assembly clearance of 30m.

The static calibration of the pressure probes using a dead weight balance quantified a maximum uncertainty below 0.4% (including the effects of the wireless telemetry). A verification test was performed by rotating the instrumented rotor quasi-statically and comparing between the rotor and bearing side pressure measurements. The pressure probe of the rotor was placed at the axial location opposing the measurement taps and the supply nozzles as shown in figure 3.3.

Figure 3.5 shows the circumferential pressure profile at a supply pressure of 8 bar. The two

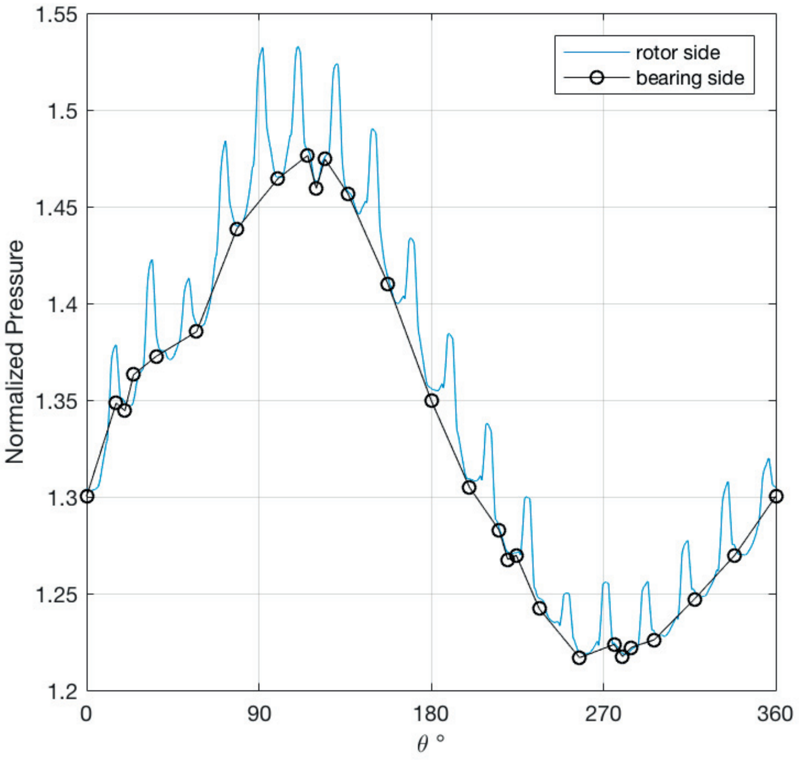

Figure 3.5 – Comparison of the gas film pressure profiles from the rotor and stator (bearing) sides at 8 bar supply pressure. The rotor side measurement exposes more details compared to the spatially sampled stator side measurements. The pressure peaks corresponds to the location of 18 air supply restrictors.

measured profiles are in good agreement, hence verifying the measurement of the instrumented rotor. The pressure scan from the rotor side is higher in details, and captures the supply nozzles shown as 18 pressure peaks. The overall pressure profile is not axisymmetric due to a slight rotor eccentricity, as well an unequal mass flow rate from the different supply nozzles. More on the captured flow physics of the EP bearing is discussed in Chapter 4.

3.6 Effect of Centrifugal Force on Pressure Measurement

The pressure transducers are fixed in a way so that their sensing surfaces are parallel to the rotating plane of the rotor - figure 3.3. The centrifugal force can affect the pressure measurement by influencing the membranes of the transducers through a shearing force, and it can also affect the air column inside the probe as discussed by Uffrecht and Kaiser [30]. The effect of centrifugal force on pressure measurement is studied by subjecting the pressure probe to ambient (pushing the rotor axially outside of the bearing surface), and consequently ramp up the speed. It is observed that the pressure dropped by 2.77% at 37 krpm. Figure 3.6

shows the drop in pressure due to the centrifugal force as a function of speed. This curve is used to correct the pressure measurements along the experimental campaign.

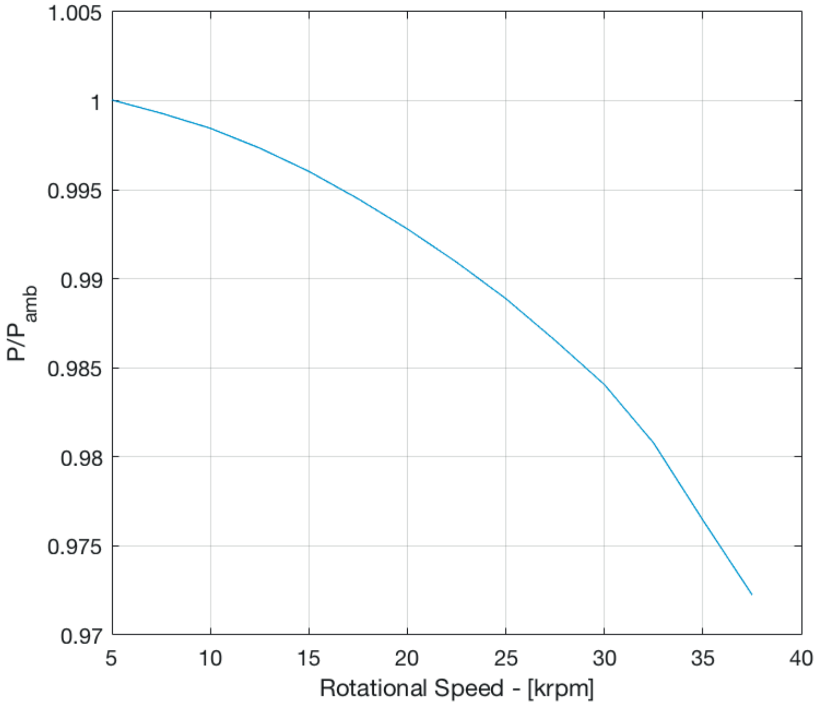

Figure 3.6 – Pressure drop due to the centrifugal force subjected on the air column of the pneumatic channel up 37.5 krpm.

3.7 System Identification of Embedded Pressure Probes Using a Mockup and Siren Disk [1]

In order to assess the feasibility of pressure measurements using remotely mounted pressure transducers, a calibration mockup was prototyped and tested. In performing time-resolved pressure measurements, the dynamic characteristics of the probe are of paramount importance, as they can drastically influence the meaurement both qualitatively and quantitatively. Bean [31] identified six parameters for the characterization of pressure transducers used in time-resolved measurement: (1) gain, (2) phase lag, (3) resonant frequency, (4) damping ratio, (5) rise time, (6) and overshoot. The identification of these parameters requires dynamic calibrators, which are capable of generating periodic pressure signals with controlled amplitude and frequency, or aperiodic step or impulse pressure signals with a short rise time and controlled amplitude. Aperiodic calibrators are generally based on shock tube or fast opening valve concepts [31–38], whereas periodic calibrators are either variable volume generators, rotating valves or sirens [31, 32, 35, 39–44]

---

[1] The work presented in this section was in collaboration with Dr. Ceyhun Sahin during her postdoc at the Laboratory for Applied Mechanical Design between the period 2015-2017.

A dedicated study on the improvement of high frequency/amplitude periodic calibrators showed that siren type devices were the most promising solution to generate high amplitude pressure signal on a large range of frequencies [39]. It was also reported that sirens can produce periodic - not necessarily sinusoidal - low and medium pressure signals up to 1 kHz [45]. However, distortion of the generated signal into a saw-tooth like form was observed. Fridh et al. [46] reported pressure tap calibration up to 4 kHz using a reference pressure signal generated by a rotating hole-disk system. Unfortunately, the full description of such system is not available in the public domain.

For that reason it was decided to design and build a Siren Disk pressure calibrator capable of exciting the pressure probes at a range of pressure amplitudes (up to 2.5 bar peak-peak), and frequencies (up to 10 KHz). The Siren Disk is used for the identification of transfer functions of different pressure probe geometries. The transfer function is obtained through the comparison of the probe signal to a flush mounted reference transducer that is subjected to the same pressure signal.

3.7.1 Siren Disk Description and Design

The Siren Disk test rig is comprised of (1) a Siren Disk assembly, (2) a driving electrical motor, (3) a pressure source, (4) a reference sensor, and (5) a test probe to be calibrated in the vicinity of the reference sensor. The target pulsation frequency is 10 kHz with pressure amplitudes starting from 0.5 bar atm up to 3.5 bar atm.

The Siren Disk is designed to generate interruptions at the exit of a nozzle - Figure 3.7. The nozzle is placed downstream of a pneumatic line with a maximum gauge pressure of 8 bar - pressure regulated upstream. The nozzle is convergent, with an inlet and exit diameters of 20 mm and 10 mm respectively, and a length of 40.7 mm.

The main constraint in the disk design is the tip speed that is limited to 110 m/s due to mechanical stress. Another constraint is ensuring equal and synchronized opening and closing times for the reference transducer and the test probe. Finally, the distance between the reference transducer and the test probe needs to be kept minimal - Figure 3.8. These design constraints yield a 280 mm diameter disk, with 80 holes, a pitch of 10 mm between holes, and a maximum rotational speed of 7500 rpm. Such design is able to produce a hole passing frequency (hpf) of 10 kHz. The disk holes are of a semi-oval shape having straight side walls, hence, guaranteeing synchronized opening and closing over both the reference transducer and the test probe. A micrometric x-y table allows the accurate alignment of the reference transducer and the test probe with the center of the nozzle and the siren disk holes. An optical proximity probe is placed on top of the Siren Disk holes in order to measure the hpf.

Structurally, the Siren Disk is designed for minimum inertia and maximum stiffness. A thin stainless steel disk plate with the 80 holes is bolted between two rigid holders with web

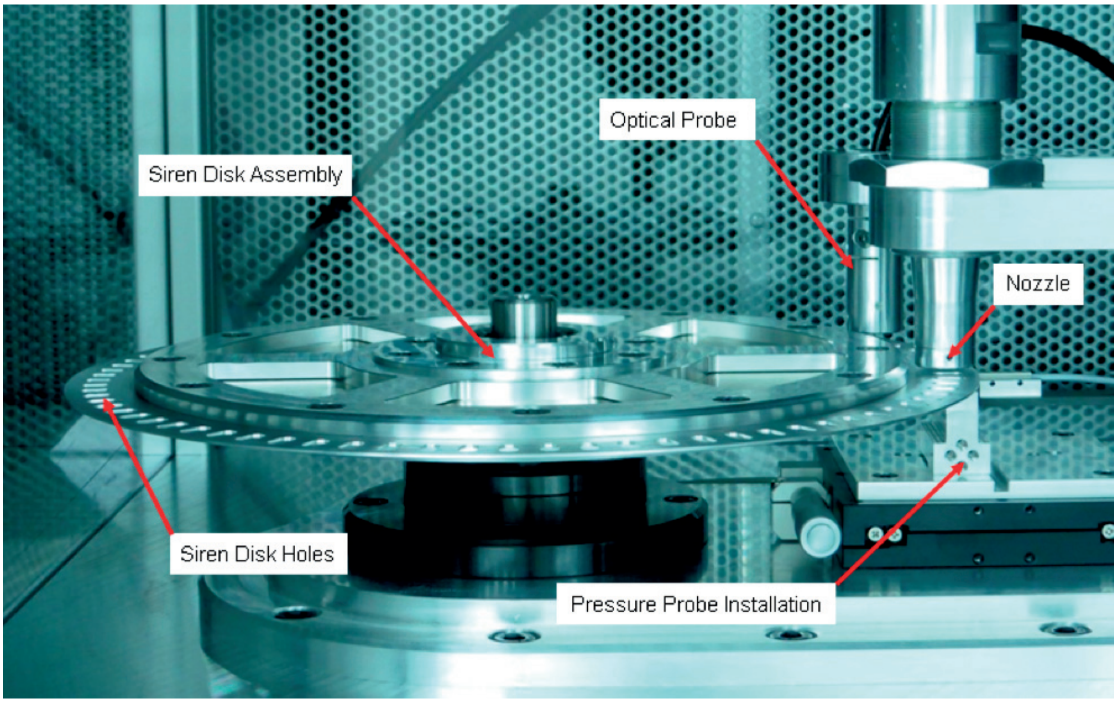
Optical Probe
Siren Disk Assembly
Nozzle
Siren Disk Holes
Pressure Probe Installation

Figure 3.7 – Photograph of the Siren disk calibration apparatus.

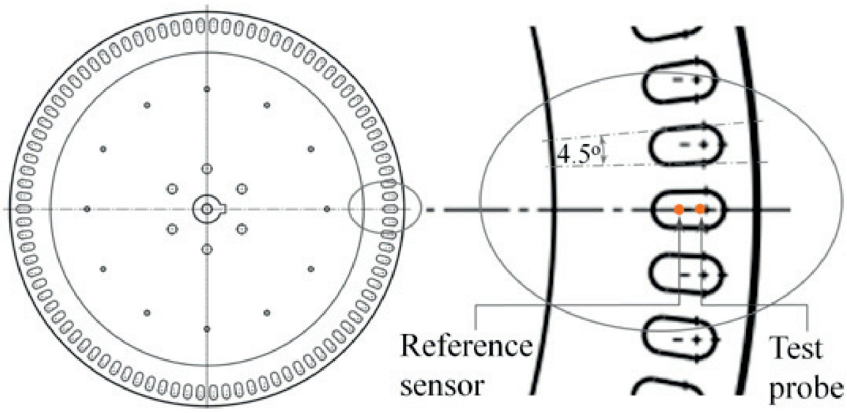
4.5°
Reference sensor
Test probe

Figure 3.8 – Holes of the siren disk and the relative positions of the probe and the reference transducer.

supports. The thin disk minimizes the distance between the nozzle exit and the measurement point. The Siren Disk is assembled on a spindle, which is connected to an electric motor via flexible coupling - Figure 3.9. Dynamically, there are two excitation sources to the rotor, (1) the synchronous rotor imbalance (rotational speed), and (2) flow induced excitation resulting from the interaction between the air jet and the Siren Disk (hpf). Therefore, the rotor assembly was designed such that its eigenfrequencies do not coincide with the rotational speed or the hole passing frequency.

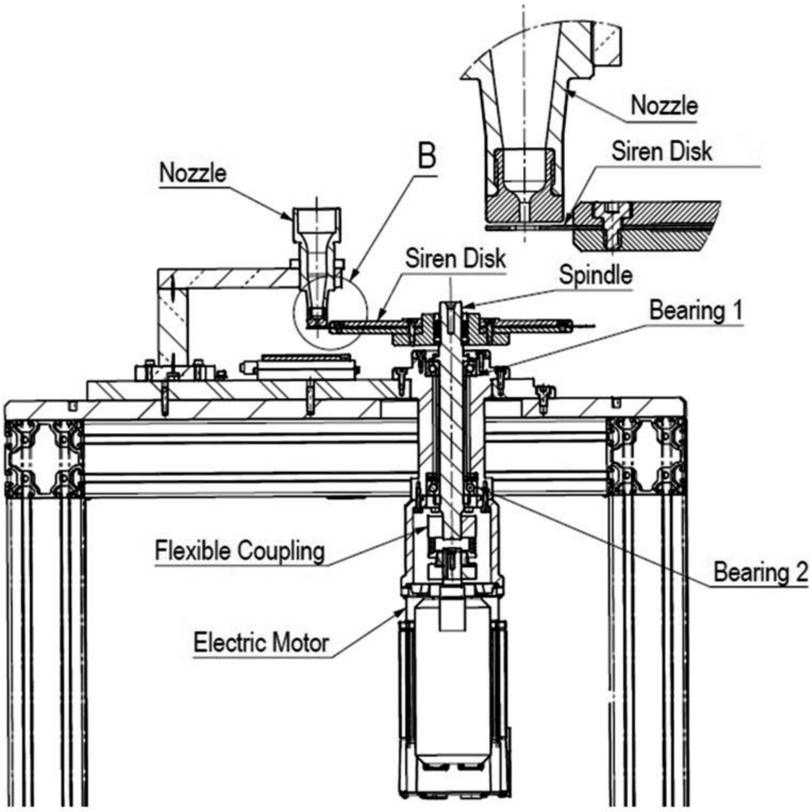

Figure 3.9 – Schematic of the siren disk apparatus.

3.7.2 Siren Disk Qualification

Four L-Shaped probes with different lengths are tested to qualify the Siren Disk and the identification method - Figure 3.10. The pressure transducer is placed at the end of the horizontal side, while the supply nozzle is facing the vertical end of the pneumatic channel. Tube lengths and aspect ratios are summarized in Table 3.1.

Table 3.1 – Geomtry of the four L-shaped pressure probes

Probe	**Vertical Length, L_V** [mm]	**Horizontal Length, L_H** [mm]	**Total Channel** [mm]
1	16.5	14	30.5
2	23.5	19	42.5
3	21	29	50
4	21	4	25

Two Kulite xcq-062 pressure transducers are used in the test rig. The first serves as a reference transducer with a range of 7 bara. The second is implemented inside the test probe with a range of 35 bara. Both transducers are equipped with identical protective B screens that limit their flat response to 20 kHz [47]. The screens attenuate the high frequency components

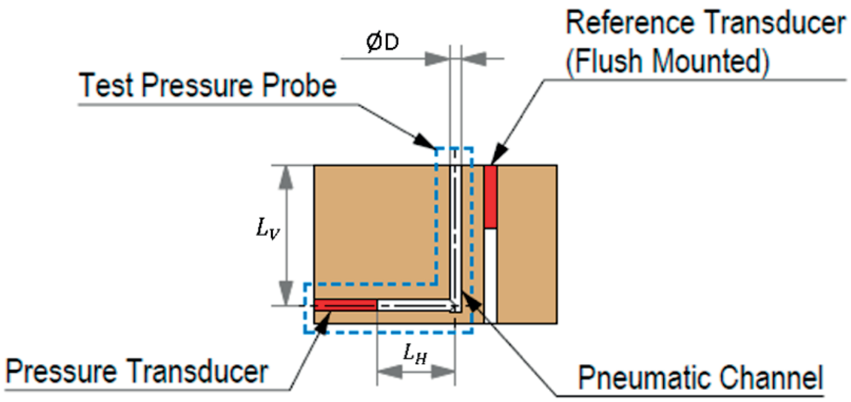

Figure 3.10 – L-Shaped Pressure Probe Mockup Layout.

(>20 kHz) of the measured pressure signal. The sensitivities are 1.4 mV/V/bars and 0.286 mV/V/bars for the reference transducer and the test probe respectively.

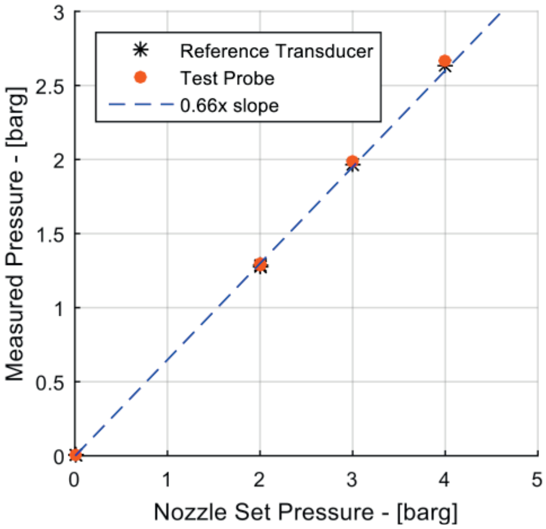

Figure 3.11 – Pressure drop through the Siren Disk nozzle.

The data is acquired at a sampling rate of 200 kHz in order to ensure at least 20 samples per cycle at the highest rotor speed of the siren disk. The pressure excitation is introduced as a ramp in the rotor speed of the Siren Disk from 0 Hz up to 10 kHz (0-7500 rpm) in 15 seconds followed by a similar deceleration ramp. The test ramps provide time intervals of 50 milliseconds with a constant hpf (±17 Hz). The pressure level was randomly changed during the hpf ramp (0 – 4.5 barg), yielding signals at different amplitudes for a given frequency. The different pressure levels help in identifying the system's dependency on the peak-to-peak amplitude. This procedure is applied for the four L-shaped probes under investigation.

Figure 3.11 shows the measured pressures across the siren disk opening compared with the nozzle pressure at zero disk speed. It is observed that the nozzle set pressure drops by 35%

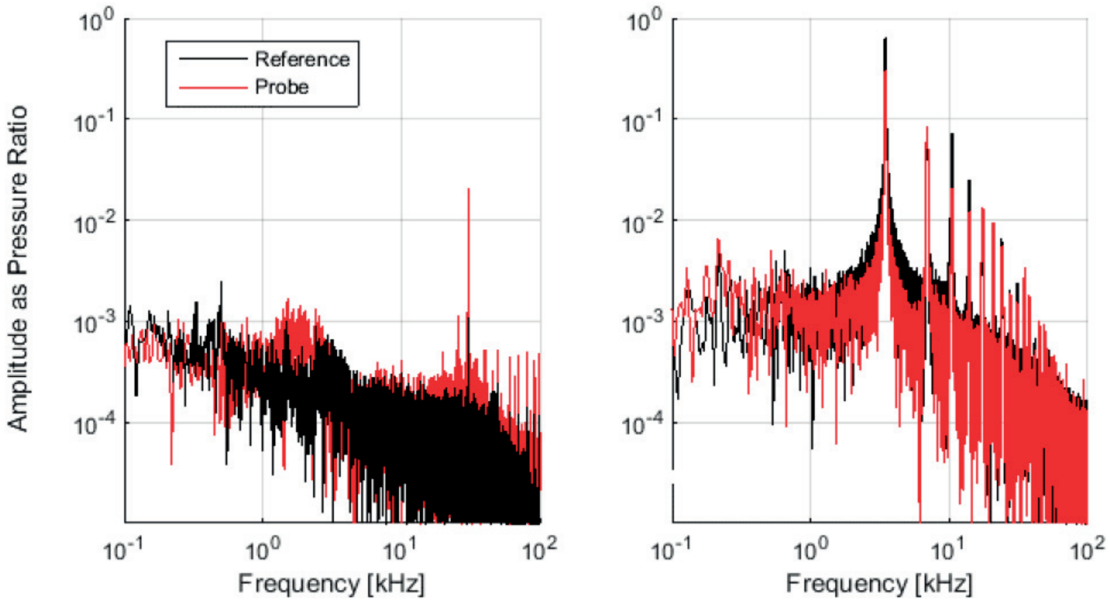

Figure 3.12 – Frequency spectrum for (a) uninterrupted flow and (b) periodic flow at 3.5 kHz, measured by the reference transducer and Probe-3.

(±1%) in gauge value. The figure also demonstrates that both the reference sensor and the probe are exposed to the same steady pressure.

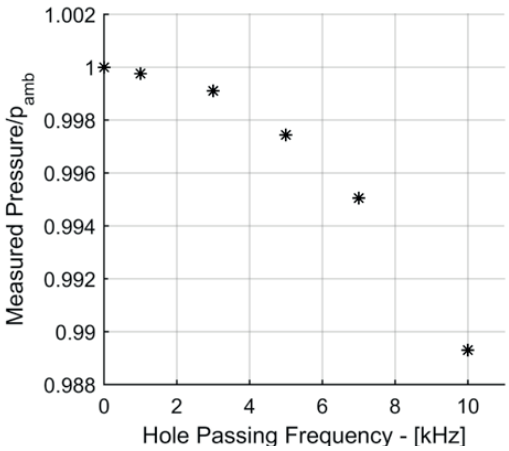

Figure 3.13 – Pressure drop due to disk rotation.

Figure 3.12a shows the pressure signal spectrum of the uninterrupted impinging jet - i.e. disk at zero rotational speed. The observed response is attributed to turbulent pressure fluctuations. However, it is considered negligible when compared to the spectrum excited by the rotation of the Siren Disk - Figure 3.12b. The frequency spectrum of both the reference transducer and probe-3 clearly shows the existence of the fundamental frequency as well as its harmonics, which is a consequence of the step change in pressure levels due to the opening/closing cycles produced by the disk. Comparing the probe to the reference transducer, it is observed that while the signal components are at the same frequencies, yet the amplitudes are varying for each harmonic. Figure 3.12b also shows that signal components beyond the 5th harmonic can be neglected as they are at least two orders of magnitude smaller than the fundamental component.

A final qualification is the study of the windage effect due to the Siren Disk rotation. The static pressure is measured during the rotation of the Siren Disk while the supply nozzle is closed. Figure 3.13 represents the relative pressure drop as a function of the hpf (i.e. rotor speed), showing a maximum static pressure drop due to rotation of approximately 1% at maximum hpf. Hence, the wind effect is negligible compared to the target pressure levels in this study.

3.7.3 Proof of Concept

The four probes under investigation were tested up to10 kHz. Figure 3.14 compares the time domain pressure signal for the reference transducer and test probe-3 at four different excitation frequencies. It is observed that the signal of the test probe is amplified - Figure 3.14d - or attenuated - Figure 3.14a, b, and c, and also delayed, as a function of the excitation frequency. Such behavior is the typical signature of the pneumatic channel in the probe. Another interesting observation is the distortion of the probe's signal creating a saw tooth, even at relatively low excitation frequencies.

At low hfp, the reference signal has a shape similar to a square. However, at higher hpf, the harmonics of the reference signal are less pronounced, yielding a signal closer to a sine wave - Figure 3.14a and b. This can be attributed either to the cutoff frequency of the transducer screens (20 kHz), or to the aerodynamic nature of the jet. Nonetheless, the results confirm the Siren Disk's capability to generate periodic pressure signals up to 10 kHz, while achieving amplitudes at the same order of magnitude of the mean pressure.

Six data sets are obtained at several pressure levels (1.5 bara to 4.5 bara) - Figure 3.15. Five sets are used in the transfer function development (data sets 1-5), and one (data set 6) is used as a test case for signal reconstruction.

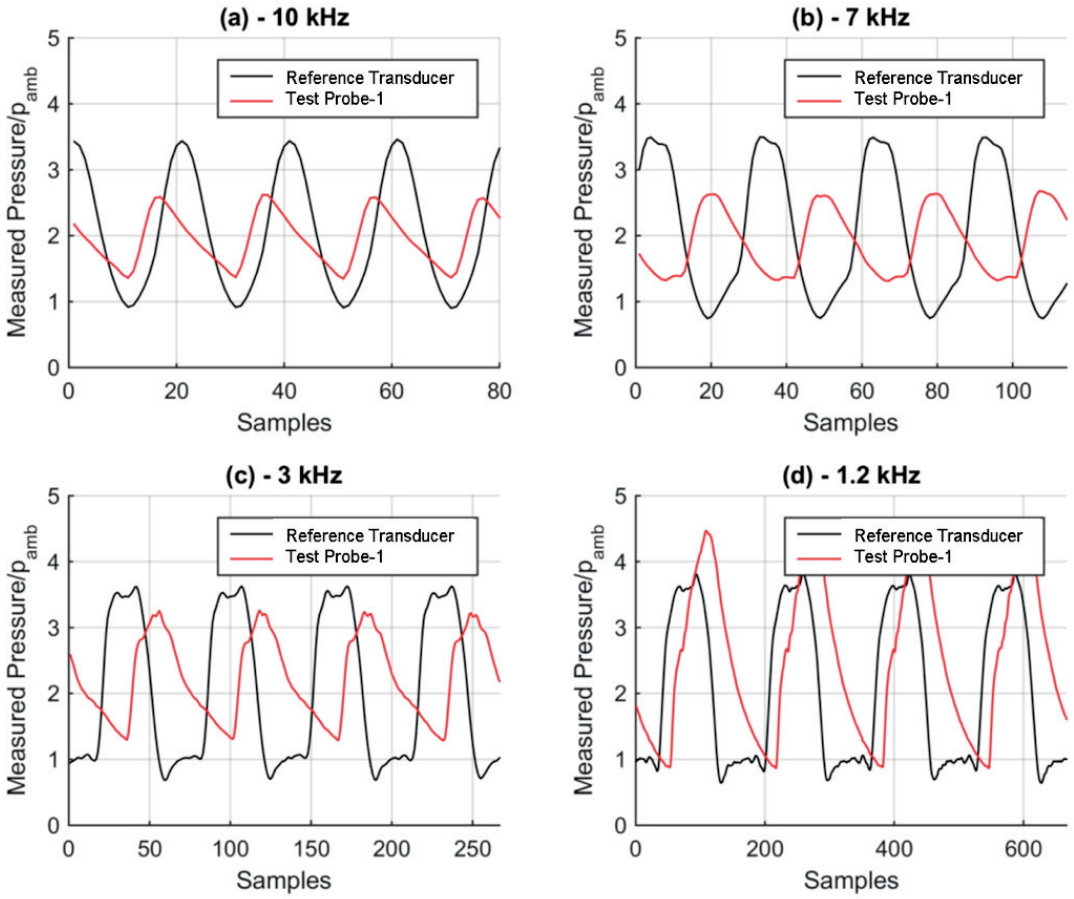

Figure 3.14 – Reference and test probe time domain signals for excitations of 10, 7, 3 and 1.2 kHz for Probe-3.

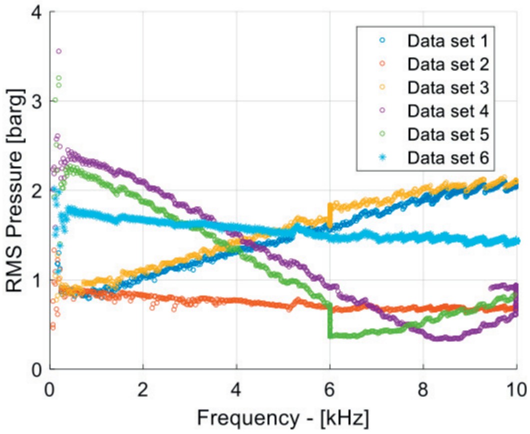

Figure 3.15 – Reference data pressure levels for Probe-3.

3.7.4 Non-linear Transfer Function Identification

In order to reconstruct the original signal based on the test probe signal, the latter's dynamic response needs to be identified. This is done by building a transfer function between the reference and test probe. A typical method is to create a non-parametric transfer function in the frequency domain by taking the ratio between the Fourier (or Laplace) Transforms of the probe and the reference transducer.

A linear system identification approach was first attempted, however, the signal reconstruction based on the inverse transfer function was unsuccessful. These results signaled the potential non-linear behavior of the pneumatic channels. Hence, a different methodology is developed for that purpose.

Methods based on the Fast Fourier Transform (FFT) are presented by several authors in prior works [37, 48, 49]. The signal decomposition based on such a method is an excellent mean to identify the frequency spectrum. However, the FFT was proven inadequate in the calculation of the phase angle. This is due to the increasing uncertainty in handling harmonics of low amplitude [50–53]. Since the phase shifts play an essential role in the accurate reconstruction of the measured data - Figure 3.14, the FFT methodology should not be adopted for applications where the details of the pressure signal are important. Alternatively, a Fourier series decomposition is used, where the periodic signals of the reference and the test probe ($q(t)$) are represented as the sum of the offset (mean) and the periodic components at the fundamental frequency and its harmonics:

$$q(t) = q_0 + \sum_{n=1}^{n_h} A_n \cos(n\omega t) + \sum_{n=1}^{n_h} B_n \sin(n\omega t) = q_0 + \sum_{n=1}^{n_h} Q_n \sin(n\omega t + \Phi_n) \tag{3.1}$$

$$Q_n = \sqrt{A_n^2 + B_n^2} \tag{3.2}$$

$$\Phi_n = \arctan\left(\frac{B_n}{A_n}\right) \tag{3.3}$$

where

$$q_0 = \frac{1}{T}\int_0^T q(t)dt \tag{3.4}$$

$$A_n = \frac{2}{T}\int_0^T q(t)\cos(n\omega t)dt \tag{3.5}$$

$$B_n = \frac{2}{T}\int_0^T q(t)\sin(n\omega t)dt \tag{3.6}$$

This decomposition procedure is performed on signal segments obtained at a given hpf with the objective of characterizing the nature of the transfer function. As a first step, the optical signal of the hole passing is used to identify the fundamental frequency of the segment through an FFT. Consequently, one pressure cycle of the segment is considered for the Fourier series. Only the five first harmonics are included, as they were shown previously to be the most predominant of the spectrum - Figure 3.12. A linear transfer function for each harmonic - gain and phase lag - is calculated as follows:

$$G_n(\omega) = \frac{Q_{n_{meas.}}(\omega)}{Q_{n_{ref.}}(\omega)} \tag{3.7}$$

$$\Phi_{n_{correction}}(\omega) = \Phi_{n_{meas.}}(\omega) - \Phi_{n_{ref.}}(\omega) \tag{3.8}$$

where n is the order of the harmonic, starting with n = 1 for the fundamental frequency. The gains of the initial 5 harmonics were calculated and averaged (Eq. 3.7) for the different pressure signals (1.5 bara to 4.5 bara - data sets 1 to 5) - Figure 3.16. In a linear system, the gain at a given frequency would be the same whether or not it is a fundamental or a harmonic (i.e. $G_2(\omega) = G_1(2\omega), and G_2(\omega) = G_1(2\omega)$). It is observed though, that the gain functions are different for each harmonic in terms of amplitude and shape, thus confirming the highly nonlinear character of the pneumatic channel.

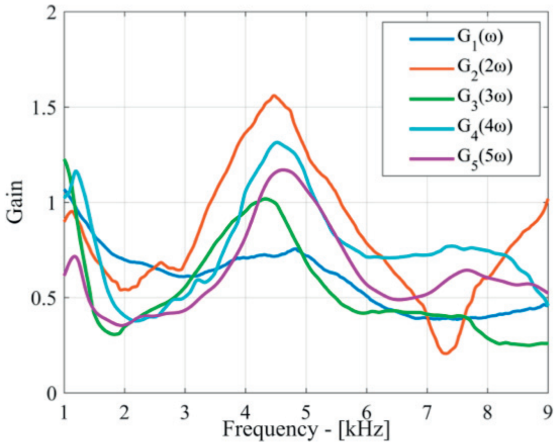

Figure 3.16 – Harmonics gains for Probe-3 - plotted with respect to absolute frequency values.

In addition, the offset gains (Eq. 9) are calculated and averaged at the five different mean pressure levels:

$$G_0(\omega) = \frac{q0_{meas.}(\omega))}{q0_{ref.}(\omega)} \tag{3.9}$$

Figure 3.17 represents the averaged offset gain and the fundamental phase lag as a function of the fundamental hpf for the 4 probes under investigation. It should be noted that the offset and the amplitude are inter-dependent due to the nature of the Siren Disk. The minimum pressure of the generated pressure signal is independent of any variable, and is constant at ambient. Therefore, increasing the nozzle pressure would increase the offset and the amplitude simultaneously, and vice versa. The error bars indicate the deviation in gain and phase lag due to the nozzle pressure level variation. The non-constant nature of the offset gain is emphasizing the signature of a non-linear system.

The phase shifts of the fundamental frequency are highly dependent on the probe geometry, suggesting diverse natural frequencies for the different probes - Figure 3.17 b, d, f, h. The resonant frequency of the four probes - identified through the 90° phase shift - vary between 1.5 and 2.1 kHz. The highest resonant frequencies are achieved by the shortest channels, which is in agreement with basic principles of organ pipe or Helmholtz resonator models.

The mathematical implications of the identified non-linearity are:

1. The gain at a given frequency is dependent on the order of the harmonic ($G_2(\omega) \neq$

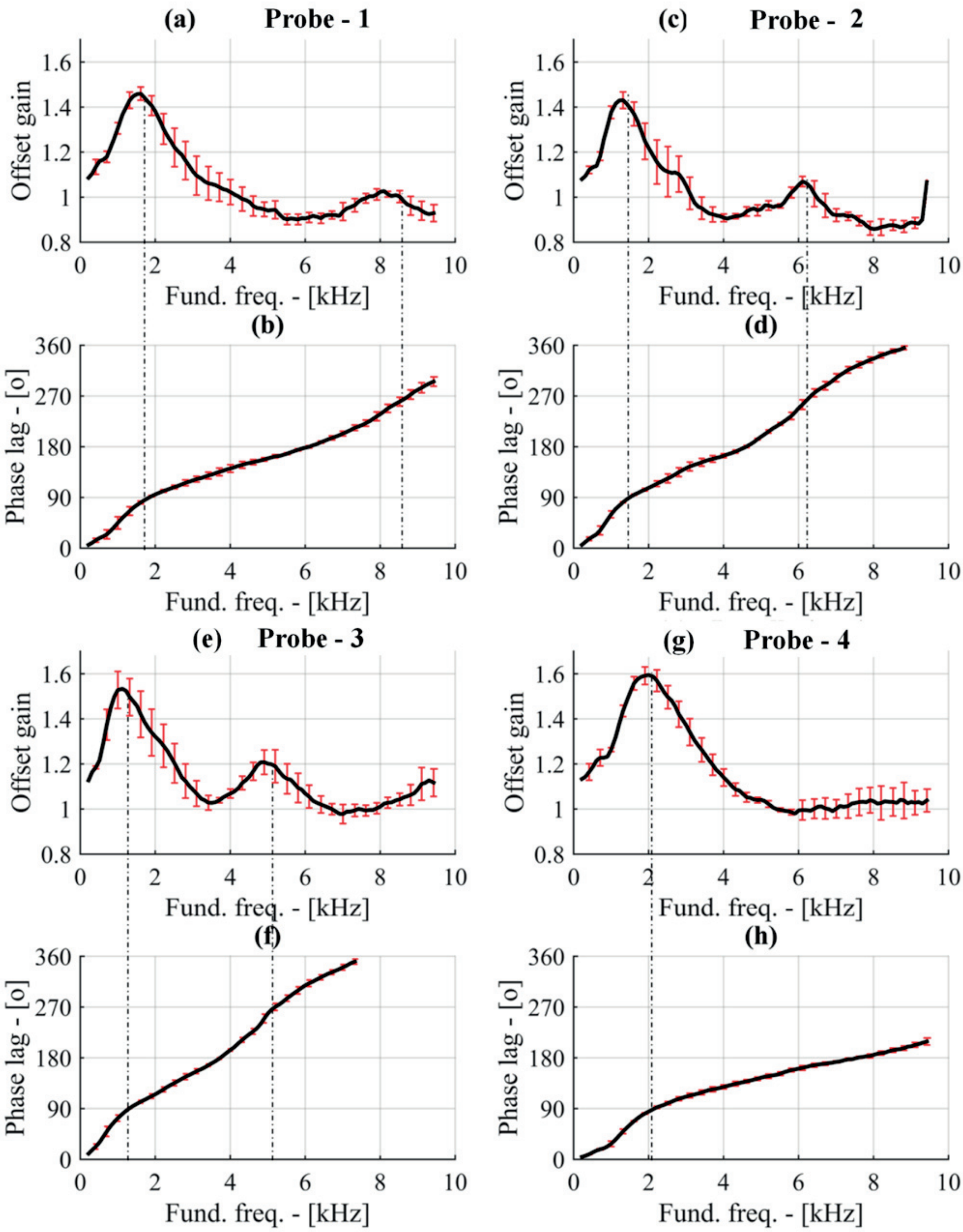

Figure 3.17 – L-shaped probes offset gain and phase lag.

$G_1(2\omega)$).

2. The offset gain G_0 is a function of the hpf.

3. The gains are dependent on the amplitude/mean of the input pressure signal.

The non-linear gain function is then described as follows:

$$G_n = G_n(\omega_1, A, \bar{A}) \tag{3.10}$$

where ω_1 is the fundamental frequency, A is the amplitude, and $\bar{A}$ is the signal offset. In order to assess these implications, the averaged harmonic gain functions of probe-3 are plotted with respect to the fundamental frequency and analyzed - Figure 3.18. The error bars due to the varying nozzle pressure are shown similar to Figure 3.17 and are contained within a 10% band. It is observed that the errors increase around frequencies where the gradient of the functions varies significantly. However, it will be shown later -section 3.7.6 - that the error propagation is insignificant due to the low amplitudes of the harmonics relative to the fundamental.

Given the presented non-linearity, a multi-dimensional transfer function approach is developed for the system identification of the test probes. It is consisting of a set of sub transfer functions describing the pressure averaged gain and phase lag for the offset and the harmonics up to the 5th order. The transfer functions are mathematically represented by piecewise polynomial fits. The gain functions for the harmonics are deduced relative to each fundamental frequency (hpf).

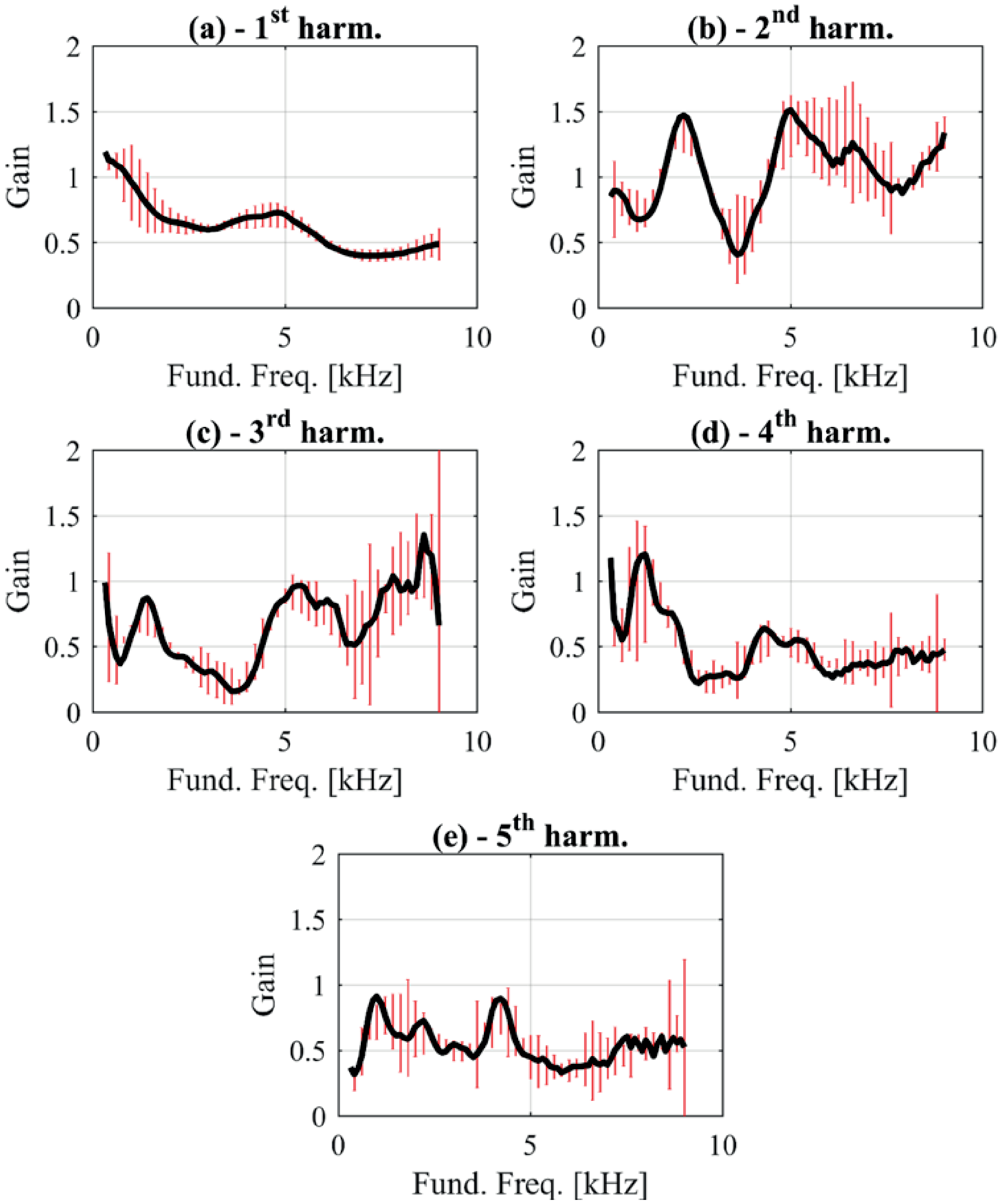

Figure 3.18 – Harmonic gains for Probe-3 - Error bars cover 6 different pressure levels.

3.7.5 Signal Reconstruction

The probe signal of data set 6 (not used in the system identification) is reconstructed using the multi-dimensional transfer function developed a priori. The signal reconstruction on a cycle at a $hpf = \omega_1$ is computed as follows:

$$q_{recon.}(t) = \frac{q_{0_{meas.}}}{G_0(\omega_1)} + \sum_{n=1}^{5} \frac{Q_{n_{meas.}}}{G_n(\omega_1)} \sin\left(n\omega_1 t + \Phi_{n_{meas.}} - \Phi_{n_{correction}}(\omega_1)\right) \tag{3.11}$$

Figure 3.19 compares samples of reconstructed signals with reference and measured signals of data set 6 suggesting excellent agreement between the reference and reconstructed signals. The presented examples in Figure 3.19 are for Probe-3 and at four excitations frequencies (1200 Hz, 3000 Hz, 7000 Hz and 9520 Hz). The figure shows that the transfer function identification and the reconstruction method are successful even at fundamental excitation frequencies far beyond the probe's resonant frequency (1.325 kHz for Probe-3).

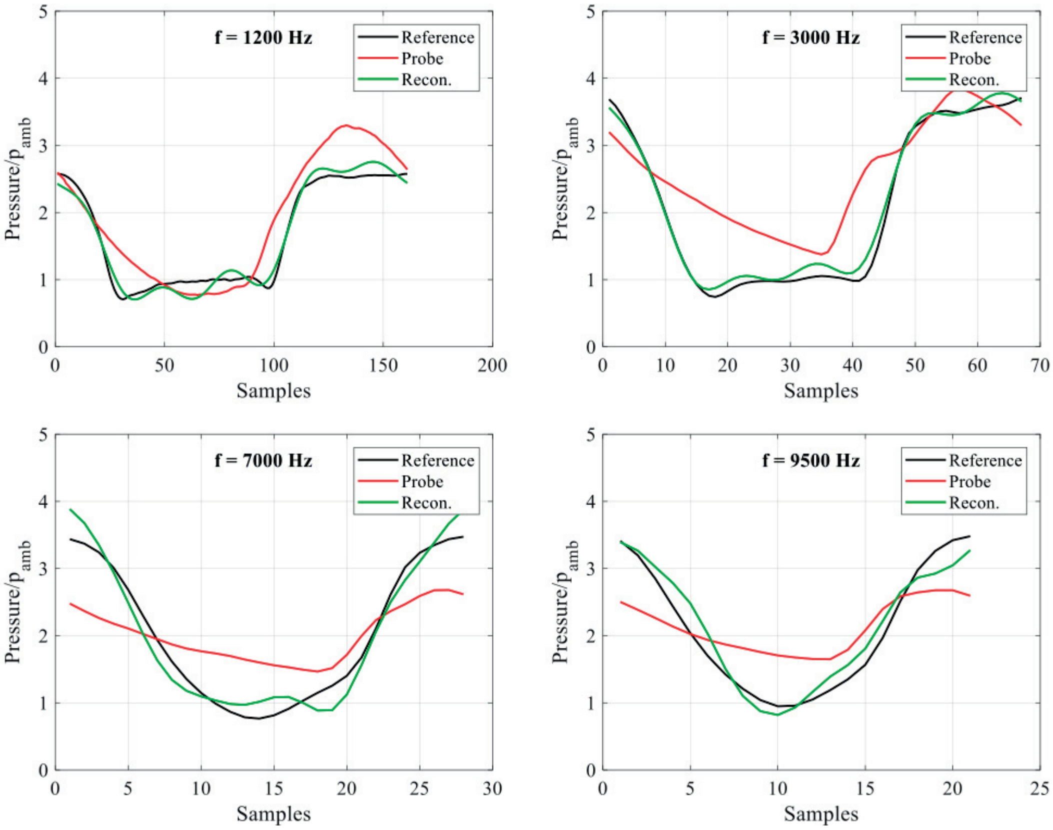

Figure 3.19 – Measured and reconstructed signals for excitations of 1.2, 3, 7 and 9.5 kHz for Probe-3.

3.7.6 Accuracy of Signal Reconstruction

The signal reconstruction accuracy is estimated using a goodness of fit (gof) variable, which compares the reconstructed signal to the reference signal as follows:

$$gof = 1 - \frac{\sqrt{\sum (q_{ref.} - q)^2}}{\sqrt{\sum (q_{ref.} - \overline{q_{ref.}})^2} \tag{3.12}}$$

The resulting goodness values (data set 6) are plotted as a function of the hpf for each probe - Figure 3.20. For the purpose of comparison, the probe data before reconstruction are phase corrected, and used to calculate a baseline goodness relative to the reference signal. The reconstructed signal has goodness values less than 80% for low (<1 kHz) and high (>8 kHz) frequencies. In the range of 1 kHz to 8 kHz, goodness values higher than 80% are achieved. However, with recurring drops at frequencies where the second harmonic gradients change sign - Figure 3.18. Note that the goodness of the reconstructed data samples shown in Figure 3.19 vary between 70% and 85%, suggesting that a goodness of 70% represents a good match between the two signals. These results confirm the adequacy of the averaged multidimensional transfer function approach in the system identification, and signal reconstruction of pneumatic channels.

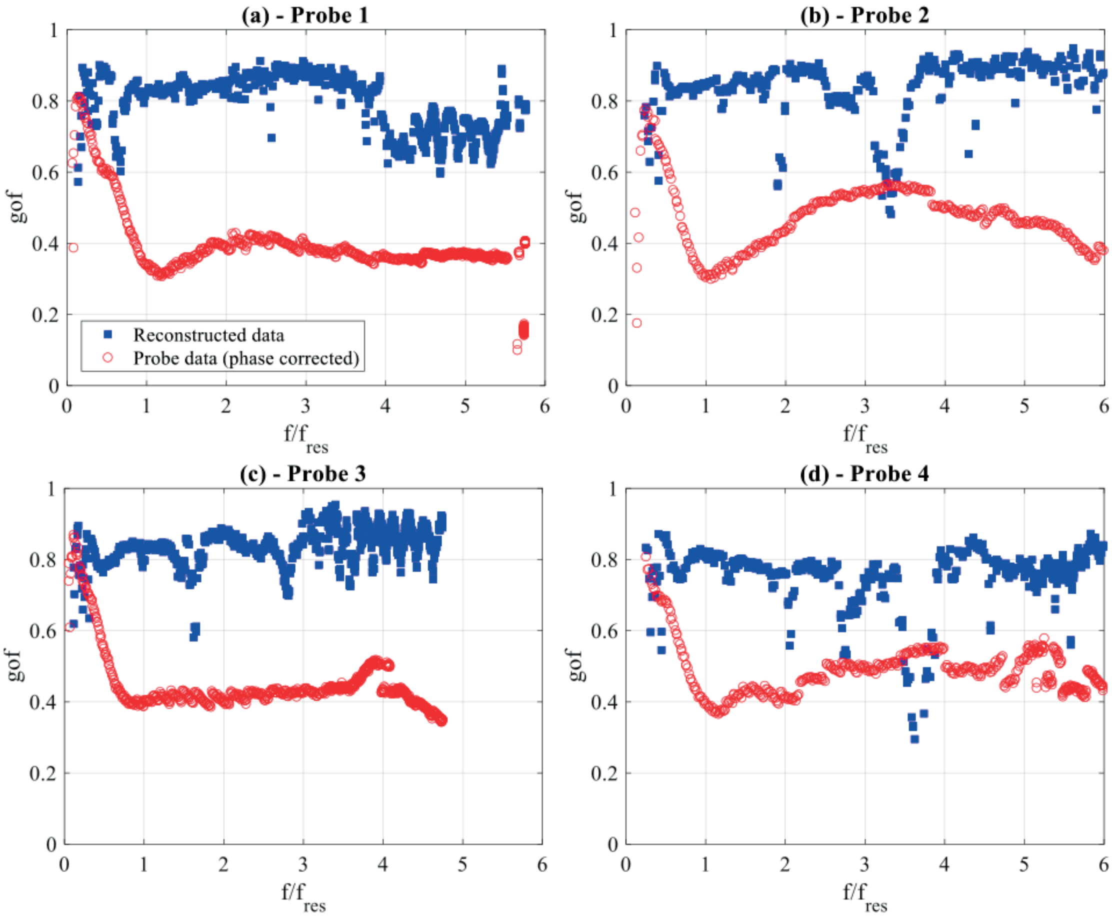

Figure 3.20 – Goodness of fit values of reconstructed signals for L-Shaped probes (data set 6).

3.8 In-situ System Identification of Embedded Pressure Probes on Externally Pressurized Bearings

The sole purpose of the previous section was to confirm the feasibility of pressure measurements using remotely mounted pressure transducers through pneumatic channels, as well as the development of a signal reconstruction procedure. Therefore, the exact same transfer functions developed using the mockup and the Siren disk cannot be directly extended for use on the actual embedded pressure probes in the instrumented rotor. Compared to the actual running conditions on gas bearings, the previously developed transfer function had the following issues:

1. The excitation pressure signal is of a different nature in the two cases. The Siren disk maintained a minimum pressure value equal to 1 atmosphere independent of the excitation frequency. Making the mean pressure value controlled solely by the peak pressure value. On the other hand, inside the bearing, the complete pressure signal shifts up or down as a function of frequency (rotational speed) due to the centrifugal

growth of the rotor, as well as the pressure build up due to the bearing hydrodynamics.

2. The mockup probes had the same overall dimensions as the ones embedded in the rotor, however the sealing technique was completely different. Also, manufacturing errors between the two probes can influence the system dynamics.

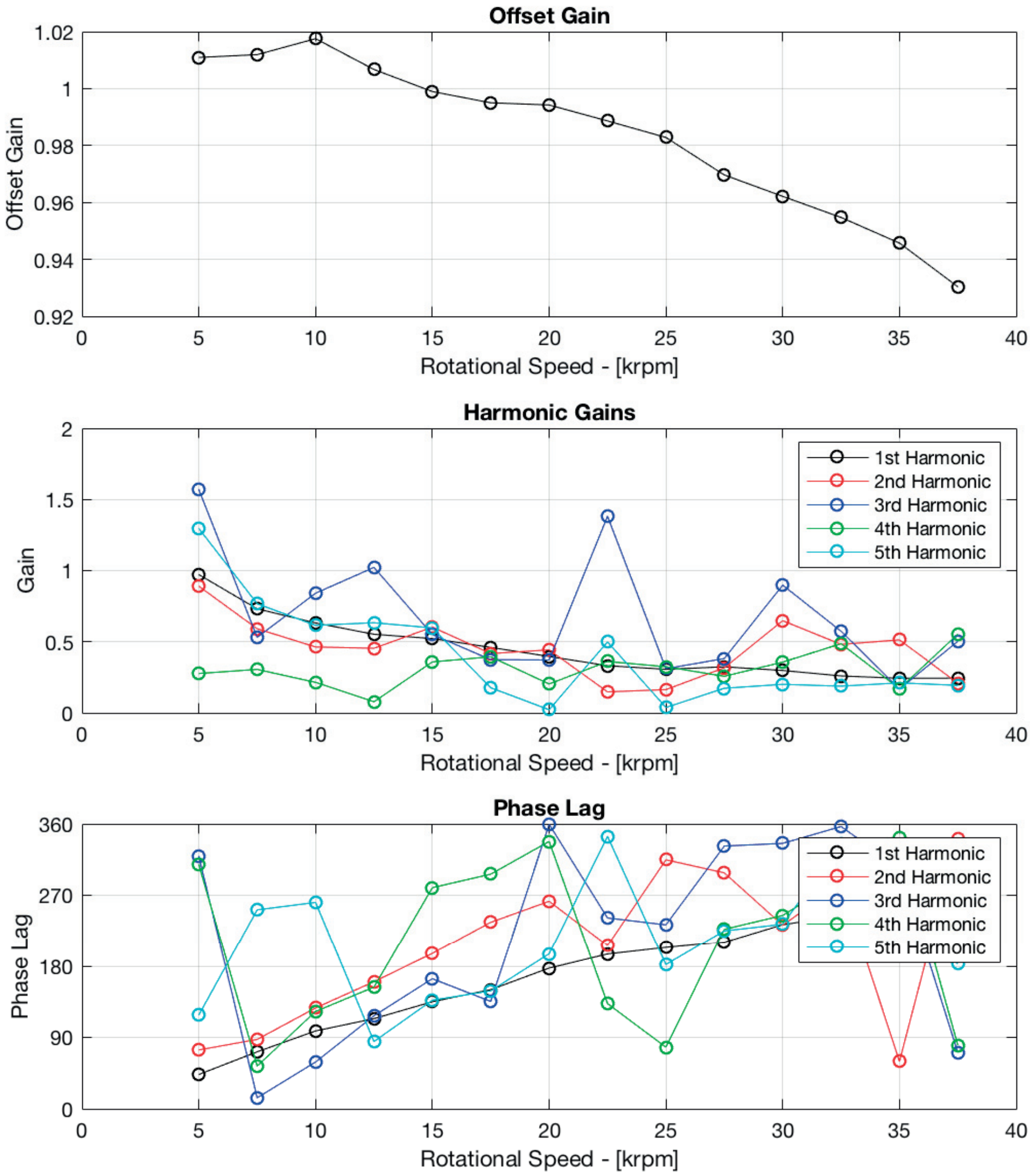

Figure 3.21 – In-Situ transfer function of embedded Probe-1 using the instrumented EP bearing as a reference signal generator.

Therefore, it was deemed essential to perform an in-situ identification of the embedded pressure probes inside the rotor using an instrumented EP journal bearing. The technique developed is using an EP bearing equipped with 25 micro pressure taps along the circumference, which are connected to Scanivalve pressure scanners - figure 3.3. The pressure profile resulting from the pressure taps is considered as the true reference signal. The position of the instrumented rotor is adjusted axially in order to ensure coincidence between the plane of measurement of the embedded probe and the plane at which the pressure taps are located. Details on the EP journal bearing design are given in chapter 4.

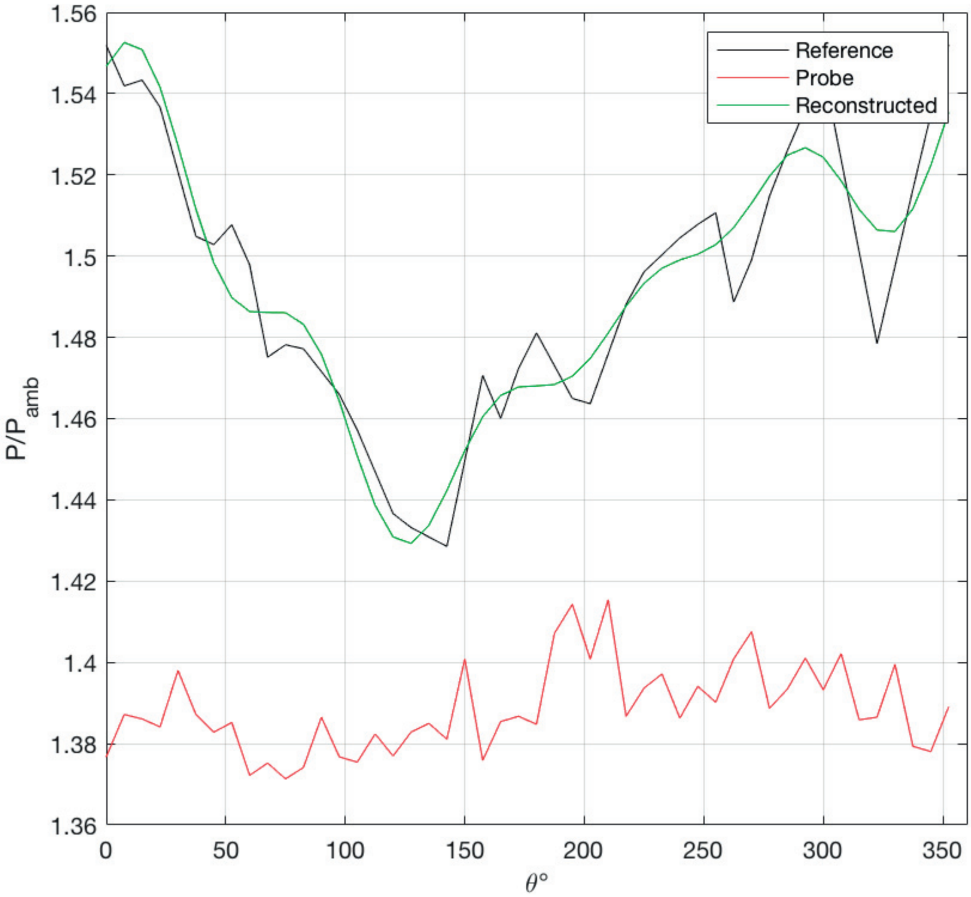

Figure 3.22 – Pressure signal reconstruction of Probe-1 at 37.5 krpm and a supply pressure of 10 bar using 5 harmonics.

The same identification technique used with the Siren disk identification is adopted to develop the transfer function of the probes. Due to mechanical assembly restrictions, only two probes were identified and used in the rest of the experimental campaign - probes 2 and 3 in Table 3.1.

Figure 3.21 plots the transfer function in the form of offset gain, harmonics gain, and phase

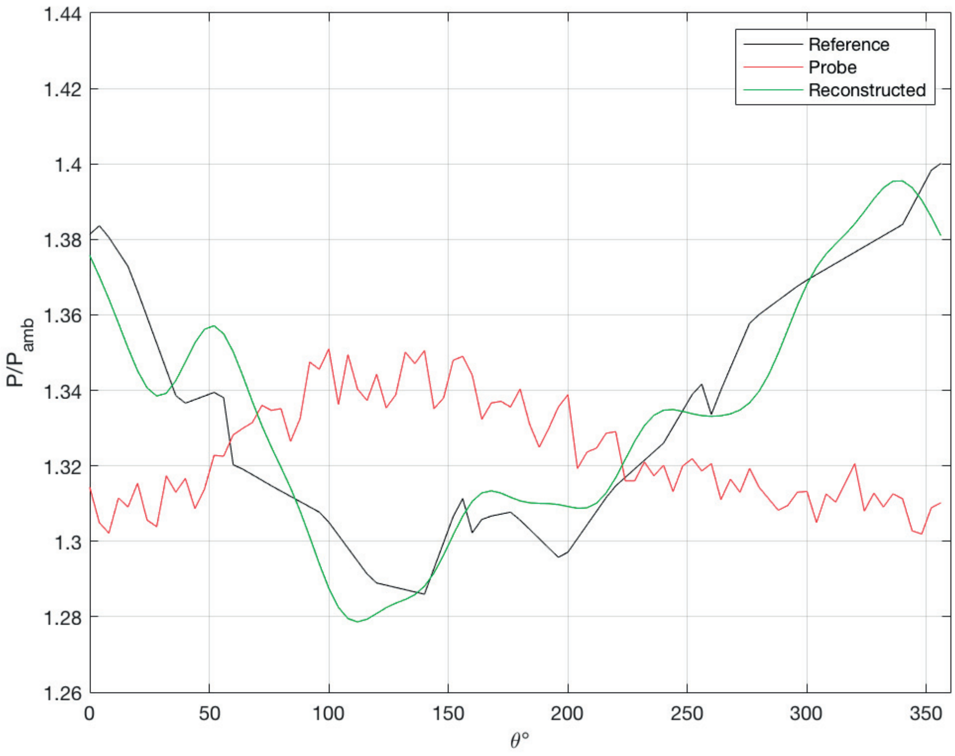

Figure 3.23 – Testing the capability of the transfer function to reconstruct different sets of data at the same control and independent variables (gof > 70%). The transfer function is developed using a different data set than that reconstructed.

lag up to 37.5 krpm for probe 3. It is observed that the offset gain is decreasing as a function of speed, which is considered a signature of system nonlinearity. Examining the gains of the first five harmonics, a strong attenuation is observed as a function of frequency. Comparing gain values of different harmonics at a given frequency, it is observed that they do not match in magnitude, which is considered another sign of system nonlinearity. Only 5 harmonics are presented in this section, it will shown in chapter 6 that a maximum of 5 to 6 harmonics are needed to reconstruct the signal accurately.

The inverse transfer function is used to reconstruct the measured signal as described in the previous section. Figure 3.22 presents a sample of the reconstruction in time domain at 37.5 krpm and a supply pressure of 10 bar. Such reconstruction quality corresponds to a goodness of 70%.

This probe identification using EP bearings is the cornerstone of the quality of the produced measurements. Therefore, it was of pinnacle importance to perform a systematic fitness test for the developed transfer functions in order to have confidence in their blind use on other bearings - without a reference signal. The fitness test is comprised of 3 levels of testing:

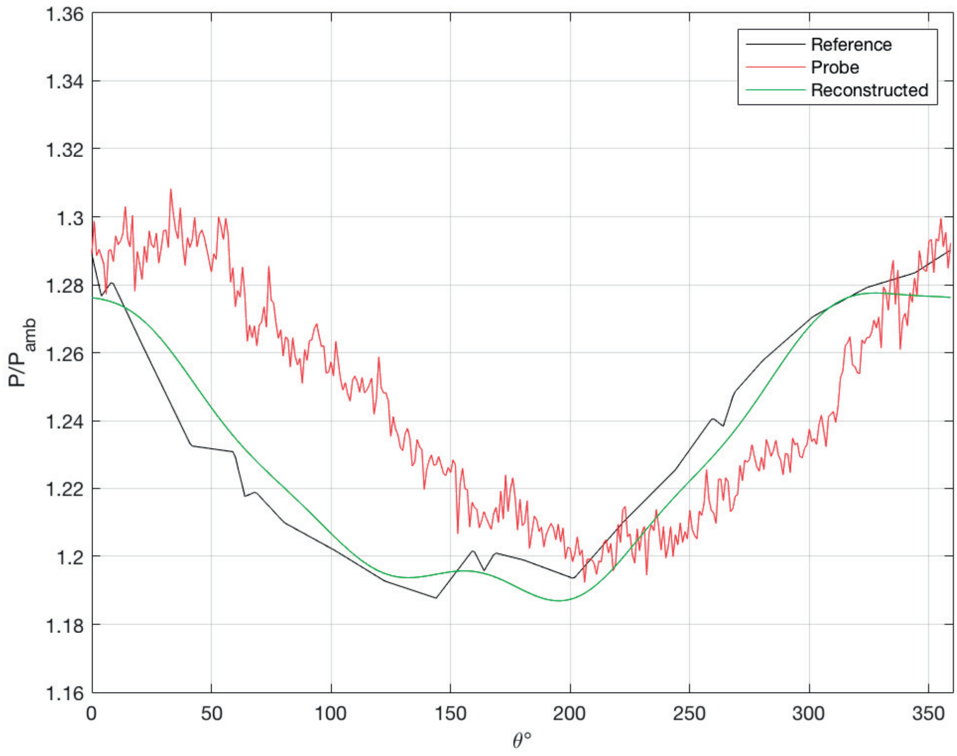

Figure 3.24 – Testing the capability of the transfer function to reconstruct data at a different supply pressure and a constant rotational speed (gof > 85%). The transfer function is developed at 7 bar, and the reconstructed data is measured at 5 bar.

1. Using the developed transfer function to reconstruct other data sets for the same control and independent variables (supply pressure and rotational speed).
2. Using the developed transfer function to reconstruct data at lower supply pressure.
3. Using an interpolated transfer function to reconstruct data between two known transfer functions (intermediate speed).

The first test was performed using a transfer function developed using a certain data set, and is used to reconstruct data from 2 other sets at the same test conditions - figure 3.23. The second test was using a transfer function developed at 5 krpm and with 7 bar of supply air pressure, then it was used to reconstruct data at the same speed but at a 5 bar. Reducing the supply pressure shifted the pressure signal from 1.31 bar to 1.23 bar. The reconstruction results were judged satisfactory as shown in figure 3.24. Finally, the third test was performed using a transfer function resulting from the averaging of two transfer functions at 10 krpm and 20 krpm. The transfer function is then used to reconstruct a signal acquired at 15 krpm. The result was satisfactory (gof > 80%) given the large averaging window - figure 3.25. The

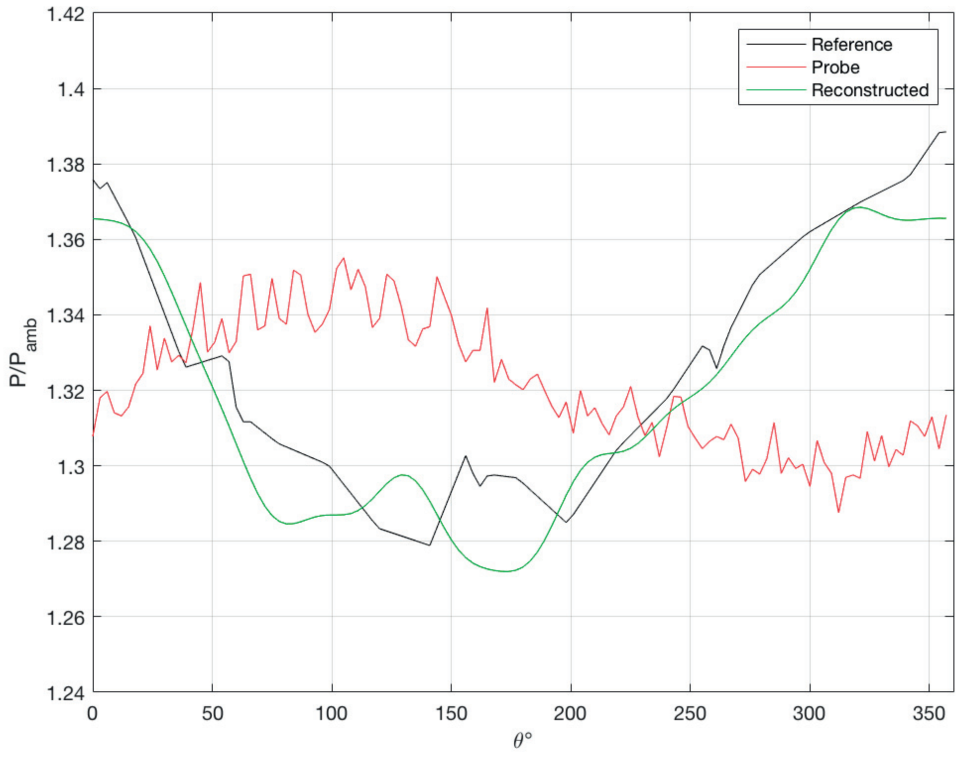

Figure 3.25 – Testing the capability of the transfer function to reconstruct measurements using interpolated gain and phase values - (gof > 70%). A transfer function is developed by interpolating two transfer functions at 10 krpm and 20 krpm in order to reconstruct measurements at 15 krpm.

general transfer function developed is computed at each 2.5 krpm, making the blind range for interpolation very small, hence, making the transfer function more robust. Passing the fitness test signaled the readiness of the developed transfer function to be used on other bearings.

3.9 Chapter Conclusions

The chapter presented the concept and design of the instrumented rotor used in the pressure profile measurement within the gas film of foil and aerostatic bearings. The following conclusions are made:

- An instrumented rotor with wireless telemetry and embedded pressure probes is designed and prototyped. The rotor is capable of measuring the pressure profile within the gas film of foil and aerostatic bearings at two axial positions simultaneously, and up to 37.5 krpm.
- The embedded pressure probes are remotely mounted pressure transducers near the

rotor center and connected to the measurement point through pneumatic channels built inside the rotor.

- The remote mounting distorts (attenuation and phase lag) the measured pressure signal due to the pneumatic channel.
- A pressure signal generator (e.g. Siren disk) is used for the system identification (transfer function development) of the probe (pneumatic channel + transducer).
- Using a Fourier series is used to develop a transfer function, as well as to reconstruct the time domain signal in order to subtract the effects of the pneumatic channel.
- The embedded pressure probes of the instrumented rotor are in-situ identified using an aerostatic bearing instrumented with pressure taps that describes the circumferential pressure profile. Measurements from the instrumented rotor are compared to the measurement of the instrumented bearing (reference signal).
- Comparing the rotor side (probe) to the bearing side (taps) measurements a good match was observed at quasi-static conditions.

4 Externally Pressurized Gas Journal Bearings Measurement Campaign

Before embarking on the experimental campaign on foil bearings, it was deemed necessary to test the instrumented rotor on benchmark bearings. Externally Pressurized Gas Journal Bearings (EPGJBs) were chosen for the task, mainly due to their load bearing capability at stationary conditions, as well as their potentials for high-speed operation. This chapter presents and discusses the results of the experimental campaign studying EPGJBs. The results are presented in two main sections. The first, presents measurements of spatially sampled pressure fields inside the gas film using bearings instrumented with pressure taps. The results are compared to a finite difference bearing model, and based on the compressible Reynolds equation. The second section, presents results using the instrumented rotor described in Chapter 3 to measure the continuous pressure profiles within the gas film of the same bearings. Pressure profiles are presented at different speeds and supply pressures.

Part of the work presented in this chapter is published as:

- Shalash, K., Guenat, E., and Schiffmann, J., 2018. ***Spatially Sampled Pressure Profile Measurements in Externally Pressurized Gas Journal Bearings.*** Tribology Transactions, pp.1-28.

4.1 Introduction

Externally pressurized gas journal bearings (EPGJB) are a widely-adopted technology to support high-speed rotors [54], and precision machine tools [55]. The technology is attractive due to its high stiffness and contact-free operation even at zero rotational speed. Such qualities are at the kernel of high accuracy applications like manufacturing spindles and inertial instruments [56, 57]. The main disadvantages of the technology are: 1) its dependence on a continuous supply of a compressed fluid, 2) its high sensitivity to geometrical accuracy, hence, demanding tight manufacturing tolerances, 3) its susceptibility to dynamic instabilities, and 4) its vulnerability to pollution and contamination.

The load capacity in fluid film bearings is provided by the pressure field within the bearing clearance. Although knowledge of the pressure field as a function of the rotor position is imperative for the understanding of the behavior of rotor-bearing systems, as well as for the validation of bearing models, measurements of pressure profiles inside the gas film of EPGJB are very scarce in the literature.

Most of the experimental effort to measure the flow field inside fluid film journal bearings were done on oil lubricated bearings. Roberts and Hinton [58] measured the radial and axial pressure profile inside a short (L/D = 1/3) circumferentially grooved bearing at different Reynolds numbers (40-50000). The bearing had a nominal diameter of 100 mm, and a clearance of 0.55 mm. Six equidistant piezo resistive transducers placed along a helix were used to measure the fluid film pressure. The sensors were connected to the bearing via 0.5 mm pressure taps. Results were in good agreement with theory for low eccentricity cases.

Brito et al. [59] performed similar measurements for a hydrodynamic journal bearing with two axial grooves. The measurements investigated the influence of lubricant supply conditions on the pressure and temperature profiles inside the bearing, as well as the rotor eccentricity. Pressure taps of ⌀1 mm were drilled along the mid-plane of the bearing, and connected to high precision Bourdon pressure gauges. The rotor nominal diameter was 100 mm with a diametrical clearance of 171 ± 4 µm. Cristea et al. [60] measured the pressure and temperature inside the oil film of a circumferential grooved journal bearing. The pressure was measured using ⌀1.5 mm pressure taps, the rotor nominal diameter was 100 mm, the diametrical clearance was 122 ± 4 µm.

The literature reports several studies presenting the pressure profile measurement in axial thrust bearings using pressure taps [1, 61–65]. However, few publications reported pressure measurements in gas journal bearings.

In 1961, Laub [66] reported the earliest zero rotational speed pressure profile measurement inside an EPGJB. The author used 6 pressure taps in the axial direction and 10 in the circumferential direction. The bearing was described to have 192 nozzles divided on 4 rows. No details on the manufacturing tolerances were given.

In 1962, Lemon [67] presented pressure profile measurements and compared it to analytical solutions. The bearing had pocketed (recessed) supply restrictors, yet the full dimensions of the bearing under investigation were not presented and experimental details were not provided.

The report by Burt in 1969 [68] is the most detailed experimental pressure measurement in EPGJBs that is available in the open literature. The tests considered a rotor supported on two journal bearings and one axial bearing. The journal bearings had two rows of 4 equidistant supply nozzles, with a relatively large diameter (1.12 mm for a 46 mm bearing diameter). The author reported large deviations in the measured bearing clearance relative to the nominal clearance (not quantified in the report). Only the axial pressure profile was measured using 7 equidistant pressure taps along the bearing length and at the same circumferential position. The supply flow rate was also measured to be 25% above the design value. Laminar flow theory was used to compute the axial pressure profile, however, the model underestimated the pressure compared to the measurement. The load capacity was overestimated by roughly 50% at zbar = 0.5. Better agreement in load capacity was achieved by changing the bearing design to a lower Reynolds number flow regime, suggesting an influence of turbulence on the performance of EPGJBs.

In 1979, Pink and Stout [69] presented pressure profile measurement in an EPGJB with feeding pockets. The results were presented at zero rotational speed and solely for the sake of numerical result validation. The paper is the most recent in the literature concerned by the gas film pressure in EPGJBs, but unfortunately, details of the measurements were not provided.

Reviewing the literature reveals a gap in experimental flow field benchmark data for gas lubricated EPGJBs. The few available articles are either incomplete, or missing crucial details, hence, making the experimental literature insufficient for a thorough model development and validation.

4.2 Spatially Sampled Pressure Profile Measurements Using Instrumented bearings

This section provides point measurements of the axial and circumferential pressure profiles inside a 40 mm diameter (L/D = 1) EPGJB at different supply pressures and static loads. The section also presents the bearing pressure profile measurement at different rotational speeds and up to 25 krpm. The corresponding mass flow rates are also measured, allowing the deduction of the bearing discharge coefficients. Quasi-static load displacement measurements were executed to investigate the bearing load capacity and stiffness as a function of supply pressure. Deviations between the computations of a hydrodynamic EPGJB model and the measured data are discussed in the framework of compressible flow theory providing insight into the origin of the deviation.

4.2.1 Numerical Modelling [1]

The steady state isothermal compressible Reynolds equation for EPGJBs is adopted as presented in Lo et al. [70], and discretized and solved using the finite difference method implemented in Guenat and Schiffmann [71]. The working fluid (air) is considered an ideal gas.

The supply restrictors are modeled as a source term present in the Reynolds equation that is active only at the nodes corresponding to the positions of the restrictors in the fluid film domain. An isentropic and adiabatic expansion through the nozzles from stagnation is assumed, with the mass flow rate expressed as follows:

---

[1] The model implementation and the simulations presented in this section were performed by Mr. Eliott Guenat at the Laboratory for Applied Mechanical Design between the period 2016-2017.

$$\dot{m} = A p_s \phi \left(\frac{2\rho_s}{p_s}\right)^{\frac{1}{2}} \tag{4.1}$$

where, depending on whether the flow is choked or not:

$$\phi = \begin{cases} \left(\frac{\gamma}{2}\left(\frac{2}{\gamma+1}\right)^{\frac{\gamma+1}{\gamma-1}}\right)^{\frac{1}{2}} & \text{if } \frac{p}{p_s} \leq \left(\frac{2}{\gamma+1}\right)^{\frac{\gamma}{\gamma-1}} \\ \left(\frac{\gamma}{\gamma-1}\left[\left(\frac{p}{p_s}\right)^{\frac{2}{\gamma}} - \left(\frac{p}{p_s}\right)^{\frac{\gamma+1}{\gamma}}\right]\right)^{\frac{1}{2}} & \text{if } \frac{p}{p_s} > \left(\frac{2}{\gamma+1}\right)^{\frac{\gamma}{\gamma-1}} \end{cases} \tag{4.2}$$

A discharge coefficient should be defined to model the actual mass flow rate through the restrictor. The sensitivity of the discharge coefficient to the fluid flow condition, and the restrictor's geometry, makes the development of a generic model very challenging. To the knowledge of the author there are no models covering the specific geometry and flow conditions of the restrictors under investigation. The empirical correlation proposed by Belforte et al. [1] is developed using orifice restrictors, which are different than the restrictors under investigation (Different diameter, and L/D. To be discussed in details in section 4.2.4). However, they are considered the closest possible to the latter. Hence, the correlation is used to estimate the discharge coefficient in the present study.

A grid dependency analysis has been executed starting with 90 nodes as an initial seed. The normalized load (pressure field integral) was used as a control variable with a residual error defined as follows:

$$r_\varepsilon = \frac{\overline{W}^n - \overline{W}^m}{\overline{W}^m} \tag{4.3}$$

where n is a denser grid than m. In total 5 grids have been compared, the selected grid has 9360 nodes (65 axial and 144 circumferential) and yields a residual error r_ε in the order of 10^{-3} (0.1%) which is considered satisfactory.

4.2.2 Test Bearing Description

The test bearings are made out of DIN EN 1982 Bronze. Each bearing has two feeding rows of 18 restrictor nozzles (100μm diameter and 1.1mm long). The two rows are located at $\overline{z}$=±0.5 where $\overline{z}$=Z/R. The two journal bearings are identical in terms of nominal dimensions and air supply, however one of them was designed to measure the axial pressure profile (bearing A), and the other to measure the circumferential pressure profile (bearing B). The supply and measurements have two physically separated internal passages inside the bearing structure. The tested bearings have a nominal radial assembly clearance of 30μm.

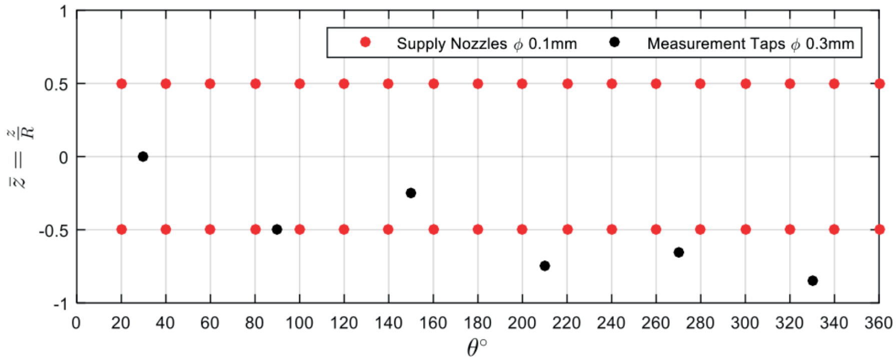

Figure 4.1 – Pressure tap locations in bearing A for axial pressure profile measurement.

The pressure measurements are made through Ø0.3 mm pressure taps at various locations inside the test bearings. A symmetric axial pressure profile around the bearing mid plane is assumed. Hence, bearing A is designed to have 6 measurement points capturing half of the axial pressure profile at $\overline{z}$ = -0.85, -0.75, -0.65, -0.5, -0.25, and 0. The taps are located on 3 equidistant axial planes between the supply nozzles - Figure 4.1. Bearing B has 25 pressure taps along the bearing circumference (packaging maximum) yielding the circumferential pressure profile inside the bearing - Figure 4.2.

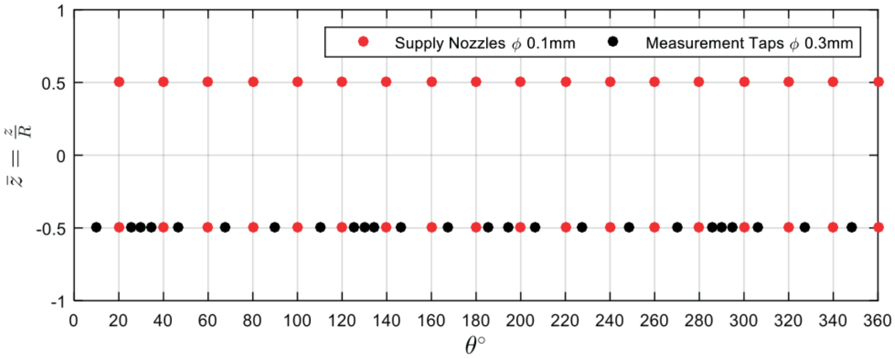

Figure 4.2 – Pressure tap locations in bearing B for circumferential pressure profile measurement.

4.2.3 Dimensional Metrology of the Rotor and the Test Bearings

The effect of manufacturing tolerances on the performance of EPGJBs was the focus of several investigations. Stout and Rowe [72] studied the effect of manufacturing errors on orifice and slot entry bearings, and concluded that a double entry bearing is less sensitive to the effects of manufacturing errors than single entry bearings. Pink and Stout [73] extended the work by introducing a tolerancing procedure for compensated EPGJBs, and showed that minor dimensional variations in the restrictor or the clearance can produce significant discrepancies in load capacity. Following these efforts, Stout [74] dedicated an article discussing in details possible manufacturing errors in EPGJBs and their corresponding effects on performance. He included the effects of the bearing roundness, form, and alignment, along with the restrictor geometry, and bearing assembly clearance. The author highlighted major deviations in load capacity due minor deviations in the bearing geometry. Stout and Pink [69] showed that knowledge of the geometrical deviations in orifice compensated EPGJBs can be used to estimate the deviation in performance of such bearings.

Hence, special attention is given to ensure the accurate geometrical control of the rotor-bearing system before embarking in the test program. The test rotors and bearings are measured using a commercial optoelectronic reader that converts the linear movement of the measurement probe into an electronic signal. The rotor has a diameter of 39.369 mm ± 1.16 μm. Bearing A has a diameter of 39.442 mm $\pm 1.48 \mu$m. Bearing B has a diameter of 39.437 mm ± 1.87 μm. As a consequence the measurements yield a radial clearance of 36.5 μm ± 1.88 μm in bearing A, and 33.86 μm ± 2.2 μm in bearing B.

For the bearing A, the supply nozzles and the measurement taps are laser drilled from the outside of the bearing using 4 mm counterbores for access, which are sealed after the manufacturing - Figure 4.3a. The supply nozzles and the measurement taps were inspected and measured with a digital microscope – Figure 4.3b. The supply nozzles measurement indicates a mean diameter of 111 μm, with deviations within 6.6%. Hence, indicating an overall oversizing of the supply nozzle by 11%. The measurement taps are within 3% of the design value ($\varnothing$0.3mm). For bearing B, the supply nozzles and the measurement taps were drilled from the inner diameter of the bearing using a special EDM (Electric Discharge Machining) electrode setup. The drilling accuracy lies within 5%.

4.2.4 Mass Flow Measurement and Discharge Coefficient Deduction

The mass flow rate was measured for each of the two bearings simultaneously at different supply pressures. Figure 4.4a shows that the mass flow increases linearly with the supply pressure, which is a clear indication of choked restrictors. The difference between the two bearings is due to the larger supply nozzle diameter and clearance of bearing A as indicated above. It was also observed that the measured mass flow rate was not affected whether or not the rotor was assembled inside the bearings. This can be explained by considering the effective (smallest) throttling discharge area, which is governed by the nozzle cross-sectional

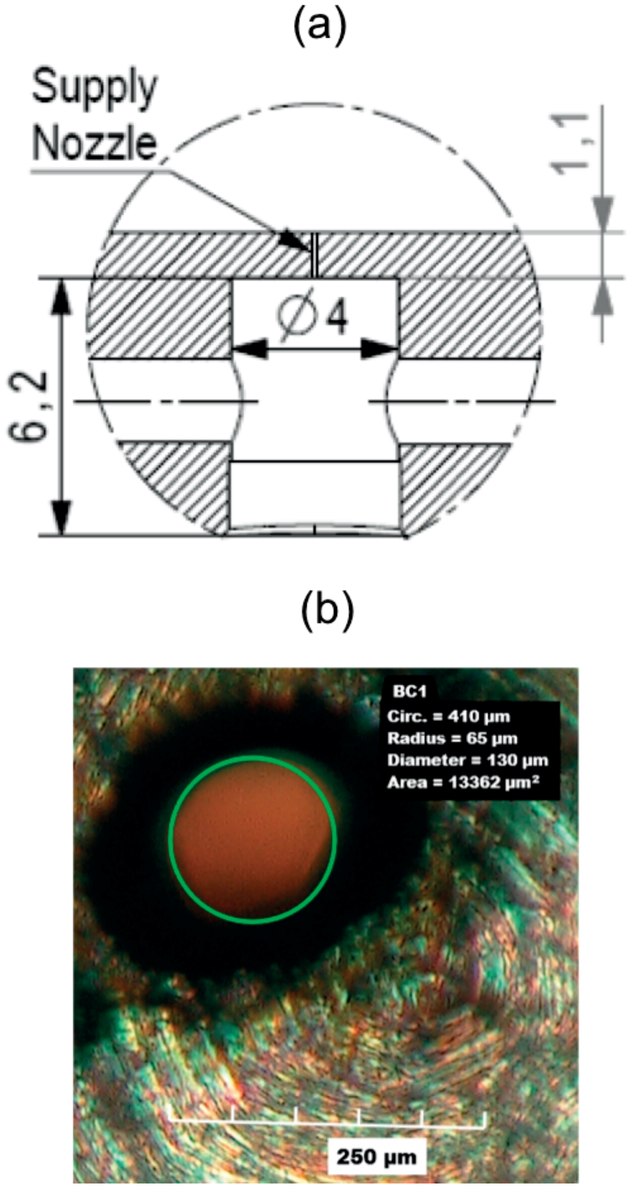
(a)
Supply Nozzle
1,1
Ø4
6,2
(b)
BC1
Circ. = 410 µm
Radius = 65 µm
Diameter = 130 µm
Area = 13362 µm²
250 µm

Figure 4.3 – (a) ⌀0.1mm bearing supply nozzle geometry (dimensions in mm), (b) nozzle and tap inspection and measurement using digital microscopy.

area $A = \frac{\pi d^2}{4}$, and not the curtain area $A = \pi dC$.

The measured mass flow rate is then compared to theoretical mass flow rates based on isentropic expansion through the restrictor. Hence, deducing the discharge coefficient as follows:

$$C_d = \frac{\dot{m}_{actual}}{\dot{m}_{\text{isentropic}}} \tag{4.4}$$

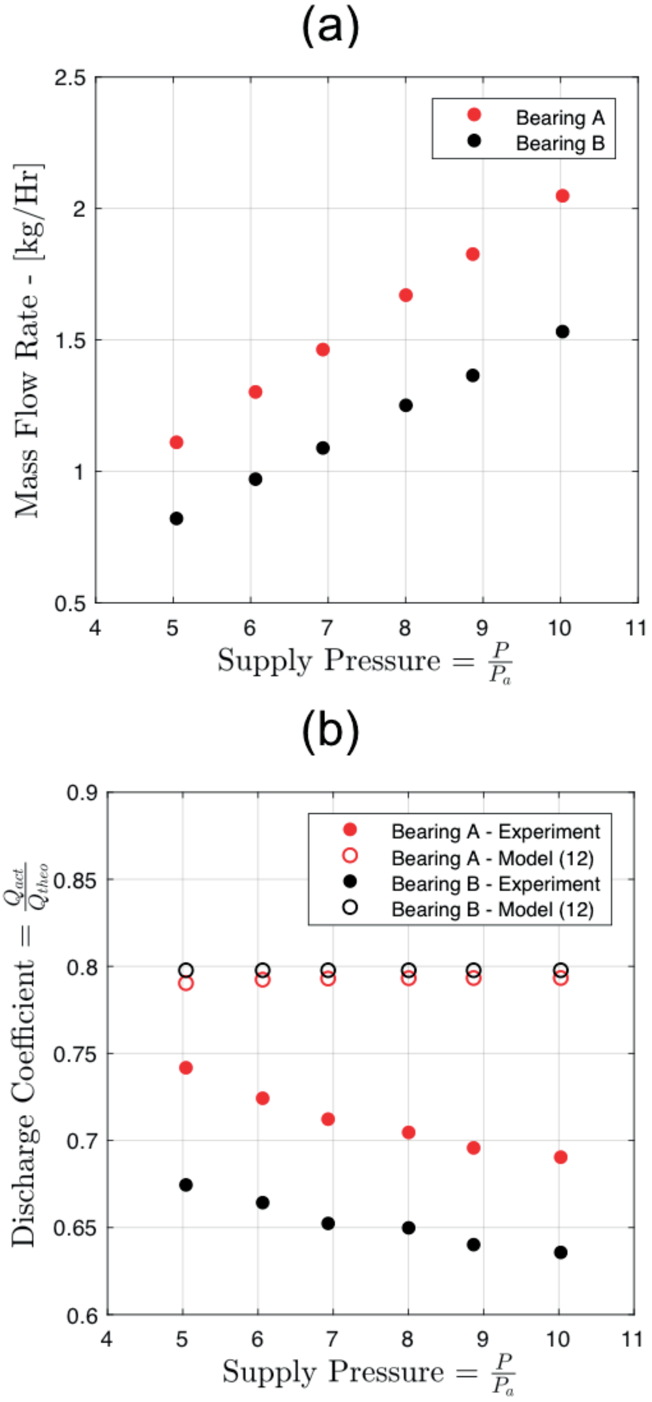

Figure 4.4 – (a) Mass flow rate measurement for the two test bearings as a function of supply pressure ($\overline{W}$=0.04), and (b) corresponding deduced discharge coefficients.

Although the flow is choked, the measured discharge coefficient evolves inversely proportional to the supply pressure - Figure 4.4b. This is due to the increase in the bearing pressure drop with the increase in the supply pressure. The estimated discharge coefficients in the model of Belforte et al. (12) overestimates the measured experimental values by up to 15% – Figure 4.4b. This is attributed to the shorter restrictors (l/d = 0.75 to 1.5), and larger diameters (0.2, 0.3, and 0.4mm) used in the development of the empirical model. The manufactured restrictors in bearings A and B are long, with a length equal to 11 diameters. It is also worth mentioning that the manufactured restrictors in bearing A are slightly convergent due to the nature of the laser drilling technique. Moreover, and contrary to the model of Belforte et al. [1], the restrictors under investigation are not of the inherent type since the film thickness and the restrictor diameter are of the same order of magnitude. The restrictor's Reynolds number ($Re = \frac{\dot{m}d}{A\mu}$) ranged between 7777 and 4626 depending on the supply pressure level.

The uncertainty in the deduced discharge coefficient due to the uncertainty in the nozzle diameters is 12% and 9.3% for bearings A and B respectively. Hence, the measured mass flow rates are used as input to the bearing model. Making the assumption that all the nozzles have the same geometries in a first approximation allows the deduction of the mass flow rate for a given nozzle.

4.2.5 Effect of Supply Pressure on Circumferential and Axial Pressure Profiles

The axial and circumferential pressure profiles are measured at zero rotational speed for different supply pressures. Figure 4.5b, d, and f compares the measured and the model computed axial profiles inside bearing A supporting only the rotor (no external load and imposing the measured mass flow rate from Figure 4.4a). The maximum pressure is at the length corresponding to the location of the supply nozzles row ($\overline{z} = -0.5$). The pressure drop between $-0.5 \leq \overline{z} \leq 0$ is attributed to dispersion and to non-axial flow effects [75], which are the result of manufacturing variations in the supply nozzles that causes the air to flow around the bearing from regions of high pressure to low pressure. It should be stressed that the measurement points are located between the feeding restrictors, and not at the same circumferential angle– Figure 4.1. It is observed that doubling the non-dimensional supply pressure from 5 to 10, increases the pressure inside the bearing only by an average of 22%, which indicates that the restrictor flow resistance is high compared to the fluid film resistance.

Numerically, the pressure at the position of measurement taps is obtained from the model at the corresponding positions according to Figure 4.1 and Figure 4.2 and by imposing the measured mass-flow and supply pressure as operating conditions. The influence of the variance in the bearing geometry as well as deviations in the supply nozzles diameters are used to obtain a band of prediction. Mean geometrical values are used for a nominal simulation. It is found that the pressure field is strongly influenced by slight deviations in the bearing clearance and in the supply nozzle diameter. The bounds of the manufacturing uncertainty at the point $\overline{z} = 0$ yield pressure deviations between -7.7% and 8.9% relative to nominal. The model is in good agreement with experimental measurements between $-0.5 \leq \overline{z} \leq -1.0$, highlighting the effectiveness of the measurements for model validation. Overestimation in pressure is observed between the supply nozzle and the middle of the bearing. Possible explanatory hypotheses are:

1. The effect of dispersion and circumferential flow are significant in the test bearing. Dudgeon and Lowe [76] studied the two effects on the performance of EPGJBs and attributed large model overestimation to these factors.
2. Certain supply nozzles (potentially close to measurement taps) are beyond the standard deviation of the measured nozzles, hence, creating circumferential flows.

In support of the circumferential flow hypothesis, a simple numerical optimization is performed using the bearing model, where the individual diameter of each nozzle is multiplied by a factor to perturb the mass flow rate of each nozzle. In a first case, the 36 nozzles adopted factors varying between 0.4 and 2 (wide range). In a second case, the factors varied between 0.94 and 1.06 (tight range). For each case, the optimizer finds the set of factors minimizing the absolute error between the computed and the measured axial pressure profiles. Both cases, seems to capture some pressure drop in the center of the bearing. However, the first case is in better agreement with the experiment as shown in Figure 4.6. Hence, implying that the deviation in the nozzle diameters is creating a circumferential flow, which in turn is suggested to be the root cause of the pressure depression in the center of the bearing.

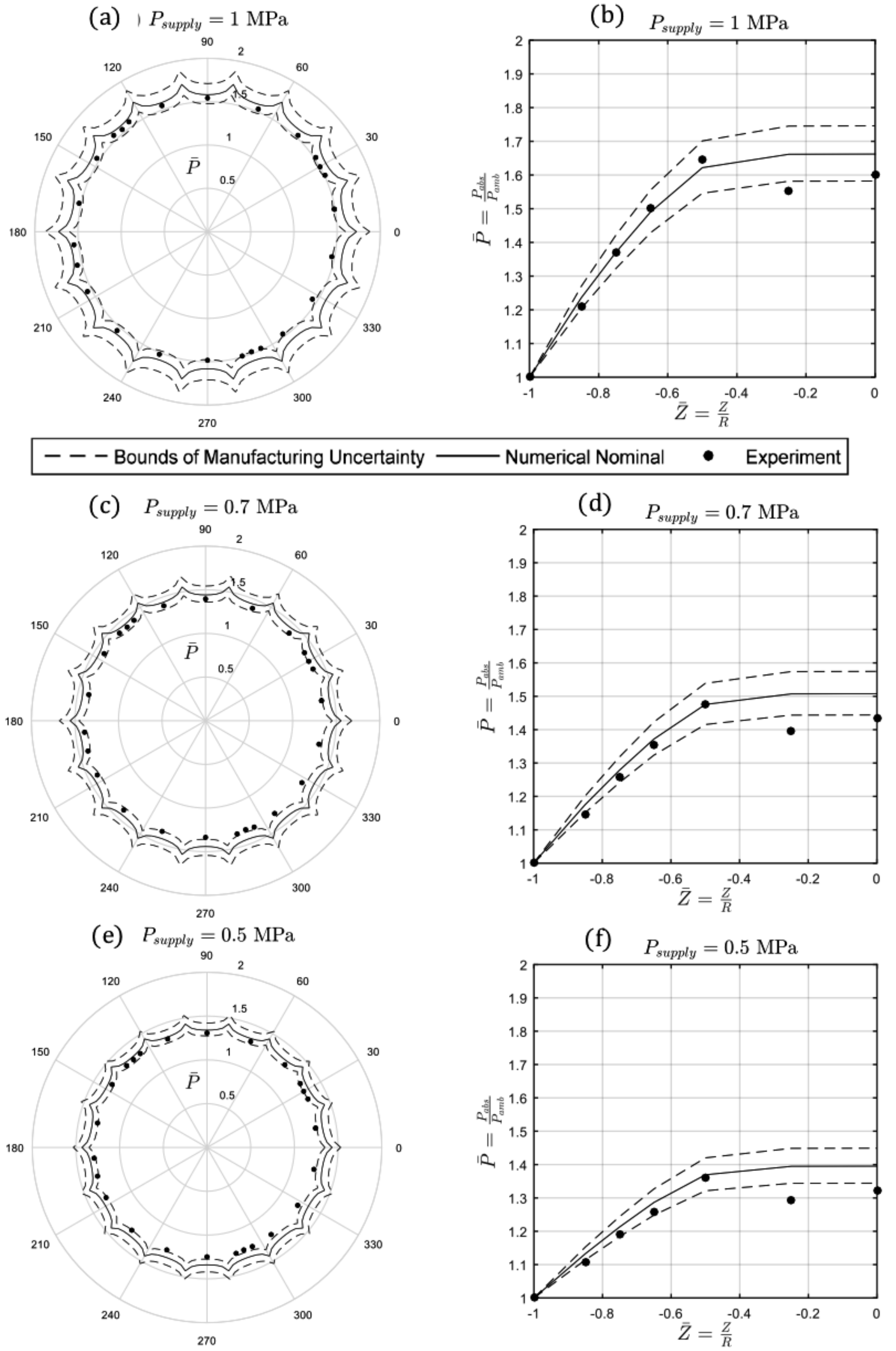

Figure 4.5 – Measured and predicted circumferential and axial pressure profiles at different supply pressures ($\overline{W}$=0.04).

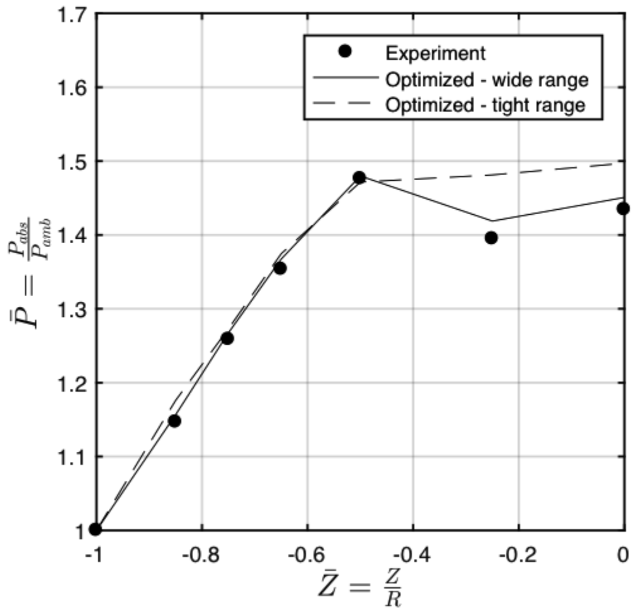

Figure 4.6 – Numerical axial pressure profile with optimized nozzle diameters compared to measurement.

Figure 4.5a, c, and e presents the same exercise for the circumferential pressure profile in bearing B – without external load. Both the experiment and the simulation show a clear pressure gradient between the supply restrictors, with the pressure building up near the nozzle locations and dropping slightly in between them. Qualitatively, the model is considered in good agreement with the experiment. A slight over estimation of the pressure, however, persists. Yet, the error is lower in comparison to the axial profile validation. This can be attributed to the specific location of the measurement at $\overline{z} = -0.5$ which is away from the pressure depression region in the center of the bearing. It should be noted that the circumferential and axial profiles are measured inside two different bearings (i.e. different clearances and supply nozzle diameters).

In order to quantify the recurring error between the simulation and the experiment, the pressure values of the model at the measurement points are compared against the corresponding experimental values. The error is defined as follows:

$$\text{Error } = \frac{\overline{p}_{\text{ model}} - \overline{p}_{exp}}{\overline{p}_{exp}} \tag{4.5}$$

For the design case of 0.7 MPa, the error along the bearing circumference at $\overline{z} = -0.5$ had a mean of 5.52%, a maximum and a minimum of 10.11% and 2.68% respectively. The error is reaching a maximum at 330° and a minimum at approximately 120°, phasing roughly 180°. Such observation suggests a slight eccentricity towards 120°, which is also observed during the measurements of the rotor position.

4.2.6 Effect of Rotational Speed on Circumferential and Axial Pressure Profiles

In order to assess the effect of the rotor speed on the fluid film pressure, the pressure profiles at the design supply pressure of 0.7 MPa were measured at different rotational speeds up to 25 krpm. It should be stressed that since the axial and circumferential profiles are measured inside two different bearings with slightly different clearances, the bearing compressibility numbers ($\Lambda = \frac{6\mu\Omega R^2}{P_a C^2}$) are different for the same rotational speed (maximum compressibility 0.86 and 1.0 for bearing A and B respectively). It is observed that Increasing the rotational speed, increases the pressure inside the bearings. Qualitatively, the shape of the pressure profile was unaffected by the rotational speed. It is hypothesized that fluid film pressure increase is due to the centrifugal growth of the rotor, which is calculated according to Dubbel [77] as:

$$\Delta h = \frac{\rho_{Rot}\Omega^2 R}{E}\left[2c_1 r^2 + (c_1 - c_2) R^2\right] \tag{4.6}$$

where

$$c_1 = \frac{3+\nu}{8} \tag{4.7}$$

$$c_2 = \frac{1+3\nu}{8} \tag{4.8}$$

where Δh is the reduction in radial clearance, ρ the rotor material density, ω is the rotor speed, R and r are the rotor's outer and inner radii respectively, E is the Young's modulus, and ν is the Poisson ratio. For the Steel rotor used in the tests, the centrifugal growth at 25 krpm results in a 1.3 μm decrease in radial clearance (3.56%). Two cases are simulated, one with nominal clearance, and second reduced by 1.3 μm corresponding to the rotor spinning at 25 krpm - Figure 4.7. The results of the simulations plotted in Figure 4.7 are in good agreement with the measurement, and therefore highlighting the importance of considering centrifugal growth in EPGJB models.

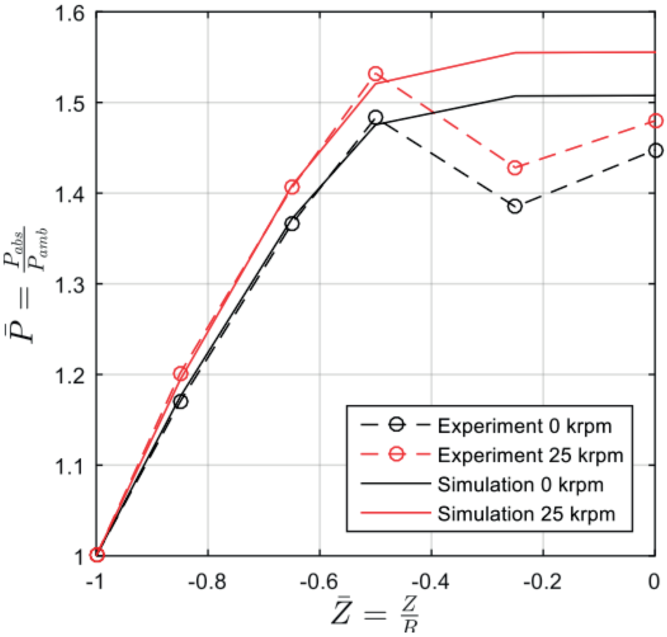

Figure 4.7 – Effect of centrifugal growth on the fluid film pressure profile ($\overline{W}$=0.04).

The mass flow rate is measured at the different test speeds, showing no evident effects at the nominal supply pressure of 0.7 MPa. This is because the throttling area is unaffected by the centrifugal growth of the rotor (1.3 μm in radius), also the pressure buildup downstream of the nozzles maintains the choked condition.

4.2.7 Effect of Load on Displacement

Fleming et al. [78] confirmed the assumptions of Powell [75] and showed that the stiffness of EPGJBs is not significantly affected by the rotational speed. Cunningham and Gunter [79] suggested that measured stiffness values at zero rotational speed of such bearings is sufficient to estimate the rigid body modes of the rotor. Hence, it was found essential to quantify the stiffness of the bearings under investigation.

The quasi-static load-displacement auxiliary setup introduced in chapter 2 was attached to the test rig in order to measure the resulting displacement for a given load at zero rotational speed. The accuracy of the proximity probe is ±1.3%, the accuracy of the load cell is ±1%. The uncertainty propagation for the eccentricity ratio and stiffness deduction is estimated to be ±6.57% and ±1.64% respectively (including the uncertainty in the measured bearing clearance).

Figure 4.8a shows the measured load versus eccentricity ratio at different supply pressures in bearing B. The load capacity increases both with eccentricity and with the supply pressure. It is observed that the effect of supply pressure on load capacity is more predominant at high eccentricities ($\epsilon \leq 0.5$).

At very large eccentricities ($\epsilon \leq 0.8$) and for low supply pressures (0.3 and 0.4 MPa), an area of zero stiffness (instead of the expected single inflection point) is observed. This phenomenon can be explained by considering a single nozzle under load, which will build up pressure as the eccentricity increases. At a certain threshold eccentricity, the pressure will drop drastically due to blockage (reduction in curtain area). Considering the rotor-bearing system under investigation, and given their circular nature, at a given eccentricity, the supply nozzles are not loaded equally. Hence, some nozzles are heavily blocked and stop contributing to load capacity, while others are at peak pressure. Such behavior would propagate along the loaded bearing circumference as the eccentricity continues to increase. Thus, the net reaction force will be nearly constant at this range of eccentricities. Finally, the aggressive change in slope near $\epsilon = 1.0$ is due to the mechanical contact of the rotor with the bearing surface.

Figure 4.8b presents a deduced normalized stiffness ($\frac{d\overline{W}}{d\epsilon}$) versus eccentricity ratio for the different supply pressures. The observed stiffness is highly nonlinear as a function of eccentricity. Thus, implying the necessity of deducing the stiffness at a given eccentricity ratio, within the design process of EPGJBs.

In order to assess the bearing model, a comparison of the measured and computed load capacities is presented. For a given eccentricity ratio, the bearing load is evaluated by integrating the pressure over the fluid film domain. The pressure field is simulated with two different approaches. The first is assuming a constant discharge coefficient for the nozzles (independent of the local film thickness), and accounting only for the reduction in the minimum discharge area (curtain area vs. restrictor area), in addition to the local thermodynamic conditions (heat capacity ratio, pressure and density at supply conditions). The initial unloaded case uses the

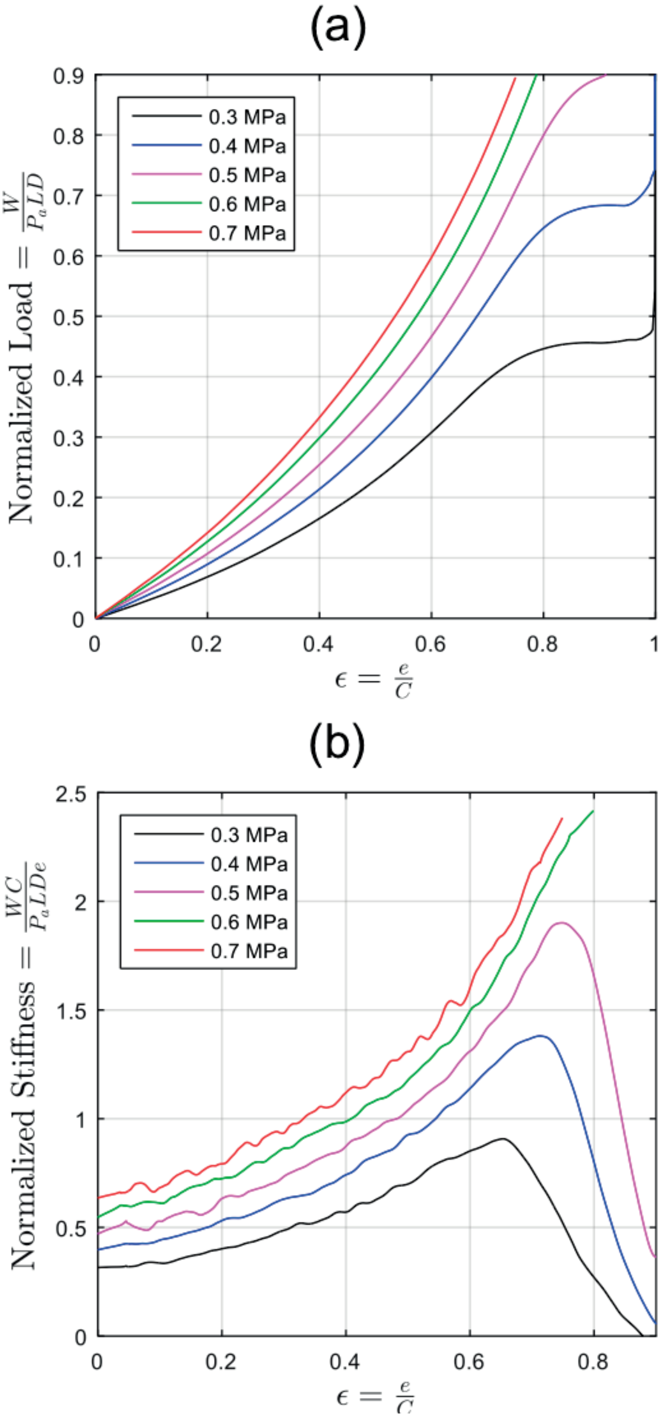

Figure 4.8 – (a) Measured normalized load capacity as a function of the eccentricity ratio at different supply pressures and at 0 rotational speed, and (b) corresponding deduced normalized stiffness.

measured mass flow rate as a starting point - Figure 6a. The second uses the model of Belforte et al. [1] for estimating the discharge coefficient as a function of the local film thickness and Reynolds number.

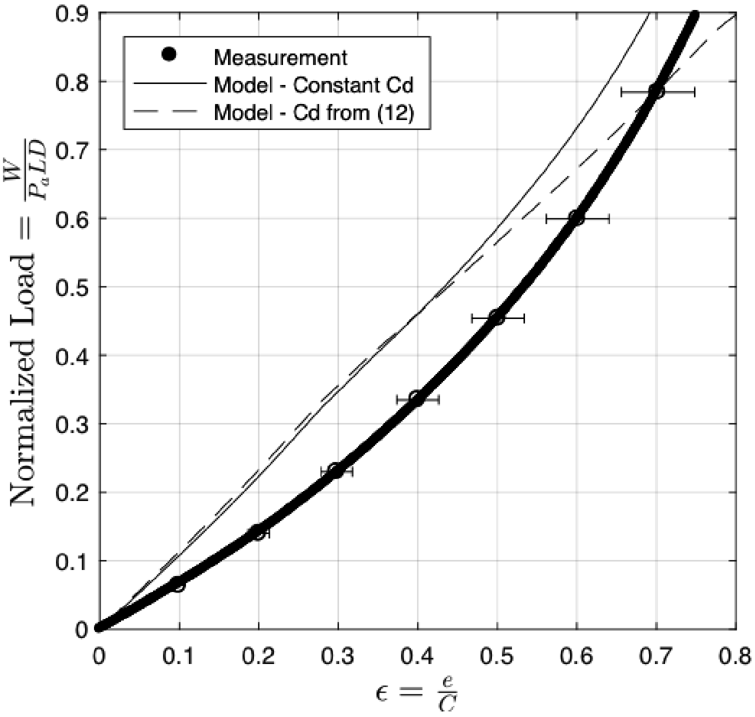

Figure 4.9 – Normalized measured load as a function of the eccentricity ratio compared to model data obtained (i) by imposing a constant measured Cd and (ii) by applying the Cd correlation from reference [1].

Figure 4.9 compares the model predictions and the experimental measurement at 0.7 MPa supply pressure and at zero rotational speed. The two approaches similarly overestimate the bearing load capacity up to half the clearance, with a maximum of 50% overestimation (at ϵ=0.25). Up to that eccentricity, both the measurement and the simulations adopt a relatively linear trend, beyond which the two approaches behave differently. The constant Cd approach evolves into a non-linear trend similar to the measurement, while gradually decreasing the overestimation as a function of eccentricity. The approach using the Belforte et al. [1] model is maintaining its linear trend and intersecting with the measured values at ϵ=0.655. Both simulation approaches show a slight change in slope at ϵ=0.26, signaling the transition onset of the throttling area, making the mass flow rate dependent on the rotor position. Similar trends are observed at different supply pressures. Higher levels of overestimations were reported at large eccentricities by Burt [68], and Dudgeon and Lowe [76] -100% and 130% overestimation respectively.

4.2.8 Effect of Static Load on Pressure Profiles and Mass Flow Rate

Given the observed disparity between the computed and the measured load capacity, it was deemed necessary to further investigate the root cause of this discrepancy. Therefore, the circumferential pressure profile is measured at zero rotational speed for a supply pressure of 0.7 MPa at four different loading levels exerted along the 180° direction ($\overline{W}$=0,0.314,0.628,0.942) and represented in Figure 4.10. The pressure profile at no load is relatively axisymmetric around the bearing center. As the load increases, the pressure is observed to increases on the loaded side of the bearing and decreases on the opposite side.

The same modelling approaches described in the previous section are used for comparison with the measurements. The models are capable of describing the qualitative evolution of the pressure profile with a high level of details. However, they are slightly overestimating the pressure values at the loaded side of the bearing. Such observation corroborates with the initial observation of the load capacity computation. At an eccentricity ratio of 0.618, the two pressure profiles (constant Cd and Cd by [1]) are practically overlapping at the loaded side, thus yielding similar computed load capacity as suggested in Figure 4.9. At high eccentricity (ϵ=0.768), the results of the two modeling approaches deviate significantly, with the constant Cd approach in good agreement with the experiment, again verifying the conclusions from the load capacity computation.

It is hypothesized that the pressure buildup inside the loaded bearing is highly sensitive to the mass flow rate through the individual supply nozzles, which are influenced by the rotor position. At a given choked pressure ratio across the nozzle, the two variables governing the mass flow rate through the nozzle are the throttling area (cross-section or curtain), as well as the discharge coefficient ϵ.

Figure 4.11 shows the reduction in the measured total mass flow rate, as well as the two modeling approaches, as a function of eccentricity. Comparing the measurement to the constant Cd modeling approach - which is also identifying the area reduction as a function of eccentricity, it is observed that the mass flow rate is not reduced as much as the throttling area, evidencing that the discharge coefficient is variable at different eccentricities (loads). Hence, in order to compensate for the relatively higher mass flow rate, it is then deduced that the discharge coefficient is inversely proportional to the gas film thickness once the curtain area is engaged – within the measured range, as at very large eccentricities ($\epsilon \leq 1.0$), the discharge coefficient will tend to diminish. The discrepancy between the total nozzle area and the measured mass flow rate can be also explained by the potential dissimilarity among the nozzles. Hence, shifting the transition of the nozzle area towards higher eccentricity ratios.

The second approach (Discharge coefficient model of Belforte et al. [1]) shows a clear mismatch in mass flow rate even at concentric position, hence, confirms the inadequacy of the model in the estimation of the discharge coefficient of the bearings under investigation. It is suggested that this discrepancy is a consequence of the larger L/D ratio of the restrictors in compared to the ones investigated by Belforte et al., thus underlining the need for new correlations

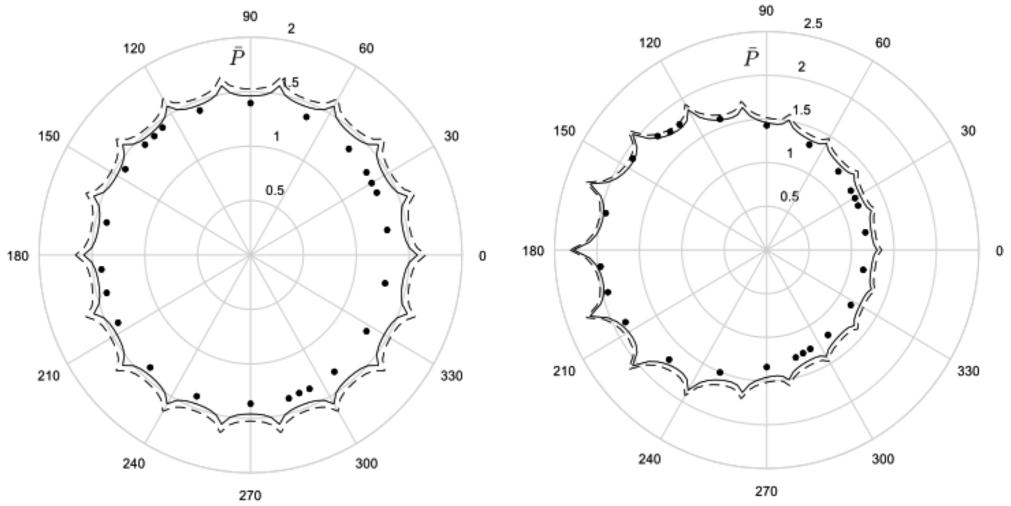

(a) *No load*

(b) *Experiment*
$\bar{W} = 0.314$; $\epsilon = 0.383$
Model
$\epsilon = 0.383$

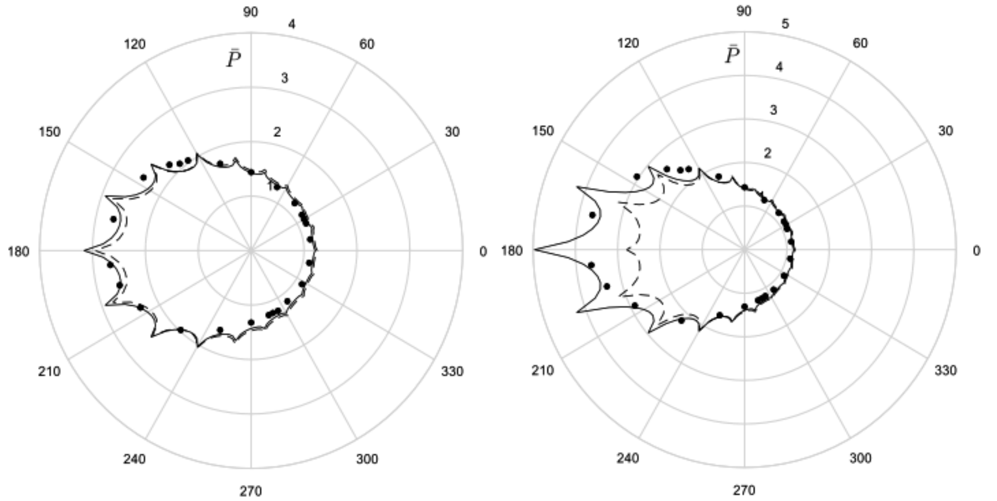

(c) *Experiment*
$\bar{W} = 0.628$; $\epsilon = 0.618$
Model
$\epsilon = 0.618$

(d) *Experiment*
$\bar{W} = 0.942$; $\epsilon = 0.768$
Model
$\epsilon = 0.768$

● Experiment
—— Model - Constant Cd
— — Model - Cd from (12)

Figure 4.10 – Measured circumferential pressure profiles under different loads for a supply pressure of 0.7 MPa and zero rotational speed compared to model data obtained (i) by imposing a constant measured Cd and (ii) by applying the Cd correlation from reference [1].

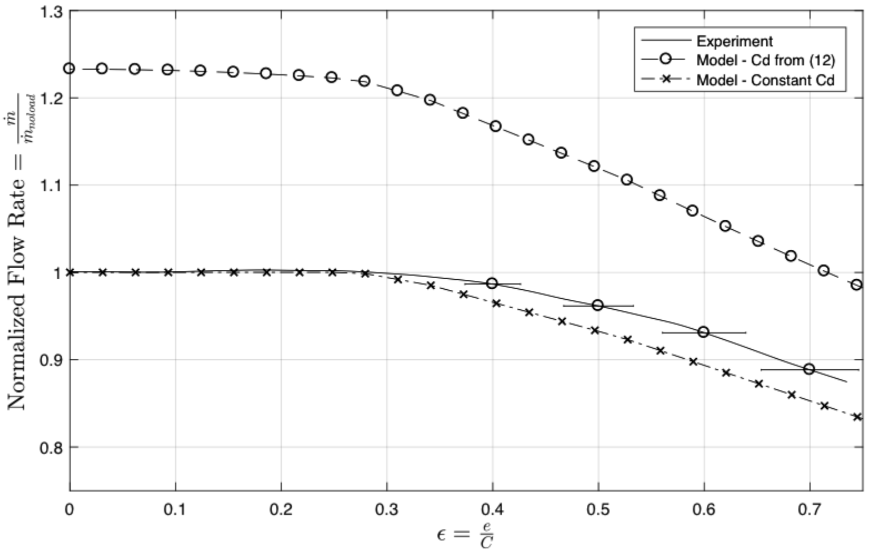

Figure 4.11 – Effect of load on mass flow rate and effective throttling area at 0.7 MPa supply pressure.

for predicting discharge coefficients of more capillary-like restrictors. Further, the evolution of the effective throttling area (identical to mass flow rate evolution at a constant Cd) in Figure 4.11 and the evolution of the measured discharge coefficient as a function of the supply pressure suggest that the discharge coefficient for more capillary-like restrictors varies less with eccentricity and more with the supply pressure compared to classical restrictors according to Belforte et al [1].

4.3 Continuous Pressure Profile Measurements Using the Instrumented Rotor

This section presents continuous pressure profile measurements within the gas film of EPGJBs using the instrumented rotor described in Chapter 3. The pressure profiles are compared to the bearing side measurements at different supply pressures at quasi-static conditions. A complete quasi-static pressure field inside the bearing is presented, which is highlighting the imperfections of the pressure field. Finally, the pressure is measured inside the bearing at different rotational speeds up to 37.5 krpm.

4.3.1 Quasi-static Pressure Field Measurement at Different Supply Pressures

The instrumented rotor was supported on the instrumented EPGJBs described in the previous section, with the embedded pressure probes measuring inside bearing B - figure 4.1. The continuous pressure profiles were measured at the axial position corresponding to the location of the measurement pressure taps as well as the supply nozzles($\overline{z} = -0.5$). The instrumented shaft was rotated quasi-statically to scan the complete pressure profile. A comparison between the two measurement techniques (rotor vs. bearing) at different supply pressure is presented in figure 4.12, highlighting a good agreement between the two techniques. The rotor side measurements captures the details of the pressure profile within the bearing clearance. The increase in pressure at the location of each nozzles is highlighted through 18 local pressure peaks along the circumference. On the macro level, an increase in pressure at 130°, and a decrease at 280° are observed along the circumference, which are explained by the combined effects of load, potential misalignments, as well as manufacturing errors that partially or fully blocks some supply nozzles. It should be highlighted at this point that the bearing is only loaded by half of the rotor weight in the direction of 180°. The results of this comparison strengthen the validation of the measurement techniques, as the same pressure profiles (qualitatively and quantitatively)are measured using the instrumented rotor and the bearing.

Following this initial step, the instrumented rotor is used to scan the pressure profiles at different axial positions covering the complete bearing length, and yielding a complete pressure field of the gas film inside the EPGJB clearance. The pressure profile is scanned every 1 mm along the bearing length, by pushing the rotor axially using a micro-metric screw. The measured pressure field inside bearing B is shown in figure 4.13, where it can be clearly observed that:

1. The pressure profile is not axisymmetric around the bearing center.
2. Supply nozzles are not equally pressurizing the bearing.
3. A pressure depression is present in the bearing center.

This measurement sheds more light on the problems of pressure depression and the overestimation of load capacity identified in figures 4.4, 4.5, and 4.8. The instrumented rotor provided an empirical evidence to the previously made conjectures on the unequal air supply of the nozzles, and also the pressure depression in the bearing center between the two rows of supply nozzles. Such behavior is due to manufacturing errors in the bearing nozzles, as well as potential misalignments. The distorted pressure field highlights another potential reason for the discrepancy between the calculation and the measurement of the load capacity - figure 4.8. The pressure drop between the two rows of supply nozzles is clearly shown in the field measurements, hence experimentally confirming the conjectures made by Powell [75] on the pressure depression in the center of EPGJBs. These conclusions would have not been possible to confirm empirically without the use of the instrumented rotor.

Figure 4.14 presents a contour map of the pressure field inside the bearing. It is observed that the supply nozzle at around 194° is fully blocked. A combined parallel and angular misalignments are causing the high pressure region to be skewed around 180°.

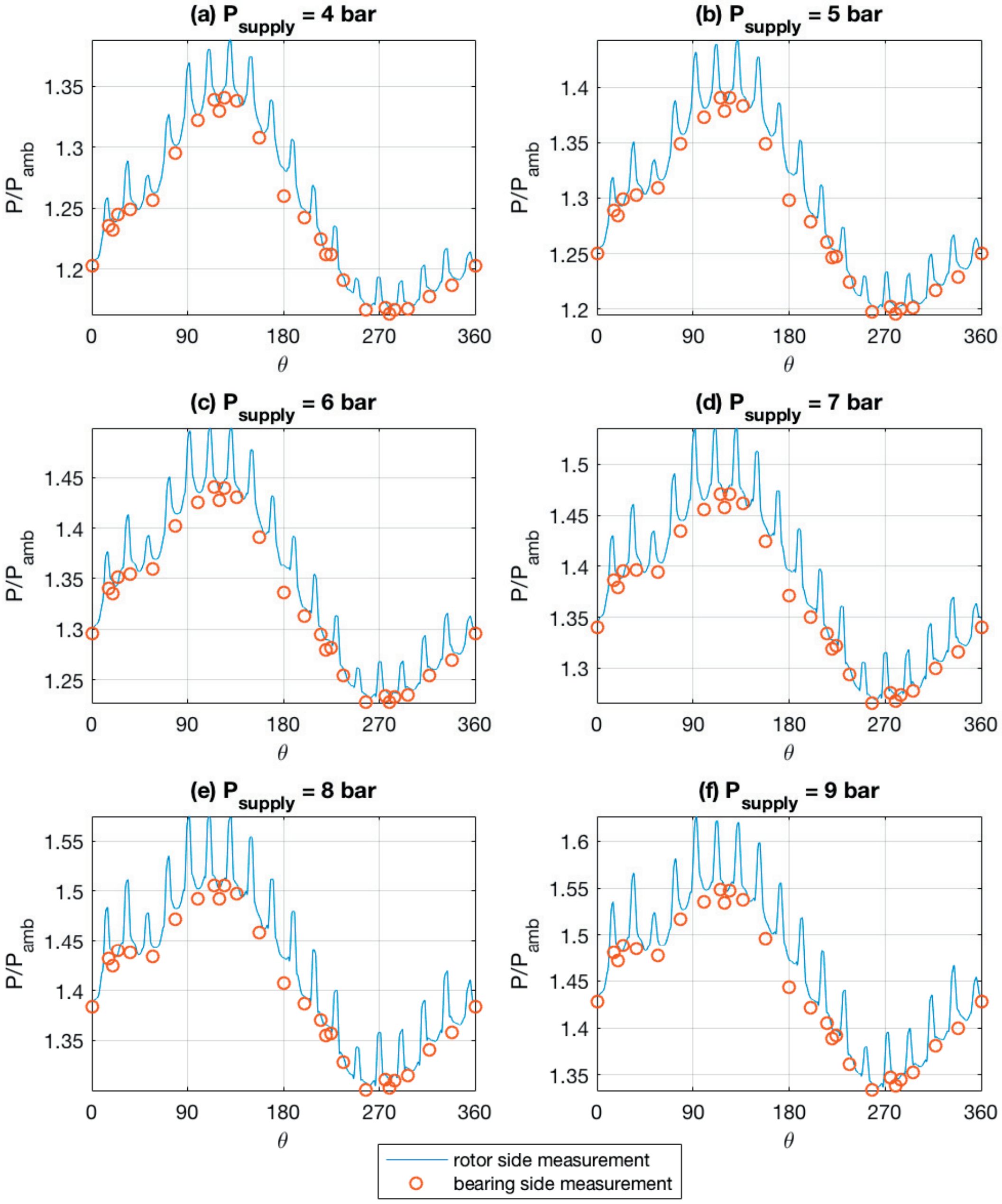

Figure 4.12 – Measured circumferential pressure profiles at different supply pressures comparing the rotor side to the bearing side measurements at $\overline{z} = -0.5$ ($\overline{W}$=0.04).

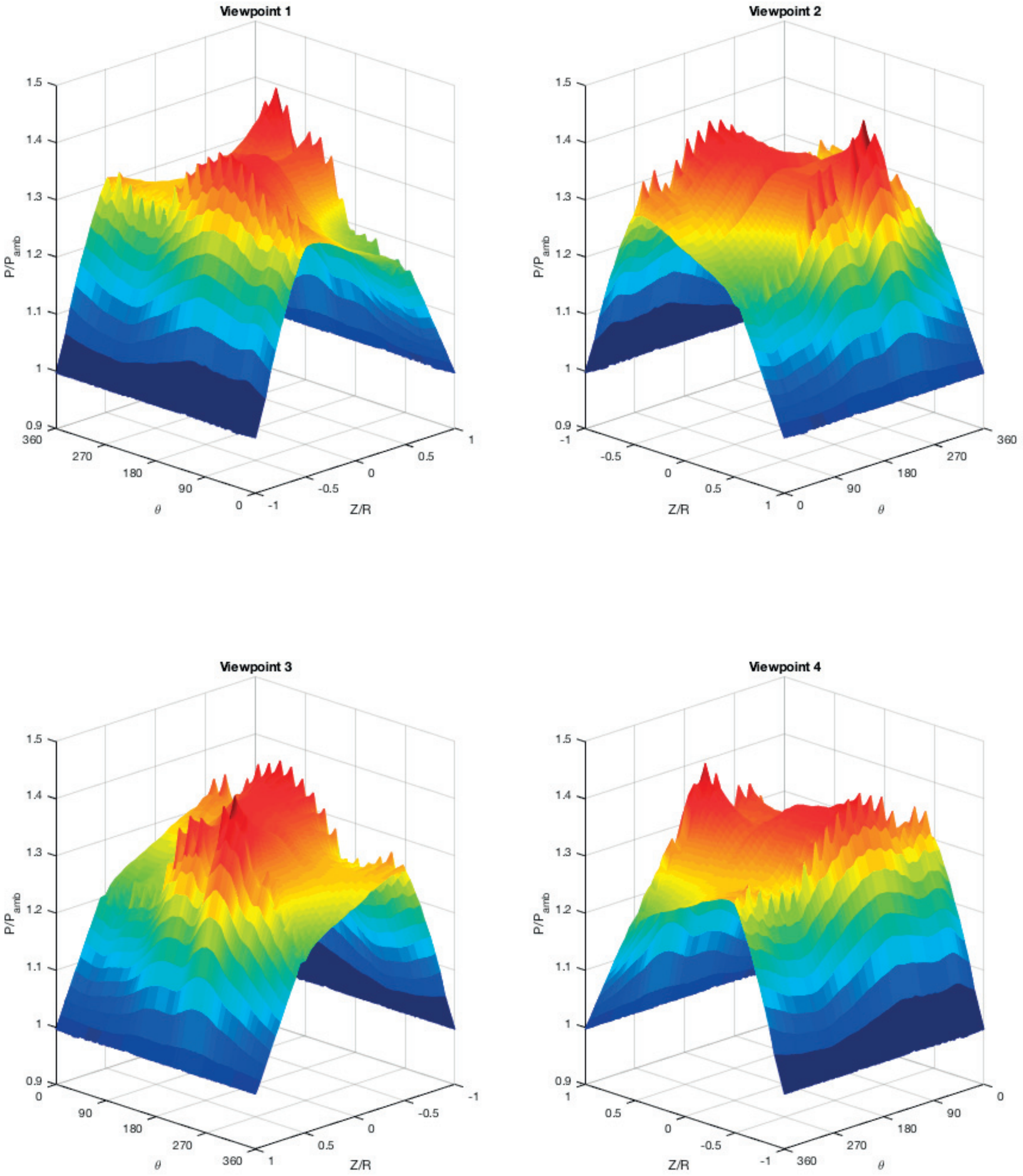

Figure 4.13 – Measured pressure field within the gas film of externally pressurized journal bearing B, at quasi-static conditions ($\overline{W}$=0.04), and at a supply pressure of 6 bar (gauge).

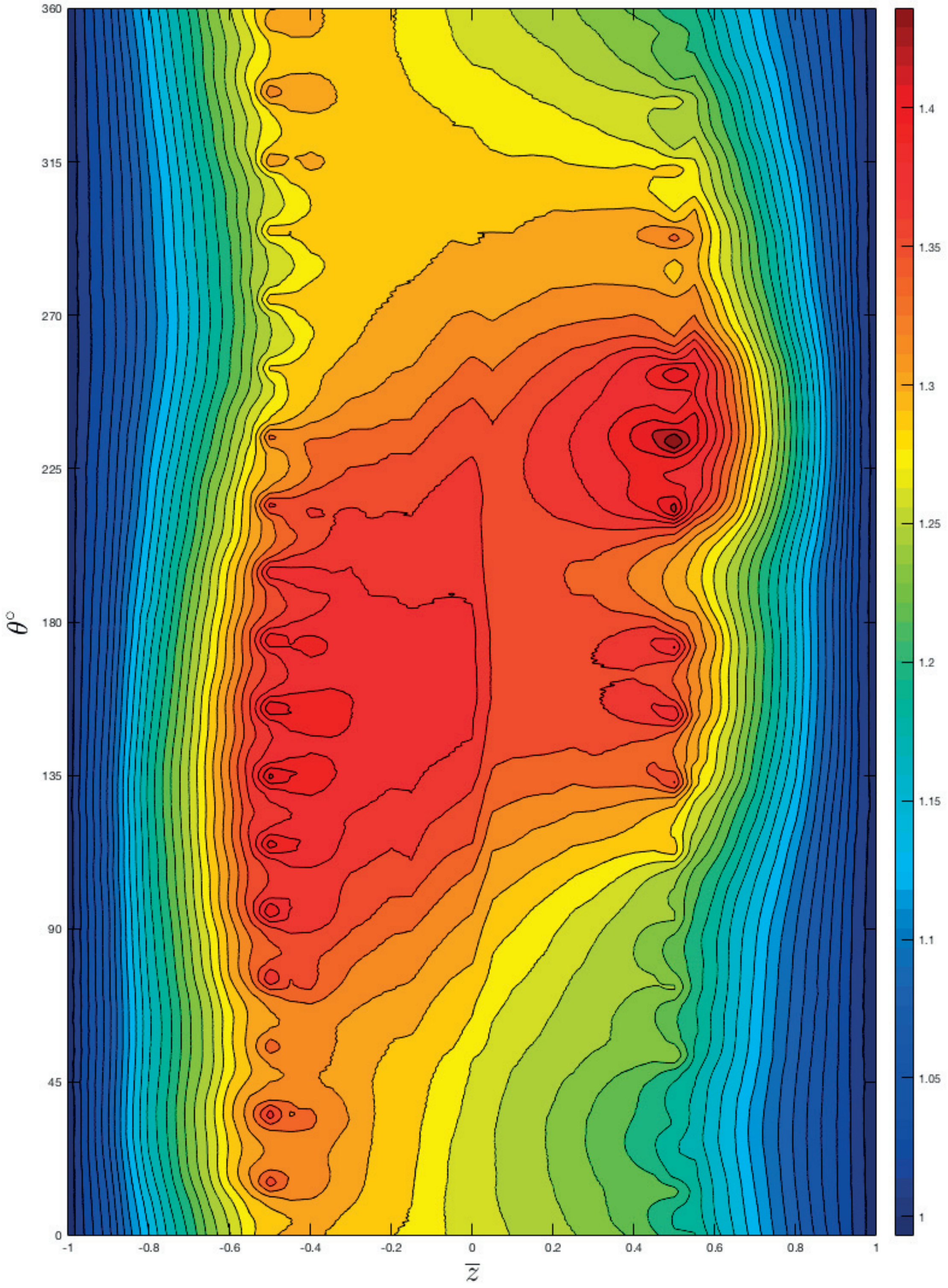

Figure 4.14 – Measured pressure contours within the gas film of externally pressurized journal bearing B, at quasi-static conditions ($\overline{W}$=0.04), and at a supply pressure of 6 bar (gauge).

4.3.2 Circumferential Pressure Profile Measurement at Different Rotational Speeds

The instrumented rotor is tested on EPGJBs up to 37.5 krpm. The dynamic response of the rotor supported on the EPGJBs at a supply pressure of 10 bar (gauge pressure) highlights a critical speed at 14.4 krpm, at which the maximum synchronous vibration amplitude of the rotor is 33μm at the back bearing - figure 4.15.

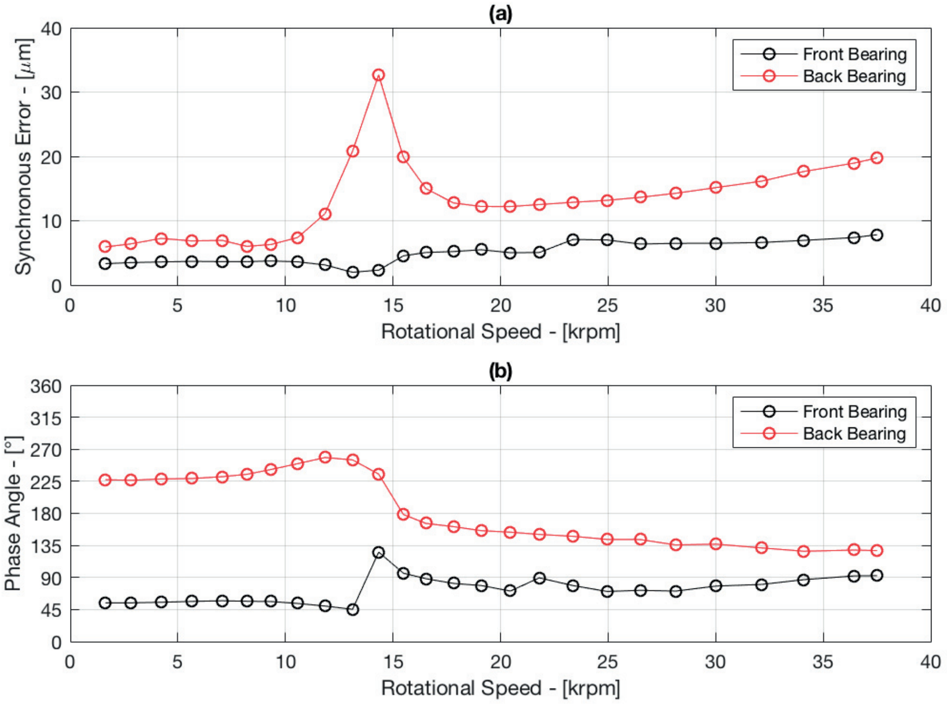

Figure 4.15 – Dynamic response of the instrumented rotor in terms of (a) peak-peak amplitude, and (b) phase lag measured from the front and back bearing measured at a supply pressure of 10 bar (gauge).

Pressure profiles are measured at $\overline{z} = -0.5$. As expected and explained in section 4.2.6 the pressure builds up within the bearing clearance as the speed increases due to the centrifugal rotor growth, which is consequently reducing the bearing clearance. Figure 4.16 shows the pressure profiles at 10 to 37.5 krpm. The profiles are measured using probe 3, and corrected using the transfer function presented and developed in the previous chapter. Five harmonics are used to reconstruct the signal.

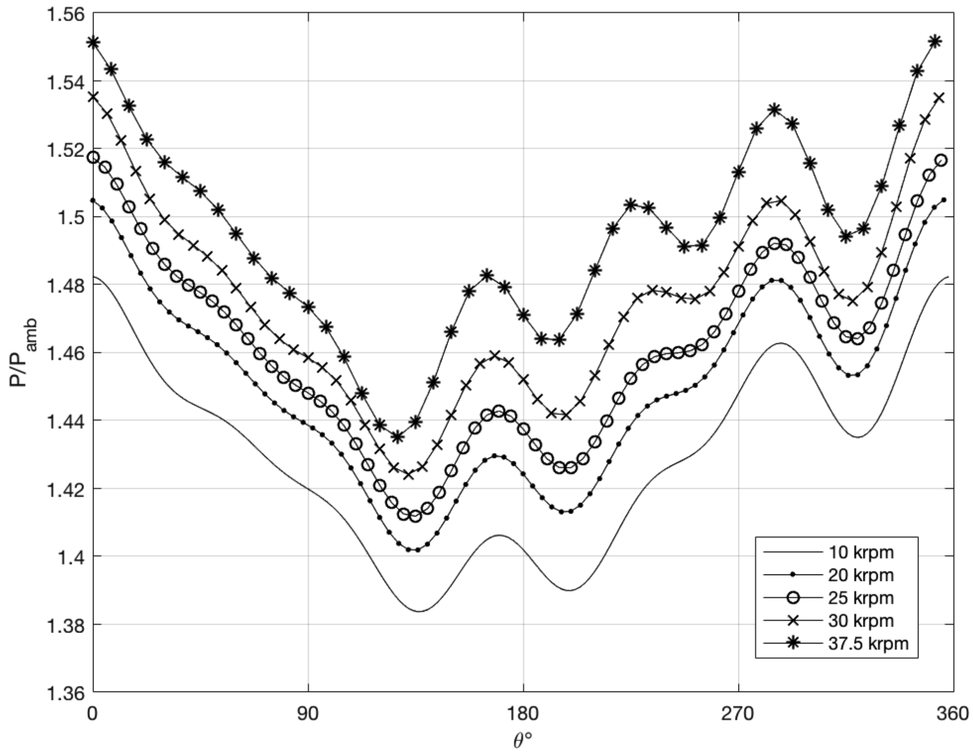

Figure 4.16 – Circumferential pressure profiles at different rotational speeds, $P_{supply} = 10 bar$ (gauge) , and at $\overline{z} = -0.5$.

4.4 Chapter Conclusions

The chapter presents a comprehensive set of benchmark measurement data for externally pressurized journal bearings. A novel test rig dedicated mainly for pressure measurement within the micro gas film of the bearing is presented. The following conclusions are made:

1. The axial and circumferential pressure measurement successfully validated the bearing model by Lo et al. [70].
2. Discrepancies in the supply nozzle shapes create circumferential flows at zero rotational speed inside the bearing, which are the main cause of the pressure drop in the bearing center between the two rows of nozzles.
3. The simulated bounds of manufacturing errors result in pressure deviations between -7.7% and 8.9% relative to the nominal (based on mean geometrical values).
4. The empirical model by Belforte et al. [1], which has been validated for small L/D restrictors is not adequate for the estimation of the correct mass flow rates through the nozzles. This is likely due to the different range of the nozzle geometries used in the

development of the empirical correlation. The restrictors implemented the bearings of this investigation are clearly outside of the range of available discharge correlations in literature.

5. Knowledge of the exact mass flow rate of each individual nozzle as a function of the film thickness is required for the accurate estimation of the load capacity. This is highlighted in the presented pressure profiles at different loads, which were strongly influenced by the discharge coefficient of each individual nozzle. As a consequence of the lack of this knowledge, the simulated loaded pressure profiles, as well as the load capacity, are overestimated by up to 50%.
6. The measured load capacity, and the deduced stiffness, show a non-linear stiffening behavior, in particular above 20% eccentricity. Hence, highlighting the importance of stiffness estimation at the specific design eccentricity.
7. The load capacity can be overestimated by the model by up to 50%, this shall be taken into consideration while defining the design's factor of safety.
8. The instrumented rotor successfully measured the pressure field within the bearing clearance at different supply pressures and speeds. The measurements confirmed the imperfection of the bearing under investigation, as well as the potentials for misalignment.

Finally, it should be stressed that further research should be directed towards developing more universal discharge coefficient models – especially for micro-holes ($\varnothing \leq 0.1$ mm), with large l/d restrictors. It is believed that the presented pressure measurements will serve as a comprehensive validation platform for EPGJB model development.

5 Foil Bearing Manufacturing

This chapter discusses the challenges of foil bearing manufacturing. First, a general description of the manufacturing process is presented. Followed by a process optimization to minimize shape errors in the formed foils due to springback. A modification for the bump foil forming die yielded significant improvements in the reproducibility and accuracy of manufacturing. Another attempt to further improve the manufacturability was adopting the cantilever beam compliant structure, which showed superiority in manufacturing compared to bump foils. Manufacturing errors for the classical bump foil, the modified bump foil, and the cantilever beam foil were measured and statistically quantified. Finally, the effect of these manufacturing errors on the overall roundness of the bearing, the static stiffness, as well as the expected critical mass for a given rotor setup is also presented in this chapter.

The work presented in this chapter is published as:

- Shalash, K., and Schiffmann, J., 2017. ***On the manufacturing of compliant foil bearings.*** Journal of Manufacturing Processes, 25, pp.357-368.
- Shalash, K., and Schiffmann, J., 2017, June. ***Comparative Evaluation of Foil Bearings With Different Compliant Structures for Improved Manufacturability.*** In ASME Turbo Expo 2017: Turbomachinery Technical Conference and Exposition (pp. V07AT34A014-V07AT34A014). American Society of Mechanical Engineers.

5.1 Introduction

The classical foil bearing is constructed of three main components, which are the bearing sleeve, the bump foil, and the top foil - Figure 5.1. The first is considered the main holder of the foils, the second is a corrugated foil which acts as a compliant structure to support the rotor, and the latter is a cylindrical foil that creates the fluid film wedge along with the rotating shaft. Although foil bearings are a relatively old technology [80], they still suffer from some practical issues, among them is the problem of fabrication. The literature is very limited on the topic of foil bearing manufacturing [3, 81–83]. Moreover, the presented

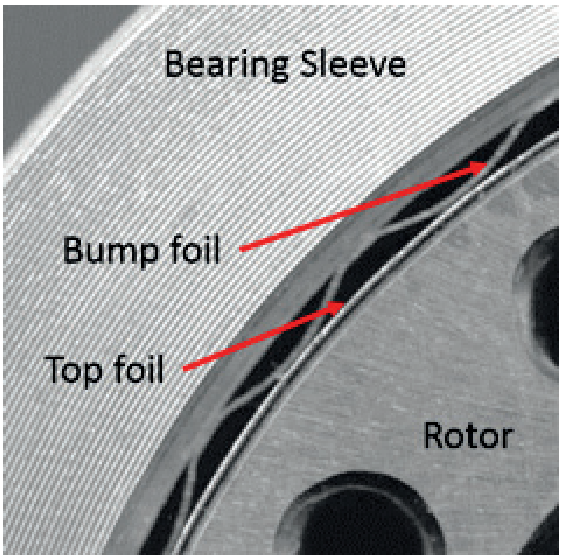

Figure 5.1 – Foil bearing construction elements.

know-how in these manuscripts is considered alike and relies mainly on experience and trial and error. It was recently shown that such techniques produce inaccurate foils in terms of dimensions [84]. The lack of available manufacturing know-how and analysis is hindering the scientific development, as well as affecting the performance of foil bearings.

5.2 Motivation and Nature of the Issue

The key role of the bump foil is to provide a compliant underlying structure. The foil bearing compliance is governed by the bump foil material and geometry. Iordanoff [2] deduced an analytical formula for a single bump compliance, where he accounted for the effect of the welded and the free bumps. Iordanoff used the bump length, height, pitch, and thickness which are considered the standard descriptive variables of the bump foil geometry as shown in Figure 5.2:

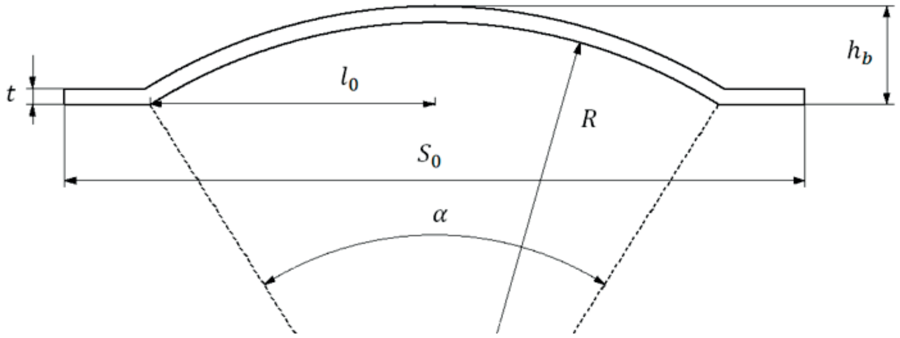

Figure 5.2 – Geometrical design variables of a bump foil that influence its compliance.

The main manufacturing complication in foil bearings is the fabrication of the bump foil (the source of compliance), as the sleeve and the rotor can be manufactured with good accuracy. The foil forming process includes stamping and heat treatment of metal sheets of a certain thickness. Metal forming processes, however, suffer from an elastic-driven change in the shape after the load release, which is due to the finite modulus of elasticity and the yield strength of the material, a phenomenon called “springback”. Therefore, geometrical uncertainty of a bump foil due to manufacturing noise will generate uncertainty in its compliance, and hence will affect the dynamic performance of the rotor bearing system. These uncertainties might have a positive effect on the system, such as breaking symmetry, however they should be quantified.

Springback is usually geometrically compensated for in tooling design, and/or by over bending of metal sheets. Increasing creep and decreasing yield strength by increasing temperature during loading is expected to decrease the springback [85–87]. There has been an extensive amount of research in the area of springback compensation [88–91], however none of it was directly concerned with foil bearings. Hence, manufacturing guidelines for accurate foil bearings are missing. For the simple case of a flat foil formed to an arc shape, springback is geometrically quantified by the change in radius and angle of the arc after the load is removed. Figure 5.3 shows the final formed top foils for different heat treatments at a constant loading pressure (formed with the same die), and highlights both the springback and the sensitivity of the foil shape to the manufacturing process. The foil at the bottom of the figure has the largest springback and the lowest heat treatment temperature, while the foil at the top has the lowest springback and the highest heat treatment temperature.

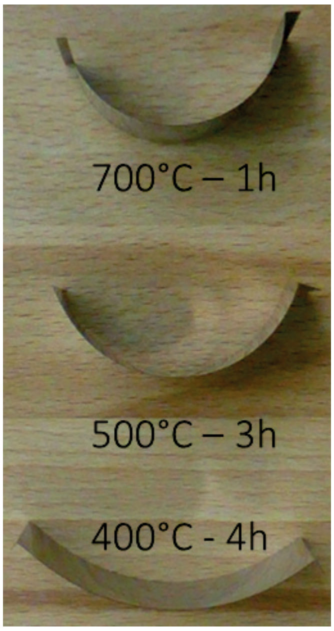

Figure 5.3 – Effect of heat treatment temperature and duration on springback showing reduced residual error with increasing heat treatment temperature.

Fixing the bump pitch and the foil thickness, and using basic Euclidean geometry, the bump could also be described using the bump radius, and angle. The rationale behind adopting different descriptive variables is that springback directly affect these two geometrical features.

$$h_b = t + R - cos(\frac{\alpha}{2}) \tag{5.1}$$

$$l_0 = R\,sin(\frac{\alpha}{2}) \tag{5.2}$$

A sensitivity analysis on the bump radius and angle has been performed in view of assessing the propagation of the bump geometry uncertainty on compliance. The mean bump radius and angle are used as input variables to model the bump compliance both varying on a hypothetical range of +/- 5% around a mean design value [3]. Figure **??** shows a normalized bump foil performance map that highlights the effect of bump radii and angle deviations on bump stiffness.

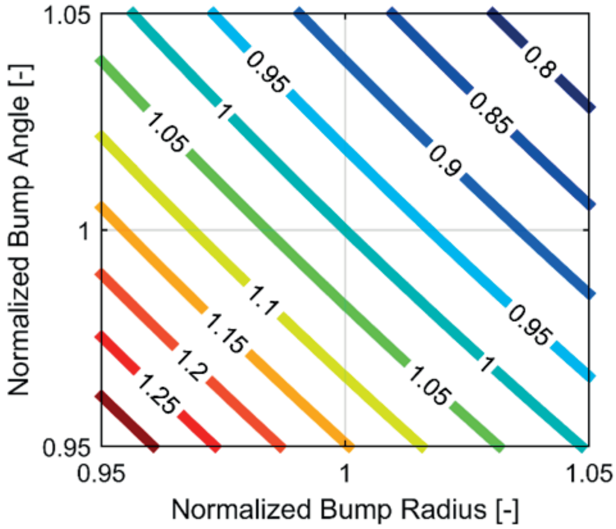

Figure 5.4 – Effect of bump radius (abscissa) and angle (ordinate) deviation on the normalized bump stiffness (contours) – bump foil stiffness map. The Iordanoff [2] model is used to calculate the stiffness.

The sensitivity is around 5% change in stiffness for each 1% change in the bump angle. Similar conclusions could be drawn on the effect of the bump radius deviation. It was found that a 1% change in bump radius yields a 5% change in stiffness. A theoretical robust design, however, should exhibit a sensitivity slope equal or close to zero (changes in geometry shall not affect the performance variable). It is worth mentioning that the manufacturing tolerance in bump radii of foil forming dies can be within 1% without taking into account for other process related deviations. It is therefore concluded that the bump foil compliance is far from robust for a classical bump foil design, as it is highly sensitive to minimal changes in the geometry, thus highlighting the importance of the accurate manufacturing of bump foils.

5.3 Goals and Objectives

The goal of this chapter is to shed light into the foil bearing manufacturing know-how and to propose a more robust compliant foil design compared to the classical one. The objectives are to:

1. Assess known manufacturing procedures.
2. Investigate the effect of manufacturing process variables on springback.
3. Quantify the manufacturing errors.
4. Propose new and more robust compliant foil designs, and compare them back to back.
5. Assess the effect of manufacturing errors on foil bearing performance.

5.4 Manufacturing Process Assessment

5.4.1 Material selection

Choosing the proper foil material is of a great importance to the foil bearing design, as the material limitations will impact the overall bearing performance [92, 93]. The foils should be compliant, withstand heat, and offer the required damping to the rotordynamic system. It was shown in the literature that Inconel is an adequate solution, as it exhibits an acceptable modulus of elasticity and can withstand high temperature, which is important if the foil bearing is to be implemented in high temperature applications [13, 94, 95]. Stainless steel is a cheaper alternative, with some drawbacks like lower operational temperature when compared to Inconel, and sensitivity to certain coatings [93, 96–98]. San Andrés et al. [99] used copper in their metal mesh foil bearing for its enhanced Coulomb damping characteristics when compared to an equivalent Stainless Steel metal mesh. San Andrés et al. [100]and Kim et al. [101] reported using chromium molybdenum steel for the top and bump foils. Xu et al. [102] used Beryllium-Copper alloy in an oil lubricated leaf type foil bearing. Also, Kulkarni et al. [103] used the same material for bump foils, signifying its use for its self-lubricating properties. Although the Beryllium–Copper alloy exhibits excellent metal working capabilities, the existence of such a toxic material in a foil bearing is debatable for some applications. In this work Stainless Steel 1.4310 was selected as the foil material.

5.4.2 Foil shaping

In order to shape the foils, the cut foils are pressed inside a tooling (die) with the required foil geometry and then exposed to high temperature. The die is usually manufactured of a heat resistant alloy (Inconel – Stainless steel) to allow the toolings to withstand thermal fatigue. DellaCorte et al. [104] and Ruscitto [3] proposed a rule of thumb using flat dies for the bump foils, where the foils are pressed, and produced in a flat form, then rolled around a mandrel to get the required curvature.

A mandrel diameter 2/3 of the required final diameter of the bump foils is suggested to compensate for the springback effect. For the top foils a roller is proposed to produce the required curvature. DellaCorte et al. [104] also executed a qualitative sensitivity study on the required forming load to achieve adequate bump foil deformation, and concluded that a unit load of 28 MPa is satisfactory to achieve the required foil shapes. Dykas et al. [83] published a similar fabrication guideline where 20 MPa were used to form annealed Inconel foils X-750. Better foil quality was claimed using Polytetrafluoroethylene (PTFE). However, no quantitative measurements were done on the springback of the foils, assuming that Inconel foils would maintain their formed shape. Yet, a major problem with the cold forming of the foils is the springback effect, which is an unceasing threat to the foil accuracy.

In this work the forming technique uses dies which are designed to produce the required curvature and features of both the top and bump foils as shown in Figure 5.5. The die should be manufactured to perfection and exhibit a good surface finish which would be reflected on the produced foils, for EDM cut dies, a surface roughness Ra of 0.2 is achievable. The foil is then carefully placed and fixed inside the tooling, then pressed before undergoing the heat treatment. It is worth mentioning that a drawback for this technique is the necessity to manufacture a die for each bearing diameter and each foil thickness.

5.4.3 Heat Treatment

The heat treatment is a critical step in the foil fabrication. Depending on the material of the foil, as well as the state of the formed material, the heat treatment would significantly change. For Inconel foils, precipitation hardening transforms the shaped foils from the annealed state and increases the material strength. There are several heat treatment recipes possible for any material [105], and for foil bearings it is desirable to select the recipes yielding high spring properties and fatigue resistance to remain constrained by the functionality of the foils as compliant structures. DellaCorte et al. [104] summarized some of the possible heat treatment recipes for Inconel X-750 foils. For Stainless Steel, the formed foil requires stress

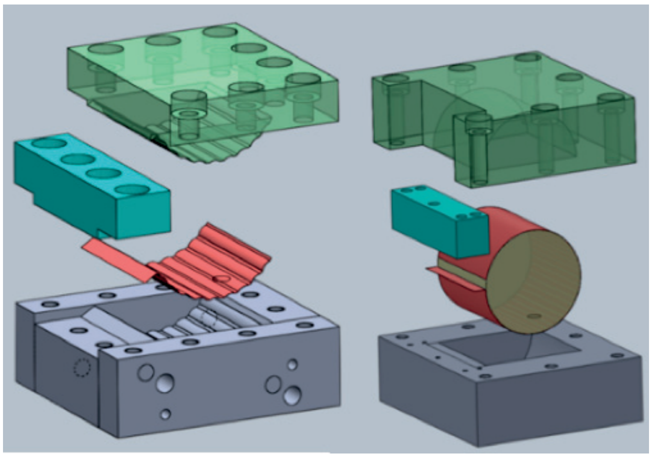

Figure 5.5 – Forming dies used to form the top (right) and the bump foils (left). The cut foils are placed into the dies, pressed and then subjected to the heat treatment process.

relief annealing, that is the heat treatment to reduce residual stresses after cold working. One major difference between heat treatment of Stainless Steel and Inconel is the fact that Stainless Steel requires being heat treated inside the pressed die, as the available Stainless Steel in the market is usually partially hardened, and the annealed stainless steels are usually not heat treatable for hardening purposes.

5.4.4 Coating

A drawback of foil bearings running at low speeds is the mechanical contact occurring between the rotor and the top foil. For this reason the top foils are usually coated with a dry lubricant to accommodate for the friction between the two elements during startup and shutdown. Coating is the last process of manufacturing the foils. Rubio and San Andrés [106]used Teflon® as a dry lubricant, also, Song and Kim [97] used it to coat one side of the top foil with an extra thin layer of Chromium Nitride on the top of it. Shafts are also coated with dry lubricants, DellaCorte et al. [107] coated a 35mm diameter shaft with a 0.35mm thick layer of PS304 running on foil bearings. The large arena of solid lubrication technology is beyond the scope of this chapter, however, advancements in this technology goes inseparably with the foil bearing development [108–110].

5.5 Non-Intrusive Geometry Measurement

A crucial step in the assessment of manufacturing deviations is an accurate measurement technique. The foil bearing fabrication literature relies either on the accuracy of the forming dies, or adopts ad-hoc measurements methods, both techniques will not quantify springback accurtely. The structure of the formed bump foil requires a profilometer to measure its full profile. Most of high accuracy profilometers are mechanical devices, which use a stylus to probe and measure dimensions. Such technique, however, is not feasible due to the foil compliance. Hence, an optical non-intrusive geometrical measurement technique has been established to quantify the springback. A numerical code has been developed internally by Mr. Lucas Alloin[1] to assess the manufactured foils in an inexpensive, fast, and fully automated manner. The code receives high resolution two dimensional scans of the formed foils (4800 dpi), and treats the images to measure the overall radius of the foil, and the radii of each of the bumps constructing the foil. The algorithm relies on treating the grey scaled pixels representing the scanned foil cross-sections as data points, subsequently recognizes the bumps and fits circles through them, as well as the overall foil radius using a Nelder–Mead method algorithm - Figure 5.6. The fitting of the circles identifies the radii and their corresponding center coordinates. Consequently, the bump angle (α), the intersection angle (θ), the bump height, and clearance are calculated. Similar but less accurate techniques could be found in [111, 112].

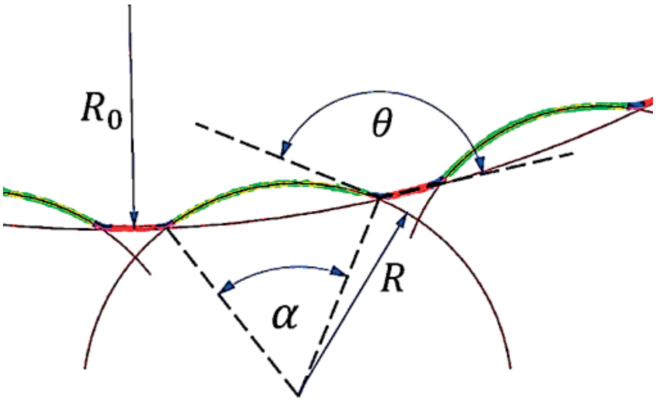

Figure 5.6 – Optical measurement of a manufactured foil using a high resolution scanner and a post-processor code.

5.6 Optimization of the Manufacturing Process

Since there is no reliable published manufacturing procedure for foil bearings, it was decided to discover the optimum procedure to minimize springback. When experimenting for different factors affecting a certain response, the one factor at a time approach is proven to be expensive, time consuming, and does not necessarily fully explain the observed phenomena [113]. Founded on these facts, Design of Experiment (DoE) procedures have produced different algorithms to plan and analyze experiments. Factorial design is a DoE algorithm developed by Fisher in the 1930s, where a number of levels is selected for each factor (variable), and then experiments are executed in all possible combinations of these factors [114]. Such algorithm is useful in system characterization, which would permit the optimization of the studied manufacturing process.

---

[1] Mr. Alloin developed this work under the supervision of the author during an internship at the Laboratory for Applied Mechanical Design in 2014.

A DoE approach is used to decide and plan the necessary experiments to produce sufficient data to understand the different manufacturing process variables (factors) affecting the springback measured as the bump foil overall radius (response). After executing the data collection procedure, a model is developed to quantify the effects of each factor. Afterwards, an analysis of variance inference is performed to identify the significance of each factor. The three factors under investigation are: (i) the forming pressure, (ii) the heat treatment temperature, and (iii) the heat treatment duration.

5.6.1 Full Factorial and Modified Composite Designs

A three factor two level factorial design has been chosen for the initial exploration of the experimental domain. The levels of forming pressures are 300 and 400 bars, heat treatment temperatures of 500°C and 600°C, and heat treatment durations of 3 and 5 hours. The chosen measured response is the overall radius of the bump foil error compared to the design value of 20.73mm. It can be shown that the overall radius of the bump foil is a comprehensive measure of the springback effect.

Table 5.1 – Full factorial experimental design

Experiment	**Forming pressure**	**Heat treatment temperature**	**Heat treatment duration**	**Springback Error**
[-]	[bar]	[°C]	[h]	**[%]**
1	300	500	3	-13.65
2	400	500	3	-9.69
3	300	600	3	-2.67
4	400	600	3	-4.23
5	300	500	5	-9.26
6	400	500	5	-9.41
7	300	600	5	-4.63
8	400	600	5	-3.33

The results in Table 5.1 show that a minimum springback error of -2.67% is obtained from experiment 3. The best contenders are results from experiments 3, 4, 7, and 8. The common factor between those points is a heat treatment temperature of 600°C.

As the factors are three different physical quantities, a normalization is required for the different factors. The upper and lower values of each factor are normalized to 1 and -1 consecutively. A linear model with interaction is developed taking the following form:

$$Y = \beta_{mean} + X_P\beta_P + X_T\beta_T + X_D\beta_D + X_PX_T\beta_{PT} + X_PX_D\beta_{PD} + X_TX_D\beta_{TD} + \epsilon \tag{5.3}$$

Table 5.2 summarizes the estimation results, presenting the model coefficients, the relative effects, the squared errors, t-statistics, and p-values. It can be seen that the temperature has the highest relative effect with a magnitude of -47.74%. The negative sign of the effect indicates that increasing the temperature factor would decrease the springback error. Pressure and time factors also have negative effects on the response, but they are much lower in magnitude as well as the effects of interactions. The results suggests a high insignificance of the pressure factor (P value above 70%). Hence, it was omitted and the regression was repeated only for the temperature and duration factors as well as their interaction and the results summarized in Table 5.3. The model and the temperature were both significant above 99%. However, the time and interaction factors were shown insignificant.

Table 5.2 – Statistical inference of full factorial design

	Coef. [β]	**RE**	**SE**	**tStat**	**pValue**
Mean	7.11		0.87	8.16	7.76%
P	-0.44	-6.24%	0.87	-0.51	70.01%
T	-3.39	-47.74%	0.87	-3.9	16.00%
D	-0.45	-6.35%	0.87	-0.52	69.58%
P:T	0.51	7.16%	0.87	0.58	66.35%
P:D	0.16	2.20%	0.87	0.18	88.70%
T:D	0.72	10.08%	0.87	0.82	56.20%

In conclusion, increasing the heat treatment temperature significantly reduces the springback. This is attributed to both an increase in creep and a decrease in the yield strength of the stainless steel. The forming pressure is an inert factor having an insignificant effect on the foil quality compared to the other factors, consequently it was removed from the studied factors in the following experiments. The heat treatment duration effects also exhibited low confidence levels, however it was decided to keep it under investigation for further experiments.

Table 5.3 – Statistical inference of modified full factorial design

	Coef. [β]	**RE**	**SE**	**tStat**	**pValue**
Mean	7.11		0.56	12.77	0.02%
T	-3.39	-47.74%	0.56	-6.1	0.37%
D	-0.45	-6.35%	0.56	-0.81	46.30%
T:D	0.72	10.08%	0.56	1.29	26.76%

A sequential augmentation was necessary to further explore the experimental domain, and to increase confidence intervals. For this purpose, a two-level modified composite design with single centered point is adopted, with an alpha value (distance of axial point to the center of the experimental domain) of 3 (instead of 1). The reason for changing the value of alpha is to confirm the positive effect of a high heat treatment temperature, while going beyond the uncertainty of the furnace. The model is modified to account for the removal of the pressure factor and the inclusion of second order effects as follows:

$$Y = \beta_{mean} + X_T\beta_T + X_D\beta_D + X_T X_D\beta_{TD} + {X_T}^2\beta_{TT} + {X_D}^2\beta_{DD} + \epsilon \tag{5.4}$$

The results of experiments 1, 3, 5 and 7 are retained, where the forming pressure is 300bar. In order to be consistent, this same pressure is used in the additional experiments. This design produces variance inflation factors below 3, implying a low multicollinearity.

Table 5.4 – Composite experimental design

Experiment	**Heat treatment temperature**	**Heat treatment duration**	**Springback Error**
[-]	[°C]	[h]	
1	500	3	-13.65
3	600	3	-9.69
5	500	5	-2.67
7	600	5	-4.23
9	400	4	-20.77
10	700	4	-2.44
11	550	1	-9.15
12	550	7	-3.91
13	550	4	-8.25

The modified composite design domain was bounded by a heat treatment temperature between 400°C and 700°C, and a heat treatment duration between 1hr and 7hrs. Table 5.4 summarizes the results of the composite design. The minimum relative error of 2.44% comes from experiment 10. Table 5.5 shows the different relative effects and their corresponding p-values. Note the high relative effect of temperature and its corresponding low p-value, yielding a high confidence level. The highest relative effect is the interaction between temperature and duration, yet the p-value is very high, yielding a very low confidence level concerning the effect of this factor.

Table 5.5 – Statistical inference of composite design

	Coef. [β]	**RE**	**SE**	**tStat**	**pValue**
Mean	7.47		2.34	3.19	4.95%
T	-7.85	-105.06%	2.74	-2.87	6.42%
D	-4.38	-58.60%	2.74	-1.6	20.80%
T:D	12.67	169.58%	19.62	0.65	56.43%
T2̂	4.08	54.57%	4.04	1.01	38.71%
D2̂	-1	-13.34%	4.04	-0.25	82.10%

The model shows an optimum value of temperature equal to 675°C, which would yield a minimum foil radius springback error of 2.2%. However, since the optimum temperature is critically close to the recrystallization temperature of Stainless Steel at 700°C, the adopted optimum temperature was decided to be 650°C for a duration of 5 hours – Figure 5.7. Even though the duration's confidence level is relatively low, it is known that aging time inversely affects springback. Also, enough time is needed to heat the die equally, 5 hours resulted the minimum springback.

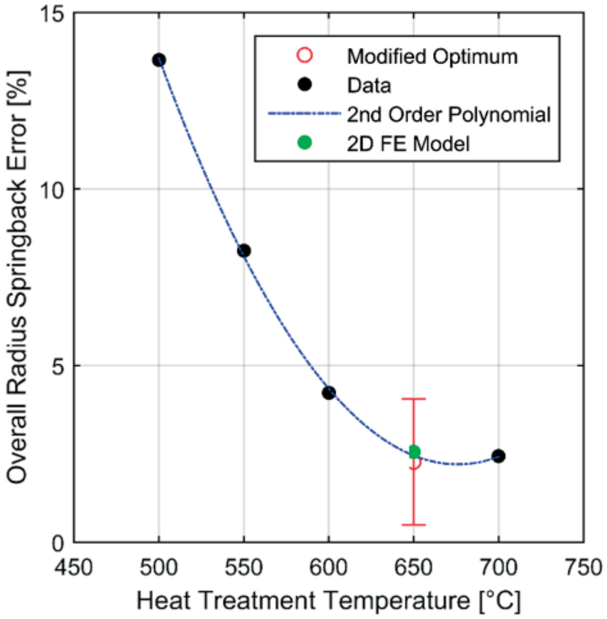

Figure 5.7 – Effect of heat treatment temperature on the bump foil overall radius springback.

5.7 Manufacturing Uncertainty Assessment

After the identification of the optimum manufacturing process a statistical manufacturing uncertainty quantification is done using 14 foil samples that would correspond to 126 bumps. Before the first use of the die, a profile measurement for the concave and convex parts was done using the mechanical probe measuring system Hommel T8000 of Jenoptik. The purpose of the measurement is to ensure the correct dimensions and tolerances of the foil shaping die after EDM machining. The standard deviation of the probe measurement is less than 1 micron for the bump radius. Three profiles were measured on each of the two parts of the die and the average values are used as reference. The measurement showed an average error of 0.09% in bump radius for the concave part, and 0.35% for the convex part compared to the design dimensions. These results were considered satisfactory to proceed the foil manufacturing procedure.

Measurements of the bump radii and their corresponding bump angles are represented in Figure 5.8. The results shows a linear correlation due to the finite length of the bump arc. To avoid the estimation procedure being sensitive to outliers in the measured data, the lowest and highest 5% of the bump radii were trimmed. The correlation shows a sensitivity between the bump radius and angle errors of approximately 1%/%. The geometrical interpretation of the correlation is presented in Figure 5.9.

Figure 5.10 shows a scatter of the measured bump samples on the bump foil performance map. The resulting error in stiffness spans between -20% and 40% of the nominal design value and therefore suggests a significant deviation between the expected and the resulting bump

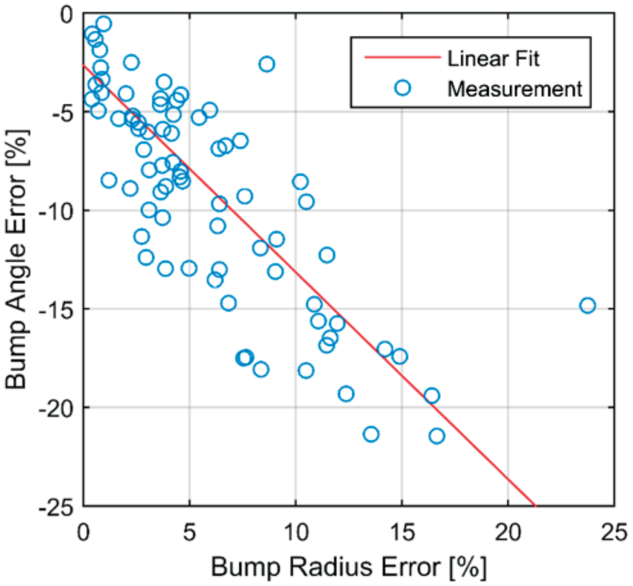

Figure 5.8 – Correlation between measured bump radius and angle springback errors suggesting a linear correlation.

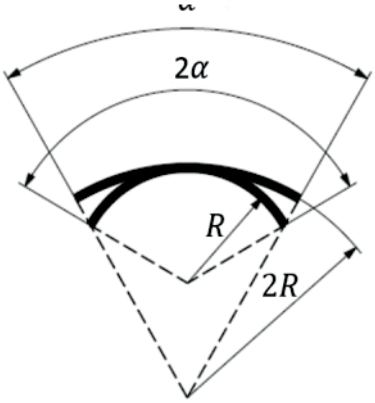

Figure 5.9 – Effect of springback on the geometry of the bump.

stiffness. Hence, this result experimentally highlights the lack of robustness of the produced foils.

A non-parametric Kernel distribution was fitted to describe the statistical distribution of the 126 measured bump radii and their corresponding bump angles. Due to the linear and inversely proportional relationship between the bump radius and angle, the normalized statistical distribution for both variables is identical in shape, yet one is positively skewed and the other is negatively skewed. Figure 5.11 shows the fitted distribution augmented to 100,000 samples and normalized by design value. The normalized mean and mode are 1.05 and 1.02 respectively. The larger mean compared to the mode signifies a clear positive skewness of the bump radii, which is a tendency to obtain oversize bump radii as a result from springback.

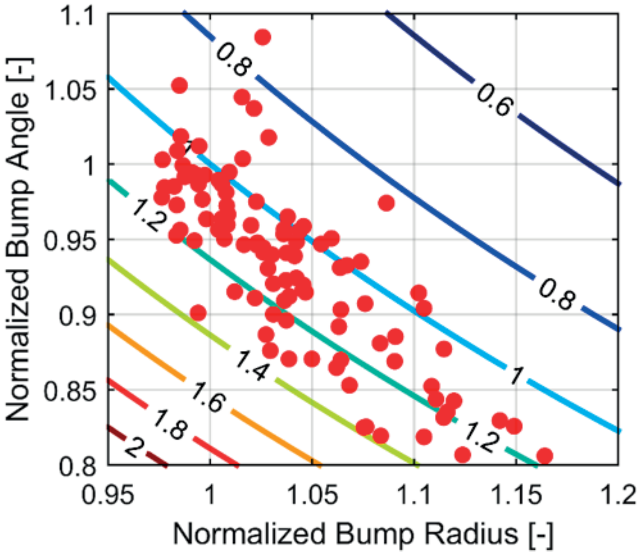

Figure 5.10 – Scatter of measured bumps on the bump foil performance map suggesting significant increase in bump stiffness as a result of manufacturing deviations.

The distribution of the normalized bump radii ranges between 0.95 to 1.3.

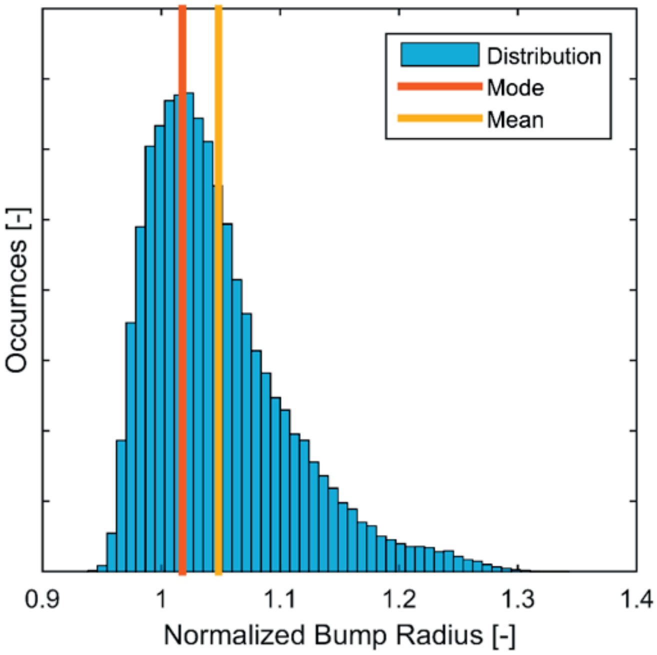

Figure 5.11 – Augmented statistical distribution of measured normalized bump radii.

A Monte Carlo simulation using the augmented random sample distributions for the bump radii and corresponding angles as input for the Iordanoff model [2] has been performed. The analysis yields a normalized mean stiffness of 1.108 and a mode of 1.095 (i.e. approximately 10% above the design value). The distribution is close to normal, ranges between 0.7 and 1.6

with a relative standard deviation of 12.4%.

5.8 Effect of Foil Bearing Manufacturing Errors on Local Clearance and Circularity

Geometrically, and based on the hypothesis that the bump arc length is considered constant (no local elongation occurs), the effect of springback on the bump geometry is an increase in the bump radius, yielding a decrease in the bump angle. Such change in shape is expected to reduce the bump height, hence increase the local nominal assembly clearance – Figure 5.12. The actual bump height after the springback effect is defined as follows:

$$h_{b_D} = R_D - [X_D - R_{Sleeve}] \tag{5.5}$$

$$M = \sqrt{X_{act}^2 + R_{act}^2 - 2X_{act}R_{act}\cos(\frac{\alpha_{act}}{2})} \tag{5.6}$$

$$h_{b_{act}} = h_{b_D} - [R_{Sleeve} - M] \tag{5.7}$$

The deviation in the bump height directly influences the local clearance at the point of irregularity, yielding a non-circular inner diameter for the bearing.

$$C_{Local_{act}} = R_{Sleeve} - h_{b_{act}} - \frac{D}{2} - t \tag{5.8}$$

$$Nominal\ Clearance\ Error = \frac{C_{Local_D} - C_{Local_{act}}}{C_{Local_D}} \tag{5.9}$$

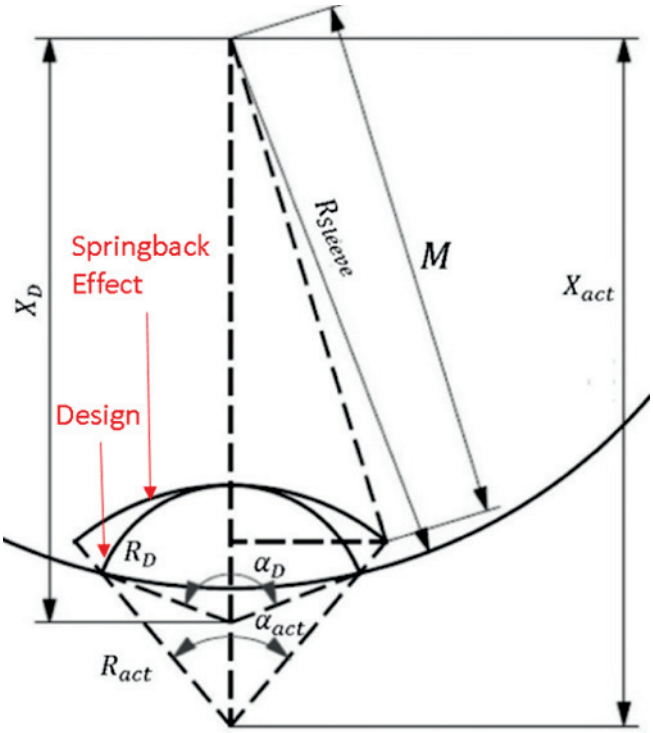

Figure 5.12 – Effect of springback error on bump height.

Local clearance calculation of the manufactured Gen II bump foils ranges between -50% and 150% of the design clearance – based on equation (5). The mean corresponds to a 50% increase in clearance with a relative standard deviation of 70% compared to the design value, suggesting that even the optimized manufacturing process yields significant deviation from the targeted design values. It should be emphasized that the magnitudes of the nominal clearance error are a function of the rotor and bearing sleeve diameters, as well as deviations in the actual bump height, which are the main driver of the overall deviations.

It is concluded that deviations in the bump radius and/or angle affect the bump height and hence perturb both the local design clearance and stiffness along the bearing circumference, which would yield effects similar to selective shimming [115] and tailored compliance [116]. However, their magnitude and locations are uncontrollable and random by nature - Figure 5.13.

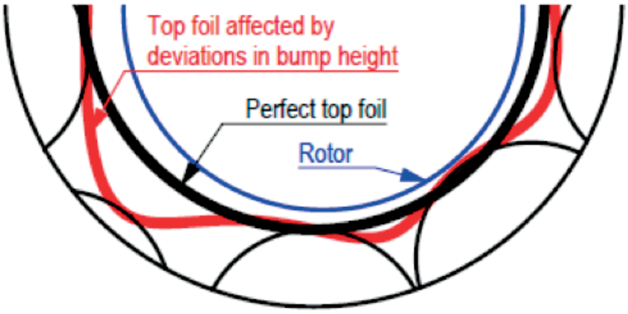

Figure 5.13 – Sketch of amplified implications on the bearing geometry due to manufacturing deviations.

5.9 Finite Element Analysis of the Bump Foil Forming Process

In order to identify both the springback phenomenon and its distribution along the bump foil and to assess the effect of the bump foil geometry on springback and therefore on manufacturing deviation a Finite Element simulation for the forming process was implemented on ABAQUS® v6.14 [2]. The model simulates a 2D rigid tooling geometry and a 0.1mm thick stainless steel sheet as represented in Figure 5.14. The analysis of the forming process was divided into three phases where the first is the closing of the die, the second simulates the heat treatment, and the last is the die opening - Figure 5.15. The first and the third parts are dynamic simulations with high strains, plastic deformations and important friction effects, thus, explicit simulations were adopted. The heat treatment phase is a quasi-static simulation with a coupled temperature displacement analysis. To simulate the effect of the fixing binder, the foil area that should be in contact with the binder is fixed to the die. Two different surface-to-surface contacts have been created between the foil and the two part of the die.

The elasto-plastic relation of the 1.4310 stainless steel has been defined with a Ramberg-Osgood model at different temperatures [117]. A Norton power law is used to take into account for creep [118]. The parameters are calibrated based on experimental data from ambient temperature to 1000°C [119].

Coupled temperature-displacement plain strain with second order accuracy elements are adopted in this model. Linear elements are chosen for their better hourglass control for quadrilateral elements. As the simulation was mainly concerned with springback, the position of the free tip of the foil after the opening of the die was chosen as an indicator for grid independence. The displacement during the closure of the die converged with less than 2.5% relative error for 5 elements in the foil thickness, yielding an element thickness of 0.02 mm. It was shown that odd numbers of elements describes the physics with a better accuracy due to the existence of a neutral fiber. A sensitivity analysis was executed to determine the damping

---

[2] Mr. Simon Wicki is acknowledged for preliminary work on the development of the Finite Element model during his semester project under the supervision of the author at the Laboratory for Applied Mechanical Design in 2016.

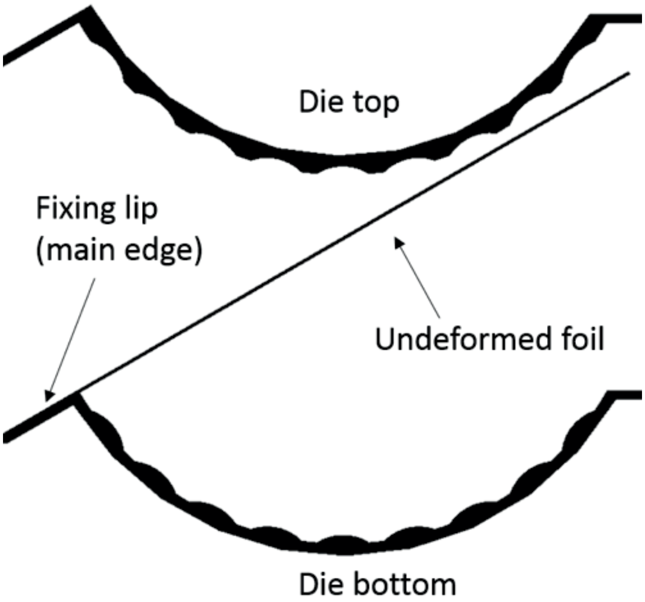
Die top
Fixing lip
(main edge)
Undeformed foil
Die bottom

Figure 5.14 – FE computational domain representing the two rigid dies and the undeformed foil before the die closing.

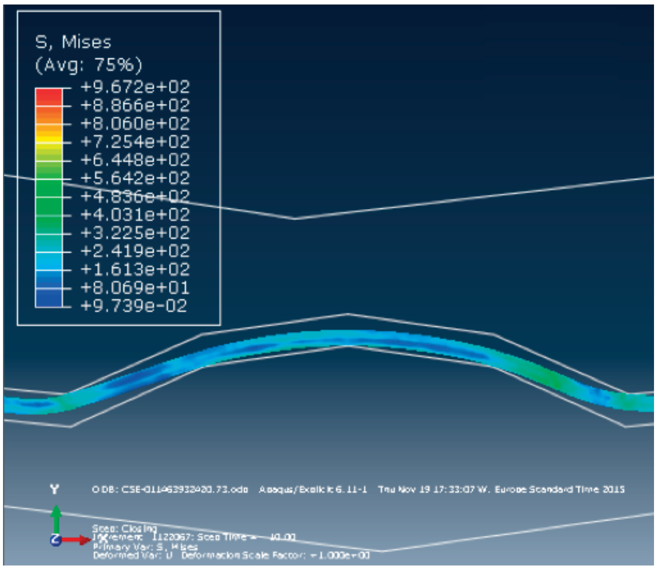
S, Mises
(Avg: 75%)
+9.672e+02
+8.866e+02
+8.060e+02
+7.254e+02
+6.448e+02
+5.642e+02
+4.836e+02
+4.031e+02
+3.225e+02
+2.419e+02
+1.613e+02
+8.069e+01
+9.739e-02
Y
Z
ODB: CSE-011463932420.73.odb Abaqus/Explicit 6.11-1 Thu Nov 19 17:33:07 W. Europe Standard Time 2015
Step: Closing
Increment 1122067: Step Time = 10.00
Primary Var: S, Mises
Deformed Var: U Deformation Scale Factor: +1.000e+00

Figure 5.15 – Von Mises stress on one bump during the closing of the die.

coefficient yielding a critically damped response. It was shown that a damping coefficient of 0.3 yields the minimum time to achieve a steady state position.

The effect of friction on springback was investigated in prior work, which suggests that springback is sensitive to friction coefficients [120–125]. Hence, a sensitivity analysis was performed for friction level between the foil and the die. The standard Coulomb friction model was

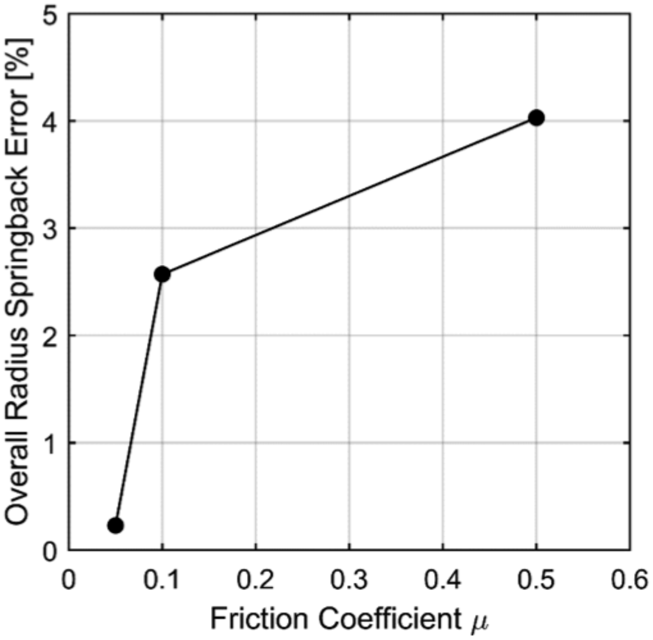

Figure 5.16 – Effect of friction coefficient between the die and the formed foil on bump foil overall radius springback.

adopted and simulated for different levels of friction. The results confirm that springback is highly dependent on the friction coefficient. A friction coefficient of 0.05 yields the minimum springback - Figure 5.16. However, a friction coefficient of 0.1 is used in the model as it fits the experimental data, also a friction coefficient below 0.1 between Stainless steel and Inconel is very difficult to achieve experimentally.

Simulation results of the foils after load release and heat treatment were used to quantify springback with the same treatment used for the experimental investigation described above. Figure 5.17 represents the comparison of radius and intersection angle springback error for each bump for both the FE results and the experimental measurements of the manufactured bump foils. The FE results lie within the standard deviation of all the experimental measurements and follow the same trend. Bump number 1 is the first bump near the foil lip, and bump number 9 is last bump at the free end. The figure suggests that the two variables have similar trends along the foil. In addition, it can be seen that larger springback occurs near the foil lip (fixture), this is due to the large change in curvature at this point, which would influence the bumps in close proximity. The error bars on the figure represents the standard deviation (2-sigma) of the manufacturing process on each bump, and not of the measurement procedure, which is estimated to be negligible compared to that of manufacturing process. Note that the bumps towards the free end yield lower errors suggesting that the clamping of the foil at the lip itself is responsible for part of springback. The resulting overall bump foil radius is plotted in Figure 5.7 thus suggesting good agreement between the numerical methodology and the experiments presented above.

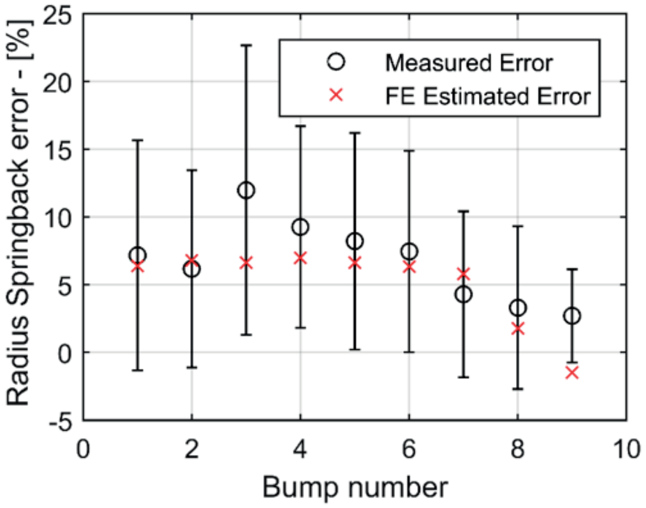

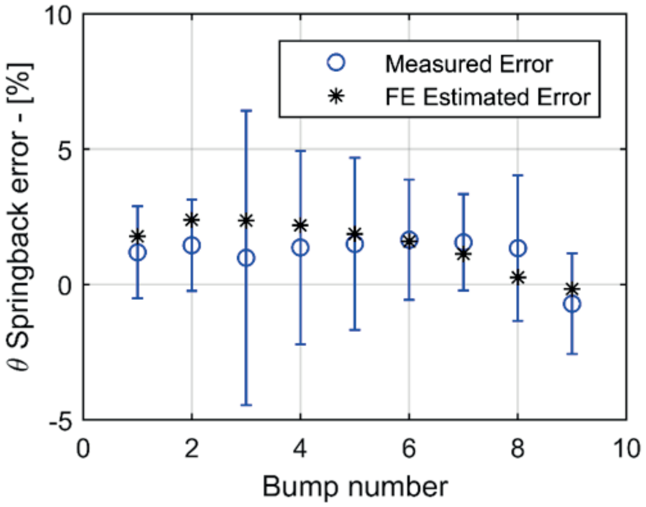

Figure 5.17 – FE model validation with measured bump radius error (Top) and intersection angle θ (Bottom) for each bump.

Figure 5.18 shows the von Mises stress distribution along the foil length after the closure of the die at a friction coefficient of 0.1. Since springback after the die opening is directly related to the stress level the latter can be used to identify the locations of major springback. The stress levels suggest that the main stress pike occurs at the main edge of the foil used for fixture. Local maxima appear in the sharp bends of the foil after each bump to follow the main circular profile, thus corroborating the θ-springback error represented in Figure 5.17, the sharper the intersection angle, the higher the stresses, hence, the higher are the intersection angle springback errors - analogous to the bending of a metal sheet with large bend angles. Local minima are observed within the bump themselves. The results therefore suggest that the main driver for springback of the classical bump foils are the discontinuities of curvature at the bump-land transitions.

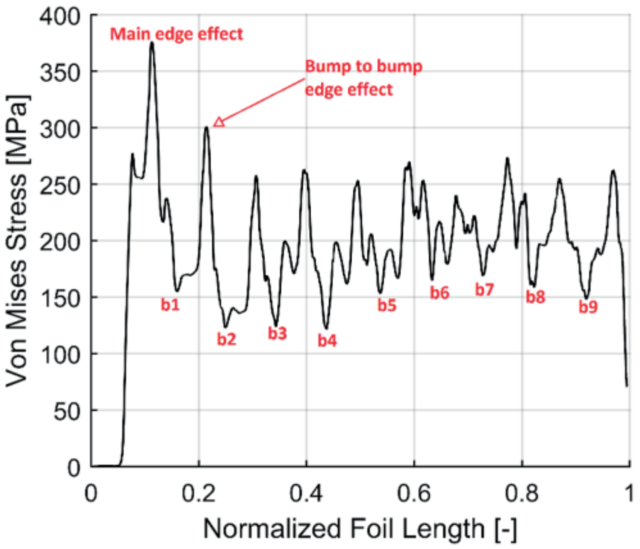

Figure 5.18 – Von Mises stress along the formed foil with local maxima indicating the transition between the bump and the land region and local minima occurring on the bumps themselves.

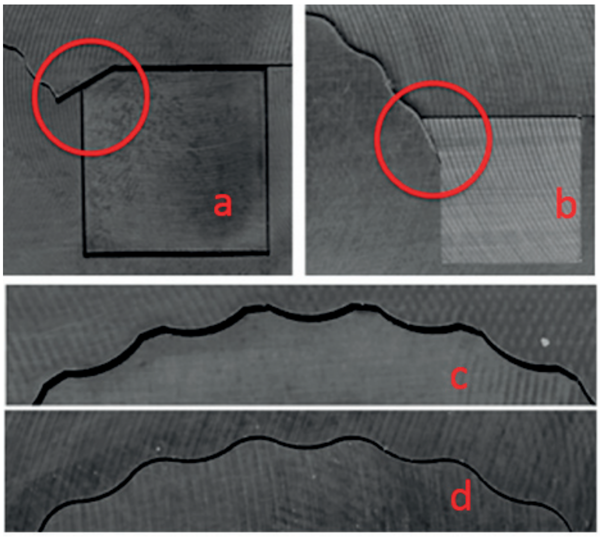

Figure 5.19 – Original (a, and c)and modified (b, and d) die designs.

5.10 Improved die design

Based on this analysis, a second die was designed to reduce springback, while maintaining the same bump foil compliance and foil thickness. The rationale behind the new design is the reduction of the foil curvature by eliminating the 90° bend at the main edge for fixture, and replacing it with an edge that follows the curvature of the bearing. In addition, the sharp bends between the bumps are replaced by a smooth curve, resulting in a final shape similar to a sinusoidal wave along the overall bump radius - Figure 5.21. The geometrical modifications were a consequence of the reduction of the distributed stress along the foil, which is expected to reduce the springback as a consequence. A comparison between the two forming dies is represented in Figure 5.19 comparing the two fixtures (a and b) and the classical and sinusoidal bumps (c and d).

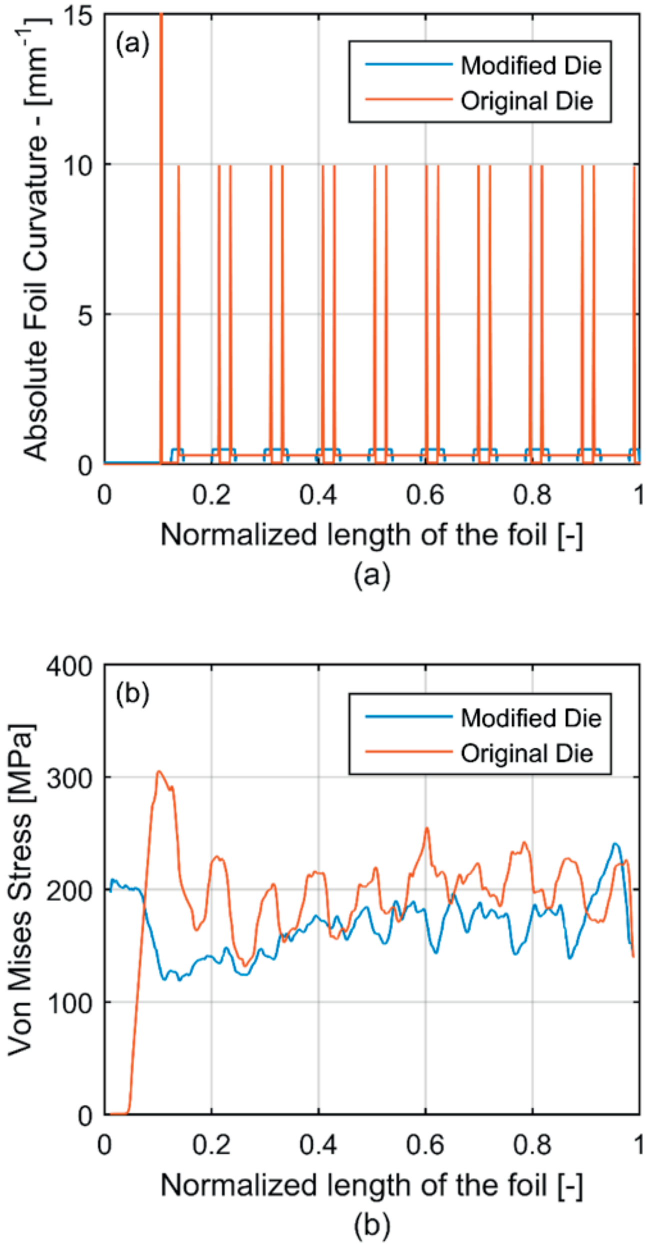

(a)

(b)

Figure 5.20 – Die curvature and Von Mises stress along the formed foil comparing original and modified die designs.

Figure 5.20 shows the absolute curvature of both die geometries (a), and the comparison between the two geometries in terms of von Mises stress after the die closure (b). The mean stress along the foil was reduced by 17.4% compared to the original design. The springback was reduced by 69% in a cold forming simulation.

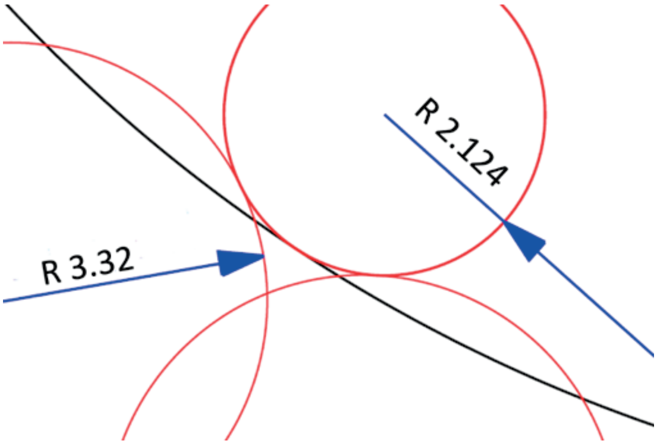

Figure 5.21 – Geometrical features of the modified bump foil eliminating the sharp theta angle.

The modified foil die was prototyped in Inconel X750 using EDM. 6 foil samples were tested at the optimum forming conditions mentioned previously. The modified design produced better foils in terms of mean and variance. The mean normalized bump radius is 1.0096, and ranges between 0.95 and 1.068 compared to 0.95 to 1.3 for the classical bumps. The relative standard deviation drops from 12.4% to 1.7%. Figure 5.22 shows the probability density functions of the original and modified forming dies in terms of normalized bump radius. The reduction in variance suggests a significant improvement in accuracy and robustness.

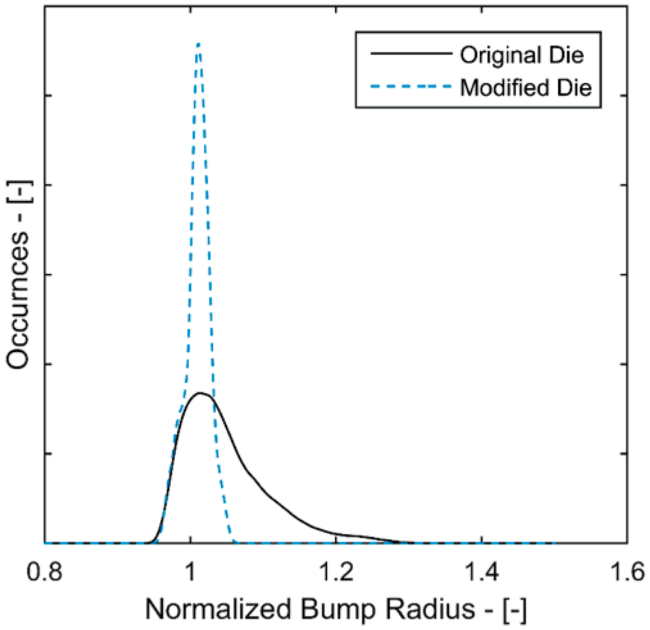

Figure 5.22 – Kernel distribution of the normalized bump radius comparing the original die design to the modified die design and highlighting the improvement in robustness (precision) and accuracy.

5.11 Cantilever Type Compliant Structure

In an attempt to further improve the manufacturability of the compliant structure and to avoid the springback deviation effect, the Cantilever type compliant foil structure [126–128] was investigated, as its manufacturing does not rely on metal forming techniques. A flat foil is laser cut or chemically etched, creating segments of cantilevers within the foil – Figure 5.23. The stiffness of the cantilevers can be easily estimated for small deflections based on beam theory. Figure 5.24 shows the dimensions of the Cantilever foil beams.

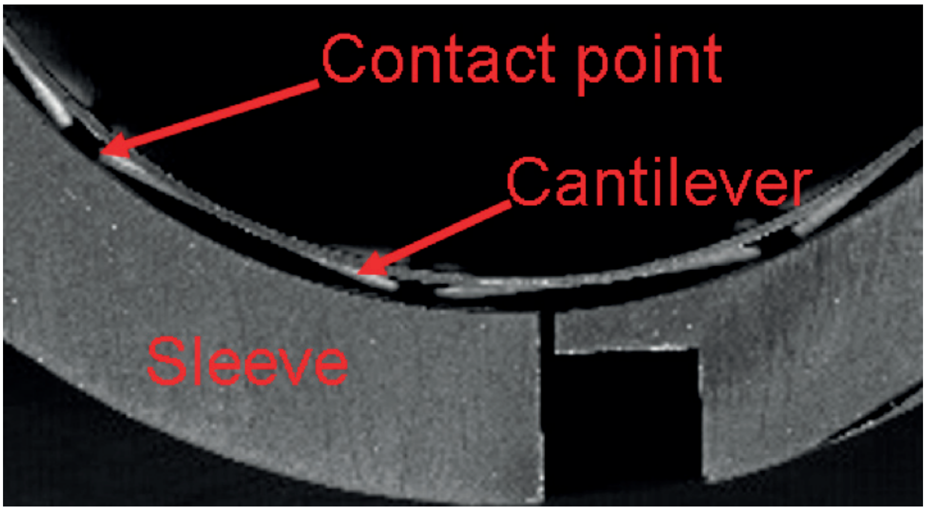

Figure 5.23 – Cantilever compliant foil bearing (all beams are in contact with the sleeve).

The laser cutting ensures an accurate cantilever geometry, hence eliminating the effect of geometrical deviations due to manufacturing uncertainty related to metal sheet die forming.

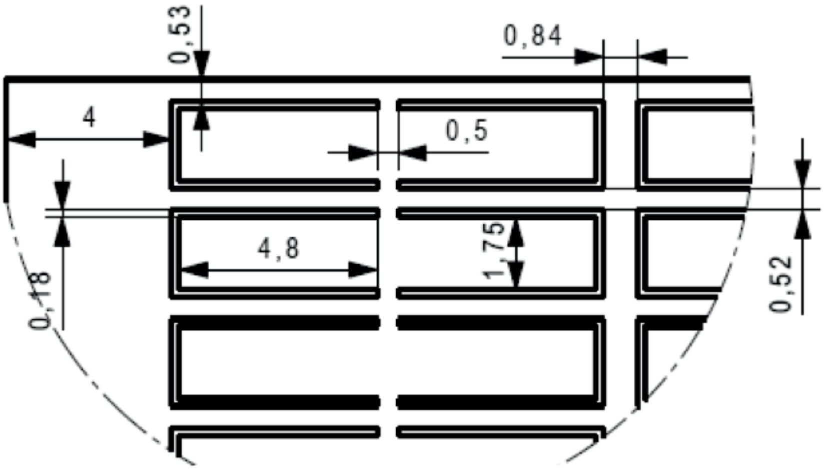

Figure 5.24 – Dimensions of the cantilever beam foil.

After cutting, the foil is wrapped and placed inside the bearing sleeve, the potential energy stored in the wrapped foil will ensure the engagement of the cantilevers on the bearing sleeve.

The cut foil can be also heat treated around a mandrel to get a plastic round shape before placing it inside the bearing sleeve - Figure 5.25.

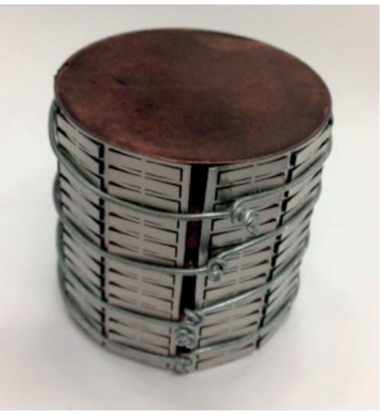

Figure 5.25 – Heat treatment of Cantilever beam foils.

It is worth mentioning that for this design the heat treatment process would not affect the essence of the compliant structure compared to the bump foil structure. The cantilever will perform similar to bump type compliant structures in terms of nonlinear sequential engagement and structural damping.

The manufactured cantilever foils under investigation are measured using an optical tool. Deviations in the beam length and width are ± 0.44% and ± 2.19% respectively. The deduced effect on compliance using a simple linear cantilever model:

$$S = \frac{{L_{beam}}^3}{3EI} \tag{5.10}$$

yields variations within ± 3.56%. Where L_{beam} is the length of the cantilever beam, E is the modulus of elasticity, and I is the second moment of area. Deviations within the cantilever beam thickness were considered negligible given the relatively small surface area of the foil (131mm x 40mm). The effect on local clearance is estimated through analyzing the effect of deviations of cantilever beam lengths on the sagitta (represents the bump height in a cantilever beam foil). The error in the sagitta lies within ± 0.9%, making the deviations in bearing local assembly clearance within ± 7%, which is considered a major improvement compared to the Gen II bump type classical foil bearings, where the local clearance deviations are within -50% and +150%.

5.12 Effect of Foil Bearing Manufacturing Errors on Rotordynamics

Since the local clearance deviations influence the local fluid film it seems evident that they also influence the rotordynamic bearing performance. In order to asses these effects the foil bearing model of Kim and San Andrés [129], and adopted by Schiffmann and Spakovszky [115] is used as a platform for a Monte Carlo simulation assessing the effect of random deviations in bearing local clearance on the stability of the rotor. The model adopts the frequency domain method; hence it is incapable of simulating the time domain orbit evolution or of predicting limit cycles beyond the onset speed of instability. The model solves the compressible Reynolds equation using the perturbation method of Lund [130]. Small perturbations around an eccentric rotor are introduced to yield partial differential equations for the zeroth and first order pressure perturbations. The partial differential equations are solved using the finite element method of Faria and San Andrés [131] and Faria [132]. Integration of the zeroth order pressure field yields the static force components for a given static eccentricity. The integration of the first order terms of the pressure field determines the direct and the cross-coupled stiffness and damping coefficients. A detailed description of the bearing under investigation is summarized in table 5.6.

Table 5.6 – Foil bearing model parameters

Foil bearing parameters	
D [mm]	40
L/D [-]	1
C [μm]	80
$\alpha_{\mathbf{comp}}$ **[-]**	0.67
γ**[-]**	0.14
$\mathbf{R_D}$ **[mm]**	3.32
$\alpha_{\mathbf{D}}$ **[∘]**	63.15
t [mm]	0.1
Fluid	Air
Ambient Pressure [kPa]	101.325

The Monte Carlo simulation uses shimming as a mechanism to introduce local clearance disturbances to the bearing. By adding shims at the bump locations along the bearing circumference and randomly changing their heights, local changes in the bearing clearance are introduced – effects that mimic Figure 5.13. The number of shims is equal to the number of bumps and are located at the same angular location (21 shims – 17.14° apart). One thousand bearing scenarios were simulated for each bearing design with a uniform statistical distribution for the shim thickness that results from the evaluation of the manufactured and measured foils. The shim height for the classical bump, the Sinusoidal bump, and the Cantilever beam range between -50% to +150%, ±50%, and ±7% respectively of the bearing assembly clearance.

The stability criterion used in the simulation is the critical mass parameter defined by Pan [133] and modified by Schiffmann and Spakovszky [115]. Figure 5.26 shows the critical mass as a function of compressibility number for inaccurate bearings of different designs compared to the perfect bearing. The results suggest that random deviation in the local clearance have significant effects on the bearing stability. For the classical bump design, only 311 cases of the 1000 simulations converged to a solution, signifying the existence of 689 cases were there was either a touchdown or the numerical scheme could not converge due to very large rotor eccentricities. Note that almost all the converged cases yield better dynamic performance compared to the perfect geometry bearing, which is in some cases improving the critical mass by four orders of magnitude. For the Sinusoidal bump design, 552 cases converged, yielding mostly improved stability. The converged cases seem to disperse less compared to the classical bump design, which is a result of the reduced manufacturing deviation. Finally, for the Cantilever beam design, 979 cases converged and the stability is barely affected by the manufacturing deviations. It should be noted, that the accurate manufacturing of the Cantilever beam foil bearing, which results in less deviations in the local bearing clearance is the main reason behind its good performance repeatability. It is also deduced that a ±7% tolerance on the circularity of the foil bearing clearance is acceptable from a stability point of view.

These results suggest that manufacturing deviation affect the local bearing clearance, which has a significant effect on foil bearing stability. This effect can either be very favorable or inversely result in reduced performance or even local touchdown. The consequence is that manufacturing deviation due to the bump foil springback introduces difficulties/challenges in controlling and predicting the dynamic behavior of a foil bearing supported rotor.

Radil et al. [134] investigated the effect of radial clearance on foil bearing load capacity. The authors concluded that reducing the clearance by half can reduce the load capacity by 70%, and doubling it decreased load capacity by 30%. The authors reported an optimum value of clearance for maximum load capacity. This highlights the importance of defining appropriate manufacturing tolerances for foil bearings, as well as developing novel foil bearing designs that eliminate the root cause of the manufacturing problem, i.e. unpredictable and non-repetitive springback.

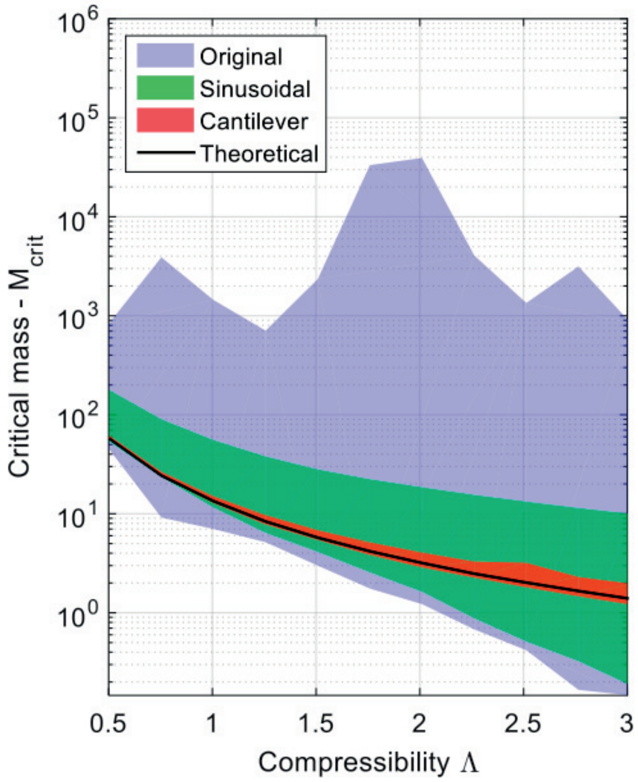

Figure 5.26 – Effect of bump foil manufacturing errors on the stability of foil bearings. Perfectly manufactured bearings should all lie over the black theoretical line. The results highlight the robustness of the cantilever beam design in terms of accuracy and precision. (Only feasible solutions are plotted)

5.13 Static Load-Displacement Measurements

The auxilliary setup described in Chapter 2 is used to perform load-displacement tests on the different bearings. The tests are performed on a rotor shaft supported on two radial foil bearings. The loading is done via two torque arms connected via wires to the rotor shaft, the load is gradually exerted using lab jacks. Two load cells are implemented within the loading loop to measure the force during pulling and pushing. Optical proximity probes are fixed on the bushing of each bearing for measuring the resulting displacement due to the load. Three bearing designs were tested: (1) Baseline (bump type Gen II) bearings composed of three bump foil pads (120 degrees' arcs) and one top foil per bearing, (2) bump type Sinusoidal adopting the same layout as bearing 1, and (3) Cantilever type bearing with a single foil as the compliant structure and one overlaid top foil. The bearings under investigation are summarized in Table 5.7. The design bump heights are similar for bearings 1 and 2 and equal to 0.8mm, the bump heights are measured relative to the bearing sleeve, hence curvature effects are taken into consideration. The equivalent variable for cantilever bearing 3 is the sagitta of the beam that is equal to 1mm.

Table 5.7 – Test bearings under investigation

Test Bearing	Compliant Structure	Material
1	Bump Type Gen II	Stainless Steel
2	Bump Type Sinusoidal	Stainless Steel
3	Cantilever Type	Stainless Steel

The test program measured load and displacement at three equally spaced points along the bearing circumference (120°). It is common practice to use load-displacement curves to quantify the actual assembly clearance between the bearing and the rotor [16,24,40]. In this work the foil bearing clearance is defined as the distance the rotor travels before experiencing significant resistance from the bump foils. The accuracy of the optical probe is ±1.3%, whereas the one of the load cell is estimated ±1%. The uncertainty propagation for the stiffness calculation yields ±1.64% (See chapter 2).

Load displacement curves of test bearing 1 - Figure 5.27a left - shows significant changes in slope for the three load cases, yielding changes in the bearing radial stiffness distribution as shown in Figure 5.27a right. Such a behavior results in a bearing anisotropy manifested mainly at high bearing numbers, where the bearing stiffness is mainly driven by the underlying structure. The bearing clearance ranges between 0.16mm to 0.2mm. Test bearing 2 (sinusoidal bump foil) yields slightly improved results compared to test bearing 1 – Figure 5.27b, with the bearing clearance ranging between 0.17mm and 0.2mm at three different equally spaced measurement points along the bearing circumference. Deviation in clearance still persists, yet deviations in stiffness are reduced compared to the classic Gen II bearing. Test bearing 3 yields significant improvement both in stiffness and clearance robustness along the bearing circumference. The measured clearance ranges between 0.14mm and 0.16mm - Figure 5.27c left. The measurement suggests that the Cantilever compliant structure can produce stiffness levels similar to those of the bump design - Figure 5.27c right. The discrepancies both in clearance and stiffness are significantly reduced compared to the two other bump type bearings under investigation (≈ -50% deviation). This is a direct consequence of the fact that Cantilever foil manufacturing does not rely on shaping through dies and plastic material deformation and are therefore not exposed to springback induced deviation. It is therefore suggested that a compliant Cantilever type structure is a promising candidate for both improving the understanding of foil bearing technology and the predictability of this technology.

Hysteresis loops are visible in all load displacement curves, which are considered a signature of Coulomb friction. It can be clearly shown that the Cantilever bearing 3 exhibits the most pronounced hysteresis compared to bump type bearings 1, and 2. It can be speculated that the slight reduction in hysteresis shown in the sinusoidal bearing 2 compared to the classical Gen II bearing 1 is due to the different geometrical features. The sinusoidal shape is in contact with the bearing bushing (sleeve) on specific lines between the bumps instead of flat segments when compared to classical Gen II bump foil – Figure 5.19. Such reduction in contact would be expected to influence the Coulomb friction, hence the resulting hysteresis.

(a) Test bearing 1 – classical bump foil

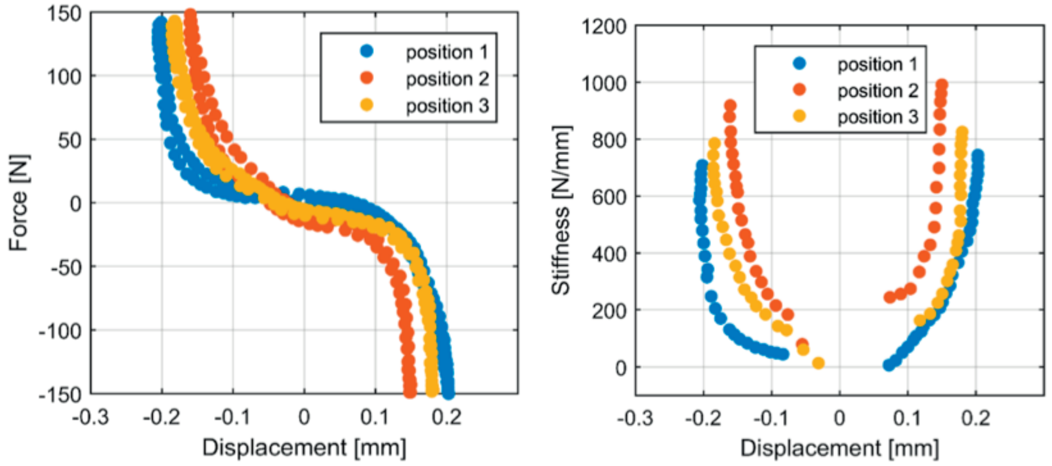

(b) Test bearing 2 – sinusoidal bump foil

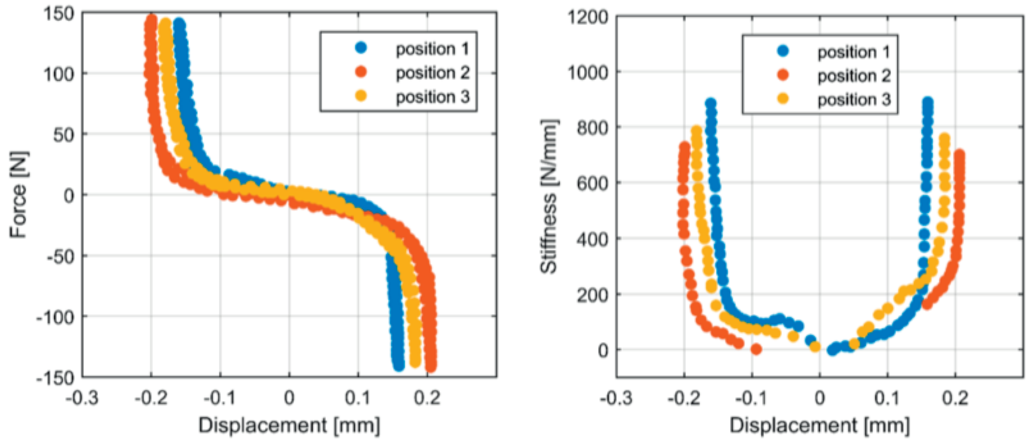

(c) Test bearing 3 – cantilever beam foil

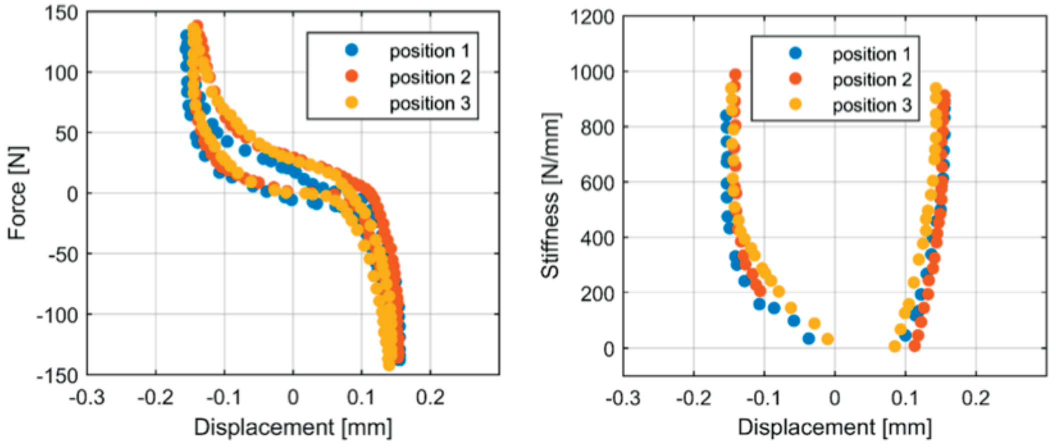

Figure 5.27 – Measured load-displacement and deduced stiffness-displacement for different foil bearings at three points inside the bearing. The results confirm the superiority of the cantilever beam foil bearing in terms of manufacturing robustness (precision).

5.14 Chapter Conclusions

A review of the available knowledge in the fabrication of foil bearings was briefly presented. It was shown that the available know-how is not sufficient for the accurate manufacturing of foil bearings. The bump foil compliance was shown to be sensitive to the bump angle and radius, even for small errors of bump geometry (5% error in compliance for each 1% error in bump radius). A manufacturing procedure was selected using forming dies adopting the overall curvature of the bump foil. Due to the complexity of the bump foil shape, an optical measurement technique was developed for the purpose of the detailed geometrical measurement of the formed bump foils. Consequently, a DoE approach was used to identify the effect of heat treatment temperature, duration, and forming pressure on the foil springback. A FE model was developed to simulate the forming process of the foil inside the die. Manufacturing uncertainties manifested as springback were quantified statistically, and different compliant structures were investigated from a manufacturing perspective.

The following conclusions were made:

- It was shown that the heat treatment temperature is the significant factor affecting the measured springback. It was also shown that the optimum temperature for Stainless Steel (1.4310) foil forming is 650°C.
- The results of uncertainty quantification showed a 6% mean bump radius error, and the measured samples ranged between -5% to 30% error, which highlights the lack of robustness of both the manufacturing process and the bump foil design. The analysis showed major deviations in bearing clearance and compliance due to springback inducing significant effects on bearing performance.
- A linear correlation was found between the bump radius and bump angle errors, which is explained by the finite arc length of the bump.
- A Monte Carlo simulation was done with the quantified uncertainty distributions for the bump geometrical errors. The mean of obtained compared to design stiffness is an increase by 10% with a relative standard deviation of 12.4%.
- The FEA suggests that the stress levels within the foil are very sensitive to the shape of the die. It was shown that modifying the geometry of the forming die, by eliminating all the sharp bending locations, as well as aggressive changes in the bump foil curvature, the mean stress along the foil can be reduced by 17.4%, and springback by 69%.
- The modified die design was prototyped and tested and proving significant improvements. The accuracy improved in terms of the mean bump radius error, which reached a value 1% instead of 6% in the original design. The robustness also improved by having a significantly lower range of error for the different measured samples to range between -5% and 6% instead of ranging between -5% and 30% in the original die design, and a reduction in relative standard deviation from 12.4% to 1.7%.

- Generation II foil bearings rely mainly on sheet metal forming techniques, hence suffer from springback problems that would change the bump radii and angles, which would directly affect the bearing local clearance and compliance. A statistic was constructed for bump foils manufactured using an optimized procedure. The statistic shows an error in local bearing clearance varying between -50% and +150%. A large variance is also present suggesting a lack of robustness of the optimized manufacturing process. It should be noted that in this work only Stainless Steel (1.4310) foils and curved forming dies were investigated.

- A Cantilever compliant structure design replacing the bump design was investigated from a manufacturing point of view. Since such designs do not rely on metal forming to achieve the design compliance.

- The effect of manufacturing errors was further investigated on the rotordynamic stability of foil bearings supported rotors. A Monte Carlo simulation was performed including random deviations in the local bearing clearance. The results suggest that the effects of manufacturing errors on the local bearing clearance can have a significant and uncontrollable effect on the bearing stability and performance. For the classical bump design only 31.1% of the simulated bearings were feasible and mostly more stable compared to the perfect bearing design. However, the stability threshold varies significantly for the different bearings. The more accurate Cantilever design shows significant improvements, with 97.9% feasible bearings. For a given rotor mass, the stability threshold was found nearly constant for the all the Cantilever bearings under investigations. Although, the presented simulation is not experimentally validated due to the difficulty of testing large numbers of bearings under similar conditions, the results are the outcome of a well-established and experimentally validated foil bearingmodel. The effects of manufacturing errors on the foil bearing performance are similar to selective shimming, a concept also validated [115].

- Results of theMonte Carlo simulations show that a ±7% manufacturing tolerance on the circularity of the foil bearing clearance is acceptable from a stability point of view.

- Cantilever, Sinusoidal, and Classic foil bearing designs were statically tested using a load displacement auxiliary test-rig. It was found that the Cantilever foil bearing yields less deviations than bump type elastic foil bearing structures. The bearings under investigation showed that the Cantilever bearing structure varied in clearance between 0.14mm to 0.16mm, the Sinusoidal bearing varied between 0.17mm to 0.2mm, and finally the baseline Classical Gen II bearing deviated between 0.16mm and 0.2mm.

- Foil bearing manufacturers are recommended to adopt improved die designs (e.g. Sinusoidal Bump) in order to improve the accuracy of manufacturing, if they are wishing to maintain the sheet metal forming process. Otherwise, adopting a different manufacturing process (e.g. Cantilever Beam) will further improve the accuracy and robustness of manufacturing.

6 Compliant Foil Journal Bearings Measurement Campaign

This chapter presents circumferential pressure profile measurements within the gas film of a ⌀40mm (L/D = 1) Gas Foil Journal Bearing (GFJB) at two axial planes ($\overline{z} = 0$, and -0.5) using the instrumented rotor introduced in chapter 3. A detailed description of the bearing under investigation is provided. The measured pressure profiles are compared to the computational results of the model of Kim and San Andrés. To the knowledge of the author, this chapter provides fluid film pressure measurements which are presented for the first time in the foil bearing literature.

6.1 State of the Literature

The literature attempting the measurement of fluid film variables in gas foil bearings (pressure and thickness) is limited to the NASA report by Ruscitto et al. [3]. The authors planned to simultaneously measure the pressure and the film thickness inside an operating foil journal bearing. The bearing under investigation was of the bump type, with one bump foil (360°), and one overlaid top foil, which were both made out of Inconel X-750 for the purpose of the intended application (gas turbine engine). The authors adopted a floating bearing configuration, where the test rotor was supported on roller element bearings and was driven by a turbine. The rotor was instrumented with custom made gap and pressure sensors to measure the circumferential profiles inside an overhung floating test foil bearing. The sensors were powered and their signal was transmitted using a slip ring assembly. The fluid film profiles were measured at different loads (up to 200 N), and speeds (up to 60 krpm).

Ruscitto et al. [3] were unsuccessful in measuring the pressure profiles, due to the cutoff frequency of the used pressure sensor, which was essentially a proximity probe that measured the deflection of a flexible membrane. The authors confirmed the flawed pressure measurement by testing their instrumented rotor on a plane gas bearing with a static pressure tap. The comparison was not in favor of continuing the pressure measurement campaign.

The film thickness measurements were successful, and were compared to a foil bearing model -

figure 6.1. The comparison yielded a large descripency between measurement and simulation, with an underestimation of the gas film thickness, a corresponding overestimation in the pressure profile within the gas film can be deduced. 31 years later, San Andrés and Kim [135] attempted a second comparison with the measured film thickness using foil bearing model that takes into account the elasticity of the top foil. The authors were not satisfied by the clearance definition and value given by Ruscitto et al. [3] for their test bearing, and hence, chose a clearance value that matches the measured minimum film thickness. Even with this modeling approach, the model presented was only able to capture the location and the value of the minimum film thickness inside the bearing, the rest of the profile was significantly underestimated. These results clearly suggests that a significant gap exists between experimental data and GFJB models.

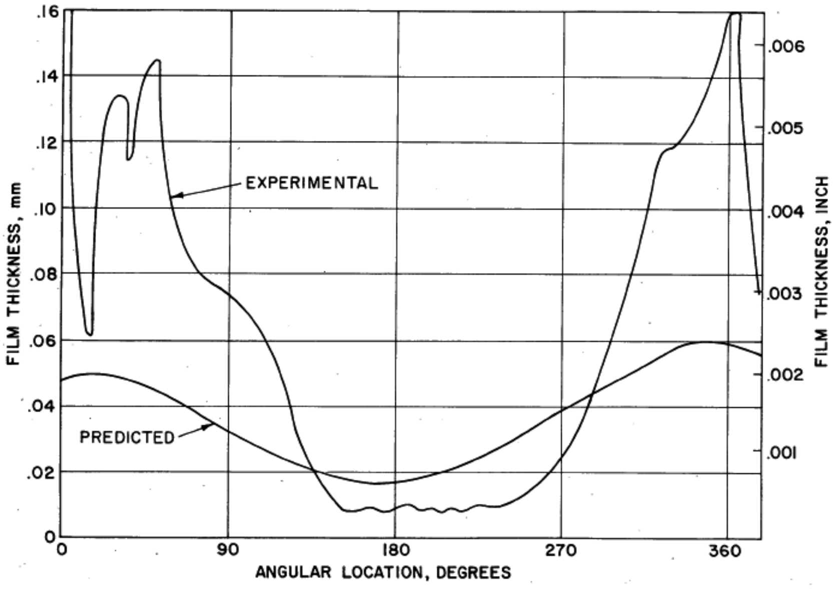

Figure 6.1 – Comparison between measured and predicted film thickness within the gas film of a journal foil bearing, highlighting a significant underestimation by the model. [Reproduced from reference [3], and used with permission of the National Aeronautics and Space Administration]

6.2 Description of Bearing Under Investigation

The GFJB under investigation is of the sinusoidal type described in the previous chapter. The bearing has 3 stainless steel bump foil pads (120°), and 1 continuous stainless steel top foil coated with PTFE. In order to adjust the assembly clearance of the bearing, round metal shims (top foil) are used to reduce the clearance.

The test bearing was measured with an inner bore probe in order to identify the circularity of the bearing under investigation. The measurements showed more than 300μm (peak-

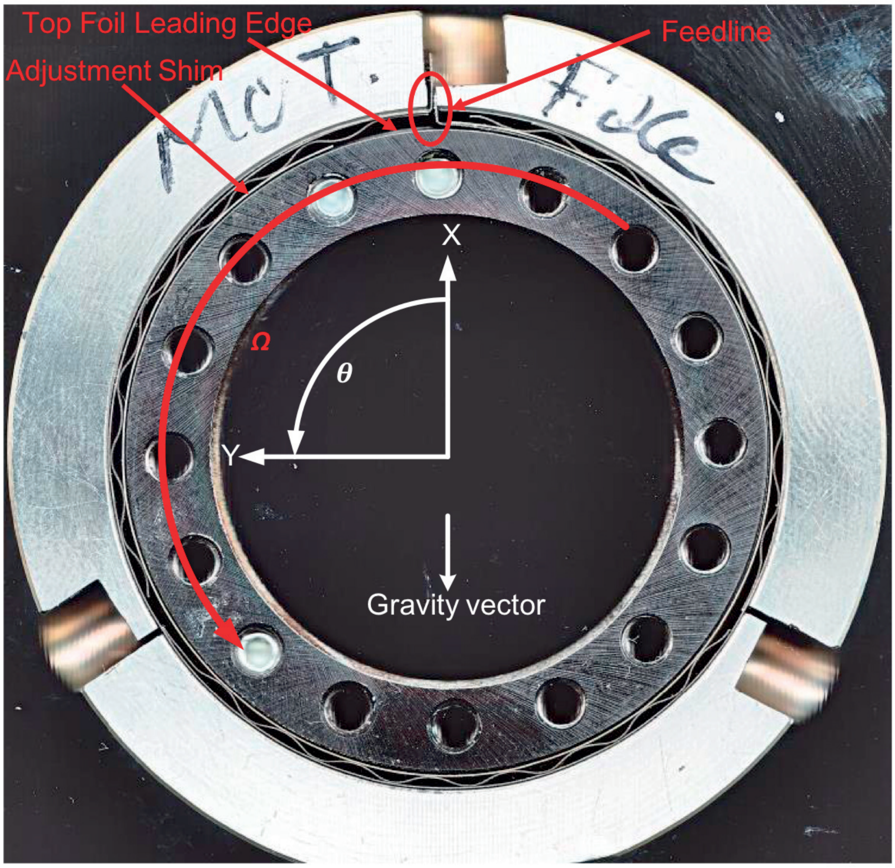

Figure 6.2 – Photograph of the actual test foil bearing under investigation highlighting the location of the feedline, the direction of rotation, and the angular reference.

peak) of runout error. Figure 6.3 shows the measured circularity profile in the bearing center. Such deviations are expected to significantly influence the pressure profile measurements. The bearing inner diameter was also measured at 3 points (60°) using a Société genevoise d'instruments de physique (SIP) machine. The measurements were executed at a constant maximum load of 10 grams, yielding the following diameters: 39.50, 39.44, and 39.29 mm, hence, confirming the lack of circularity of the foil bearing. Given that rotor diameter is 39.37 mm, the measured bearing diameters yields clearance values of 0.065, 0.035, and -0.04 mm.

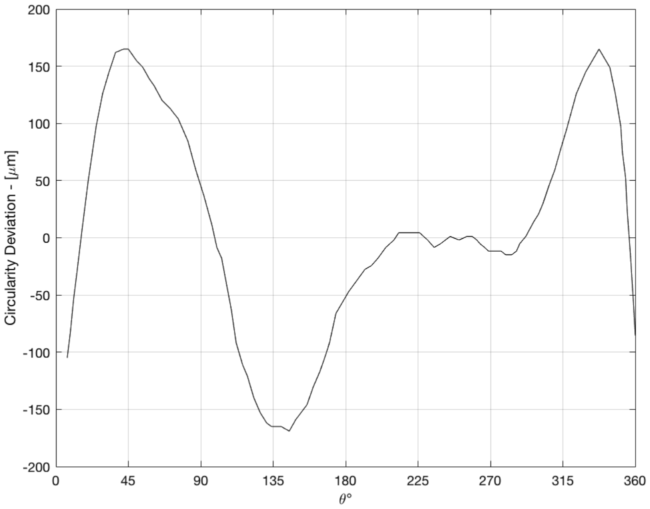

Figure 6.3 – Circularity deviation measured in the middle of the foil bearing under investigation. ± 150 μm deviation in circularity is observed. A perfectly precise bearing should yield a horizontal straight line at 0 μm.

6.2.1 Load-Displacement

The load-displacement auxiliary setup described in chapter 2 is used to identify the load-displacement characteristics of the GFJB under investigation. The curves shows a relatively high preload, as no apparent displacement occurs at no load - figure 6.4. Hence, the bump foils are immediately engaged at the onset of displacement. A hysteresis loop is observed signaling the existence of Coulomb friction damping.

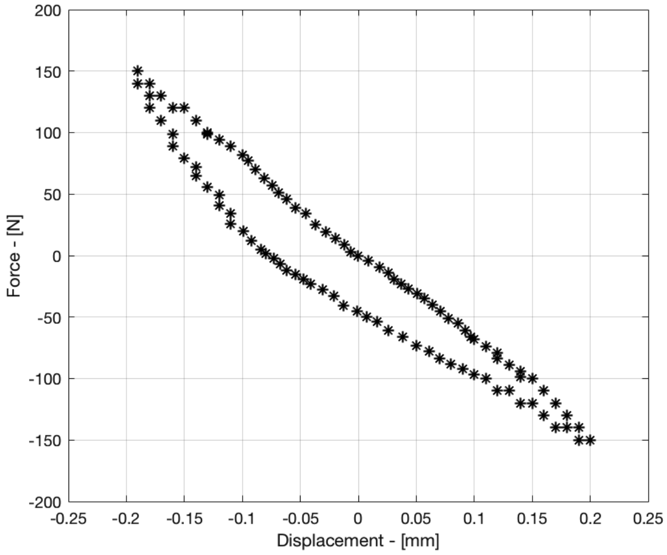

Figure 6.4 – Load-displacement curve of the foil bearing under investigation (back bearing). No visible assembly clearance (displacement at no load) is observed.

6.2.2 Bearing Preload Estimation

Given the compliance of the GFJBs, the assembly clearance of the bearing is a murky concept. An alternative to the clearance is the preload, which is the pressure exerted on the rotor due to the GFJB assembly. As the rotor spins and pressure builds up inside the bearing, at a certain rotational speed, the pressure is sufficient to push away the top foil and a gas film is created. A large preload would ensure high rotordynamic stability [15, 115], on the expense of thermal loss and seizure risks, and vice-versa.

DellaCorte et al. [136] suggested a procedure to estimate the preload pressure using break-away torque measurements at different static loads. The auxiliary break-away torque setup described in chapter 2 is used to perform this experiment. The experimental procedure starts with placing the bearing around a dummy rotor (same rotor diameter, and surface coating as the instrumented rotor), the bearing is then loaded statically using a deadweight. Consequently, the torque arm connected to the dummy rotor is gradually loaded. The force measured at the onset of the rotor's break-away multiplied by the length of the torque arm is the break-away torque for a given static load.

The slope of the friction force versus static load is the apparent friction coefficient. By extrapolation, the breakaway force at zero static load is the friction force. Dividing the friction force by the apparent friction coefficient yields an average normal preload force, which is circumferentially pressing the top foil against the rotor. Dividing the normal force by the bearing's circumferential area (perimeter x length), yields an average preload pressure.

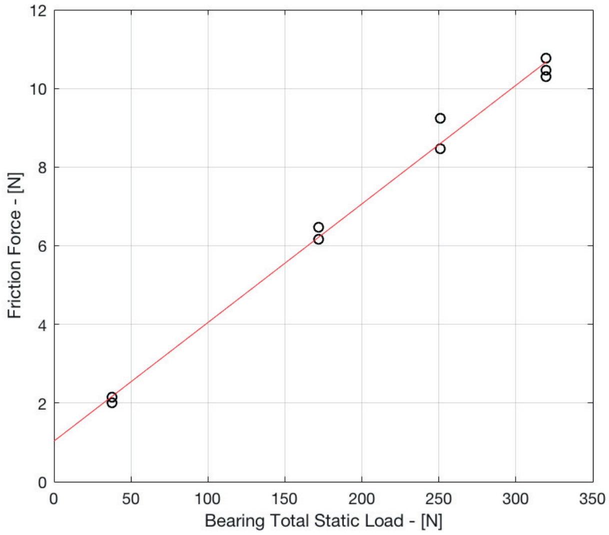

Figure 6.5 – Friction force versus static load used to quantify the bearing preload pressure.

The bearing under investigation was tested up to 319.5 N of static load. Figure 6.5 plots the friction force versus static load. The extrapolation yielded a friction force of 1.032 N at zero static load, and an apparent friction coefficient of 0.03. Hence, yielding a preload pressure of 6.85 kPa.

6.3 Dynamic Response of Instrumented Rotor

The running cycle starts from stationary conditions, ramping up to 30 krpm (linear ramp 5s/1000 rpm), cruising at speed, and free spinning down to stationary. Figures 6.6 and 6.7 presents a waterfall plot of the dynamic response of the rotor through the front and back bearings. The front bearing is the one close to the coupling, while the back bearing is the one where the pressure measurement are executed. Observing the waterfall plot, a clear synchronous amplitude is following the speed increase. The front bearing is clear of any subsynchronous vibrations, a minute supersynchronous (2x, and 3x) vibration is observed. The back bearing adopts a similar synchronous behavior, yet some nearly negligible subsynchronous vibrations are present at a constant frequency that appears at 26 krpm, at a frequency of 135 Hz (0.31x F_{rot}).

The synchronous dynamic response (peak-peak amplitude), and phase lag measured from the front and back bearings are presented in figure 6.8. A large amplification due to resonance is observed at 9.3 krpm, beyond which no other critical speeds are encountered up to 37.5 krpm while the rotor is vibrating conically.

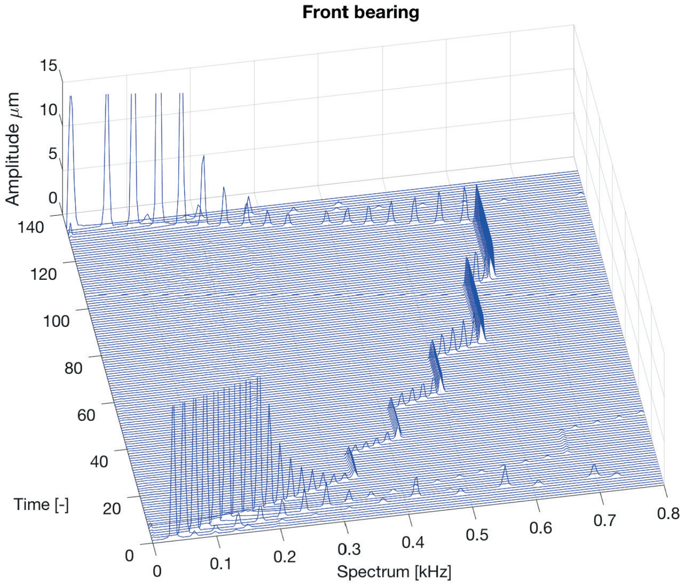

Figure 6.6 – Waterfall plot of the instrumented rotor response measured from the front foil bearing [peaks are cropped for visibility, maximum amplitude is 150 μm at approximately 150 Hz].

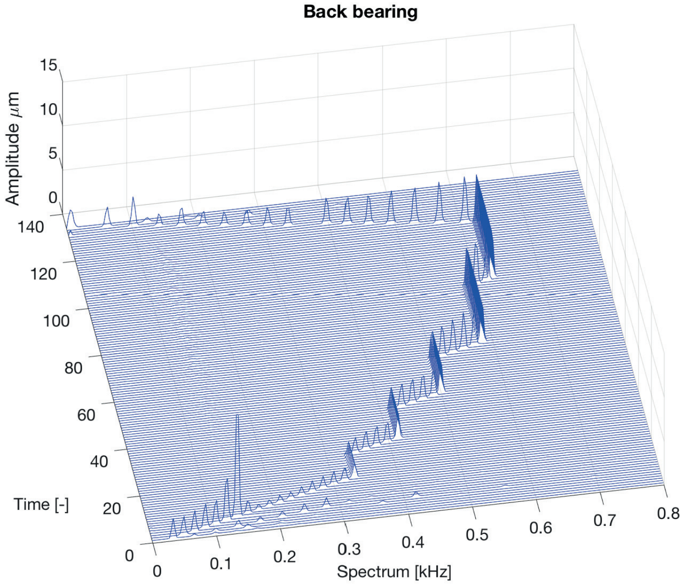

Figure 6.7 – Waterfall plot of the instrumented rotor response measured from the back foil bearing where the pressure measurement are executed.

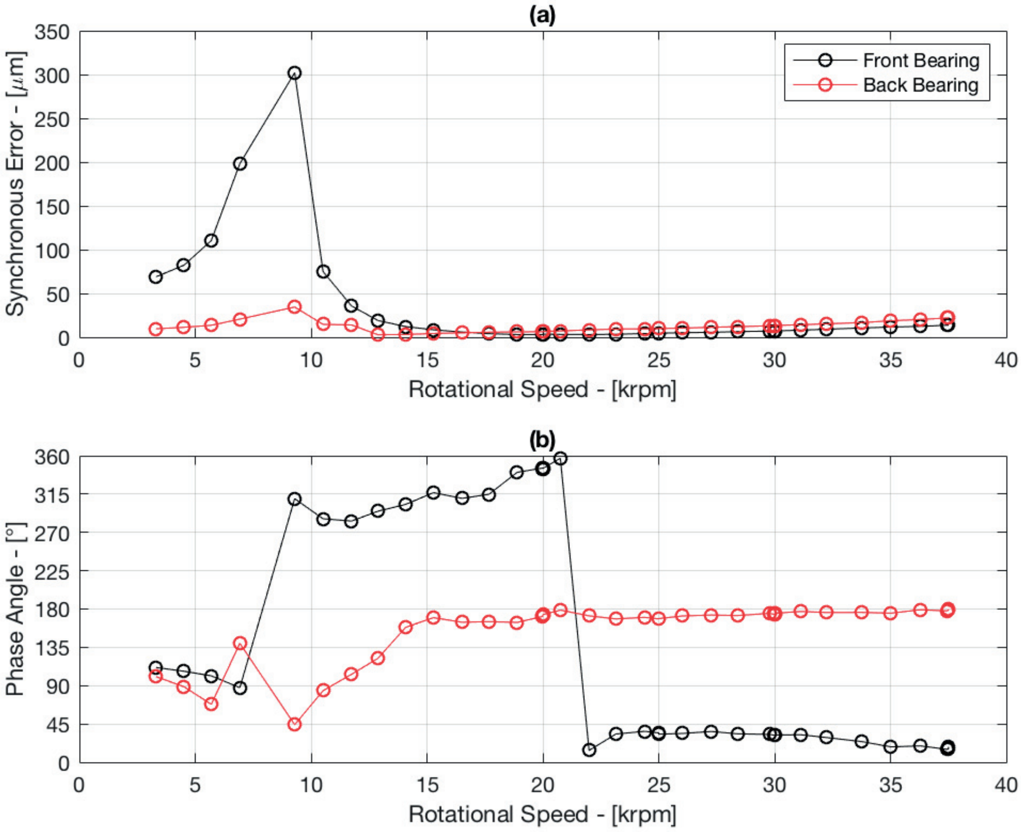

Figure 6.8 – Dynamic response of the instrumented rotor in terms of (a) peak-peak amplitude, and (b) phase lag measured from the front and back bearings.

6.4 Static Eccentricity

The mean of the x-y proximity probes signal is interpreted as the static eccentricity of the rotor. The eccentricity is defined as the center of the rotor orbit normalized by the bearing clearance. In rigid bearings, this is usually done by measuring the minimum and maximum rotor travel within the bearing clearance using the x-y proximity probes. However, since foil bearings are compliant by nature, and the rotor can travel beyond the assembly clearance of the bearing, such technique is impossible. Therefore, the absolute distance between the center of the orbit and the proximity probe is measured, which can give an indication of the behavior of the eccentricity. The distance is measured relative to the stationary rotor position. Figure 6.9 shows the vertical and horizontal components measured during a coast down from 37.5 krpm to stationary conditions. The vertical component is measured below the rotor and opposite to the gravity load vector. It is observed that the rotor withdraws away from the probe towards the bearing center by 9.5 μm at maximum speed in an exponential trajectory. The horizontal component starts by abruptly withdrawing away from the probe by 9.7μm at 4.8 krpm, then inflects and starts reapproaching the probe to remain at a distance of 4μm at maximum speed.

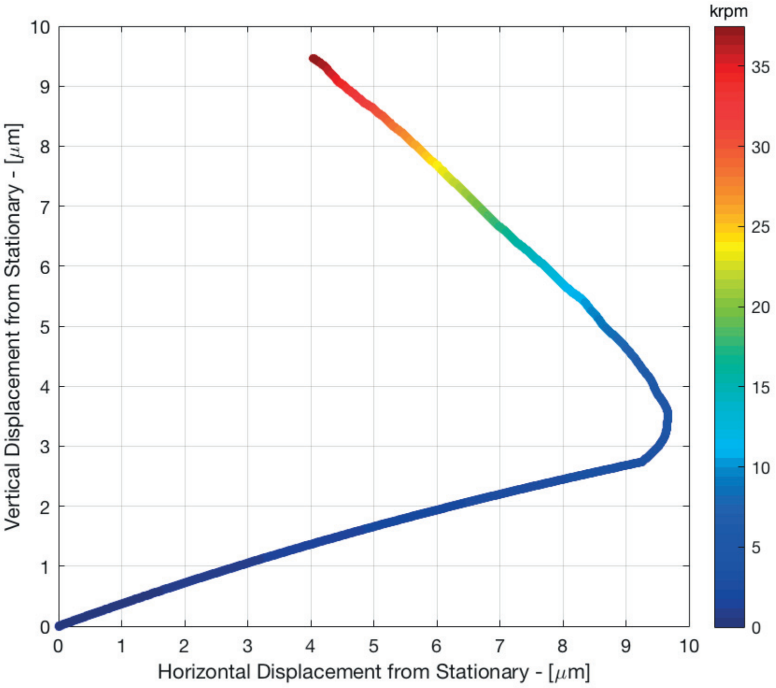

Figure 6.9 – Static rotor position at different speeds measured from the horizontal and vertical proximity probe placed below the rotor.

6.5 Rotor Orbits

The time-domain x-y signals of the proximity probes on the front and back GFJBs are used to deduce the rotor orbit. The signals are subjected to a lowpass filter with a cutoff frequency 5x of the fundamental (rotor speed). The mean is then subtracted from the filtered signals.

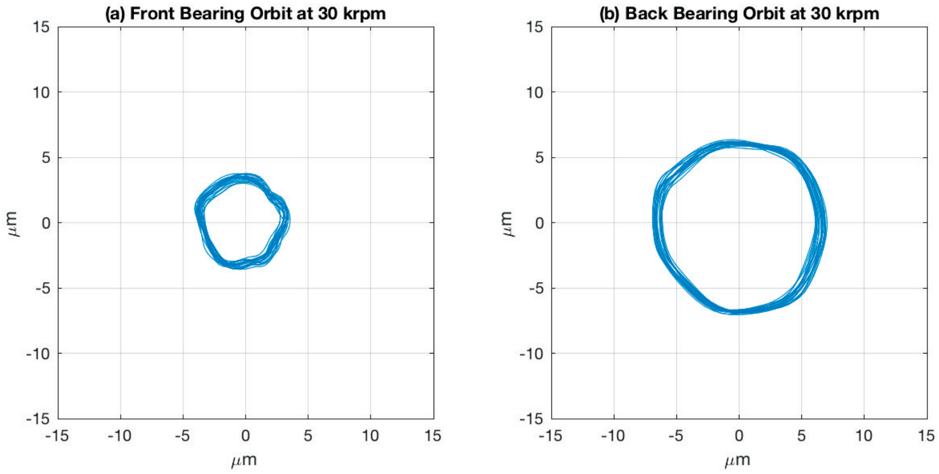

Figure 6.10 – Rotor orbits measured from the (a) front, and (b) back bearings at 30 krpm.

Figures 6.10 and 6.11 show the orbits at the front and back bearings at 25 and 37.5 krpm respectively. The orbits were clear of any signs of subsynchronous vibrations, hence confirming the observations of the waterfall plots. The front bearing had smaller orbits compared to the back bearing, which is a result of the imbalance response. The maximum orbit observed beyond resonance is of 20 μm at maximum speed of 37.5 krpm.

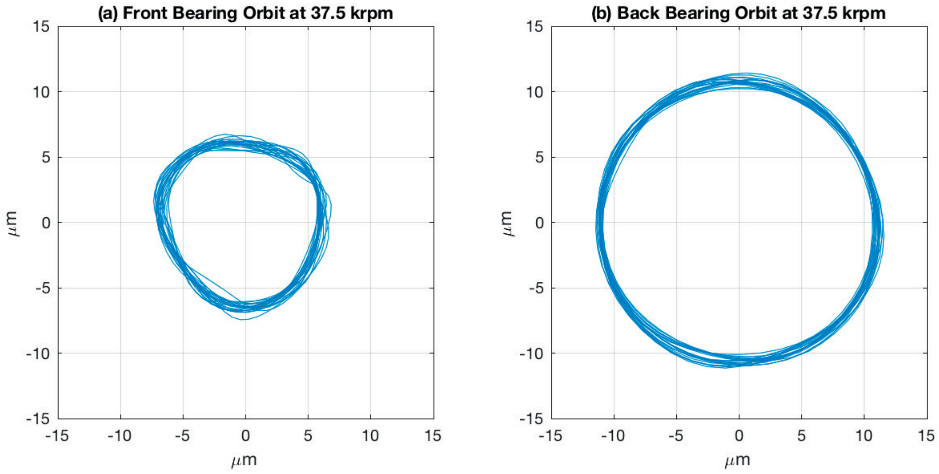

Figure 6.11 – Rotor orbits measured from the (a) front, and (b) back bearings at 37.5 krpm.

6.6 Liftoff Speed Identification

The rotor liftoff speed is defined as the speed necessary to produce enough pressure to completely carry the rotor's weight, at which the friction torque inside the bearing is minimal. It is also signals the beginning of the hydrodynamic lubrication regime. As the current state of the test-rig does not allow the direct torque measurement, coast down tests are used to measure the minimum torque speeds. The rotor-bearing system is described as follows:

$$\left(J_{rot} + J_{mot} + J_{\mathrm{coup}}\right)\dot{\omega} = T_{FB} + T_{REB} + T_{\mathrm{windage}} \tag{6.1}$$

Where J_{rot} is the test rotor inertia, J_{mot} is the electric motor rotor inertia, J_{coup} is the coupling inertia, $\dot{\omega}$ system deceleration, T_{FB} is friction torque of the two GFJBs, T_{REB} is friction torque of the electric motor's roller element bearings, and $T_{windage}$ is the windage loss of the motor. Rotor speed coast down is plotted versus time, and numerically differentiated producing the deceleration $\dot{\omega}$. The total rotor inertia is calculated from CAD. The product of the deceleration and the inertia yields the friction torque of the complete rotor assembly. Plotting the friction torque versus the corresponding rotational speed yields the Stribeck curve. However, and in order to identify the friction torque of the GFJBs alone, the same coast down test is done for the electric motor alone and the equation of motion becomes:

$$J_{mot}\dot{\omega} = T_{REB} + T_{\mathrm{windage}} \tag{6.2}$$

Consequently, the roller element bearings friction torque and the windage losses inside the electric motor are quantified for the full operational speed range. T_{REB} and T_{windage} are substituted into equation 6.1 to yield the friction torque of the two GFJBs.

Figure 6.12 shows the GFJBs friction torque versus the instrumented rotor speed. Two local minima are observed at 13.1 and 21.3 krpm, the two points corresponds to the liftoff speeds of the back and front bearings respectively. The front bearing is more challenging for liftoff due to the influence of the mechanical coupling.

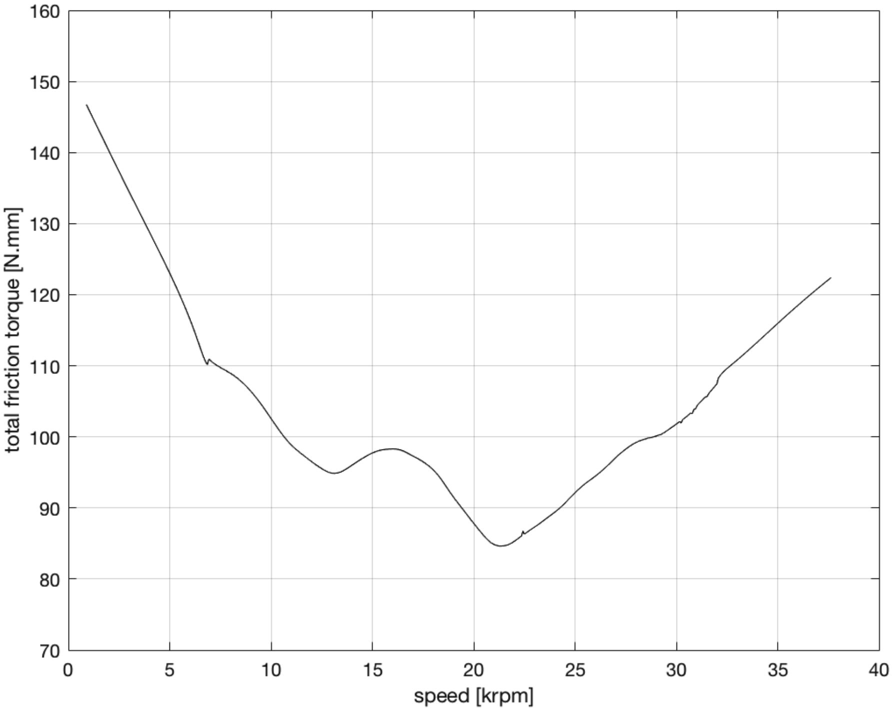

Figure 6.12 – Friction torque as a function of rotational speed.

6.7 Gas Film Pressure Measurement

The pressure measurements are streamed and clocked simultaneously with the proximity measurements and the analog trigger signal. The pressures were measured at a constant light load (rotor weight), but at different rotational speeds up to 37.5 krpm. The pressure signals are ensemble averaged at steady state conditions. Following that, the raw signal is converted from volt to bar and subjected to the corresponding transfer function developed in chapter 3 for signal reconstruction. Consequently, the reconstructed signals are corrected for the effect of centrifugal force as quantified in figure 3.6.

As highlighted in chapter 3, the reconstructed signal is sensitive to the number of harmonics below a certain threshold. In order to ensure that the measured signals are reconstructed beyond this threshold, a sensitivity analysis is performed at which signals are reconstructed at using different number of harmonics - figure 6.13. It is found that the signal is highly sensitive to the number of harmonics up to 6, beyond that increasing harmonics does not bring further information to the measured profile.

The instrumented rotor was placed in a position where one probe is located at $\overline{z} = 0$, and a second probe is located at $\overline{z} = -0.5$. Figure 6.14 shows the measured profiles at 15, 25, 30, and 37.5 krpm. The fluid film pressure is increasing with the rotational speed potentially due to

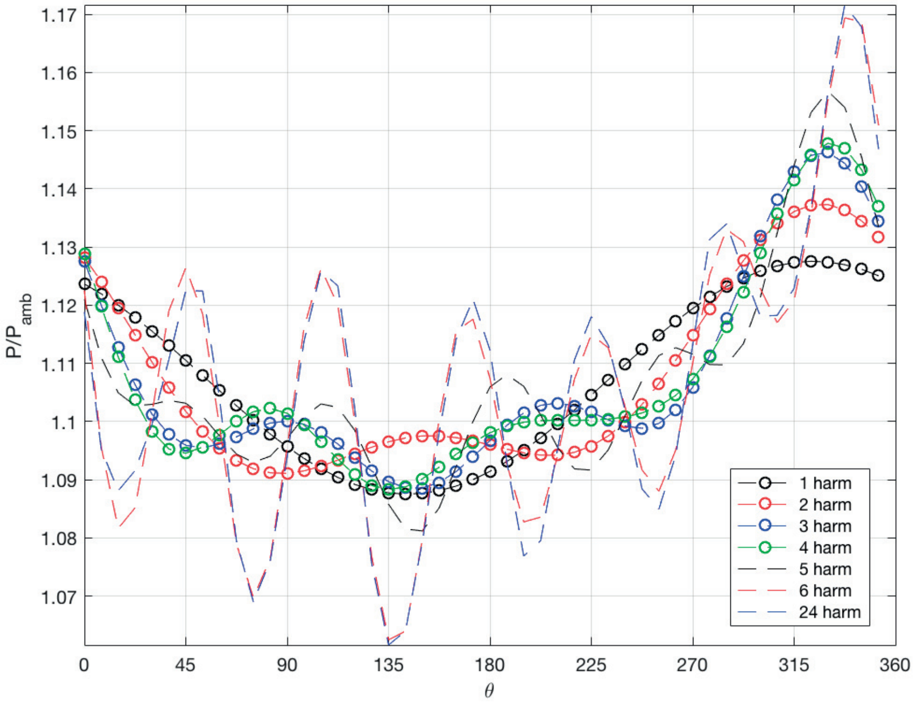

Figure 6.13 – Pressure profile evolution with increasing number of harmonics used in signal reconstruction. Increasing the number of harmonics used in the signal reconstruction beyond 6 does not bring further improvement to the reconstructed signal.

the centrifugal growth of the rotor, as well as the increasing rotor orbit that grows by 120% between 20 krpm and 37.5 krpm. The pressure profiles at the bearing center are larger in magnitude than the profiles at $\overline{z}$ = -0.5 - figure 6.15. The measured profiles are not adopting a smooth bell-shaped pressure profile probably due to the significant lack of circularity of the bearing under investigation. Instead, five pressure peaks are observed both at $\overline{z}$ = 0, and -0.5,. The peaks in pressure match in position for the profiles measured at $\overline{z}$ = 0, and -0.5, it is worth noting here that the profiles are measured with different probes, and reconstructed using different transfer functions. Hence, yielding further confidence in the measurement and the signal reconstruction. Subambient pressure is observed only near the trailing edge of the top foil at 15, and 25 krpm.

The two measured profiles are used to estimate the bearing load. The profile measured at $\overline{z}$ = -0.5 is assumed to be equal to the profile at $\overline{z}$ = 0.5 (symmetric assumption). By integrating the pressure field a load of 6.8 N is estimated, which is approximately 70% of the fraction of rotor weight acting on the bearing. Given the large interpolations involved in this procedure, as well as the optimistic symmetric assumption, the result was found satisfactory.

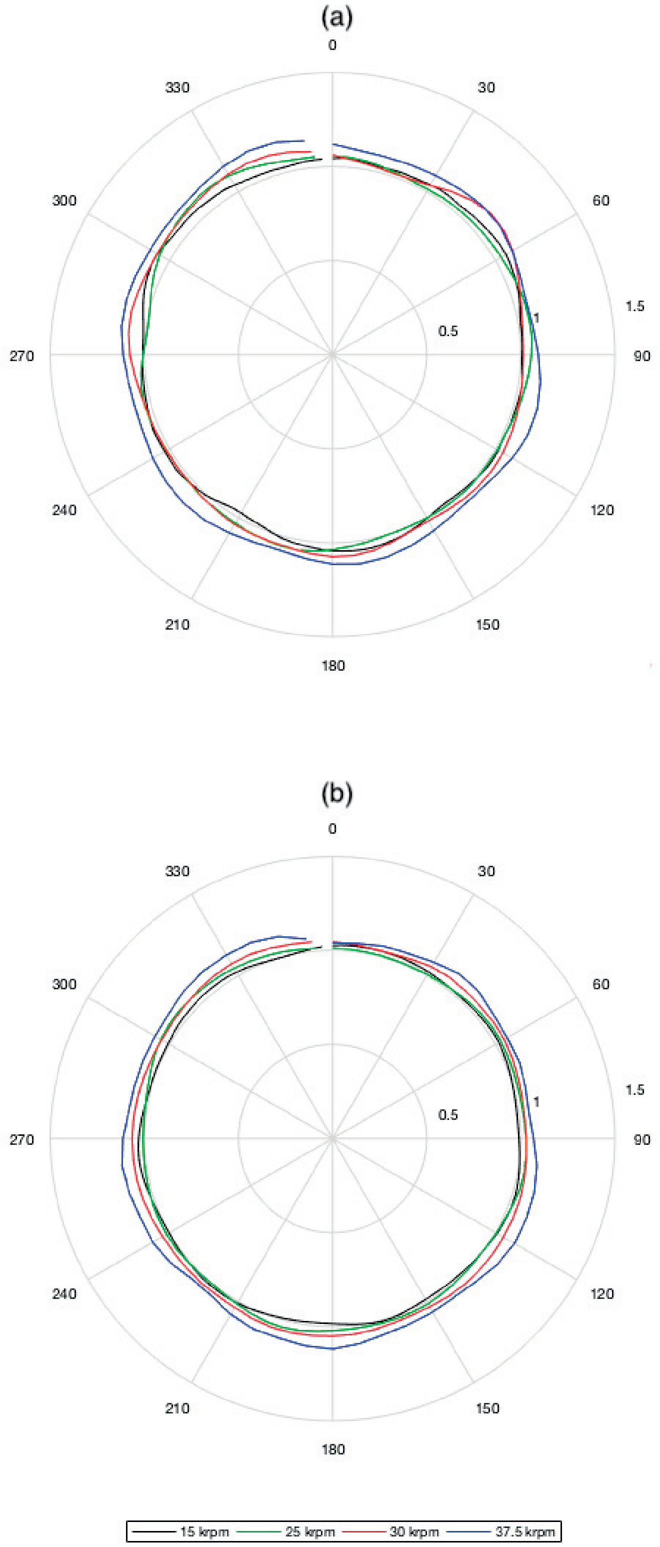

Figure 6.14 – GFJB pressure profiles measured at at different rotational speeds at (a) $\overline{z} = 0$, and (b) $\overline{z} = -0.5$. Refer to figure 6.2 for reference coordinates.

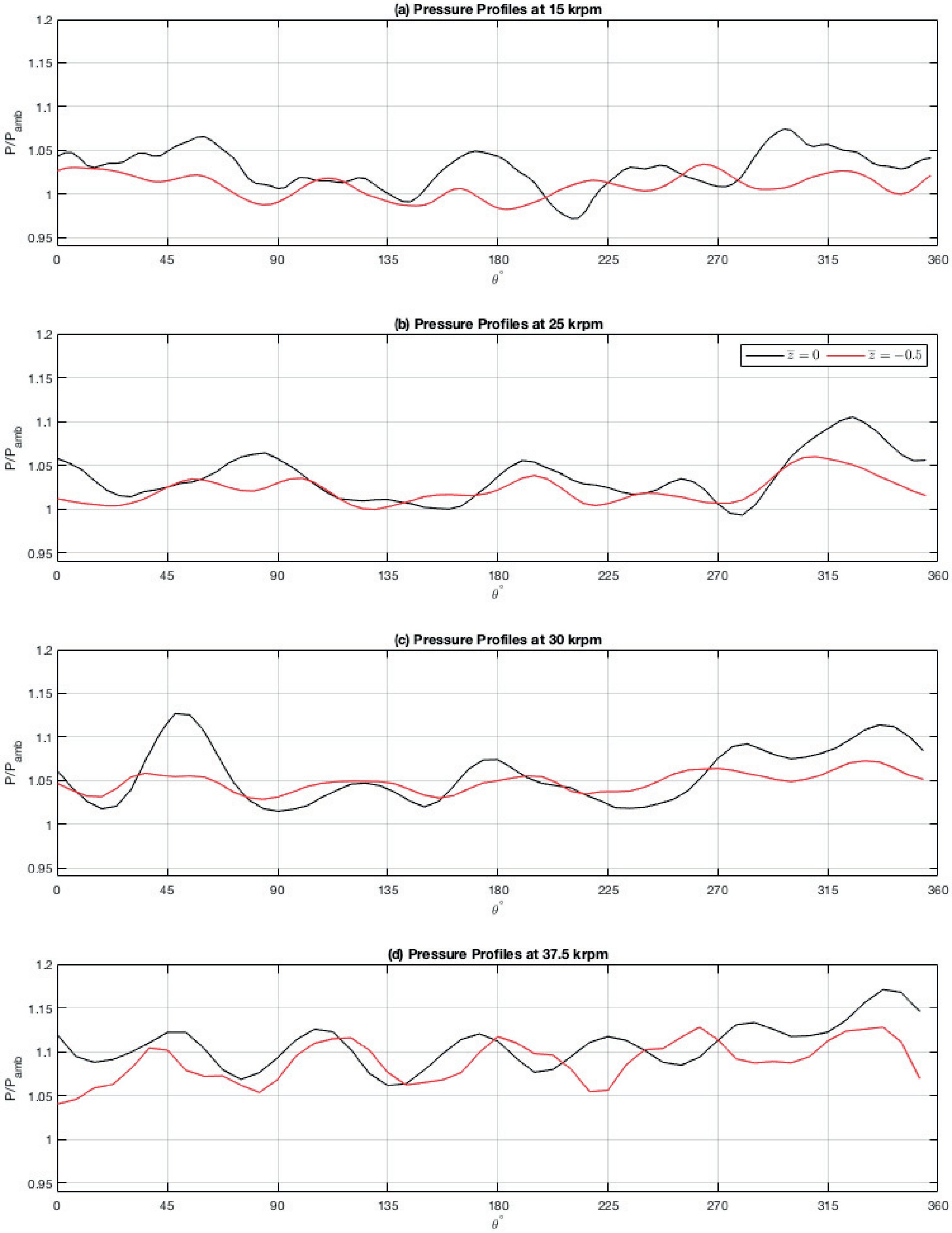

Figure 6.15 – Comparison of pressure profiles measured at $\overline{z} = 0$, and -0.5 at different rotational speeds.

6.8 Model Description

A validation attempt is presented through the use of the foil bearing model proposed by Kim and San Andrés [129], and adopted by Schiffmann and Spakovszky [115]. The model adopts the frequency domain method; hence it is incapable of simulating the time domain orbit evolution or of predicting limit cycles beyond the onset speed of instability. The model solves the compressible Reynolds equation using the perturbation method of Lund [130]. Small perturbations around an eccentric rotor are introduced to yield partial differential equations for the zeroth and first order pressure perturbations. The partial differential equations are solved using the finite element method of Faria and San Andrés [131] and Faria [132]. Integration of the zeroth order pressure field yields the static force components for a given static eccentricity. The integration of the first order terms of the pressure field determines the direct and the cross-coupled stiffness and damping coefficients. The bearing parameters simulated are summarized in table 6.1. The model is also capable of simulating the effect of shimming (local disturbance of the circularity of the bearing). The position and height of the shim are given as input to the model.

Table 6.1 – Foil bearing model parameters

Foil bearing parameters	
D [mm]	60
L/D [-]	1
C [μm]	30
$\alpha_{\mathbf{comp}}$ **[-]**	0.67
γ**[-]**	0.14
$\alpha_{\mathbf{D}}$ **[$\circ$]**	63.15
t [mm]	0.1
Fluid	Air
Ambient Pressure [kPa]	101.325

6.9 Model Validation Attempt

Comparing the measured and estimated pressure profiles at the bearing center - figure 6.16, a clear mismatch is observed. The model's pressure profile is of a classic bell-shaped form, with the peak pressure towards the attitude angle. Based on the outcome of chapter 5, it is hypthesized that this apparent mismatch is a consequence of the geometrical deviations induced by the manufacturing process. This is also suggested supported by figure 6.3. An attempt to match the measurements was executed using shimming patterns along the rotor circumference in order to disturb the bearing circularity. The result of the simulation highlights the potentials for qualitatively similar pressure profiles once the perfect circularity assumption is omitted - figure6.16. The shimming pattern is described as 9, 21, and 21 μm thick shims, at 40, 270, and 320° from the feedline. Similar estimated pressure profiles were presented by Kim and San Andres [15] for a shimmed (non-circular) GFJB.

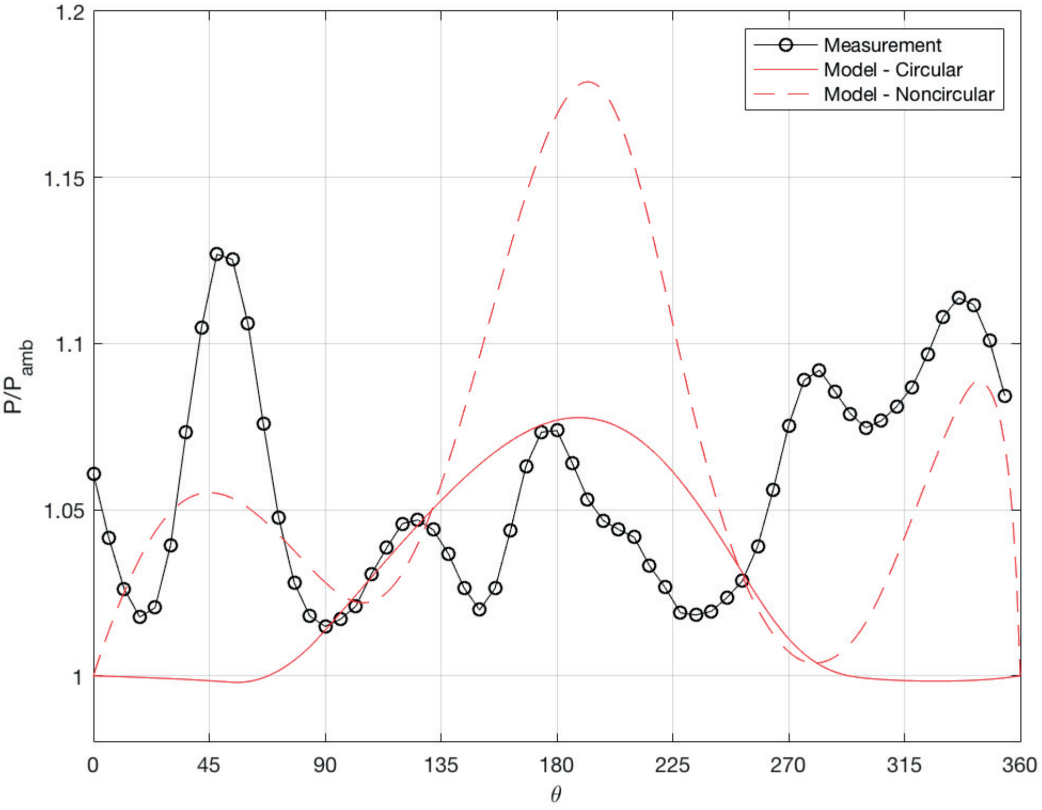

Figure 6.16 – Comparison of measured and predicted pressure profiles for circular and non-circular GFJBs.

6.10 Bearing Loading

In an attempt to consolidate the measurement campaign, it was decided to load the GFJBs during the pressure measurement. A simple foil under tension is wrapped around the rotor and pulled using the loading mechanism described in chapter 2. It is worth mentioning that such loading concept is the basis from which stemmed the compliant foil bearing technology. Such concept was first presented by Blok and vanRossum in 1953 [80]. Figure 6.17 shows a photograph of the loaded instrumented rotor.

The test GFJB was loaded with 30 N, at 270°, while rotating at 35 krpm. The pressure profiles were measured at steady-state conditions. A pressure peak was observed at 280°. In a second attempt to validate the foil bearing model, a comparison is presented in figure xx. It can be clearly observed that the model matches the pressure measurements with good accuracy only at the loaded region. Similar behavior was observed by several authors [135, 137, 138] in their attempt to validate their proposed models using the fluid film thickness measurement of Ruscitto [3].

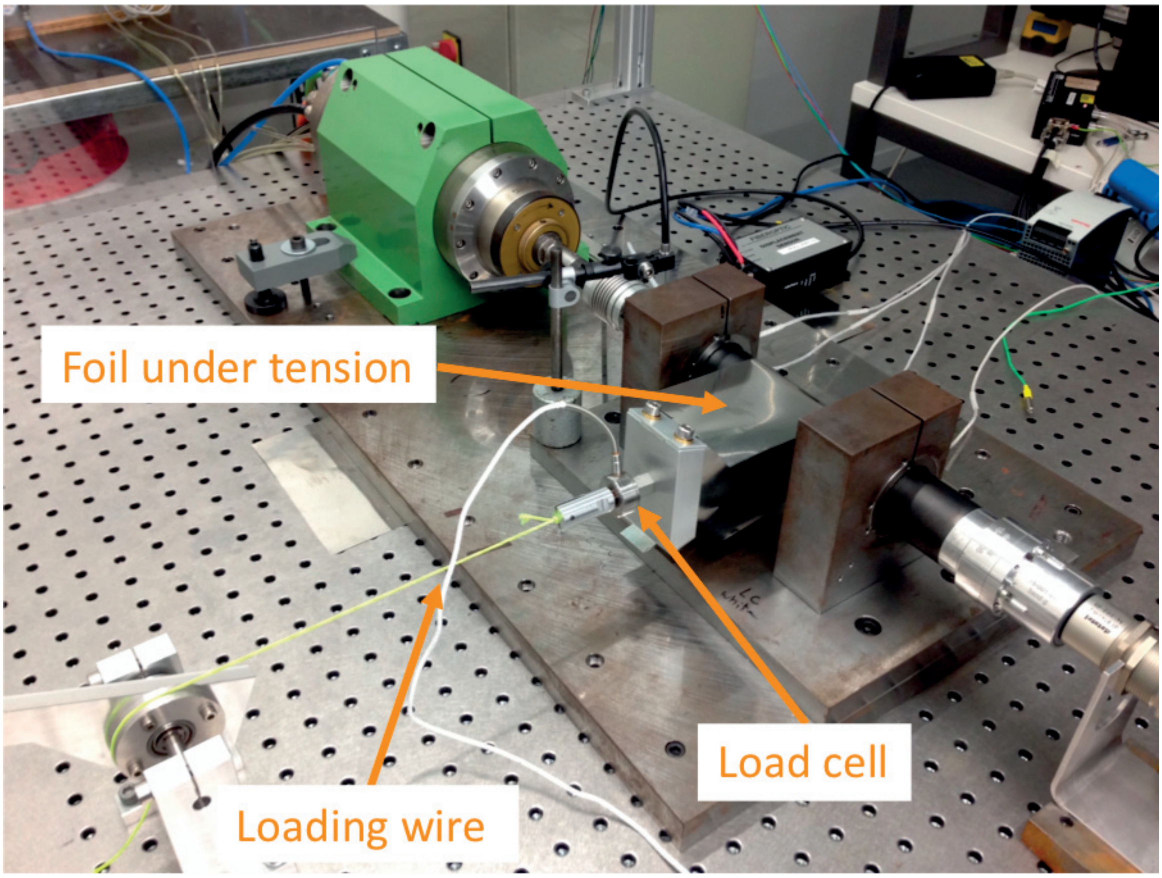
Foil under tension
Load cell
Loading wire

Figure 6.17 – Photograph of the instrumented rotor supported on GFJBs and loaded using a simple foil under tension.

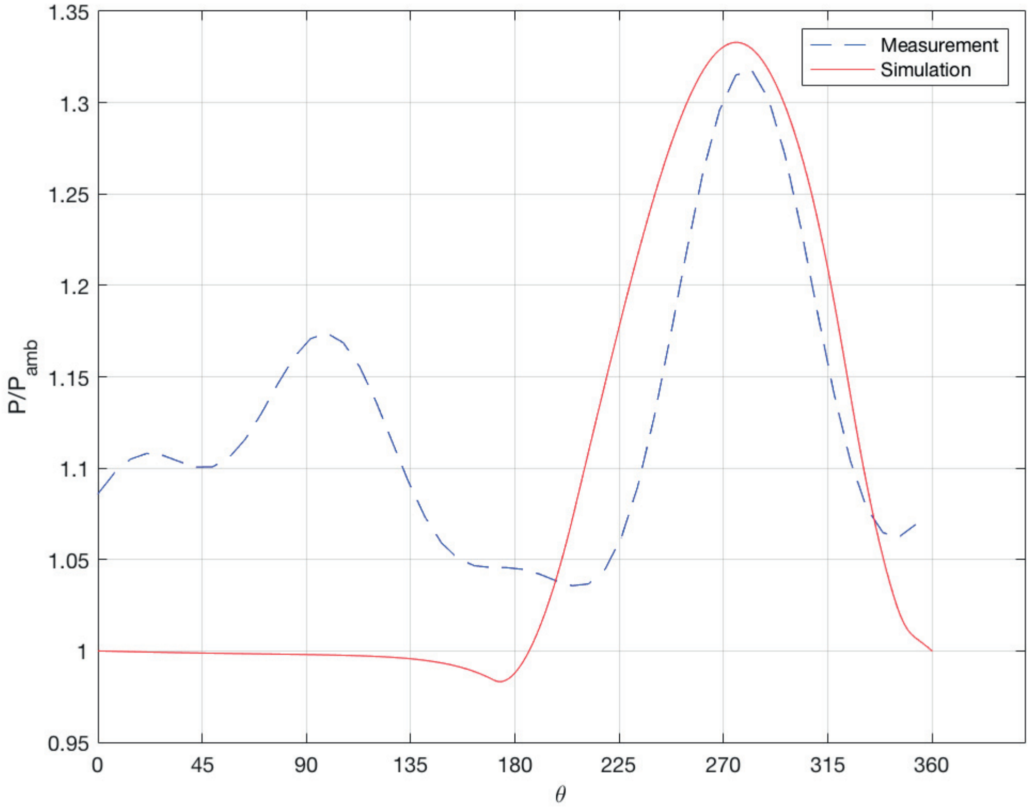

Figure 6.18 – Loaded pressure profile measured at 35 krpm and 30 N in the middle of the GFJB and compared to the model predicted pressure profile.

6.11 Chapter Conclusions

The chapter presented results of an experimental measurement campaign focused on GFJBs. The bearing characteristics under investigation were identified using geometrical measurements, load-displacement tests, and preload estimation. The rotordynamic response of the instrumented rotor supported on GFJBs highlighted the stable operation of the rotor, the critical speed at approximately 9 krpm, and the growing rotor orbit. The liftoff speed is estimated to be 21 and 13 krpm for the front and back bearings respectively.

The measured pressure profiles within the fluid film are not adopting a classical bell-shaped profile at light loading condition (9 N). A comparison between the foil bearing model of Schiffmann and Spakovszky [115] highlighted large discrepancy between measurement and simulation at these conditions. After loading the bearing by 30 N at 35 krpm, the comparison between the model and the measurements were in a very good agreement at the loaded region of the bearing. It is concluded that given the nature of compliant foil bearings, lightly loaded fluid film measurements are difficult to match using foil bearing models due to the high level of uncertainty resulting mainly from manufacturing and misalignment errors. The influence of such errors is less pronounced on the fluid film once the bearing is significantly loaded.

7 Epilogue

7.1 Summary

This thesis presented pressure profile measurements within the gas film of EPGJBs and GFJBs. After describing the test rig used in this experimental campaign, an instrumented rotor design was presented. The rotor is equipped with embedded pressure probes and a wireless telemetry system. The remote mounting of the pressure transducers within the embedded probes distorts the measured signal through attenuation and phase lag. Special effort was dedicated to the system identification and calibration of the probes. At quasi-static conditions the measured signal from the probe matches the pressure profile measured through an EPGJB equipped with pressure taps that covers the bearing circumference. At rotating conditions, the probes were identified by a transfer function, which is later used to reconstruct the distorted signal. The instrumented rotor was tested up to 37.5 krpm on EPGJBs.

The instrumented rotor was used to investigate the performance of EPGJBs equipped with pressure taps capable of measuring the axial and circumferential pressure profiles. The measured pressure profiles were used to validate the model of Lo et al. [70]. The effects of manufacturing errors in the supply nozzles and the clearance were highlighted through the measurement, and confirmed through the model. The empirical discharge coefficient model developed by Belforte et al. [1] did not match the measured mass flow rates through the bearing's micro supply nozzles. The inadequacy of the discharge coefficient model along with manufacturing deviations due to the finite tolerance fields were the reason behind a mismatch in measured and estimated load capacity. The instrumented rotor confirmed the imperfection of the bearing under investigation through a complete pressure field measurement. The effect of the rotational speed increased the pressure along the circumference due to the centrifugal growth of the rotor.

A review of the available knowledge in the fabrication of foil bearings was presented. It was shown that the available know-how is not sufficient for the accurate manufacturing of foil bearings. The bump foil compliance was shown to be sensitive to the bump angle and radius, even for small errors of bump geometry (5% error in compliance for each 1% error in bump radius). A manufacturing procedure was selected using forming dies adopting the overall curvature of the bump foil. Due to the complexity of the bump foil shape, an optical measurement technique was developed for the purpose of the detailed geometrical measurement of the formed bump foils. Consequently, a DoE approach was used to identify the effect of heat treatment temperature, duration, and forming pressure on the foil springback. A FE model was developed to simulate the forming process of the foil inside the die. Manufacturing uncertainties manifested as springback were quantified statistically, and different compliant structures were investigated from a manufacturing perspective.

The instrumented rotor and the manufactured GFJBs were then used in an experimental measurement campaign. The GFJB characteristics under investigation were identified using geometrical measurements, load-displacement tests, and preload estimation. The rotordynamic response of the instrumented rotor supported on GFJBs highlighted the stable operation of the rotor, the critical speed at approximately 9 krpm, and the growing rotor orbit due to imbalance. The liftoff speed is estimated to be 21 and 13 krpm for the front and back bearings respectively. The measured pressure profiles within the fluid film did not adopt a classical bell-shaped profile. A comparison between the foil bearing model of Schiffmann and Spakovszky [115] highlighted large discrepancy between measurement and simulation at light loads. However, a much better agreement was found for loaded pressure profiles, precisely at the loaded region of the bearing.

7.2 Deductions

The observations of the experimental campaigns presented in this thesis created a foundation for several deductions.

The currently adopted manufacturing techniques used in the fabrication of foil bearings yield inaccurate foil bearing geometries, which as a consequence affects the local bearing clearance (circularity), and compliance. It was found that even with the observed manufacturing inaccuracies, the foil bearings were able to perform in a stable manner (no significant subsynchronous vibrations) at least up to 37.5 krpm. Hence, it can be deduced that there is no need for highly accurate rotor manufacturing with tight tolerances. The rotors used in the experimental campaigns had diameters within ± 1 μm, which is deemed unnecessary given the large deviations in the GFJB diameters ± 150 μm. The geometrical deviations influence the performance of the manufactured bearing, it is therefore found necessary to test each manufactured GFJB before system integration and assembly. Cantilever type foil bearing exhibit the potentials for higher accuracy manufacturing.

Unlike rigid journal bearings, and given the the intrinsic compliance of GFJBs, the clearance is a rather murky concept. However, the concept of preload pressure estimation is more robust. It is suggested to identify GFJBs by preload instead of assembly clearance. Higher preload entails a higher stability threshold, on the expense of higher startup torque, and higher risks of thermal seizures. Applications requiring high speed operations, with a low number of intermissions (start-stop) shall adopt highly preloaded GFJBs. On the other hand applications with a relatively low speed, and a significant number of intermissions, would rather require a low level of preload.

Manufacturing plays a pivotal role in the performance of EPGJBs. Observing the measured pressure field within the gas film of the bearing, it was found non-symmetric, and skewed. Such imperfections affects the bearing properties both statically (load carrying capacity), and dynamically (critical speed, and stability). It is important for the designer to account for these imperfections through an appropriate factor of safety.

The stiffness of GFJBs is mainly governed by the stiffness of the underlying compliant structure (bump, cantilever beam), which is approximately an order of magnitude lower than the stiffness of the gas film (once established). Hence, the critical speed of the rotor is expected at relatively low speeds. Therefore, even at the case of an intermittent touch down (boundary or mixed lubrication), the critical speed could be crossed even with a high amplitude dynamic response.

The observed mismatch at light loading between the measured pressure profiles within the gas film of GFJBs and the numerically estimated profiles in chapter 6 can be attributed to several points:

1. The lack of circularity of the foil bearing. A fundamental assumption in the model is a fully circular bearing.
2. The light loading of the foil bearing that pollutes the pressure profile.
3. The potentials for misalignment that would load the GFJBs at locations other than the weight load direction.
4. The increasing rotor orbit due to unbalance, which is not taken into account in the simulation.
5. The use of three bump foil pads, with a change in bump pitch between foils, that would locally decrease compliance.
6. The unequal distribution of compliance along the bearing circumference due to bump foil manufacturing errors.

By tackling the second point and loading the bearing, a more pronounced pressure profile was observed. The model results in that case were in good agreement with the measurements at the loaded region in the bearing. Loading the bearing creates a pressure peak that is larger in magnitude than the other potential sources of measurement uncertainty. It is concluded that fluid film measurements in foil bearings manufactured using current manufacturing techniques -namely sheet metal forming- will require a significant load in order to produce data valuable for model validation and development purposes.

7.3 Impact and Relevance

The scientific and engineering outputs of this thesis extend the understanding of gas foil bearings, which in turn paves the way for the future exploitation of the technology to support more challenging machineries. Validating foil bearing models will enable a a better understanding of the different physical phenomena governing the performance of the bearings. Falsifying other foil bearing models would highlight flaws in methodology, assumptions, and simplifications. The measurements also serve as a platform to develop models and to identify the necessary level of details (model complexity) required for the accurate simulation of the physics. Discussing the manufacturing of foil bearings serves as a guide for designers and engineers aiming to adopt this peculiar technology in their machines.

Due to their simplicity, and facultative maintenance requirements, foil bearings can enable technologies to support deep space exploration and planetary settlements. The nuclear and solar driven closed-loop Brayton cycle is an example of these technologies [139]. At the other end of the spectrum, foil bearings can also enable cheap energy conversion machines for emerging markets. Incorporating foil bearings to support aircraft engines will increase power density, and consequently decrease carbon emissions [140]. The technology is capable of supporting decentralized cogeneration energy production, which when coupled with smart grid and IoT technologies yield a sustainable and futuristic perspective of energy exploitation.

7.4 Future Work

The results of this thesis paves the road for future fundamental gas bearing research addressing both EPGJBs and GFJBs. The future work involves experimental and modeling efforts, which together shall eventually bring closure to several open issues.

The recommended future work on GFJBs includes:

1. Integrating embedded gap and a temperature sensors along with the pressure probes within the instrumented rotor for the simultaneous measurement of the pressure, temperature, and film thickness. The measured film thickness shall be used as input for foil bearing models. The resulting pressure and temperature profiles shall be fairly compared to the measurements. Such approach would be considered an accurate validation procedure for any foil bearing model.
2. Loading and heating the bearing during measurements the fluid film measurement would yield further insight into the foil bearing performance.
3. Exciting the instrumented rotor using shakers or onboard stingers in order to measure fluid film data at different excitation frequencies for a given rotor speed.
4. Developing other techniques for pressure and temperature measurements within the gas film of GFJBs from the top foil side.

5. More efforts shall be exerted to produce more accurate and robust manufacturing of compliant GFJBs.
6. The instrumented rotor shall be used to investigate fluid film data within GFJBs of different shapes and features (e.g. grooved, externally pressurized, and controllable foil bearings)

The recommended future work on EPGJBs includes:

1. Further research should be directed towards the development of more universal discharge coefficient models, which includes micro-holes ($\varnothing \leq 0.1$ mm), and large l/d restrictors.
2. Identifying the ideal manufacturing techniques to manufacture micro supply nozzles with a high accuracy and robustness.

Bibliography

[1] G. Belforte, F. Colombo, T. Raparelli, A. Trivella, and V. Viktorov, "High-speed electrospindle running on air bearings: design and experimental verification," *Meccanica*, vol. 43, pp. 591–600, Dec. 2008.

[2] I. Iordanoff, "Analysis of an Aerodynamic Compliant Foil Thrust Bearing: Method for a Rapid Design," *Journal of Tribology*, vol. 121, pp. 816–822, Oct. 1999.

[3] D. Ruscitto, J. Mccormick, and S. Gray, "Hydrodynamic air lubricated compliant surface bearing for an automotive gas turbine engine. 1: Journal bearing performance," tech. rep., Apr. 1978.

[4] D. I. Stern, "Economic Growth and Energy," in *Encyclopedia of Energy* (C. J. Cleveland, ed.), pp. 35–51, New York: Elsevier, Jan. 2004.

[5] P. Alstone, D. Gershenson, and D. M. Kammen, "Decentralized energy systems for clean electricity access," *Nature Climate Change*, vol. 5, p. 305, Mar. 2015.

[6] A. D. Hawkes and M. A. Leach, "Cost-effective operating strategy for residential micro-combined heat and power," *Energy*, vol. 32, pp. 711–723, May 2007.

[7] C. Carcasci, R. Ferraro, and E. Miliotti, "Thermodynamic analysis of an organic Rankine cycle for waste heat recovery from gas turbines," *Energy*, vol. 65, pp. 91–100, Feb. 2014.

[8] EUTurbines, "A Roadmap on Turbomachinery Research," tech. rep., EUTurbines, Sept. 2012.

[9] G. L. Agrawal, "Foil air/gas bearing technology—an overview," in *ASME 1997 International Gas Turbine and Aeroengine Congress and Exhibition*, pp. V001T04A006–V001T04A006, American Society of Mechanical Engineers, 1997.

[10] H. Heshmat, M. J. Tomaszewski, and I. Walton, James F., "Small Gas Turbine Engine Operating With High-Temperature Foil Bearings," pp. 387–393, Jan. 2006.

[11] A. Gu, "Cryogenic foil bearing turbopumps," in *32nd Aerospace Sciences Meeting and Exhibit*, Aerospace Sciences Meetings, American Institute of Aeronautics and Astronautics, Jan. 1994.

[12] J. L. Wade, D. R. Lubell, and D. Weissert, "Successful Oil-Free Version of a Gas Compressor Through Integrated Design of Foil Bearings," pp. 969–973, Jan. 2008.

[13] Y.-B. Lee, S. Bum Kwon, T. H. Kim, and K. Sim, "Feasibility Study of an Oil-Free Turbocharger Supported on Gas Foil Bearings Via On-Road Tests of a Two-Liter Class Diesel Vehicle," *Journal of Engineering for Gas Turbines and Power*, vol. 135, pp. 052701–052701–10, Apr. 2013.

[14] L. S. Andrés, D. Rubio, and T. H. Kim, "Rotordynamic Performance of a Rotor Supported on Bump Type Foil Gas Bearings: Experiments and Predictions," *Journal of Engineering for Gas Turbines and Power*, vol. 129, pp. 850–857, Dec. 2006.

[15] T. H. Kim and L. S. Andrés, "Effects of a Mechanical Preload on the Dynamic Force Response of Gas Foil Bearings: Measurements and Model Predictions," *Tribology Transactions*, vol. 52, pp. 569–580, June 2009.

[16] L. San Andres and T.-H. Kim, "Issues on Instability and Force Nonlinearity in Gas Foil Bearing Supported Rotors," in *43rd AIAA/ASME/SAE/ASEE Joint Propulsion Conference & Exhibit*, p. 5094, 2007.

[17] T. Mai, "Technology Readiness Level," May 2015.

[18] K. Radil and M. Zeszotek, "An Experimental Investigation into the Temperature Profile of a Compliant Foil Air Bearing," *Tribology Transactions*, vol. 47, pp. 470–479, Jan. 2004.

[19] S. von Osmanski, J. S. Larsen, and I. F. Santos, "A fully coupled air foil bearing model considering friction – Theory & experiment," *Journal of Sound and Vibration*, vol. 400, pp. 660–679, July 2017.

[20] K. Sim and J. Park, "Performance Measurements of Gas Bearings With High Damping Structures of Polymer and Bump Foil Via Electric Motor Driving Tests and One Degree-of-Freedom Shaker Dynamic Loading Tests," *Journal of Engineering for Gas Turbines and Power*, vol. 139, pp. 092504–092504–12, Apr. 2017.

[21] S. A. Howard, "A New High-Speed Oil-Free Turbine Engine Rotordynamic Simulator Test Rig," tech. rep., Jan. 2007.

[22] H. Heshmat, I. Walton, James F., and C. A. Heshmat, "On the Coupling of Foil Bearing Supported Rotors: Part 1 — Analysis," pp. 943–950, Jan. 2007.

[23] M. J. Tomaszewski, I. Walton, James F., and H. Heshmat, "On the Coupling of Foil Bearing Supported Rotors: Part 2 — Experiment," pp. 951–960, Jan. 2007.

[24] Y. S. Ho and N. N. S. Chen, "Performance characteristics of a capillary-compensated hydrostatic journal bearing," *Wear*, vol. 52, pp. 285–295, Feb. 1979.

[25] Y. S. Ho and N. N. S. Chen, "Pressure distribution in a six-pocket hydrostatic journal bearing," *Wear*, vol. 98, pp. 89–100, Nov. 1984.

[26] J. Tonnesen and P. K. Hansen, “Some Experiments on the Steady State Characteristics of a Cylindrical Fluid-Film Bearing Considering Thermal Effects,” *Journal of Lubrication Technology*, vol. 103, pp. 107–114, Jan. 1981.

[27] J. B. Roberts and P. J. Mason, “An Experimental Investigation of Pressure Distributions in a Journal Bearing Operating in the Transition Regime,” *Proceedings of the Institution of Mechanical Engineers, Part C: Journal of Mechanical Engineering Science*, vol. 200, pp. 251–264, July 1986.

[28] L. J. Read and R. D. Flack, “Temperature, pressure and film thickness measurements for an offset half bearing,” *Wear*, vol. 117, pp. 197–210, June 1987.

[29] N. Wang, Q. Meng, P. Wang, T. Geng, and X. Yuan, “Experimental Research on Film Pressure Distribution of Water-Lubricated Rubber Bearing With Multiaxial Grooves,” *Journal of Fluids Engineering*, vol. 135, pp. 084501–084501–6, June 2013.

[30] W. Uffrecht and E. Kaiser, “Influence of Force Field Direction on Pressure Sensors Calibrated at Up to 12,000 g,” *Journal of Engineering for Gas Turbines and Power*, vol. 130, pp. 061602–061602–8, Aug. 2008.

[31] V. E. Bean, “Dynamic Pressure Metrology,” *Metrologia*, vol. 30, no. 6, p. 737, 1994.

[32] J. P. Damion, “Means of Dynamic Calibration for Pressure Transducers,” *Metrologia*, vol. 30, no. 6, p. 743, 1994.

[33] G. Persico, P. Gaetani, and A. Guardone, “Dynamic calibration of fast-response probes in low-pressure shock tubes,” *Measurement Science and Technology*, vol. 16, no. 9, p. 1751, 2005.

[34] J. Lally and D. Cummiskey, “Dynamic pressure calibration,” *SENSORS-PETERBOROUGH-*, vol. 20, no. 4, pp. 15–21, 2003.

[35] A. Diniz, A. Oliveira, J. Vianna, and F. Neves, “Dynamic calibration methods for pressure sensors and development of standard devices for dynamic pressure,” in *XVIII Imeko World Congress Metrology. Rio de Janeiro, Brazil*, pp. 17–22, 2006.

[36] W. C. Bentley and J. J. Walter, *Dynamic response testing of transient pressure transducers for liquid propellant rocket combustion chambers.* PhD thesis, Princeton University, 1963.

[37] G. Paniagua and R. Dénos, “Digital compensation of pressure sensors in the time domain,” *Experiments in Fluids*, vol. 32, pp. 417–424, Apr. 2002.

[38] S. H. Wang, L. L. Han, and T. T. Tsung, “Dynamic Pressure Calibration of Pressure Sensors Using Liquid Step Pressure Generator,” 2010.

[39] R. E. Robinson, “Improvement of a large-amplitude sinusoidal pressure generator for dynamic calibration of pressure transducers,” tech. rep., Feb. 1972.

[40] T. Kobata and A. Ooiwa, “Square-wave pressure generator using a novel rotating valve,” *Metrologia*, vol. 36, no. 6, p. 637, 1999.

[41] D. Allegret-Bourdon, D. M. Vogt, and T. H. Fransson, “A new test facility for investigating fluid-structure interactions using a generic model,” in *Proceedings of the 16th Symposium on Measuring Techniques in Transonic and Supersonic Flow in Cascades and Turbomachines, Cambridge, UK*, 2002.

[42] P. A. H. Bolt, “Portable dynamic pressure generator for static and dynamic calibration of in situ pressure transducers,” tech. rep., Aug. 1983.

[43] J. L. Waldeck, “The development of a portable pressure source for the static and dynamic calibration of pressure transducers,” *Journal of Wind Engineering and Industrial Aerodynamics*, vol. 26, no. 2, pp. 213–230, 1987.

[44] T. A. Perls, D. O. Miles, and L. B. Wilner, “Sinusoidal Pressure Generator with Wide Amplitude and Frequency Ranges,” *The Journal of the Acoustical Society of America*, vol. 32, pp. 274–281, Feb. 1960.

[45] J. L. Schweppe, L. C. Eichberger, D. F. Muster, E. L. Michaels, and G. F. Paskusz, “Methods for the dynamic calibration of pressure transducers,” 1963.

[46] J. Fridh, T. Fransson, N.-E. Andersson, and P. Magnusson, “REDUNDANT ROTATING MEASUREMENTS IN AN AXIAL COLD FLOW TEST TURBINE: Development and Procedure,” in *The XVIII Symposium on Measuring Techniques in Turbomachinery, Thessaloniki, Greece 2006*, 2006.

[47] S. Beresh, J. Henfling, R. Spillers, and B. Pruett, “Measurement of Fluctuating Wall Pressures Beneath a Supersonic Turbulent Boundary Layer,” in *48th AIAA Aerospace Sciences Meeting Including the New Horizons Forum and Aerospace Exposition*, Aerospace Sciences Meetings, American Institute of Aeronautics and Astronautics, Jan. 2010.

[48] D. Greenblatt, J. Kiedaisch, and H. Nagib, “Unsteady-pressure corrections in highly attenuated measurements at moderate mach numbers,” in *15th AIAA Computational Fluid Dynamics Conference*, p. 2983, 2001.

[49] D. B. Sims-Williams and D. A. Luck, “Transfer function characterization of pressure signal tubes for the measurement of large amplitude pressure fluctuations,” *Proceedings of the Institution of Mechanical Engineers, Part C: Journal of Mechanical Engineering Science*, vol. 221, pp. 707–713, June 2007.

[50] H. Dishan, “Phase error in fast Fourier transform analysis,” *Mechanical Systems and Signal Processing*, vol. 9, pp. 113–118, Mar. 1995.

[51] J. K. Thompson and D. R. Tree, “Leakage error in Fast Fourier analysis,” *Journal of Sound and Vibration*, vol. 71, pp. 531–544, Aug. 1980.

[52] X. Ming and D. Kang, “CORRECTIONS FOR FREQUENCY, AMPLITUDE AND PHASE IN A FAST FOURIER TRANSFORM OF A HARMONIC SIGNAL,” *Mechanical Systems and Signal Processing*, vol. 10, pp. 211–221, Mar. 1996.

[53] D. KANG, X. MING, and Z. XIAOFEI, “PHASE DIFFERENCE CORRECTION METHOD FOR PHASE AND FREQUENCY IN SPECTRAL ANALYSIS,” *Mechanical Systems and Signal Processing*, vol. 14, pp. 835–843, Sept. 2000.

[54] G. Belforte, T. Raparelli, V. Viktorov, A. Trivella, and F. Colombo, “An experimental study of high-speed rotor supported by air bearings: test RIG and first experimental results,” *Tribology International*, vol. 39, pp. 839–845, Aug. 2006.

[55] M. Weck, S. Fischer, and M. Vos, “Fabrication of microcomponents using ultraprecision machine tools,” *Nanotechnology*, vol. 8, no. 3, p. 145, 1997.

[56] W. Haeussermann, “Inertial Instruments with Gas Bearings,” in *Kreiselprobleme / Gyrodynamics*, International Union of Theoretical and Applied Mechanics, pp. 177–192, Springer, Berlin, Heidelberg, 1963.

[57] J. C. Aurich, J. Engmann, G. M. Schueler, and R. Haberland, “Micro grinding tool for manufacture of complex structures in brittle materials,” *CIRP Annals*, vol. 58, pp. 311–314, Jan. 2009.

[58] J. B. Roberts and R. E. Hinton, “Pressure Distributions in a Superlaminar Journal Bearing,” *Journal of Lubrication Technology*, vol. 104, pp. 187–195, Apr. 1982.

[59] F. P. Brito, A. S. Miranda, J. Bouyer, and M. Fillon, “Experimental Investigation of the Influence of Supply Temperature and Supply Pressure on the Performance of a Two-Axial Groove Hydrodynamic Journal Bearing,” *Journal of Tribology*, vol. 129, pp. 98–105, June 2006.

[60] A.-F. Cristea, J. Bouyer, M. Fillon, and M. D. Pascovici, “Pressure and Temperature Field Measurements of a Lightly Loaded Circumferential Groove Journal Bearing,” *Tribology Transactions*, vol. 54, pp. 806–823, Sept. 2011.

[61] P. L. Holster and J. A. H. Jacobs, “Theoretical analysis and experimental verification on the static properties of externally pressurized air-bearing pads with load compensation,” *Tribology International*, vol. 20, pp. 276–289, Oct. 1987.

[62] R. Snoeys and F. Al-Bender, “Development of improved externally pressurized gas bearings,” *KSME Journal*, vol. 1, pp. 81–88, Mar. 1987.

[63] D. Dowson, “Laboratory experiments and demonstrations in tribology,” *Tribology*, vol. 2, pp. 217–220, Nov. 1969.

[64] S. Z. Kassab, E. M. Noureldeen, and M. A. Shawky, “Effects of operating conditions and supply hole diameter on the performance of a rectangular aerostatic bearing,” *Tribology International*, vol. 30, pp. 533–545, July 1997.

[65] G. Belforte, T. Raparelli, V. Viktorov, and A. Trivella, “Discharge coefficients of orifice-type restrictor for aerostatic bearings,” *Tribology International*, vol. 40, pp. 512–521, Mar. 2007.

[66] J. H. Laub, “Externally Pressurized Journal Gas Bearings,” *A S L E Transactions*, vol. 4, pp. 156–171, Jan. 1961.

[67] J. R. Lemon, “Analytical and Experimental Study of Externally Pressurized Air Lubricated Journal Bearings,” *Journal of Basic Engineering*, vol. 84, pp. 159–165, Mar. 1962.

[68] G. E. Burt, “Design of a Wind-Tunnel Roll-Damping Balance Incorporating Externally Pressurized Gas Bearings Operating at Large Film Reynolds Numbers,” Tech. Rep. No. AEDC-TR-69-204, DTIC Document, ARNOLD ENGINEERING DEVELOPMENT CENTER ARNOLD AFB TN, 1969.

[69] E. G. Pink and K. J. Stout, “Orifice Restrictor Losses in Journal Bearings,” *Proceedings of the Institution of Mechanical Engineers*, vol. 193, pp. 47–52, June 1979.

[70] C.-Y. Lo, C.-C. Wang, and Y.-H. Lee, “Performance analysis of high-speed spindle aerostatic bearings,” *Tribology International*, vol. 38, pp. 5–14, Jan. 2005.

[71] E. Guenat and J. Schiffmann, “Real-gas effects on aerodynamic bearings,” *Tribology International*, vol. 120, pp. 358–368, Apr. 2018.

[72] K. J. Stout and W. B. Rowe, “Externally pressurized bearings-design for manufacture,” *Tribology*, vol. 7, pp. 169–180, Aug. 1974.

[73] E. G. Pink and K. J. Stout, “Design procedures for orifice compensated gas journal bearings based on experimental data,” *Tribology International*, vol. 11, pp. 63–75, Feb. 1978.

[74] K. J. Stout, “The Effect of Manufacturing Variations on the Performance of Externally Pressurized Gas-Lubricated Journal Bearings,” *Proceedings of the Institution of Mechanical Engineers, Part C: Journal of Mechanical Engineering Science*, vol. 199, pp. 299–309, Oct. 1985.

[75] J. W. Powell, *Design of aerostatic bearings.* The Machinery Publishing Co. Ltd., 1970.

[76] E. H. Dudgeon and I. R. G. Lowe, “A theoretical analysis of hydrostatic gas journal bearings,” tech. rep., National Research Council Canada, 1965.

[77] W. Beitz and K.-H. Küttner, *Dubbel: Taschenbuch für den Maschinenbau.* Springer-Verlag, Aug. 2013.

[78] D. P. Fleming, W. J. Thayer, and R. E. Cunningham, “Experimental dynamic stiffness and damping of externally pressurized gas-lubricated journal bearings,” Tech. Rep. NASA-TN-D-8270, June 1976.

[79] R. E. Cunningham and E. J. Gunter, “Critical speeds of a rotor in rigidly mounted, externally pressurized, air-lubricated bearings,” Tech. Rep. NASA-TN-D-6350, May 1971.

[80] H. Blok and J. vanRossum, “The foil bearing-a new departure in hydrodynamic lubrication,” vol. 9(6), pp. 316–20, 1953.

[81] H. M. Chen, R. Howarth, W. M. Soyars, J. C. Theilacker, and G. Bernard, “Application of foil bearings to helium turbocompressor,” in *Proceedings of the 30th Turbomachinery Symposium*, pp. 103–114, 2001.

[82] C. DellaCorte, K. C. Radil, R. J. Bruckner, and S. A. Howard, “Design, Fabrication, and Performance of Open Source Generation I and II Compliant Hydrodynamic Gas Foil Bearings,” *Tribology Transactions*, vol. 51, pp. 254–264, May 2008.

[83] B. Dykas, R. Bruckner, C. DellaCorte, B. Edmonds, and J. Prahl, “Design, Fabrication, and Performance of Foil Gas Thrust Bearings for Microturbomachinery Applications,” *Journal of Engineering for Gas Turbines and Power*, vol. 131, pp. 012301–012301, Oct. 2008.

[84] W. Duan, Y. Sun, C. Ding, and L. Yu, “Structural Stiffness of X-750 Alloy Bump Foil Strips for Compliant Foil Bearings With Different Heat Treatments,” *Journal of Tribology*, vol. 138, pp. 031702–031702, Mar. 2016.

[85] F. Ozturk, R. E. Ece, N. Polat, and A. Koksal, “Effect of Warm Temperature on Springback Compensation of Titanium Sheet,” *Materials and Manufacturing Processes*, vol. 25, pp. 1021–1024, Aug. 2010.

[86] L. Zhan, J. Lin, and T. A. Dean, “A review of the development of creep age forming: Experimentation, modelling and applications,” *International Journal of Machine Tools and Manufacture*, vol. 51, pp. 1–17, Jan. 2011.

[87] Y. H. Moon, S. S. Kang, J. R. Cho, and T. G. Kim, “Effect of tool temperature on the reduction of the springback of aluminum sheets,” *Journal of Materials Processing Technology*, vol. 132, pp. 365–368, Jan. 2003.

[88] Z. Tekıner, “An experimental study on the examination of springback of sheet metals with several thicknesses and properties in bending dies,” *Journal of Materials Processing Technology*, vol. 145, pp. 109–117, Jan. 2004.

[89] W. Gan and R. H. Wagoner, “Die design method for sheet springback,” *International Journal of Mechanical Sciences*, vol. 46, pp. 1097–1113, July 2004.

[90] A. P. Karafillis and M. C. Boyce, “Tooling design in sheet metal forming using springback calculations,” *International Journal of Mechanical Sciences*, vol. 34, pp. 113–131, Feb. 1992.

[91] X. A. Yang and F. Ruan, “A die design method for springback compensation based on displacement adjustment,” *International Journal of Mechanical Sciences*, vol. 53, pp. 399–406, May 2011.

[92] T. H. Kim and L. S. Andrés, “Limits for High-Speed Operation of Gas Foil Bearings,” *Journal of Tribology*, vol. 128, pp. 670–673, Feb. 2006.

[93] Y.-B. Lee, C. H. Kim, T. H. Kim, and T. Y. Kim, “Effects of Mesh Density on Static Load Performance of Metal Mesh Gas Foil Bearings,” *Journal of Engineering for Gas Turbines and Power*, vol. 134, pp. 012502–012502–8, Oct. 2011.

[94] Y. Tian, Y. Sun, and L. Yu, “Structural Stiffness and Damping Coefficients of a Multileaf Foil Bearing With Bump Foils Underneath,” *Journal of Engineering for Gas Turbines and Power*, vol. 136, pp. 044501–044501–8, Dec. 2013.

[95] D. Kim, M. S. Hossain, S.-J. Son, C.-J. Choi, and D. Krähenbühl, “Five Millimeter Air Foil Bearing Operating at 350,000 RPM in a Micro Electric Motor Drive,” in *ASME/STLE 2011 Joint Tribology Conference*, pp. 163–166, Jan. 2011.

[96] D. Kim and D. Lee, “Design of Three-Pad Hybrid Air Foil Bearing and Experimental Investigation on Static Performance at Zero Running Speed,” *Journal of Engineering for Gas Turbines and Power*, vol. 132, pp. 122504–122504, Aug. 2010.

[97] J.-h. Song and D. Kim, “Foil Gas Bearing With Compression Springs: Analyses and Experiments,” *Journal of Tribology*, vol. 129, pp. 628–639, Mar. 2007.

[98] J. M. Knight, *An Experimental Study of a Self-Acting Foil Bearing at Low Values of Foil Tension.* Thesis, Monterey, California. Naval Postgraduate School, Sept. 1968.

[99] L. San Andrés, T. A. Chirathadam, and T.-H. Kim, “Measurement of Structural Stiffness and Damping Coefficients in a Metal Mesh Foil Bearing,” *Journal of Engineering for Gas Turbines and Power*, vol. 132, pp. 032503–032503, Dec. 2009.

[100] L. San Andrés, K. Ryu, and T. H. Kim, “Thermal Management and Rotordynamic Performance of a Hot Rotor-Gas Foil Bearings System—Part II: Predictions Versus Test Data,” *Journal of Engineering for Gas Turbines and Power*, vol. 133, pp. 062502–062502–8, Feb. 2011.

[101] T. H. Kim, A. W. Breedlove, and L. San Andrés, “Characterization of a Foil Bearing Structure at Increasing Temperatures: Static Load and Dynamic Force Performance,” *Journal of Tribology*, vol. 131, pp. 041703–041703–9, Sept. 2009.

[102] H.-J. Xu, Z.-S. Liu, G.-H. Zhang, and Y.-L. Wang, “Design and Experiment of Oil Lubricated Five-Leaf Foil Bearing Test-Bed,” *Journal of Engineering for Gas Turbines and Power*, vol. 131, pp. 054505–054505–4, June 2009.

[103] S. Kulkarni, S. D. Naik, K. S. Kumar, M. Radhakrishna, and S. Jana, “Development of Foil Bearings for Small Rotors,” p. V001T05A010, Dec. 2013.

[104] C. DellaCorte, K. C. Radil, R. J. Bruckner, and S. A. Howard, "Design, Fabrication, and Performance of Open Source Generation I and II Compliant Hydrodynamic Gas Foil Bearings," *Tribology Transactions*, vol. 51, pp. 254–264, May 2008.

[105] P. M. Unterweiser, *Heat treater's guide: standard practices and procedures for steel.* American Society for Metals, Aug. 1982.

[106] D. Rubio and L. San Andres, "Structural Stiffness, Dry Friction Coefficient, and Equivalent Viscous Damping in a Bump-Type Foil Gas Bearing," *Journal of Engineering for Gas Turbines and Power*, vol. 129, pp. 494–502, Feb. 2006.

[107] C. DellaCorte, A. R. Zaldana, and K. C. Radil, "A Systems Approach to the Solid Lubrication of Foil Air Bearings for Oil-Free Turbomachinery," *Journal of Tribology*, vol. 126, pp. 200–207, Jan. 2004.

[108] C. Dellacorte, J. A. Fellenstein, and P. A. Benoy, "Evaluation of Advanced Solid Lubricant Coatings for Foil Air Bearings Operating at 25° and 500°C," *Tribology Transactions*, vol. 42, pp. 338–342, Jan. 1999.

[109] C. E. DellaCorte, "NASA PS400: A New Temperature Solid Lubricant Coating for High Temperature Wear Applications," tech. rep., Aug. 2009.

[110] C. Dellacorte, "Composition optimization of chromium carbide based solid lubricant coatings for foil gas bearings at temperatures to 650 C," tech. rep., July 1987.

[111] J.-T. Gau, C. Principe, and M. Yu, "Springback behavior of brass in micro sheet forming," *Journal of Materials Processing Technology*, vol. 191, pp. 7–10, Aug. 2007.

[112] W. D. Carden, L. M. Geng, D. K. Matlock, and R. H. Wagoner, "Measurement of springback," *International Journal of Mechanical Sciences*, vol. 44, pp. 79–101, Jan. 2002.

[113] B. H. Gunter and J. R. Matey, "How Statistical Design Concepts Can Improve Experimentation in the Physical Sciences," *Computers in Physics*, vol. 7, pp. 262–272, May 1993.

[114] G. E. P. Box, *Statistics for Experimenters: Design, Innovation, and Discovery, Second Edition + JMP Version 6 Software Set.* Wiley, July 2009. Google-Books-ID: WOQZPwAACAAJ.

[115] J. Schiffmann and Z. S. Spakovszky, "Foil Bearing Design Guidelines for Improved Stability," *Journal of Tribology*, vol. 135, pp. 011103–011103, Dec. 2012.

[116] A. M. Gad and S. Kaneko, "Tailoring of the bearing stiffness to enhance the performance of gas-lubricated bump-type foil thrust bearing," *Proceedings of the Institution of Mechanical Engineers, Part J: Journal of Engineering Tribology*, p. 1350650115606482, Sept. 2015.

[117] W. Ramberg and W. R. Osgood, "Description of stress-strain curves by three parameters," July 1943.

[118] F. H. Norton, *The Creep of Steel at High Temperatures (Classic Reprint)*. Fb&c Limited, Dec. 2017. Google-Books-ID: olFktAEACAAJ.

[119] R. W. Swindeman, “Isochronous relaxation curves for type 304 stainless steel after monotonic and cyclic strain,” Tech. Rep. CONF-7805108–1, Oak Ridge National Lab., 1978.

[120] S. A. Asgari, M. Pereira, B. F. Rolfe, M. Dingle, and P. D. Hodgson, “Statistical analysis of finite element modeling in sheet metal forming and springback analysis,” *Journal of Materials Processing Technology*, vol. 203, pp. 129–136, July 2008.

[121] P. Chen and M. Koç, “Simulation of springback variation in forming of advanced high strength steels,” *Journal of Materials Processing Technology*, vol. 190, pp. 189–198, July 2007.

[122] M. Samuel, “Experimental and numerical prediction of springback and side wall curl in U-bendings of anisotropic sheet metals,” *Journal of Materials Processing Technology*, vol. 105, pp. 382–393, Sept. 2000.

[123] L. Papeleux and J.-P. Ponthot, “Finite element simulation of springback in sheet metal forming,” *Journal of Materials Processing Technology*, vol. 125-126, pp. 785–791, Sept. 2002.

[124] K. P. Li, W. P. Carden, and R. H. Wagoner, “Simulation of springback,” *International Journal of Mechanical Sciences*, vol. 44, pp. 103–122, Jan. 2002.

[125] J. R. Cho, S. J. Moon, Y. H. Moon, and S. S. Kang, “Finite element investigation on springback characteristics in sheet metal U-bending process,” *Journal of Materials Processing Technology*, vol. 141, pp. 109–116, Oct. 2003.

[126] K. Feng, X. Zhao, Z. Zhang, and T. Zhang, “Numerical and Compact Model of Metal Mesh Foil Bearings,” *Tribology Transactions*, vol. 59, pp. 480–490, May 2016.

[127] R. W. Bosley, *Compliant foil hydrodynamic fluid film radial bearing*. Google Patents, 1995.

[128] N. Prechavut and H. P. Berg, “An experimental study on structural characteristics of cantilever-type foil bearings,” *Deutscher Luft-und Raumfahrtkongress, Rostock*, 2015.

[129] T. H. Kim and L. San Andrés, “Heavily Loaded Gas Foil Bearings: A Model Anchored to Test Data,” *Journal of Engineering for Gas Turbines and Power*, vol. 130, pp. 012504–012504–8, Jan. 2008.

[130] J. W. Lund, “Calculation of Stiffness and Damping Properties of Gas Bearings,” *Journal of Lubrication Technology*, vol. 90, pp. 793–803, Oct. 1968.

[131] M. T. C. Faria and L. S. Andrés, “On the Numerical Modeling of High-Speed Hydrodynamic Gas Bearings,” *Journal of Tribology*, vol. 122, pp. 124–130, Mar. 1999.

[132] M. T. C. Faria, “Some Performance Characteristics of High Speed Gas Lubricated Herringbone Groove Journal Bearings,” *JSME International Journal Series C Mechanical Systems, Machine Elements and Manufacturing*, vol. 44, no. 3, pp. 775–781, 2001.

[133] C. H. Pan, “Spectral analysis of gas bearing systems for stability studies,” Tech. Rep. MTI-64-TR-58, MECHANICAL TECHNOLOGY INC LATHAM NY, 1964.

[134] K. Radil, S. Howard, and B. Dykas, “The Role of Radial Clearance on the Performance of Foil Air Bearings,” *Tribology Transactions*, vol. 45, pp. 485–490, Jan. 2002.

[135] L. San Andrés and T. H. Kim, “Analysis of gas foil bearings integrating FE top foil models,” *Tribology International*, vol. 42, pp. 111–120, Jan. 2009.

[136] C. Dellacorte, V. Lukaszewicz, M. J. Valco, K. C. Radil, and H. Heshmat, “Performance and Durability of High Temperature Foil Air Bearings for Oil-Free Turbomachinery,” *Tribology Transactions*, vol. 43, pp. 774–780, Jan. 2000.

[137] D.-H. Lee, Y.-C. Kim, and K.-W. Kim, “The Static Performance Analysis of Foil Journal Bearings Considering Three-Dimensional Shape of the Foil Structure,” *Journal of Tribology*, vol. 130, pp. 031102–031102–10, June 2008.

[138] K. Feng and S. Kaneko, “Analytical Model of Bump-Type Foil Bearings Using a Link-Spring Structure and a Finite-Element Shell Model,” *Journal of Tribology*, vol. 132, pp. 021706–021706–11, Apr. 2010.

[139] S. A. Howard, R. J. Bruckner, C. DellaCorte, and K. C. Radil, “Gas Foil Bearing Technology Advancements for Closed Brayton Cycle Turbines,” *AIP Conference Proceedings*, vol. 880, pp. 668–680, Jan. 2007.

[140] R. Bruckner, “A Propulsion System Analysis of Oil Free Turbomachinery for Aviation Turbofan Engines,” American Institute of Aeronautics and Astronautics, July 2004.

Curriculum Vitae

Karim Shalash

Born December 20th 1987 in Alexandria (Egypt)
Citizen of Egypt

Education

2013	**Master of Science in Mechanical Engineering** Arab Academy for Science and Technology (Alexandria, Egypt) Thesis "*Numerical Simulation and Investigation of a Novel Gas Turbine Film Cooling Scheme*"
2010	**Bachelor of Science in Mechanical Engineering** Arab Academy for Science and Technology (Alexandria, Egypt) Concentration: Power and Energy

Professional Experience

2013 - present	**Swiss Federal Institute of Technology in Lausanne (EPFL)** Laboratory for Applied Mechanical Design (LAMD) Doctoral Assistant
2012 - 2013	**Optumatics LLC** Engines Development Division CFD Technical Analyst
2011 - 2011	**Suez Canal Container Terminal** Equipment Division Site Mechanical Engineer
2010 - 2011	**Bauer Foundations** Equipment Division Field Mechanical Engineer

Ce document a été imprimé au Centre d’impression EPFL,
imprimerie climatiquement neutre, certifiée myClimate.